THE UNIVERSITY *of* EDINBURGH

A Study of the Post-Translational Modifications of Histone H4 by Fourier Transform Ion Cyclotron Resonance Mass Spectrometry.

Muhammed Karim, *BSc (Hons), MRes*

Part 1

A Thesis Submitted for the Degree of Doctor of Philosophy

School of Chemistry
College of Science and Engineering
The University of Edinburgh

July 2014

Declaration

I declare that this thesis was composed by myself and is based on work carried out at the University of Edinburgh between September 2009 and August 2012. Unless otherwise stated, this work is wholly original and has not been submitted in any form for the award of another degree or professional qualification.

Muhammed Karim

July 2014

Acknowledgements

Firstly I would like to thank Professor Andrew Pitt for offering me a position on the Doctoral Training Centre in Cell and Proteomic Technologies, in spite of my lack of experience in the field of mass spectrometry! I am grateful for the funding provided by the EPSRC and for financial assistance provided by the BMSS.

I wish to express my sincere gratitude to staff at the Scottish Instrumentation and Resource Centre for Advanced Measurement Science (SIRCAMS). I owe a great debt of thanks for Dr Logan Mackay (The Boss) for his support during my time at SIRCAMS. I am grateful to Dr David Clarke (Uncle Dave) for his guidance and willingness to discuss my work at a moments notice. I am also grateful to Dr Stefan Weidt for his technical expertise and to Dr Daniel Winters for assisting me with data analysis.

I would like to thank Dr Bernard Ramsahoye for his initial donation of lactic acid treated samples, and for subsequently training me in the processes of cell culture and histone extraction at the Edinburgh Cancer Research Centre. I am grateful for his continued support and constant interest in my progress. I would also like to thank Jayne Culley of Dr Ramsahoye's group for generating histone samples which formed much of the results presented in Chapter 3 of this thesis.

I would like to acknowledge Professor Dave Goodlett, formerly of the University of Washington for allowing me to work in his laboratory for extended periods alongside his students. I am grateful for his guidance and his willingness to collaborate.

I would like to thank Professor Adrian Bird of The Wellcome Trust Centre for Cell Biology at the University of Edinburgh, first for his donation of histone samples, and more importantly for allowing me to perform the histone extraction procedure on whole mouse brains in his laboratory.

Finally I wish to acknowledge my most distinguished PhD supervisor; a truly unique individual. The one, the only..... Dr Pat Langridge-Smith (The Godfather!).

Abstract

Post-translational modification (PTM) of proteins is known to be a method by which protein function can be regulated. The addition of selected chemical groups at specific amino acid residues can act as a switch by which the function of a modified protein can be attenuated. Histones are a group of proteins which are found in the nucleus of eukaryotic cells and interact with DNA, providing it with a structural foundation upon which the chromosome is built. Histone proteins have numerous sequence variants and are known to be extensively post-translationally modified in a dynamic manner. These modifications have a direct effect on the interacting DNA resulting in increasing or decreasing levels of gene transcription.

Advancements in analytical instrumentation, when coupled to high resolution separation techniques permit the analysis of increasingly complex biological mixtures. Fourier transform ion cyclotron resonance mass spectrometry (FT-ICR MS) offers unrivalled mass resolving power and mass measurement accuracy, allowing the detailed study of mixtures of intact proteins and their post-translational modifications. These features have been exploited to provide a global view of the PTMs of histone proteins.

The work contained within this thesis is a study, by FT-ICR MS, of the modifications of one of the most extensively modified histone proteins; histone H4. Firstly, the modifications of histone H4 were examined after treatment with a potent histone de-acetylase inhibitor across several cell lines. The cell lines chosen showed a varying response to treatment with the inhibitor. From the cell lines tested, two which responded differently were further interrogated to elucidate the order in which acetylation occurs in the N-terminal region.

Secondly, the modifications of histone H4 were analyzed after exposure to lactic acid over multiple treatment times. Lactic acid is a metabolic by-product, and is of interest when considering the Warburg effect and its role in tumorigenesis. Exposure of cells to levels of lactic acid which can be present under anaerobic conditions (i.e. during intense

exercise) showed that lactate is able to inhibit histone de-acetylation. The resulting increase in hyper-acetylated forms of histone H4 could be potentially linked to increased gene expression, a typical observation in tumorigenic cells.

Finally, using a mouse model for the neurological condition Rett Syndrome, the post-translational modifications of histone H4 were investigated. The primary cause of Rett Syndrome is mutation of the DNA binding protein methyl CpG binding protein 2 (MeCP2). MeCP2 has been associated with multiple intracellular functions, one of which is chromatin remodelling. The work carried out showed a link between MeCP2 mutation and tri-methylation of histone H4. In addition, the tri-methylation was not solely identified through the presence of tri-methylated fragments in fragmentation mass spectra. Interestingly, the neutral loss of a methylene group was observed extensively during fragmentation of tri-methylated species. This unreported phenomenon made interpretation of spectra difficult; however, ultimately served as a useful marker for this modification.

Summary

The main purpose of this work was to demonstrate that mass spectrometry, while primarily a technique used in analytical chemistry, could be used as a valuable tool in medical investigation; used here in the study of epigenetics.

Chapter 3 of this thesis demonstrated that mass spectrometry could be used to establish the order in which epigenetic modifications occurred on histone H4, and that while the response of multiple cell lines was different to drug administration, the order in which modifications occurred was consistent.

Chapter 4 showed that lactic acid, a compound produced by the body, could affect histone acetylation and that this could be linked to changes in acetylation profile seen in tumorigenic tissues. The changes in acetylation were observed and quantified by mass spectrometry.

Chapter 5 was a study of the acetylation profile of histone H4seen in patients suffering from the neurological condition Rett Syndrome. It was shown that specific markers for the condition could be observed by mass spectrometry and that these markers could be of diagnostic value.

Each experimental chapter of this thesis demonstrates that mass spectrometry could be a viable tool for use in medical investigation.

Table of Contents

List of Figures

List of Tables

Glossary

m/z	Mass-to-charge ratio
ACN	Acetonitrile
ADP	Adenosine di-phosphate
AML	Acute myeloid leukemia
ANOVA	Analysis of variance
Asp-N	Endoproteinase Asp-N
ATP	Adenosine tri-phosphate
CID	Collision-induced dissociation
CML	Chronic myeloid leukemia
CRM	Charge residue model
Da	Dalton
DA	Bruker Daltonics DataAnalysis software
D-Lac	D-lactate
DMSO	Dimethyl sulfoxide
DNA	Deoxy-ribonucleic acid
DNMT	DNA methyl-transferase
ECD	Electron-capture dissociation
ESI	Electrospray ionisation
EDTA	Ethylenediaminetetraacetic acid
ETD	Electron transfer dissociation
FT	Fourier transform
FT-ICR	Fourier transform-ion cyclotron resonance
FT-ICR MS	Fourier transform-ion cyclotron resonance mass spectrometry
HAT	Histone acetyl-transferase
HDAC	Histone de-acetylase
HDACi	Histone de-acetylase inhibitor
HPLC	High performance liquid chromatography
H1	Histone protein H1
H2a	Histone protein H2a

H2b	Histone protein H2b
H3	Histone protein H3
H4	Histone protein H4
ICR	Ion cyclotron resonance
IEM	Ion evaporation model
IRMPD	Infrared multi-photon dissociation
KO	Knockout
LC	Liquid chromatography
L-Lac	L-lactate
MALDI	Matrix assisted laser desorption / ionisation
MeCP2	Methyl CpG Binding Protein 2
MeOH	Methanol
MME	Mass measurement error
mRNA	Messenger ribonucleic acid
MS	Mass spectrometry
MS/MS	Tandem mass spectrometry
NADH	Reduced form of nicotinamide adenine di-nucleotide
nESI	Nano-electrospray ionisation
PAGE	Poly-acrylamide gel electrophoresis
PDB	Protein data bank
ppm	Parts per million
psi	Pounds per square inch
PTM	Post-translational modification
RF	Radio frequency
RP	Reverse phase
RNA	Ribonucleic acid
SDS	Sodium dodecyl sulfate
T-ALL	T-cell type acute lymphoblastic leukemia
TCA	Trichloroacetic acid
TFA	Trifluoroacetic acid
TOF	Time-of-flight

TSA	Trichostatin A
UHV	Ultra high vacuum
UV	Ultraviolet
WT	Wild type

Chapter 1

Introduction

This introduction provides background information relevant to the work presented in this thesis. A description of the complex biological language of protein post-translational modifications is given, along with detailed information on the proteins chosen for this study; histone proteins. A discussion of various aspects of protein mass spectrometry is given, as well as a full description of the physical principles underlying the instruments used throughout the work. The ultimate aims of the work are listed at the end of the introduction.

The focus of this work was the investigation of the post-translational modifications (PTMs) of histone H4, a protein which plays a crucial role in the process of DNA packaging within the cell. Specifically, this work aims to utilise the many advantages associated with Fourier transform ion cyclotron resonance mass spectrometry to investigate histone PTMs.

Chapter 2 of this thesis describes the materials, methods and instrumentation used throughout the work, and each subsequent chapter presents experimental results.

Chapter 3 examines how acetylation of histone H4 (a common post-translational modification) is altered after exposure to a potent de-acetylase inhibitor. In addition to testing the potency of the compound over numerous cell lines, the order in which N-terminal residues are acetylated is determined.

Chapter 4 of this thesis builds on the results presented in Chapter 3, and focuses on the changes to PTMs after cells were exposed to an endogenous metabolic by-product. The final experimental chapter, Chapter 5, demonstrates the application of high resolution mass spectrometry to investigate the PTMs linked to a neurological condition from

samples which were derived from a primary tissue source, as opposed to the cell cultures used in the work described in the previous chapters.

1.1 Epigenetics

The storage and transmission of information within organisms is critical to the survival of the organism, and affects many of the tasks involved in respiration, damage repair and replication. A common feature across all eukaryotes and many prokaryotes is the method by which information is stored. Macromolecules are used exclusively for information transmission through generations, and for high fidelity storage. While there are several classes of biological macromolecules, only two are used in the transmission and storage of heritable information; nucleic acids and proteins.

When the human genome was fully published in the last decade, it was thought that the key to understanding many diseases lay in the genetic sequence. This has not been the case, and it appeared that information could be passed through generations without altering an organism's genome. This area of study, the heritable transmission of information leading to altered phenotype of an organism without changes to the genome, is called epigenetics and focuses almost exclusively on modifications to deoxy-ribose nucleic acids (DNA) and proteins; the two main components used to store biological information.

The central dogma (shown in Figure 1.1) initially described by Francis Crick[1], addressed how biological information was transferred through different classes of macromolecules. At the time, little was known about the inheritance of a phenotype, without altering the genotype. As such, the central dogma could be considered incomplete due to its omission of DNA and protein post-translational modifications. To some extent, every protein translated (at least in eukaryotes) is initially modified post-translationally.

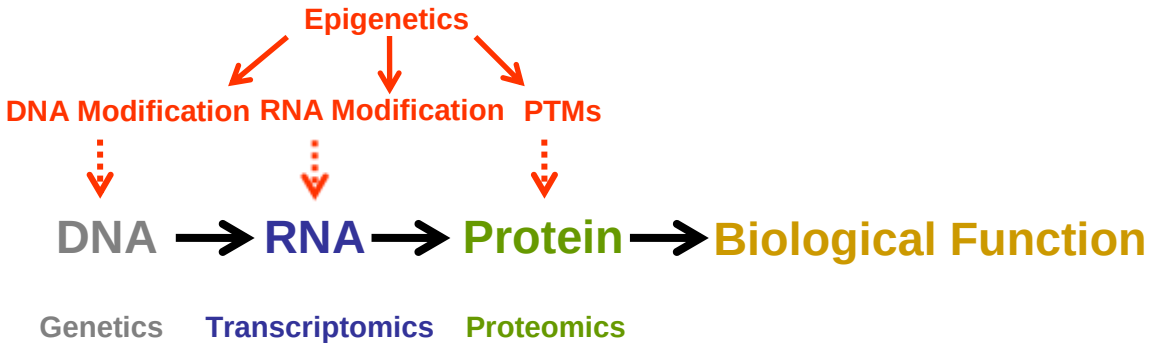

Figure 1.1: Illustration of the position of Epigenetics as part of the central dogma. Epigenetics deals with modifications of biopolymers: DNA, RNA and proteins.

1.1.1 DNA Structure and Modification

A common feature of eukaryotes is that heritable information is localised to a specific compartment of the cell (the nucleus), and the genome is encoded in DNA. DNA is structured as a double helix[2] (illustrated in Figure 1.2 (a)) and multiple forms are known to exist e.g α-, β- and z- etc[3]. The concept of the central dogma postulated by Crick suggested a direction to the passage of information contained in nucleic acids, and that once information was captured as a protein, it could not subsequently be released. The intermediate steps (DNA ⟶ RNA) and (RNA ⟶ protein) are termed transcription and translation respectively. Crick also recognised that DNA replication was a special process which did not involve RNA. Transcription is the process where the information contained in the single letter nucleotide sequence is re-written from DNA to RNA, and translation is the process where the newly transcribed information (contained in the single letter RNA sequence) is translated into protein, from three letter codons into single amino acids.

In the nucleus, DNA is found in discrete units called chromosomes, composed of DNA and proteins (collectively called chromatin) which provide their structure. Since the entire genome of an organism is contained in each cell, DNA must be heavily compacted, yet still accessible to carry out the processes of gene expression and replication. Proteins provide the means by which the genome can be packaged to fit into the nucleus of each cell and still be accessible for transcription. Figure 1.2 (below) illustrates how DNA is stored in the cell.

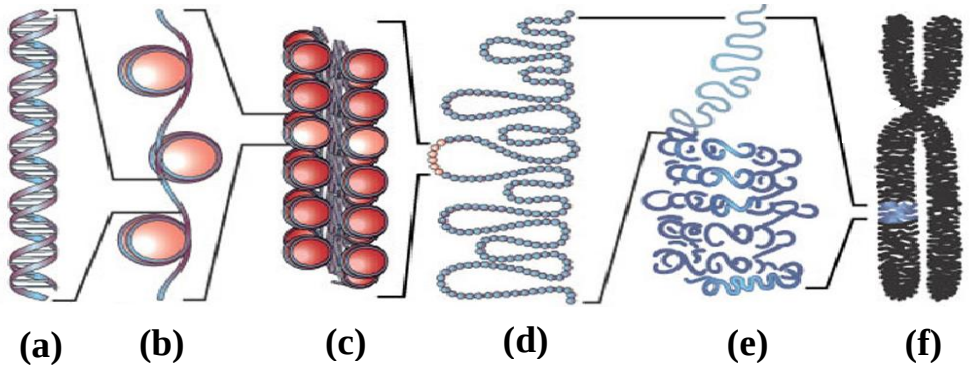

Figure 1.2: The organisation of DNA in the cell. The DNA double helix (a) is wound around the core histones to form beads of nucleosomes (b). The nucleosome beads are packed into 30 nm fibres (c), which are further coiled and stacked (d) and (e) to form an intact chromosome (f). Figure adapted from ref [4].

While the DNA sequence can be considered a blueprint for building a cell, it gives little quantitative information on the amount of each protein required, their interactions and the order in which large protein complexes are assembled. It has emerged that DNA can be modified by the addition of small moieties at a specific locations. Of the four DNA bases, cytosine is known to be modified by the addition of methyl and hydroxy-methyl groups at carbon-5 of the pyrimidine ring, only when present in a CG dinucleotide (referred to hereafter as CpG), and can be modified on both strands or on a single strand (hemi-modified). Figure 1.3 below shows modified forms of cytosine.

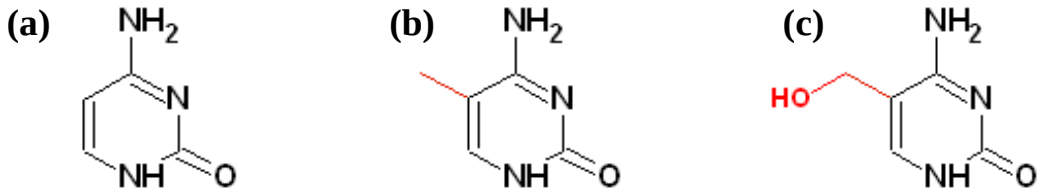

Figure 1.3: Modified forms of the DNA base cytosine. The site and nature of the modification is highlighted in red. (a) cytosine, (b) 5 methyl-cytosine, (c) 5 hydroxymethyl-cytosine.

DNA methylation is one mechanism by which genetic information potential can be extended, and is associated with a condensed chromatin structure (termed heterochromatin), leading to reduced gene expression[5]. Early studies into DNA methylation suggested a link with the distribution of active and inactive chromatin in the nucleus. This link was subsequently refined to show that methylation was often found at the promoters of inactive genes, suggesting involvement of DNA methylation in gene

silencing[6-8]. Methylation is essential in parental imprinting, X chromosome inactivation and development[9,10]. Although the mechanism by which methylated DNA represses gene activation is still under debate, one widely accepted view is that gene silencing is achieved through direct interference of the methyl group with the binding of transcription factors[11]. Another possibility is that modified DNA is able to recruit methyl CpG binding proteins which mediate repression through altering chromatin structure[12,13].

Modifications are added to the DNA molecule by groups of enzymes; DNA methyl transferases and hydroxy-methyl transferases, which fall into several classes based on their mode of action. There are three primary DNA methyl transferase (DNMT) enzymes in eukaryotes; DNMT1, DNMT3a and DNMT3b, which fall into two classes, namely maintenance and *de novo* methyl transferases. It is known that after fertilization, the methylation pattern is completely erased from the gametes, followed by establishment of a new pattern by *de novo* methylation [14]. DNMT3a and DNMT3b are *de novo* methyl transferase enzymes which are able to methylate CpG dinucleotides in un-methylated and hemi-methylated DNA. They are present at high levels in embryonic stem cells, but at much lower levels in adult tissues. DNMT1 is a maintenance methyl transferase enzyme with high affinity for hemi-methylated DNA. This was the first methyl transferase enzyme characterised, and due to its specificity for hemi-methylated DNA it is most active during DNA replication, when it is recruited to reproduce the methylation of the parent DNA strand to the daughter strand [15,16].

The function of hydroxy-methylated DNA is not well understood. Few genes have been identified which code for enzymes able to modify DNA with this group, but hydroxy-methylation may play an important epigenetic role.

The possibilities for DNA modification represent a means by which genes can be activated or silenced without altering DNA sequence, i.e. epigenetically. The other primary mode of epigenetic gene control is through alteration of chromatin structure, specifically by post-translational modification to its protein components.

1.1.2 Histone Proteins and Nucleosome Structure

The nucleosome can be described as the smallest repeating unit which makes up the bulk chromatin material, and is an octamer of four histones (2 dimers of H2a and H2b, and a tetramer of H3 and H4), which bind roughly 146 bp of DNA[17]. Histones are the main protein component of chromatin and interact directly with DNA. There are five histones in total; four of which make up the nucleosome core particle (shown in Figure 1.2), and one which resides out-with the nucleosome and acts as a sliding link with DNA. The histone proteins share similar structural features; each has a C-terminal globular domain and an N-terminal tail. Only the globular domains form the nucleosome core, while the N-terminal tails project out from the nucleosome. Initial studies of nucleosome composition carried out in the 1970's were performed using reconstitution, sedimentation and gel electrophoresis and showed that equimolar amounts of each core histone were required for nucleosome formation. Much of the work by Roger Kornberg focused specifically on the structure and components of the nucleosome. In 2006 he was awarded the Nobel Prize in Chemistry for his studies of genetic information transmission.

The focus of this initial work was the elucidation of the structure of the nucleosome. Analysis of bands visualised through gel electrophoresis suggested that the components must associate into larger complexes (dimers or trimers), while nuclease digestion was used to reveal the size of the core particle, and the amount of DNA associated with each nucleosome[18-20]. This work served to confirm data from X-ray diffraction studies of the nucleosome carried out previously, and helped to establish a model suggesting that chromatin structure was formed through a repeating unit of histones and DNA[21]. Studies which employed cross-linking of histone amino groups showed that nucleosome structure was similar in native chromatin, and in solution (denatured), and suggested a packing ratio (the level of compaction of unravelled DNA in relation to the spacing of nucleosome particles) of roughly 7:1[22]. These studies also showed that the nucleosome particle was composed of hetero-dimers and a tetramer of histones; two H2a-H2b dimers associated with an H3-H4 tetramer, without H1 present[23]. Further studies would focus on higher order chromatin structure. Electron microscopy of chromatin was used to visualize linear arrays of particles[24,25], confirm the circular form of the nucleosome, and

show that nucleosomes were present as 'beads on a flexibly jointed chain' in chromatin. This work also confirmed the earlier idea that DNA was associated to the perimeter of the nucleosome, rather than the core[26], and that the overall size of the repeating unit (the nucleosome and associated DNA) was roughly 100 Å[27]. The nucleosome core particle is illustrated in Figure 1.4 below.

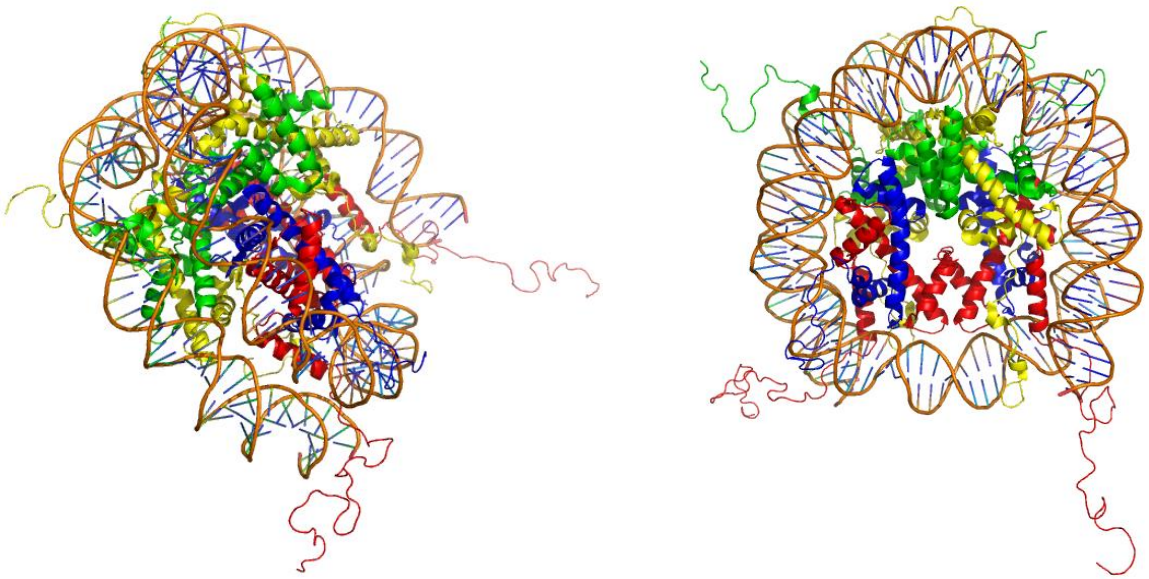

Figure 1.4: Structure of the nucleosome (RSC PDB: 1KX5). (a) front view and (b) side view. Histones are H2a-Yellow, H2b-Green, H3-Red and H4-Blue. 147 bp DNA (orange chain) are wrapped around the nucleosome core.

Nucleosome formation occurs through initial binding of DNA to the H3-H4 tetramer, followed by encapsulation by two H2a-H2b dimers. Histones H3 and H4 are the prime directors of nucleosome structure, while the H2a-H2b dimers appear to add stability[28]. Interestingly, charge reduction of the histone tails appeared to play a crucial role in assembly of the nucleosome, however it was shown that substitution of the H3 and H4 tails permitted nucleosome assembly, but had a detrimental effect on the transcription of specific genes[29,30].

In the 1980's, with nucleosome structure well understood, there was a shift in the focus of study to what would become the subject of epigenetics. The pioneers of this work were C. David Allis and Brian D. Strahl who chose to focus more on histone proteins and their post-translational modifications. While Kornberg showed that nucleosomes inhibit

transcription when gene promoters are located on nucleosomes, but that transcription could proceed when promoters were positioned away from histones[31], the interplay between histone PTMs was demonstrated in several studies by Allis. The majority of their work was conducted using the organism *Tetrahymena thermophila*. This organism has a different cell compartment organization compared to most eukaryotes, specifically it contains two nuclei; a macronucleus which houses genes transcribed during normal cellular function, and a micronucleus which is transcriptionally silent, but which is involved in the organisms duplication. This segregation of function allowed Allis and co-workers to study in great detail how PTMs were localised when associated with specific biological functions.

Originally, histones were thought to exclusively play a structural role, providing a scaffold around which DNA can wrap and be compacted. It has emerged, however, that histones are extensively post-translationally modified and that these modifications are able to disrupt interactions with DNA and alter chromatin structure. Two popular theories attempt to explain how histone PTMs affect transcription; the first suggests that modifications physically disrupt DNA/histone interactions leading to unwinding of DNA from the nucleosome. This disruption could be the result of post-translational modifications occupying space which is necessary for transcription factor binding, or through localized charge alteration due to the modification. The presence of negatively charged phosphate groups (as PTMs) would repel a DNA backbone and the neutralization of basic amino acids present in the histone N-terminal region would have a similar effect. The second theory postulates that histone modifications serve as substrates which recruit chromatin modifying enzymes. Histone PTMs include methylation, acetylation, phosphorylation, ubiquitination and sumoylation, and the majority are observed on the N-terminal tail where they induce structural changes to the globular domains which affect nucleosome stability[22].

Initially through studying nucleosome assembly, it was shown that newly synthesized histones H3 and H4 were acetylated at specific residues, and that although acetylation sites varied between histones in transcriptionally active regions, and newly formed nucleosomes, the acetylation was performed by a single histone acetyl-transferase (HAT) enzyme[32]. It was also shown that during nucleosome assembly, histone acetylation

occurred at the time of synthesis, and not after formation of the nucleosome. These acetyl groups are subsequently removed by de-acetylase enzymes[33]. In contrast to acetylation during assembly, proteolytic cleavage of N-terminal residues was also identified as a PTM which affected localization of newly formed nucleosomes. This PTM, apparently specific to H3, was found associated with transcriptionally silent chromatin, and possibly serves to direct compartmentalization of chromatin with specific biological functions[34,35]. Evidence supporting the idea that specific histone isoforms were involved in different biological functions was further reinforced with the discovery that a variant of H2a is enriched in the nucleoli of mammalian cells, and that a similar variant (in *Tetrahymena*) was found only in the transcriptionally active macronucleus[36,37]. Further study of H2a found that these variants were highly conserved, specifically that the H2a core domain, shown in Figure 1.4(a) was conserved and that the level of conservation suggested an important biological role[38]. These findings suggested that the location of these variants may be linked to their function. With the theory that histone isoforms are linked to specific biological events well established, multiple studies began to focus on the role of dynamically regulated post translational modifications. While histone families H2a and H2b include many sequence variants, histones H3 and H4 do not. However, the density of modifiable residues in their N-terminal regions, coupled to their intimate interaction with DNA in the intact nucleosome presents opportunities for the regulation of DNA templated events through post-translational modification.

L. G. Chicoine (while working for Allis) showed that different residues were preferentially modified (in H4) between transcriptionally active and silent chromatin[39]. This finding suggested that each modification site may be functionally distinct from the others; in addition they found that PTMs seldom appeared isolated, but in fact various combinations of modifications appeared together during biological events. They noted that there was an inter-dependence between modifications; i.e. that the presence of one specific modification could interfere with the addition of PTMs at other locations[40]. This, along with the observation that acetylated H4 played a critical role in transcription factor binding suggested that modified residues might play a role in defining functional chromatin domains[41,42].

While a single modification can affect the entire structure, typically a combination of modifications is observed. The large number of modifiable residues in the N-terminal tails presents multiple opportunities for epigenetic control; in addition three of the core histones have multiple sequence variants, some of which are associated with specific cellular events. Figure 1.5 (below) shows the four core histones, their most commonly observed sequence variants, and highlights the sites of modification.

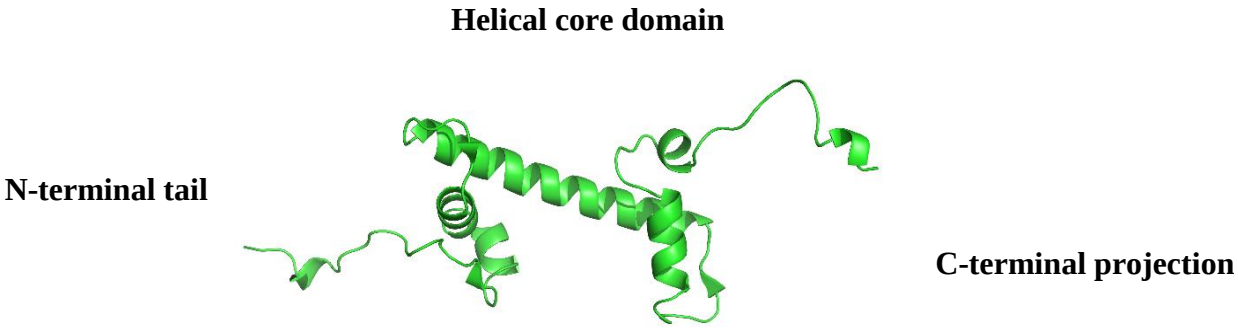


```
H2a-1       SGRGKQGGKA RAKAKTRSSR AGLQFPVGRV HRLLRKGNYS ERVGAGAPVY LAAVLEYLTA 60
H2a-1h      SGRGKQGGKA RAKAKTRSSR AGLQFPVGRV HRLLRKGNYS ERVGAGAPVY LAAVLEYLTA
H2a-1f      SGRGKQGGKA RAKAKTRSSR AGLQFPVGRV HRLLRKGNYS ERVGAGAPVY LAAVLEYLTA
H2a-1k      SGRGKQGGKA RAKAKTRSSR AGLQFPVGRV HRLLRKGNYS ERVGAGAPVY LAAVLEYLTA
H2a-3       SGRGKQGGKA RAKAKSRSSR AGLQFPVGRV HRLLRKGNYS ERVGAGAPVY LAAVLEYLTA

H2a-1       EILELAGNAA RDNKKTRIIP RHLQLAIRND EELNKLLGRV TIAQGGVLPN IQAVLLPKKT 120
H2a-1h      EILELAGNAA RDNKKTRIIP RHLQLAIRND EELNKLLGRV TIAQGGVLPN IQAVLLPKKT
H2a-1f      EILELAGNAA RDNKKTRIIP RHLQLAIRND EELNKLLGRV TIAQGGVLPN IQAVLLPKKT
H2a-1k      EILELAGNAA RDNKKTRIIP RHLQLAIRND EELNKLLGRV TIAQGGVLPN IQAVLLPKKT
H2a-3       EILELAGNAA RDNKKTRIIP RHLQLAIRND EELNKLLGRV TIAQGGVLPN IQAVLLPKKT

H2a-1       ESHHKAKGK 129
H2a-1h      ESHHKAK-- 127
H2a-1f      ESHHKPKGK 129
H2a-1k      ETHHKAKGK 129
H2a-3       ESHHKAKGK 129
```

Figure 1.5 (a): Structure of H2a (RSC PDB: 1KX5) with sequence alignment of commonly observed H2a isoforms. Shaded residues indicate sites of post-translational modification in N-terminal regions where ( ) indicates phosphorylation or acetylation, ( ) methylation or acetylation, ( ) acetylation and ( ) methylation.

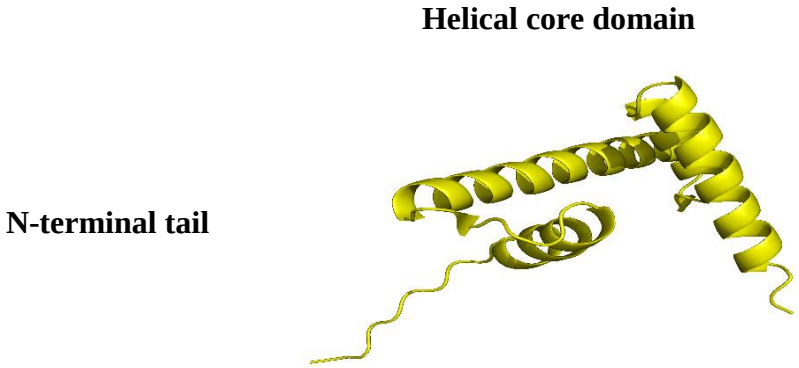


```
H2b-1b          PEPS-KSAPA PKKGSKKAIS KAQKKDGKKR KRSRKESYSV YVYKVLKQVH PDTGISSKAM 59
H2b-3a          PEPS-RSTPA PKKGSKKAIT KAQKKDGKKR KRGRKESYSI YVYKVLKQVH PDTGISSKAM
H2b-1c          PEPA-KSAPA PKKGSKKAVT KAQKKDGKKR KRSRKESYSV YVYKVLKQVH PDTGISSKAM
H2b-2b          PDPA-KSAPA PKKGSKKAVT KVQKKDGKKR KRSRKESYSV YVYKVLKQVH PDTGISSKAM
H2b-1a          PEVAVKGATI SKKGFKKAVT KTQKKEGRKR KRCRKESYSI YIYKVLKQVH PDTGISSKAM 60

H2b-1b          GIMNSFVNDI FERIASEASR LAHYNKRSTI TSREIQTAVR LLLPGELAKH AVSEGTKAVT 119
H2b-3a          GIMNSFVNDI FERIASEASR LAHYNKRSTI TSREVQTAVR LLLPGELAKH AVSEGTKAVT
H2b-1c          GIMNSFVNDI FERIAGEASR LAHYNKRSTI TSREIQTAVR LLLPGELAKH AVSEGTKAVT
H2b-2b          GIMNSFVNDI FERIAGEASR LAHYNKRSTI TSREIQTAVR LLLPGELAKH AVSEGTKAVT
H2b-1a          SIMNSFVTDI FERIASEASR LAHYNKRSTI TSREIQTAVR LLLPGELAKH AVSEGTKAVT 120

H2b-1b          KYTSSK 125
H2b-3a          KYTSSK
H2b-1c          KYTSSK
H2b-2b          KYTSSK
H2b-1a          KYTSSK 126
```

Figure 1.5 (b): Structure of H2b (RSC PDB: 1KX5) with sequence alignment of commonly observed H2b isoforms. Shaded residues indicate sites of post-translational modification in N-terminal regions where ( ) indicates phosphorylation, ( ) methylation or acetylation, ( ) acetylation and ( ) methylation.

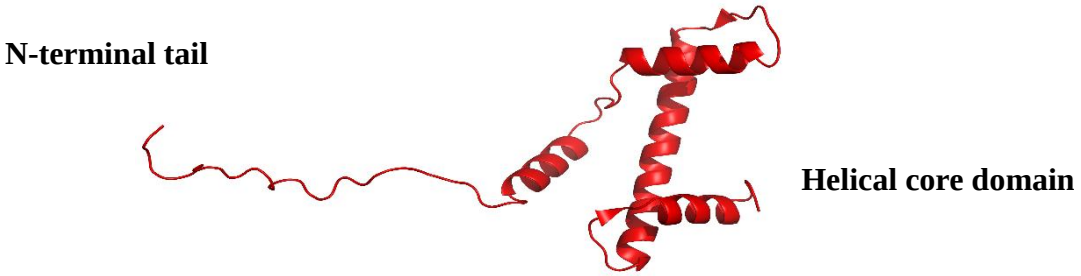


```
H3.1        ARTKQTARKS TGGKAPRKQL ATKAARKSAP ATGGVKKPHR YRPGTVALRE IRRYQKSTEL 60
H3.2        ARTKQTARKS TGGKAPRKQL ATKAARKSAP ATGGVKKPHR YRPGTVALRE IRRYQKSTEL
H3.3        ARTKQTARKS TGGKAPRKQL ATKAARKSAP STGGVKKPHR YRPGTVALRE IRRYQKSTEL

H3.1        LIRKLPFQRL VREIAQDFKT DLRFQSSAVM ALQEACEAYL VGLFEDTNLC AIHAKRVTIM 120
H3.2        LIRKLPFQRL VREIAQDFKT DLRFQSSAVM ALQEASEAYL VGLFEDTNLC AIHAKRVTIM
H3.3        LIRKLPFQRL VREIAQDFKT DLRFQSAAIG ALQEASEAYL VGLFEDTNLC AIHAKRVTIM

H3.1        PKDIQLARRI RGERA 135
H3.2        PKDIQLARRI RGERA
H3.3        PKDIQLARRI RGERA
```

Figure 1.5 (c): Structure of H3 (RSC PDB: 1KX5) with sequence alignment of H3 isoforms. Shaded residues indicate sites of post-translational modification in N-terminal regions where ( ) indicates phosphorylation, ( ) methylation or acetylation and ( ) methylation.

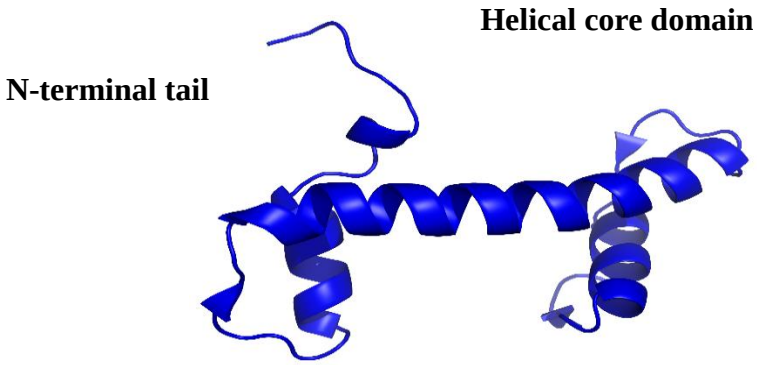

H4 SGRGKGGKGL GKGGAKRHRK VLRDNIQGIT KPAIRRLARR GGVKRISGLI YEETRGVLKV **60**

FLENVIRDAV TYTEHAKRKT VTAMDVVYAL KRQGRTLYGF GG **102**

Figure 1.5 (d): Structure and sequence of H4 (RSC PDB: 1KX5). Shaded residues indicate sites of post-translational modification in N-terminal regions where ( ) indicates acetylation and ( ) methylation.

Examination of each core histone (Figure 1.4 above) reveals structural features are conserved. Each has an N-terminal tail projecting out from the nucleosome core, and each has a helical core domain (composed of at least three α-helices). H2a has an additional C-terminal projection, not found on the other histones. Other conserved features include the density of basic amino acid residues (lysine and arginine) in all four histones, concentrated in the N-terminal regions. There is striking similarity in the sequences of two of the core histones: H2a and H4. Not only do they share similar N-terminal sequences, but the spacing between modifiable residues is conserved. Since the histone tails are accessible to the nuclear environment, the finding that several transcriptional activators contain two bromo-domains suggests that HATs may have multiple targets.

The N-terminal domain of H3 contains several modifiable residues, and studies have linked these modifications to biological events, e.g. methylation of lysine 9 is observed during transcriptional repression, while tri-methylation at lysine 4 has been suggested as a marker for active transcription[43-45]. Phosphorylation at serines 10 and 28 have been linked to chromosome condensation during mitosis, and appears in conjunction with acetylation[46]. Similarly, acetylation of the N-terminal of H4 at lysines 8 and 16 has been linked to a transcriptionally active state[47,48], while further acetylation of all H4 N-terminal lysines has been linked to higher order chromatin structure showing correlations with cell cycle progression[49].

Histone protein H1 (which is not found within the nucleosome) serves as a sliding 'linker' at the entry and exit points of the bound DNA chain. The flexibility in the positioning of H1 allows easier interaction between histone proteins and DNA. The positioning of H1 relative to the nucleosome was proposed as a result of X-ray patterns generated by Richards and Pardon in 1970[50]. They observed that removal of histone H1 from chromatin preparations did not alter the diffraction pattern. In addition, it was shown by Kornberg[19] that the other histone proteins were present in relatively equal amounts, while roughly half as much of histone H1 was present. Subsequent work on H1 focused on its interaction with DNA, and revealed that the extent of this interaction was dependent on the super-helicity of the DNA. Further work involving nuclease digestion and

sedimentation analyses revealed H1 was involved in the link between nucleosome beads[51]. A hypothesis for the function of H1 suggested that it served to stabilize nucleosome structure, based on its preferential interaction for double stranded DNA and the regular spacing between core nucleosome complexes, shown to be roughly 43 bp of DNA but which can vary between organisms[52-54].

The presence of multiple modifications on the same histone tail, or in different histones, suggests that they may work in synergy as part of a larger framework to exert some regulatory control. Current research suggests that the combination of modifications present on the histone N-terminal tails forms a 'histone code', indicating the level of gene transcription, and that an intimate association between histone modifications exists[55]. In the absence of these post-translational modifications, when the nucleosome is tightly wound, and the chromosome is compact, transcription does not occur[56,57]. Each methylation and acetylation is able to recruit or disrupt binding of transcription factors or chromatin remodelling proteins, possibly by serving as a substrate for chromo-domain or bromo-domain containing proteins respectively. The bromo-domain is a structural motif; 110 amino acids long which binds to acetylated lysine as a substrate. Multiple bromo-domains have been found in many transcriptional activators, however its function is not well understood[58].

Figure 1.6 (below) shows the most common histone post translational modifications. While the array of histone PTMs includes phosphorylation, acetylation, methylation and to a lesser extent ADP-ribosylation (primarily found on H1[59,60]), the majority of modifications present are acetyl and methyl groups (including N-terminal acetylation), and so are primarily found on lysine and arginine residues. Histone acetylation is a dynamic modification, and is mediated through the action of acetyl transferase and deacetylase enzymes. The most widely accepted theory suggests that disruption of electrostatic forces permits unwinding of DNA from the nucleosome allowing enough space for transcription factors to bind. In contrast, histone methylation is regulated by methyl transferase enzymes (distinct from those involved in DNA methylation), and appears to be a more stable and less dynamic modification.

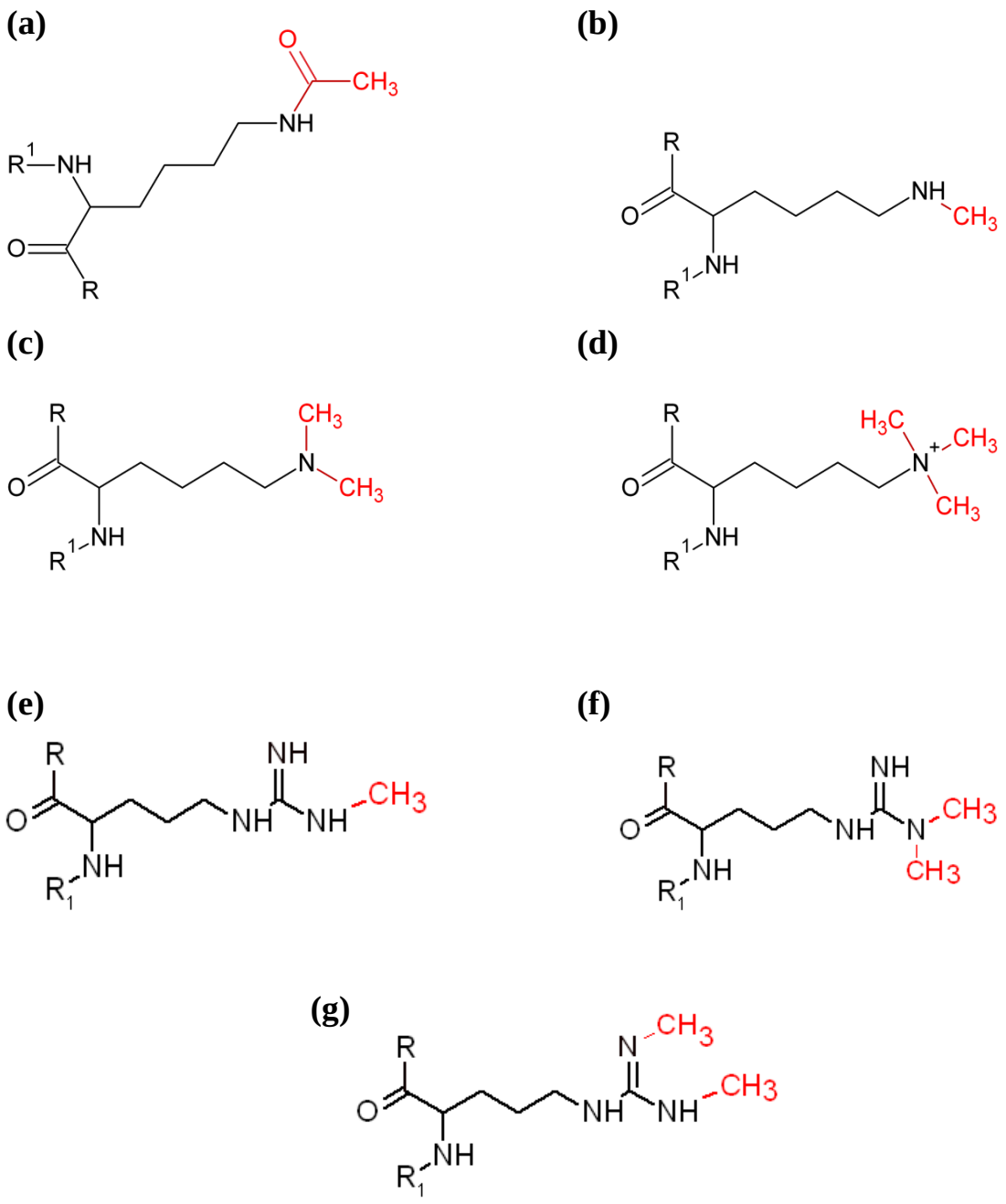

Figure 1.6: The most commonly observed histone post-translational modifications of lysine and arginine; (a) acetyl lysine, (b) methyl lysine, (c) di-methyl lysine, (d) tri-methyl lysine, (e) methyl arginine, (f) assymetric di-methyl arginine and (g) symmetric di-methyl arginine.

Acetylation of histones is not limited to specific lysine residues in the N-terminal regions. Indeed, histone acetylation was first described as a modification of the N-terminal residue through experiments which attempted to sequence these proteins[61]. This acetylation was different to that seen as a side chain modification in that it displayed a different rate of turnover, and it was shown that acetyl groups were N-linked, and not O-linked. While all histone proteins can be acetylated, H4 and H3 are acetylated to greater levels than the others[62]. The state of acetylation at any time can be thought of as a result of the action of two enzymatic activities. Histone acetyl transferases (HATs) catalyse the addition of acetyl groups (using acetyl coenzyme-A as the acetyl donor), while histone de-acetylases (HDACs) catalyse the removal of acetyl groups. Acetylation had been linked to active gene transcription, and the search for the enzymes responsible lead to the discovery that some transcription factors possessed HAT and HDAC activities[63-65]. The studies into the process of histone acetylation also revealed that the model of a simple correlation between increased acetylation and active transcription was too simplistic. In depth analysis of different HATs revealed that each had different targets, i.e. different residues would serves as binding substrates, possibly suggesting that each HAT is linked to a specific biological event[66]. These studies also showed that while HATs contain bromodomains, these bromodomains are not required for acetyl transferase activity. Instead, the bromodomains may serve to stabilise binding of other chromatin associated proteins.

The higher incidence of acetylation and methylation presents difficulties when investigating PTMs by mass spectrometry. Since multiple modifications are typically present simultaneously, the identification of an acetyl group (by mass) can be mistaken for the presence of a tri-methyl group. Both modifications are known to be present on lysine residues, a highly abundant amino acid in histone proteins.

The current paradigm of the ‘histone code’ evolved from the work of Allis, and continues to be expanded upon. Collectively, studies into histone PTMs support the hypothesis that a histone code exists. The documentation of modification patterns lends evidence to the concept that the presence of PTMs, including their chemical nature and their number are able to dictate a biological outcome. This epigenetic marking system employs

combinatorial and sequential modification of histone tails to extend the information content of the genetic code. Thus, histone post-translational modification is fundamental to all DNA directed processes. Current studies are attempting to answer some fundamental questions. Are specific PTMs associated with biological events? Is there an order to the appearance of PTMs? If so, are histone PTMs a cause or a consequence of biological processes? Ultimately, what is the specific nature of the interaction between DNA and modified histones? (e.g. how are PTMs involved in regulating transcription?). Technological developments in the 1990's and early years of the 21st century led to increased use of mass spectrometry in epigenetics research. With the emergence of proteomics as a major field of study, and improvements in analytical techniques, the study of epigenetics would embrace mass spectrometry as a tool for protein and PTM characterization. In contrast to immunological based techniques, mass spectrometry is able to give a global view of the modification state of a protein, and has become the method of choice for PTM identification. While the last ten years have seen an exponential increase in the application of mass spectrometry to histones, much of the output has been limited to a few research groups which have developed better tools to address the complex problems of protein PTMs. These tools include improved instrumentation, sample separation methods and software.

An intricate theory now exists which champions the 'histone code' hypothesis and links nucleosome structure, histone sequence variants and the presence of post-translational modifications. The work described in this thesis has attempted to build on this theory through application of mass spectrometry, specifically focusing on the dynamic nature of histone post-translational modification. In particular,

- to determine if histone PTMs can be reproducibly altered due to chemical exposure across cell lines;
- to investigate the effects of endogenous compounds on the PTM profile of histones; and
- to characterise histone PTMs relevant to a specific condition i.e. resulting from illness.

1.2 Protein Mass Spectrometry

The ability to form intact molecular ions of non-volatile macromolecules using either electrospray ionisation (ESI)[67] or matrix assisted laser desorption/ionisation (MALDI)[68] led to a drive to improve mass spectrometry instrumentation and fragmentation methods. Today, mass spectrometry is an integral part of proteomics, the field concerned with the identification of proteins from complex biological mixtures. The sequencing of the genome of an organism provides much information about the proteins which are present in the organism, but very little about their abundances, interactions and the presence of any post-translational modifications. Mass spectrometry has allowed in depth studies of proteins through accurate mass measurement of intact species, and by using fragmentation techniques for the characterisation and localisation of post-translational modifications. Traditionally proteomic studies were performed by separating a sample of interest using 2-dimensional gel electrophoresis, to identify changes in protein expression (visible as spots on a 2-D gel with varying intensities). Spots of interest would then be excised from the gel, the protein extracted, and interrogated by amino acid sequencing[69]. Today three methodologies dominate the field of proteomics, which negate the use of gel electrophoresis; 'Top-down', 'Middle-down' and 'Bottom-up' mass spectrometry.

1.2.1 Top-Down Mass Spectrometry

Top-down mass spectrometry is the study of intact proteins exclusively through mass spectrometry[70-72]. A typical top-down experiment involves infusion of a sample into the instrument, the isolation of a precursor followed by tandem mass spectrometry. The fragment ion masses generated are searched against the amino acid sequence of the protein (if known), or against a database. Calculation of the intact mass from the isolated precursor can be used to elucidate the mass of any PTMs present, while identification of fragment ions permits their localisation. Top-down experiments can provide a global view of all modifications present on a protein, and their abundances. In addition, stable isotope labelling techniques can also be used in top-down experiments. The steps involved in a top down experiment are illustrated in Figure 1.7. While top-down mass

spectrometry can be a versatile tool for protein/PTM identification, it suffers from limitations related to protein size. Fragmentation efficiency decreases with increasing protein size, in part due to the tertiary structure of gas-phase proteins. Although there is no defined upper limit for protein mass in top-down experiments, above a molecular mass of roughly 50 kDa, top-down work becomes difficult[73]. This can be overcome by reducing protein size through enzymatic or chemical digestion (i.e. by performing middle-down or bottom-up mass spectrometry).

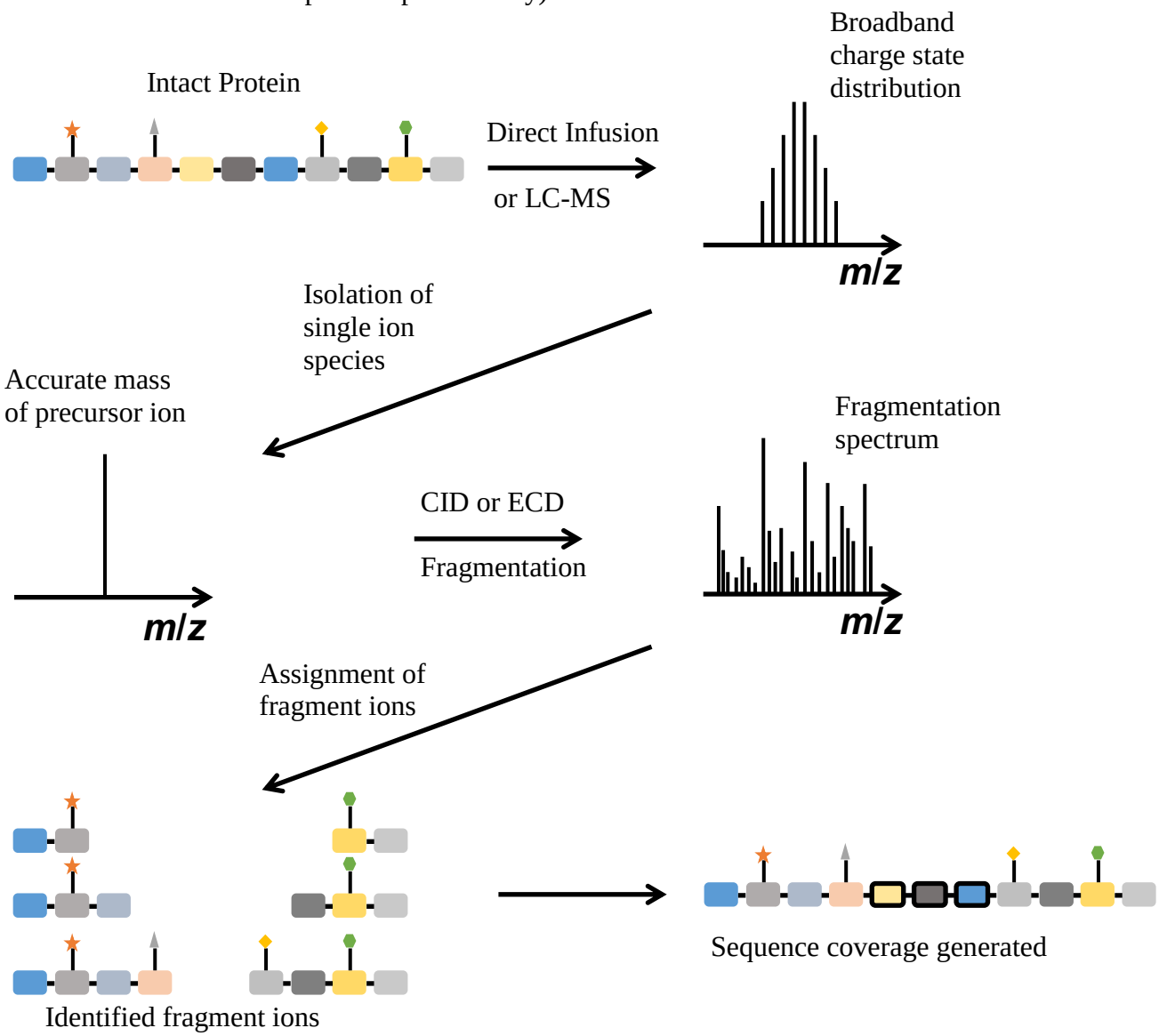

Figure 1.7: Schematic workflow of a top-down mass spectrometry experiment. A sample is infused into the instrument, an ion is selected for fragmentation, fragment ions are assigned and data is collated to determine sequence coverage of the sample.

1.2.2 Middle-Down Mass Spectrometry

Middle-down mass spectrometry involves cleavage of the amino acid sequence at low abundance residues[74,75]. Cleavage can be induced at Asp or Lys residues using endoproteinases AspN or LysC respectively, while Met residues can be cleaved using cyanogen bromide. The result is generation of large peptides, which can be separated by LC or infused directly into the mass spectrometer. Similar to top-down experiments, precursor ions are isolated and then fragmented. Fragmentation of a large peptide is significantly easier to achieve than that of a large protein, which is especially useful if the peptide is a region of a protein which may be heavily modified. In addition, middle-down experiments can provide extensive sequence coverage over internal regions of a protein which may be difficult to fragment by top-down experiments. A schematic diagram of a middle-down experiment is shown in Figure 1.8.

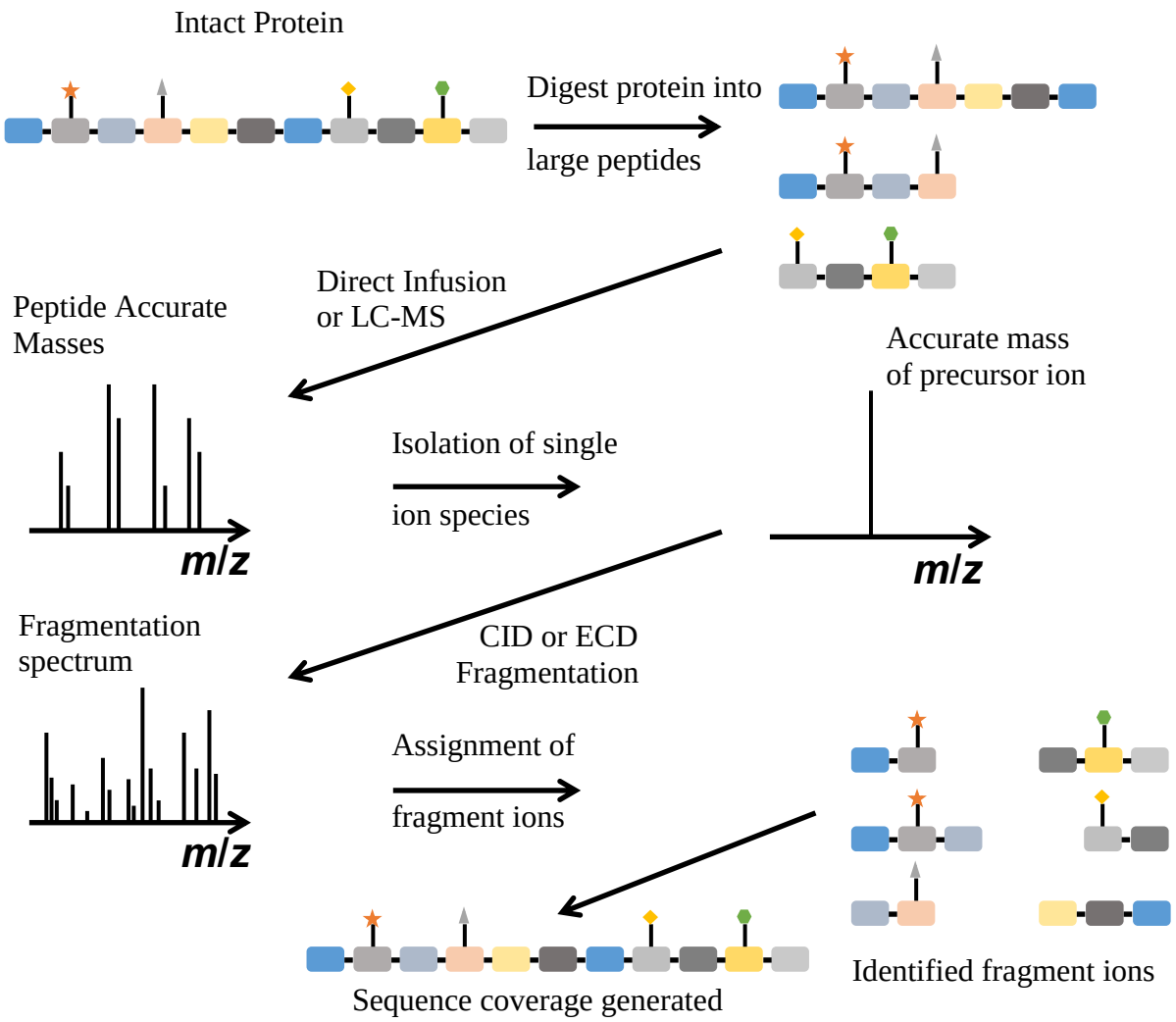

Figure 1.8: Schematic workflow of a middle-down mass spectrometry experiment. A sample is partially digested before infusion into the instrument (with optional LC). Accurate peptide masses are recorded before isolation of a precursor and subsequent fragmentation.

1.2.3 Bottom-Up Mass spectrometry

Bottom-up mass spectrometry is the most routinely used strategy for PTM characterisation[76-78]. The bottom-up method involves complete digestion of the protein by an enzyme at high abundance residues. Trypsin is typically used in bottom-up work due to its high specificity for lysine and arginine, where it cleaves at the C-terminals. Enzymatic cleavage can optionally be followed by LC separation prior to sample infusion. The advantages of bottom-up experiments are that they are suitable for high-throughput work, can be automated, and since analysis is ultimately done on peptides, bottom-up

experiments are not limited by protein size. A diagram of the steps involved in a bottom up experiment is shown in Figure 1.9.

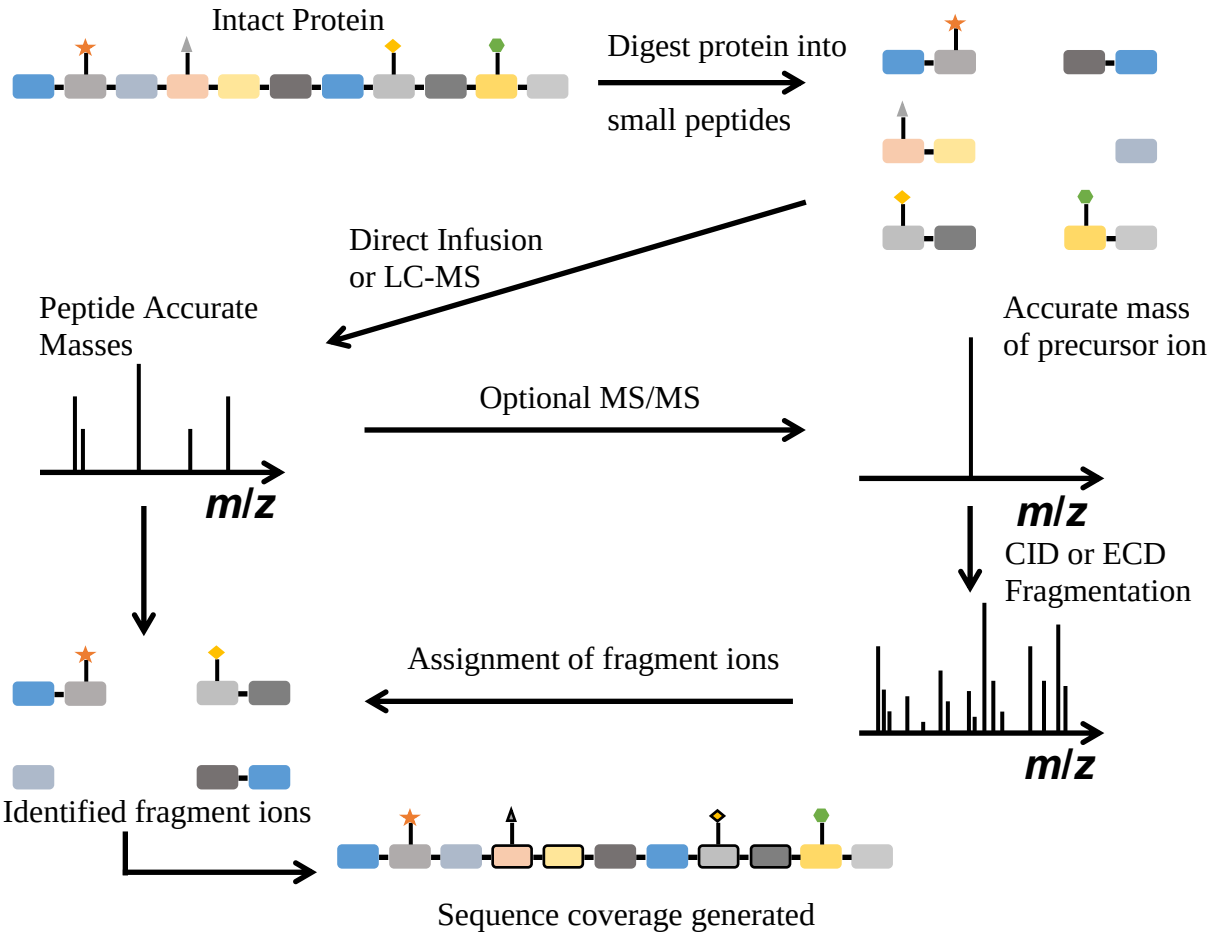

Figure 1.9: Schematic workflow of a bottom-up mass spectrometry experiment. The sample is completely digested chemically or enzymatically before infusion into the instrument, with LC separation and fragmentation as optional steps.

Traditional bottom-up experiments attempt to identify a protein through searching peptide masses against a database. The peptides serve as a mass fingerprint for the protein, and there is still the possibility to use fragmentation on larger peptides. However, the lack of an intact mass of the un-cleaved protein presents major problems when performing bottom-up experiments. Without a precursor mass, there is no knowledge of the modification state of the protein, making PTM assignment extremely difficult. In addition, complete sequence coverage is rarely achieved in bottom-up experiments

resulting in PTMs going undetected. The combinatorial nature of PTMs on proteins which are heavily modified can be difficult to determine using bottom-up mass spectrometry.

1.3 Ionisation Sources

Extensive work in the 1980's led to the development of two ionisation techniques which are in widespread use today. The unique advantage of these techniques over older sample ionisation methods was that gas-phase ions could be generated without fragmentation of the sample. This characteristic meant these methods were soon being applied to the study of peptides and intact proteins. In recognition of this achievement, half of the 2002 Nobel Prize in Chemistry was given to those credited with discovering these techniques; John Fenn for his work on electrospray ionisation[67](ESI), and Koichi Tanaka for his work on matrix assisted laser desorption/ionisation (MALDI)[68]. While Tanaka and Fenn enjoyed great success for revolutionising biological mass spectrometry, it has emerged that their work was based on observations and theories which had been established years earlier[79-83]. Both ionisation techniques were employed in this research, however most of the experiments utilised electrospray ionisation, and all the data presented utilised an electrospray source.

The principle governing MALDI is that gas-phase ions are generated through the laser ablation of a mixture of sample which has been co-crystallised with a matrix. The matrix itself is a saturated solution of a light absorbing molecule. The energy absorbed by the matrix molecules creates a plume of ions which can then be detected in a mass spectrometer. Contrary to ESI, ions generated by MALDI typically carry a single charge, which limits mass analysis to instruments with a suitably large mass range. For this reason, MALDI sources are often coupled to time-of-flight (ToF) mass analysers. Figure 1.10 is a schematic representation of the MALDI process.

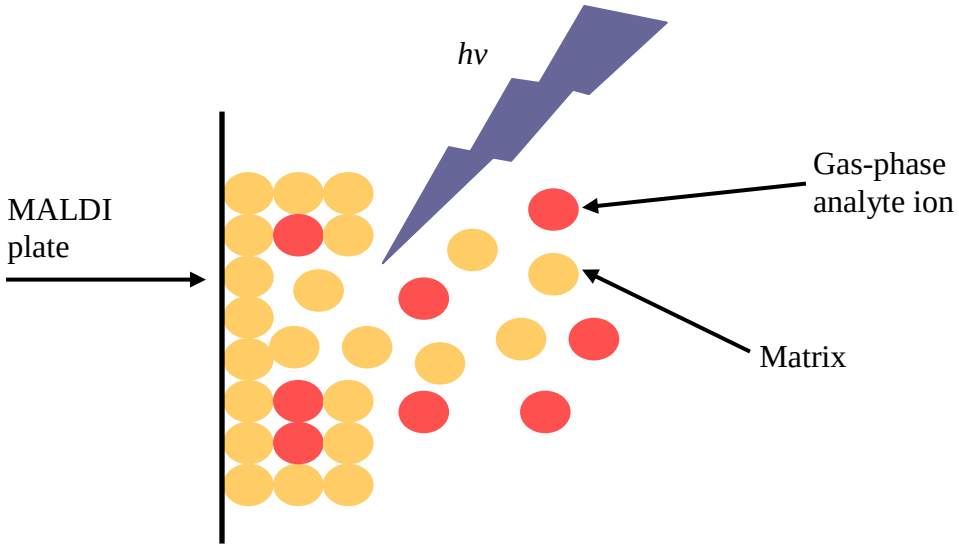

Figure 1.10: Schematic diagram of the MALDI process. Crystallized matrix (yellow spheres) and analyte (red spheres) are irradiated by a laser, and gas-phase ions are formed.

While both MALDI and ESI are considered 'soft' ionisation techniques, MALDI is carried out at near vacuum conditions, while ESI is performed under atmospheric conditions. Advantages of ESI over MALDI are that less sample preparation is required, and ESI is compatible with a wide range of mass spectrometers.

Debate still exists over the process of ion formation during ESI. In practice, ESI involves pumping a solution containing the analyte through a needle which is held at high potential relative to a counter electrode. The large electric field at the capillary tip causes charging of the liquid, which emerges as a mist of charged droplets. The droplets are attracted to the mass spectrometer inlet due to the potential and pressure gradients. A schematic diagram of the ESI process is shown in Figure 1.11.

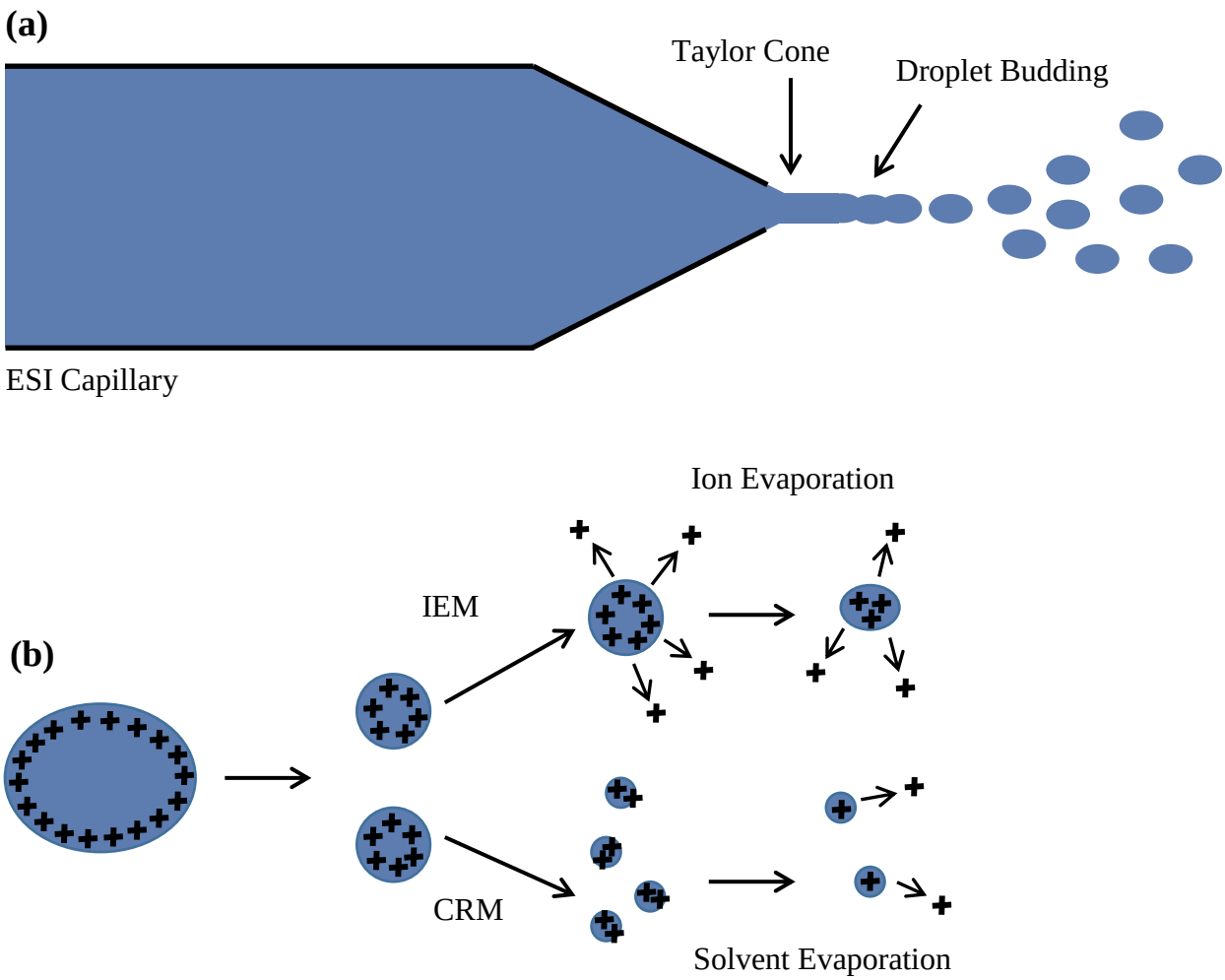

Figure 1.11: (a) Droplet formation during ESI, and (b) a representation of the competing theories describing gas-phase ion formation, where CRM is the charge reduction model and IEM is the ion evaporation model.

During electrospray ionisation, the high electrical potential at the capillary tip distorts the meniscus into what is described as a Taylor cone[84]. A fine stream emerges from the Taylor cone, and charge repulsion propagates the ejection of droplets once surface tension forces have been overcome. Continued Coulombic repulsion drives the droplets into an expanding plume, while solvent continues to evaporate from the droplets. At a critical point (the Rayleigh limit), the Coulombic forces overcome the surface tension of the droplet, which experiences a large drop in volume, but only a slight reduction in charge. The net effect, an overall increase in charge with respect to volume drives the

transfer of ions from liquid to gas-phase. Two theories exist relating to the formation of gas-phase ions from the charged droplets. The charge reduction model suggests that ions are formed by the evaporation of solvent until only gas-phase ions remain. This model was attributed to Malcom Dole, a pioneer in the field of molecular beams[80]. The competing model suggests the process of ion formation is the result of ions evaporating directly from a charged droplet[85-87]. While arguments persist regarding the precise nature of gas-phase ion formation, there is compelling evidence supporting the ion evaporation model[88-90]. ESI is typically operated at solvent flow rates up to 150 µl/min, which makes the technique compatible with high performance liquid chromatography (HPLC) for 'on-line' analysis of samples requiring separation, without the need for any desalting steps. The multiple charge states generated by ESI also permits the interrogation of protein structure to a higher level. The presence of basic amino acid side chains can result in multiple charges of a protein when in acidified solution, effecting the charge state distribution observed, For example, a denatured protein displays a wide charge state distribution (at low *m/z*), while proteins in native conformation exhibit narrow distributions at high *m/z*. The charge states observed can also be effected by solvent used; denaturing conditions (high organic content of the solvent and low pH) favour unfolded protein conformations. Denaturing solvent conditions were used throughout this work as the presence of protein species carrying many charges facilitates further study of the species by fragmentation.

1.4 Mass Analyzers

While the principles of ToF and FT-ICR MS have not changed since the first publications by Wiley and McLaren, and Comisarow and Marshall[91-93], continuous developments in instrumentation have led to higher sensitivity and resolution. The fundamental aspects of ToF and FT-ICR MS are covered in this section; however several extensive reviews are available on the subject[94-96] providing further information.

1.4.1 Time of Flight Analyzers

Time of flight mass analyzers measure the mass dependent time taken by ions of differing masses to travel from an ion source to a detector. To accurately measure the flight time of such ions, a well defined starting time is needed which can be achieved by using a pulsed ion source (typically a MALDI source).

The kinetic energy of an ion leaving the source is given by Equation 1.1 below.

$$E_k = \frac{mv^2}{2} = eV$$

Equation 1.1: The equation describing the kinetic energy of an ion where E_k is the kinetic energy (in joules), m is the mass of the partice (in kg), v is the velocity of the partice (in ms^{-1}), e is the elimentary charge and V is the applied voltage (in volts).

The ion velocity is equal to the length of the flight path divided by the flight time (Equation 1.2).

$$v = \frac{L}{t}$$

Equation 1.2: The equation describing the velocity of an ion where v is the velocity of the partice (in ms^{-1}), L is the length of the ion flight path (in metres) and t is the time (in seconds).

Substituting this expression of ion velocity into the Equation 1.1, and rearranging to solve for time, the working equation for a time of flight mass spectrometer can be derived (Equation 1.3).

$$t = L\sqrt{\frac{m}{2eV}}$$

Equation 1.3: The equation describing the flight time of an ion in a linear ion trap where t is the flight time (in seconds), m is the mass of the partice (in kg), V is the voltage applied (in volts), e is the elimentary charge and L is the length of the flight path (in metres).

There is no true limit to the upper mass range of a ToF instrument, and since time can be measured with great accuracy the only real limitation of ToF instruments lies in the length of the flight tube (i.e. the physical dimensions of the instrument)[97]. Time-of-flight instruments are known to have high ion transmission and the highest practical mass range of any type of mass analyser, but can be limited by the need of a pulsed ion source (making them impractical for coupling to high performance liquid chromatography) and have inferior precursor ion selectivity (a useful pre-requisite for MS/MS experiments).

1.4.2 Principles of FT-ICR

Accurate mass measurement of an intact protein is necessary for the confident assignment of post-translational modifications (PTMs). FT-ICR instruments offer superior mass measurement accuracy, defined as ± 10 parts per million (ppm)[98] and sufficiently high resolving power to distinguish isotopic variants (i.e. a difference in the number of ^{13}C or other heavy isotopes) contained in the compound. Fourier transform ion cyclotron resonance mass spectrometry routinely provides resolving power in excess of 1,000,000 and sub-ppm mass accuracy.

FT-ICR MS is based on the principle that an ion moving in a homogenous magnetic field will resonate at a cyclotron frequency depending on the mass and charge of the ion, and the magnetic field strength. An ion travelling in a uniform magnetic field experiences a force proportional to its mass and the strength of the magnetic field, termed the Lorentz Force. The Lorentz Force is a vector cross product of the magnetic field and the velocity of the ion, multiplied by the charge of the ion (shown in Equation 1.4).

$$\boldsymbol{F} = m\frac{d\mathbf{v}}{dt} = qv \times \boldsymbol{B}$$

Equation 1.4: The equation describing the Lorentz Force where *F* is the force (N), *m* is the mass of the particle (kg), [*dv*]/[*dt*] is acceleration (ms^{-2}), *q* is the charge of the particle (C), *v* is the velocity of the particle (ms^{-1}) and *B* is the magnetic field strength (Tesla).

The path of a particle travelling in a uniform magnetic field is bent by the magnetic field into an arc, known as cyclotron motion which is perpendicular to the plane of the

magnetic field. The direction of the cyclotron motion of the ion is dependent on the polarity of the ion, illustrated in Figure 1.12.

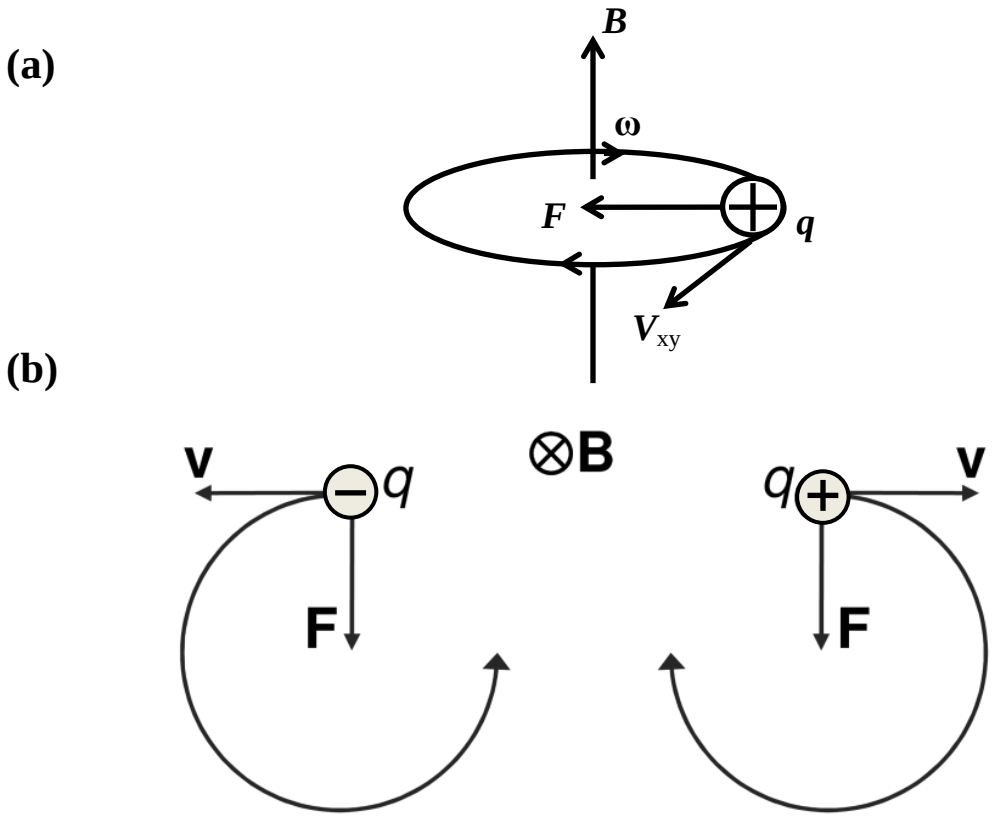

Figure 1.12: (a) Diagram showing the Lorentz Force leading to cyclotron motion, and (b) cyclotron motions of positive and negative ions. Figure adapted from Ref [94].

At constant velocity (assuming no collisions occur), the ion follows a circular orbit. The frequency with which the ion repeats its orbit (the cyclotron frequency) can be calculated using Equation 1.5.

$$\nu_C = \frac{qB}{2\pi m}$$

Equation 1.5: Calculation of the cyclotron frequency ν_c (Hz) where *q* is the charge of the particle (C), *B* is the magnetic field strength (Tesla) and *m* is the mass of the particle (kg).

Equation 1.5 can be expressed in the more convenient terms of mass to charge ratio (*m/z*), the unit used in mass spectrometry where *m* is in Daltons, and *z* is equal to *q*/*e* where *e* is the elementary charge and *u* is the atomic mass unit, shown in Equation 1.6.

$$\nu_C = \left(\frac{e}{2\pi u} \right) \frac{B}{m/z} = \frac{1.5 \times 10^7 B}{m/z}$$

Equation 1.6: The cyclotron frequency expressed in terms of mass to charge ratio (*m*/*z*) and magnetic field strength (*B*)

To illustrate this, an ion with mass to charge ratio of 1000 *m*/*z* in a 9.4 T magnetic field would have a cyclotron frequency of 141 kHz, while the same ion being detected in a uniform magnetic field of 12 T would have a cyclotron frequency of 180 kHz. The ability to measure frequency with great accuracy leads to the high mass accuracy associated with FT-ICR MS. The cyclotron frequencies of ions routinely measured by FT-ICR lie in the range of kHz to MHz, which is a convenient detection range for modern electronics. In addition, cyclotron frequency is not dependent on the kinetic energy of the ion, thus a spread in the K.E. distribution has no effect on the resolution of the instrument, which can affect ToF and magnetic sector instruments.

Equation 1.3 can be rearranged to illustrate a fundamental relationship in FT-ICR mass spectrometry; mass to charge ratio is directly proportional to magnetic field strength and inversely proportional to cyclotron frequency (Equation 1.7).

$$m/z \propto \frac{B}{\nu_C}$$

Equation 1.7: The relationship between mass to charge ratio (*m*/*z*), magnetic field strength (*B*) and cyclotron frequency (ν_c)

1.4.3 Excitation, Detection and Resolution of Ions

Detection of a useful signal in FT-ICR requires confining the ions in the ICR cell, which enter through a trapping plate. Modern instruments typically employ a cylindrical geometry for the ion trap configuration, however an assortment of configurations including cubic, hyperbolic and hybrids of these geometries also exist. Guan and Marshall provide an extensive review of several FT-ICR trap configurations detailing how how various configurations can be optimised for ion trapping or detection[99]. The cylindrical ICR cell is made up of six plates in total: two trapping plates at opposite ends of the cell, two excitation plates and two detection plates. The excitation and detection plates are located perpendicular to the trapping plates such that the intact cell is cylindrical in form. During detection, the cell is positioned in a spatially uniform magnetic field (inside the bore of the magnet), the magnetic field serves to confine the ions radially, while a potential is applied to the trapping plates for axial confinement. A schematic of a cylindrical FT-ICR cell is shown in Figure 1.13.

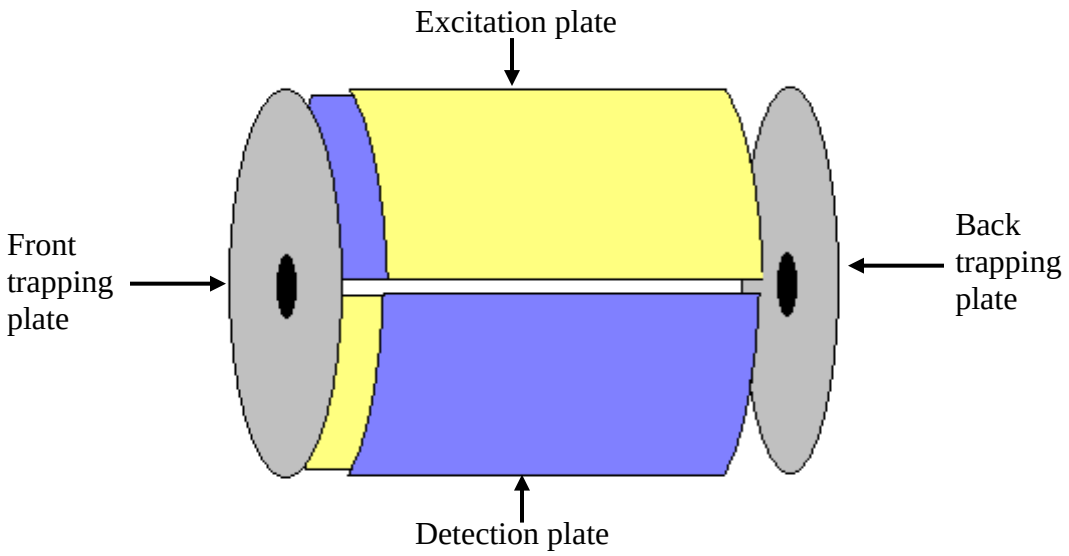

Figure 1.13: Schematic diagram of a cylindrical ICR cell. The cylindrically shaped cell is composed of six plates: Front and back trapping plates (grey), excitation plates (yellow) and detection plates (blue).

A meaningful signal can only be detected after excitation of the ions in the cell through application of a resonant frequency, forming a coherent ion packet. Prior to excitation,

the cyclotron radius of the ions is too small to detect a signal. Upon excitation, the cyclotron radius of resonant ions is increased, if the excitation event continues the ion packet spirals from the centre of the cell until it collides with the cell electrodes. As a result, excitation events are short, and the resonant frequency is applied as a pulse. After excitation, the ion packet continues to orbit at a larger cyclotron radius. Detection is achieved through measurement of an image current induced across the detection electrodes. As the ion packet passes each detection plate, positive ions attract electrons to the plate, while negative ions repel electrons from the plate. This movement of electrons creates an alternating current through an external circuit joining the detection plates. While the ion packet travels through a larger cyclotron orbit, the image current can only be detected for a short time as space-charge effects cause de-phasing of the ion packet. Furthermore, collisions between the ions and neutral molecules in the cell result in a loss of detectable signal. The image current is amplified before being Fourier transformed to generate a frequency spectrum of the ions detected. Unlike other mass spectrometers which use impact based detectors, detection by FT-ICR is non-destructive and permits further study of ions in the cell. An illustration of the stages of an FT-ICR experiment is shown in Figure 1.14.

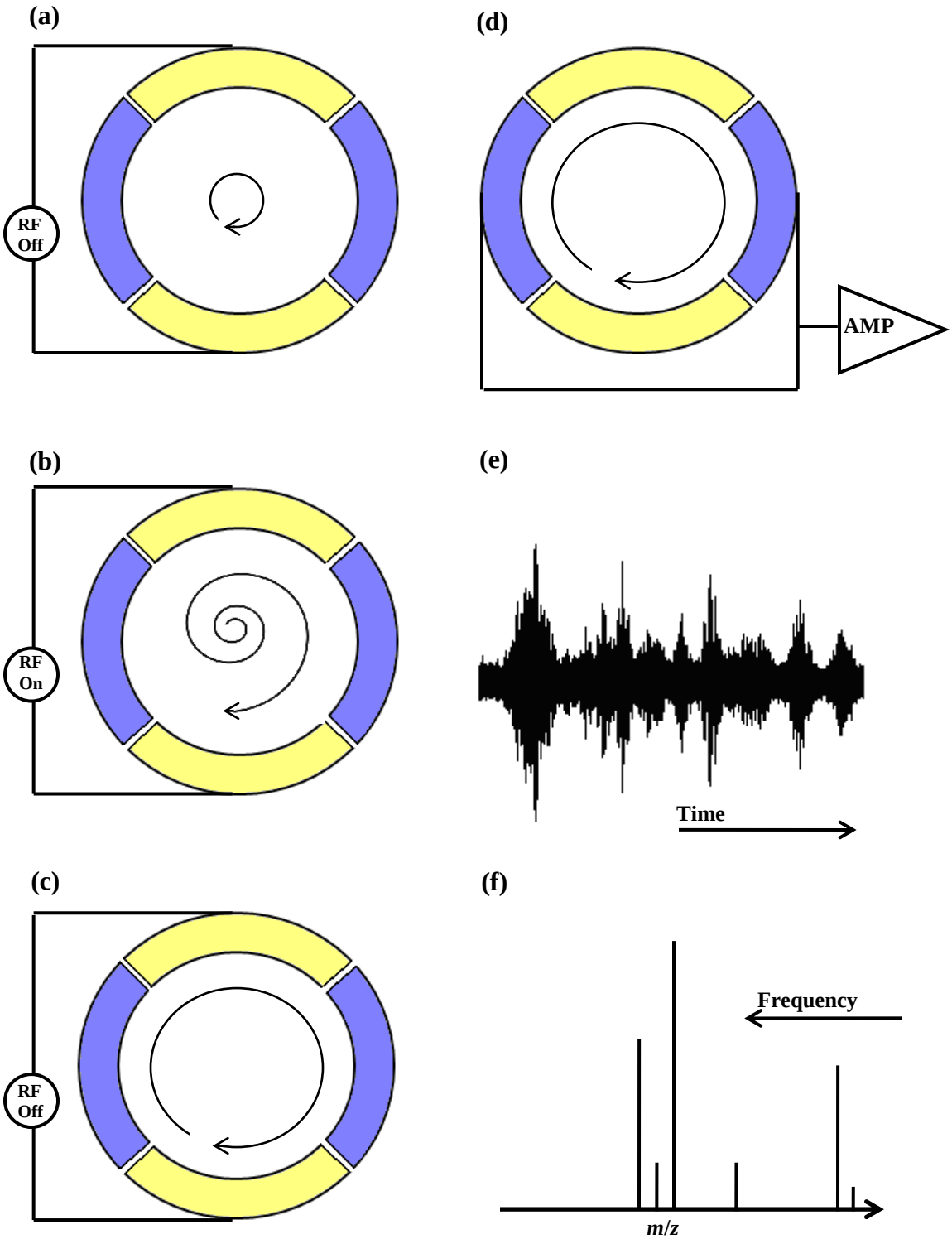

Figure 1.14: The stages of an FT-ICR experiment. Ions trapped in the cell move with a small cyclotron radius (a). An RF frequency sweep is applied to excite the ions to a larger cyclotron radius allowing detection (b and c). Coherent ion packets are detected through an induced current across the detection plates (d). The induced current is measured as a time domain transient which undergoes Fourier transformation into the frequency domain (e). The frequency spectrum generated is calibrated into a mass spectrum (f).

The resolution of acquired data is directly proportional to the length of the transient image current. The transient signal is in constant decay due to collisions between ions and neutral molecules and de-phasing of the ion packet in the cell through space-charge effects. For this reason, FT-ICR MS must be performed at high vacuum. The relationship between resolving power and transient length is shown in Equation 1.8[95].

$$R = \frac{f_c T}{2}$$

Equation 1.8: The relationship between resolution and transient length in Fourier Transform data where R is the resolving power, f_c is the cyclotron frequency (in Hz) and T is the transient length (in seconds).

Axial confinement of the ions is achieved through the application of a voltage to the front and back trapping plates of the cell. High trapping voltages can increase resolution, through increasing trapping efficiency, but this creates the undesirable effect of increasing the magnetron motion of ions within the cell. Magnetron motion is introduced to the ions as a result of the trapping potentials; it is not a component of the Lorentz force and is of no analytical use. The lower measured frequency of ions in the cell, an effect of the magnetron motion, can shift observed masses to higher *m/z* values[94].

1.5 Fragmentation of Ions

While measurement of the intact mass of an ion can provide information such as the presence of post translational modifications, and in the case of proteins some insight about secondary structure (through observation of the charge state distribution), this alone is insufficient to fully characterise any PTMs, especially when PTMs of similar mass are present. In these circumstances, the identification of any PTMs is limited by the resolving power and mass accuracy of the instrument. Isolation of an ion, and its subsequent fragmentation can provide further information on the location of PTMs.

Several fragmentation techniques have been adapted for use in FT-ICR instruments, with developments constantly being made in this area. Tandem mass spectrometry involves the fragmentation of a precursor ion (MS/MS), and provided that fragment ions are present in high abundance, this process can be repeated (MS^n). Modern FT-ICR instruments allow the comprehensive study of intact proteins by using multiple fragmentation techniques. The most common techniques are described below.

1.5.1 Fragment Ion Nomenclature

When studying proteins and peptides by fragmentation, the peptide backbone can be cleaved in three possible places; each of the covalent bonds present in an amino acid. After dissociation, gas-phase re-arrangements take place to form more stable ions where the charge can be retained on the N-terminus or the C-terminus of the fragment. Depending on the type of fragments formed, N-terminal fragments carrying the charge are called *a*, *b* or *c* ions, while C-terminal fragments are called *x*, *y* or *z* ions[100]. Fragment ions formed tend to be specific to the fragmentation method used, and usually appear in pairs; e.g. *a* ions are formed with *x* ions, *b* ions with *y* ions and *c* with *z* ions. A numerical value is also assigned to each fragment generated, indicating the number of amino acids present in the fragment. In addition to cleavage of peptide backbone bonds, it is also possible to break bonds of the amino acid side chain, termed *d*, *v* and *w* fragments; the presence of side chain fragments can greatly complicate interpretation of fragmentation spectra. Figure 1.15 is an illustration of the different fragments formed through cleavage of the bonds in the peptide backbone.

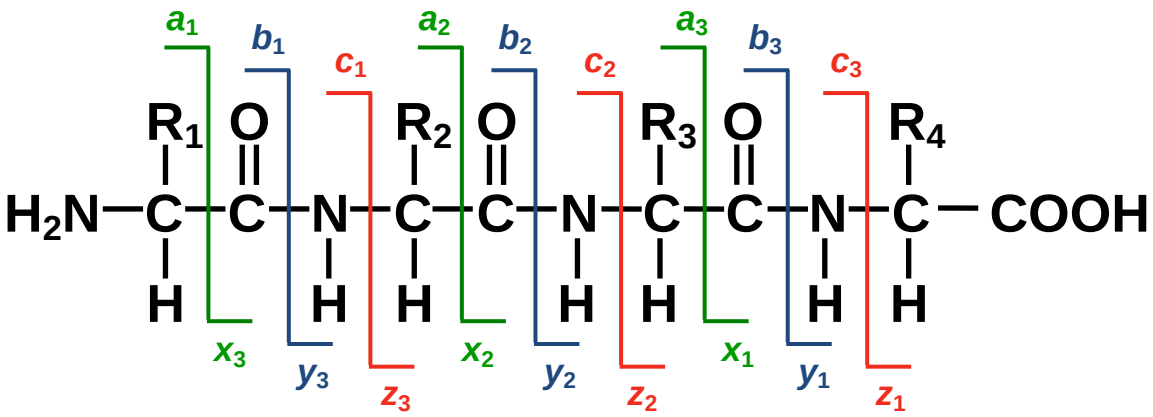

Figure 1.15: Nomenclature of fragment ions formed from the cleavage of the peptide backbone. Typically *a* and *x* ions appear together (green), *b* and *y* (blue) and *c* and *z* ions (red) are formed depending on the fragmentation method used.

1.5.2 Collision Induced Dissociation

Collision Induced Dissociation (CID) is a routinely used fragmentation technique due to its reproducibility and simplicity of application. This method works by increasing the internal energy of the precursor ion after collision with a neutral gas (typically helium, nitrogen or argon), which leads to bond dissociation in the precursor[101-104]. CID can be classified as low energy or high energy, depending on the instrument used[105]. Along with infra-red multi photon dissociation (IRMPD), low energy CID can be considered a slow heating technique, which relies on increasing the internal energy of the precursor resulting in bond cleavage[106,107]. Fragmentation of proteins by slow heating methods primarily results in dissociation of the amide bonds of the protein or peptide, producing predominantly *b* and *y* fragment ions. In addition, cleavage of amino acid side chains and loss of small neutral molecules can occur, which can make interpretation of CID spectra more difficult, especially when trying to localise PTMs. However, CID alone is of limited use when characterizing PTMs of an intact protein, due to the relationship between fragmentation efficiency and molecular size. An increase in molecular size is accompanied by an increase in the number of degrees of freedom, resulting in a greater number of channels through which energy can be dissipated. In consequence, a decrease in yield of fragment ions formed through bond cleavage on the peptide backbone is observed with increasing precursor mass, resulting in lower sequence coverage.

1.5.3 Electron Capture Dissociation

Electron capture dissociation is a relatively modern fragmentation technique which is implemented almost exclusively on FT-ICR instruments[108,109]. ECD occurs through the recombination of an electron with a positively charged ion to induce N-C_α bond cleavage, preferentially giving *c* and *z* fragment ions. The bond dissociation process has been described as 'non-ergodic'; bond breaking occurs before the precursor can dissipate energy vibrationaly, resulting in random cleavage of specific bonds along the peptide backbone which is distinct from slow heating techniques[110,111]. Most importantly, due to this fast fragmentation labile post-translational modifications and non-covalent bonds often remain intact after backbone bond dissociation. As a result, more confident assignment of PTMs is possible, and internal fragments tend to be appear at much lower abundance in ECD spectra which simplifies their interpretation[112,113]. During the capture event, a multiply charged precursor $[M + nH]^{n+}$ acquires an electron, and if sufficient energy is accumulated, the N-C_α bond of the peptide backbone is cleaved. If bond dissociation does not occur, a charge reduced species is formed $[M + nH]^{n-1+}$. Traditionally the electron source in ECD was thermal emission of electrons from a filament placed at the rear of the ICR cell. Modern instruments employ a hollow dispenser cathode in the same position, with the added benefit that the hollow design of the cathode permits IRMPD as well as ECD.

ECD has several drawbacks; its implementation is predominantly limited to FT-ICR instruments, which has limited its use for top-down mass spectrometry. ECD is also an inefficient process; the recombination product of a positively charged precursor with an electron is primarily a charge-reduced ion[114,115]. For this reason, ECD can only be used on multiply charged precursor ions; therefore it must be used in an instrument with an ESI source[116,117]. The detailed mechanisms underlying bond cleavage during ECD are still subject to debate, however this area is explored in several publications[118-121]. The two most popular theories on the mechanism of *c* and *z* fragment ion formation are the Cornell mechanism and the Utah-Washinton mechanism[122,123]. The Cornell mechanism suggests that the electron is initially captured at a highly excited Rydberg state followed by localisation to a protonated site (such as a positively charged amino acid) resulting in

the formation of a hypervalent radical. The Utah-Washington mechanism proposes that the electron is captured to a stabilised amide π orbital rendering the amide bond super-basic. The amide radical subsequently attracts a proton creating *c* and $z^{\bullet}$ fragments.

Chapter 2

Materials, Methods and Instrumentation

This chapter describes the materials, methods and instrumentation employed in this research. The materials section covers solvents and samples which were utilised. The methods section describes the techniques used for sample generation (e.g. cell culture, protein extraction) and the high performance liquid chromatography used in the separation of the sample mixtures for the LC-MS analyses. The instrumentation section provides a detailed discussion of the operation of the FT-ICR mass spectrometer.

2.1 Materials

The materials used in this work are listed in Table 2.1. This list includes materials used for sample generation, along with samples which were purchased for study and consumables such as solvents. The compound names are listed, along with the supplier name, and the purity of the compound is given if applicable.

Table 2.1: Materials used in this work, together with purity and supplier information.

Name	Purity	Supplier
Acetonitrile	LC-MS	Fisher Scientific
Methanol	LC-MS	Fisher Scientific
Water	LC-MS	Fisher Scientific
Formic Acid	~98 %	Fluka Bio-Chemika
Trifluroacetic Acid	≥98 %	Sigma
Ammonium Acetate	99 + % HPLC	Fisher Scientific
NuPAGE MES Running Buffer	N/A	Invitrogen
SeeBlue Gel Stain	N/A	Thermo Scientific
NuPAGE Bis-Tris Gels (12%)	N/A	Invitrogen
NuPAGE Sample Reducing Agent	N/A	Invitrogen
Sulphuric Acid	>95 %	Fisher Scientific
Trichloroacetic Acid	≥99.5 %	Fisher Scientific
Acetone	Analytical Grade	Fisher Scientific
Hydrochloric Acid	~37 %	Fisher Scientific
Trichostatin A	0.2 μM filtered	Sigma
RPMI 1640 Medium	Sterile-filtered	Sigma

Fetal Calf Serum	Sterile-filtered	Sigma
Penicillin/Streptomycin Mix	Sterile-filtered	Sigma
Bradykinin Acetate	≥98 % (HPLC)	Sigma
Angiotensin I Acetate Hydrate	≥90 % (HPLC)	Sigma
Angiotensin II human Acetate	~98 % (HPLC)	Sigma
Bombesin Acetate Hydrate	≥97 % (HPLC)	Fluka Bio-Chemika
Lutenising Hormone Releasing Hormone Human Acetate Salt	≥98 % (HPLC)	Sigma
Ubiquitin from Bovine Erythrocytes	~98 % (SDS-PAGE)	Sigma
Myoglobin from Horse Heart	≥90 % (SDS-PAGE)	Sigma
Deuterium oxide (d2O)	99.9 %	Sigma
Deuterated Acetic Acid	99.5 %	Arcos Organics
ESI Tuning Mix (low concentration)	N/A	Agilent Technologies
Sinapic Acid	~98 % (GC)	Sigma
Deuterated Acetic Anhydride	98.5 %	Arcos Organics
Dimethyl Sulfoxide	N/A	Sigma
SeeBlue Pre-Stained Standard	N/A	Invitrogen

2.2 Methods

The following section describes in detail the cell lines and techniques used for sample generation and purification in this research.

2.2.1 Cell Lines

Several cell lines were used to generate histone samples for LC-MS analysis, with some chosen for further fragmentation studies. The cell lines used were as follows:

K562, a human cell line of myeloid lineage derived from a 57 year old female subject suffering from chronic myeloid leukemia (CML)[124].

THP1, a human cell line of monocytic lineage derived from a male subject suffering from acute myeloid leukemia (AML)[125].

HCT-116, a human cell line of colon epithelial lineage derived from the primary colon carcinoma of a subject[126].

OCI-AML3, a human cell line of myeloid lineage derived from a 57 year old male subject suffering from AML[127].

MV411, a human cell line established from the blast cells of a male subject suffering from biphenotypic B-myelomonocytic leukemia[128].

SN1, a human cell line derived from a patient with T-cell type acute lymphoblastic leukemia (T-ALL)[129].

RAJ1, a hematopoietic cell line derived from an 11 year old male subject suffering from Burkitts Lymphoma[130].

2.2.2 Cell Culture Conditions

Cells were grown in 75 cm^2 culture flasks in RPMI medium supplemented with 10% fetal calf serum and 1% penicillin/streptomycin mix to inhibit bacterial growth. Cells were incubated at 37°C in an atmosphere of 95% O_2 and 5% CO_2 and cultured to roughly 80%

confluence. At 80% confluence the cells were harvested for acid extraction of histone proteins.

2.2.3 Histone Extraction Procedure

1 ml of nuclear isolation buffer (250 mM sucrose, 50 mM Tris-HCl, pH 7.5, 25 mM KCl, 5 mM MgCl, 0.2 mM phenylmethylsulfonyl fluoride, 50 mM $NaHSO_3$, 45 mM sodium butyrate, 10 mM 2-mercaptoethanol and 0.2% Triton X-100) was added to the cell culture and allowed to stand at room temperature for 5 minutes. After 5 minutes, the cells were scraped manually from the bottom of the culture flask and the buffer containing the cells was aspirated from the flask and dispensed into a 1.5 ml Eppendorf tube. The buffer was centrifuged at 13,000 rpm for 5 minutes to pellet the cells, which were then washed with phosphate buffered saline (PBS) and centrifuged again. The following steps were performed on ice. 1 ml of 0.2 M H_2SO_4 was added to the cell pellet, which was then agitated to facilitate exposure to the acid. The acid extraction was allowed to proceed for 60 minutes, after which the sample was centrifuged at 13,000 rpm for 15 minutes (at 4 °C). The supernatant was transferred to a new Eppendorf tube and 250 µl TCA (100%) was added and incubated for 30 minutes. The sample was then centrifuged at 13,000 rpm for 15 minutes, after which the supernatant was aspirated and discarded. The remaining pellet containing the histone proteins was washed in 1.3 ml acetone (with 50 mM HCl) and allowed to stand for 60 minutes. The sample was then centrifuged at 13,000 rpm for 15 minutes, before the supernatant was aspirated and discarded. The sample was then washed in 1.3 ml acetone and left at 4 °C overnight. After the overnight wash, the sample was centrifuged for 15 minutes at 13,000 rpm, the acetone removed and the pellet allowed to air dry before being re-suspended in H_2O.

2.2.4 Gel Electrophoresis

The presence of protein in the histone extracts was confirmed by gel electrophoresis using precast NuPAGE Bis-Tris Gels (12 %). Samples were mixed with an equal volume of reducing agent and boiled for 5 minutes. After boiling, samples were loaded into the gel lanes and run in MES buffer at 200 V for ~ 60 minutes. After electrophoresis the gel was washed briefly in H_2O before staining for 2 hours in SeeBlue Gel Stain Reagent. After staining, the gel was left to destain in H_2O overnight.

2.2.5 Reverse Phase High Performance Liquid Chromatography

All chromatography carried out in this work was performed on a Dionex Ultimate 3000 LC system which was equipped with a variety of reverse phase columns. The reverse phase columns used for the majority of this work were a Dionex monolithic PS-DVB column (50 mm x 0.5 mm), and a Vydac C_{18} RP column (250 mm x 1 mm). The buffers and gradients used are described below.

The buffers used with the monolithic column were 98% H_2O, 2% acetonitrile with 0.03% TFA (Buffer A), and 80% acetonitrile, 20% H_2O with 0.03% TFA (Buffer B). The column was heated to an operating temperature of 65 °C and equilibrated with 100% Buffer A at a flow rate of 20 µl min^{-1}. A linear gradient was applied over 25 minutes to 57.1% Buffer B, at which point Buffer B was increased to 100%. This was held for 3 minutes and then reduced to 100% Buffer A and held for a further 7 minutes.

The buffers used for the Vydac C_{18} column were similar to those used with the monolithic column, but 0.1% formic acid was substituted for the 0.03% TFA. The column was operated at 25 °C at a flow rate of 100 µl min^{-1}. The percentage of Buffer B was increased to 44% as a linear gradient over 5 minutes. From 5 to 22 minutes Buffer B was increased to 49%, and was held at 49% for a further 5 minutes. At 27 minutes, Buffer B was increased to 100%, and held at this level for 5 minutes. At 32 minutes, Buffer A was set to 100% and held for a further 5 minutes.

2.3 Instrumentation

A primary aim of this work was to utilise a range of mass spectrometry techniques in the identification and characterisation of post-translational modifications (PTMs). The main instruments used were an Applied Biosystems 4700 MALDI-ToF, a Bruker Apex Qe FT-ICR and a Bruker solariX FT-ICR, both coupled to a 12 Tesla superconducting magnet. The solariX instrument is an upgrade of the Apex Qe and features enhanced ion optics which lead to greater sensitivity. Both FT-ICR instruments are equipped with a mass resolving quadrupole which allows the selection of a single ion species for subsequent fragmentation work. Additionally, both are capable of Collision Induced Dissociation (CID) and Electron Capture Dissociation (ECD) for increased sequence coverage and improved PTM localisation.

2.3.1 MALDI-ToF MS

MALDI-ToF was used in this work to confirm the presence of histone proteins in the samples generated. The sensitivity and speed of data acquisition makes the use of this instrument a viable alternative to the use of SDS-PAGE to confirm the presence of protein in a sample. MALDI-ToF mass spectrometry was performed on an Applied Biosystems 4700 Proteomics Analyzer in reflectron mode. The matrix used was a saturated solution of sinapic acid in 50% acetonitrile with 0.1% formic acid. Sample was applied to the MALDI plate by sequentially layering 0.3 µl of the matrix and allowing to dry, followed by 0.3 µl of the histone sample, allowing this to dry and adding a top layer of 0.3 µl matrix. The laser was set to 70% maximum power and each spectrum acquired was the sum of 1000 scans. Data was analysed using the Applied Biosystems Data Explorer software, exported and plotted using Microcal Origin 6.0.

2.3.2 FT-ICR MS

Fourier Transform Ion Cyclotron Resonance mass spectrometry has several advantages over other mass spectrometry techniques including high resolution, increased mass accuracy and multiple fragmentation capabilities. The FT-ICR instruments used in this work were either a Bruker Daltonics Apex Qe, or a Bruker Daltonics solariX system. During use, both instruments were equipped with a 12 Tesla ultra-shielded magnet with a stand-alone cryo-refrigeration system. Electrospray ionisation was used as an ion source for the work, either by motor driven syringe, by using the TriVersa Nanomate for direct infusion, or by coupling the source to the Dionex LC system for online LC-MS analysis. All data was acquired in positive ion mode.

The solariX FT-ICR MS instrument is shown in Figure 2.1, and a schematic overview of the instrument is shown in Figure 2.2.

Figure 2.1: The Bruker solariX FT-ICR MS instrument coupled to a 12 Tesla superconducting magnet.

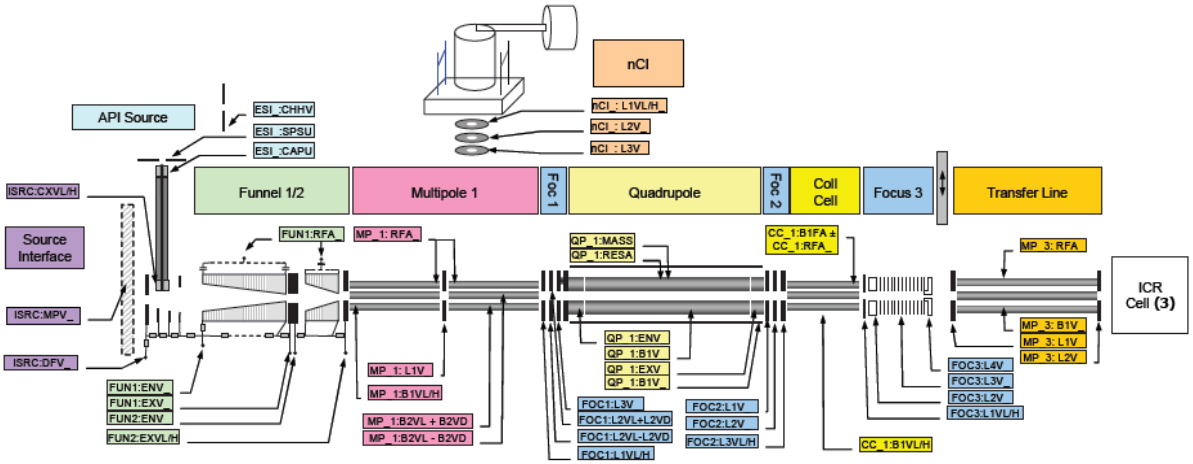

Figure 2.2: Schematic overview of the Bruker solariX vacuum cart.

Before proceeding with data acquisition, the instrument performance must be tuned for optimal sensitivity and resolution. Tuning of the instrument is effectively done in two stages; the first parameters to be optimised are those of the source and the ion optics which are responsible for ion transmission. These parameters must be tuned as the sensitivity of the instrument is dependent on them. Each instrument uses an orthogonal source design, a significant improvement over older models. The orthogonal positioning of the source drastically reduces the probability of neutral solvent molecules reaching the high vacuum regions, resulting in lower background pressure which aids detection in the ICR cell. Source tuning involves adjustment of capillary, funnel and skimmer voltages. The combined effect of these parameters allows for desolvated ions to travel through 'soft' or 'harsh' conditions. High source voltages can lead to in-source fragmentation, which under most circumstances is undesirable. Ions which have travelled through the skimmers and ion funnels can then be accumulated in the storage multipole. Accumulation times can be adjusted to compensate for low ion abundance; while during normal operation ion accumulation typically lasts for less than 1 second, this can be extended to over 30 seconds if necessary. This can bring with it a detrimental effect, the increase in accumulation time also increases the length of time required for each mass analysis, which makes coupling of the instrument to an LC system for online LC-MS analysis difficult. Under these circumstances, shorter accumulation times must be used along with a more concentrated sample. Once ions leave the storage multipole, species of interest can be selected in the mass resolving quadrupole before travelling through the transfer optics (focussing lenses and transfer lines) toward the ICR cell. The major difference between the Apex Qe instrument and the solariX is improved ion transfer optics. The solariX is equipped with a transfer line in front of the ICR cell, while in the Apex vacuum cart this was simply a drift tube. The resulting increase in ion transmission leads to the greater sensitivity of the solariX instrument.

Once a satisfactory level of sensitivity has been achieved, the remaining parameters to be optimised are those of the ICR cell which are responsible for the resolution of the instrument. A photograph of the ICR cell is shown in Figure 2.3[131].

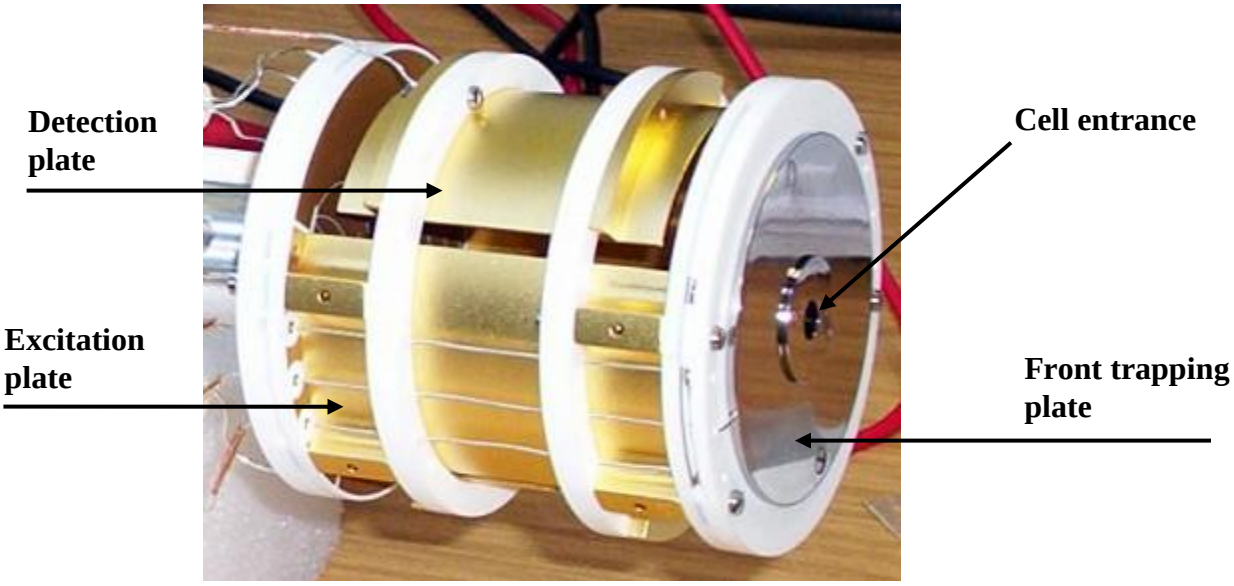

Figure 2.3: The Bruker Daltonics Infinity Cell used to trap, excite and detect ions.

While it is possible to use various trapping techniques in each instrument, SIDEKICK trapping was used throughout this work. The use of this technique alters the motion of the ions entering the cell, sending them off the central axis and closer to the excitation/detection plates. Although this makes in-cell fragmentation more difficult, this issue can be overcome with careful tuning of the instrument parameters.

2.3.2.1 On-line LC-MS

When used for online LC-MS analysis, the instrument was set to record mass analyses for the full length of the chromatography run. Each spectrum recorded was the sum of 2 mass analyses. The transient data size was 1M word for each acquisition and sine-bell squared multiplication (as windowing function) was applied during the acquisition. Ion accumulation times were typically 0.7 seconds, the source capillary voltage was set to 4500 V and the end plate offset to -500 V. Ions were trapped in the Bruker Daltonics Infinity Cell and the front and back plate trapping potentials were typically 0.55 V and 0.65 V respectively. Data was typically recorded over a mass range of 500-3000 *m/z*, and

was processed using Data Analysis software (Bruker Daltonics), then exported and plotted in Microcal Origin 6.0.

2.3.2.2 Direct Infusion

The solariX instrument was used for acquiring data from infused samples when using the TriVersa Nanomate as the ESI source. When performing optimally, the Nanomate could provide up to 90 minutes of continuous spray from a sample size of 10 µl, permitting extensive fragmentation work to be carried out. The Nanomate was set to operate in 'infusion' mode, the gas pressure was set to 0.65 psi and the spray voltage set to 1.65 kV.

2.3.2.3 Top-Down Fragmentation

Tandem mass spectrometry (both CID and ECD) was performed on the Bruker solariX instrument. During the acquisition of MS/MS spectra, the ion accumulation time was increased, often to 20 s when performing ECD. Spectra were the sum of up to 500 mass analyses, and data was acquired over a range of 500–3000 *m/z*.

Before any fragmentation data was acquired, the fragmentation parameters were tuned by infusing a 5 µM solution of equine myoglobin (Sigma) in a mixture of methanol and H_2O with 0.1% formic acid. Typically, after the successful isolation of a selected precursor, the fragmentation parameters were adjusted such that the precursor ion abundance would drop to roughly 10% of its value before spectra were recorded. These parameters (with the exception of ion accumulation times) were then applied to the sample of interest. CID involved adjusting the voltage at the collision cell to a value between 18 V and 26 V. ECD involved heating of the hollow dispenser cathode by applying a current, usually 1.8 A, and adjusting the ECD pulse length until fragmentation was successful. Pulse lengths were typically between 8 ms and 20 ms. The ECD lens and bias voltages were set to 22.6 V and 2.3 V respectively.

2.3.2.4 Middle-Down Fragmentation

Middle down fragmentation was performed on proteins of interest by fraction collection and enzymatic digestion. Endoproteinase Asp-N was used for digestion. Fractions of the selected protein were collected manually after LC separation and concentrated using a SpeedVac Plus (Savant). After concentration the sample was resuspended in 100 mM NH_4CO_3 and the enzyme was added at a ratio of 20:1 (protein to enzyme). The mixture was incubated in a water bath at 37°C for 18 hours, before desalting using C_{18} zip-tips. Once desalted, a 50:50 mixture of methanol and H_2O with 0.1 % formic acid was added before the sample was infused.

2.3.3 Data Processing

All the data acquired was calibrated and processed before being plotted using Microcal Origin 6.0 for presentation.

2.3.3.1 Calibration

All LC-MS data and broadband infusion data were calibrated externally against Agilent low concentration ESI Tuning Mix. Fragmentation data was calibrated internally using fragment ion lists generated manually by simulating a series of C-terminal ions and searching against their empirical formulae.

2.3.3.2 Data Analysis

All data acquired on the Apex Qe and the solariX instruments was analysed using Data Analysis software (Bruker Daltonics). Isotope distributions were predicted using the IsotopePattern software and laid over experimentally acquired data. Mass measurement error (expressed as parts per million) was calculated from the most abundant isotopic peak of a specific charge state using Equation 2.1[132].

$$\text{MME (ppm)} = \frac{m_{\text{obs}} - m_{\text{exp}}}{m_{\text{exp}}} \text{ x } 10^6$$

Equation 2.1: Mass Measurement Error (in parts per million) calculation, where m_{obs} is the observed mass, and m_{exp} is the expected mass.

Fragmentation data was processed for mono-isotopic peak picking using the SNAP 2.0 algorithm (Bruker Daltonics). The fragment mass lists generated were searched for *b* and *y* or *c* and *z* ions using ProSight PTM[133] by inputting the amino acid sequence and manually applying acetylation and mono-, di- and tri-methyl modifications to each modifiable lysine residue in all permutations. Each permutation was then ranked according to the number of fragment ions matched, and mass errors were set to a maximum of 10 ppm.

2.3.3.3 X-ray Crystal Structures

All X-ray structures were obtained from the RCSB Protein Data Bank (PDB). The structures were drawn using Pymol software (Delano Scientific), and PDB identification numbers are listed in the figure captions.

2.3.3.4 Sequence Alignments

All sequence alignments were performed with ClustalW2 software available online from the EBI web server[134]. Protein sequences were obtained from the UniProt Knowledgebase (www.uniprot.org).

Chapter 3

The Acetylation of Histone H4

This chapter describes experimental work carried out to study the acetylation pattern of histone H4. Although already described, a brief summary of H4 modifications is given along with their associated biological functions. The aims of the experimental work are stated, along with a description of the work performed, and the results generated.

3.1 Introduction

Eukaryotic histone H4 is known to have only one sequence variant. The protein is 102 amino acids long, and plays a critical role in nucleosome assembly as it forms half of the H3-H4 tetramer of the core particle[135]. In common with the other core histones, it contains a central globular region formed of three α-helices, and contains an unstructured N-terminal region which contains roughly 25% of the amino acid content. Also common with the other core histones, the N-terminal region is the primary site of PTMs, and similar to H2a, H4 is acetylated on the N-terminal residue. However, this acetylation is not subject to regulation by acetyl-transferase and de-acetylase enzymes. Figure 1.4(d) shows histone H4 with the sites of modification highlighted, while Table 3.1 lists the associated biological function of the PTMs.

Table 3.1: Different classes of histone PTMs and their associated biological functions. Adapted from Kouzarides[136].

Histone Modification	Residues Modified	Biological Function
Acetylation	**K**-Ac	**Transcription, repair, replication**
Methylation (Lysine)	**K**-Me, **K**-Me2, **K**-Me3	**Transcription, repair**
Methylation (Arginine)	**R**-Me, **R**-Me2a, **R**-Me2s	**Transcription**
Phosphorylation	**S**-Ph, **T**-Ph	**Transcription, repair, condensation**
Ubiquitylation	**K**-Ub	**Transcription, repair**
Sumoylation	**K**-Su	**Transcription**
ADP ribosylation	**E**-Ar	**Transcription**

There are 18 known histone de-acetylase enzymes in humans, and as explained in Section 1.1, each can have multiple acetyl lysine binding sites, and so may have a different associated function[48,66,137].

Since the modification state of the protein is the result of the interplay between HATs and HDACs, a relevant question to ask is how do PTMs change when one of these enzyme systems is inhibited? Several histone de-acetylase inhibitors (HDACi's) are now known and some show promise in the treatment of neural disorders, endometriosis and some cancers[56,138-143], however little is known of their mode of action, and of how histone PTMs change other than on the global scale. HDACi's can broadly be divided into four classes; short chain fatty acids, hydroxamic acids, cyclic tetrapeptides and benzamides[56]. One HDACi in particular, trichostatin A (TSA), is known to completely alter the PTM profile of histone H4 after mild treatment (i.e. nM concentrations over 3 hours)[144,145]. Upon withdrawal of TSA, H4 modifications return to their base level. The structure of TSA is shown in Figure 3.1 below.

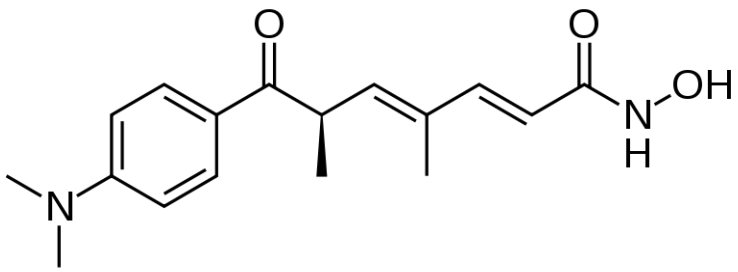

Figure 3.1: Structure of the histone de-acetylase inhibitor TSA[146].

While there are five lysine residues in the H4 N-terminal region, the distribution of PTMs is not uniform. Figure 3.2 below shows the sequence of histone H4 with the most commonly modified N-terminal residues highlighted.

SGRGKGGKGL GKGGAKRHRK VLRDNIQGIT KPAIRRLARR GGVKRISGLI

YEETRGVLKV FLENVIRDAV TYTEHAKRKT VTAMDVVYAL KRQGRTLYGF GG

Figure 3.2: Amino acid sequence of histone H4 with modified N-terminal residues highlighted according to known modifications. ( ) indicates acetylation and ( ) methylation.

The N-terminal acetylation, which can be considered as the first PTM to occur, is not under the control of acetyl-transferase and de-acetylase enzymes. As a result, H4 not carrying the N-terminal acetylation is typically not observed. The next main sites of modification are lysines 5, 8, 12 and 16. Each of these is known to be dynamically acetylated in response to biological stimuli, either alone or in combination. The final N-terminal site of modification is lysine 20, which is primarily a site of methylation (mono-, di- or tri-methylation). This site is not known to be acetylated, and in contrast to acetylation, methylation appears to be a more stable modification, with patterns changing little through cell cycle progression and duplication. Histone methylation of H3 and H4 has been linked to nucleosome stability; while acetylation is thought to play a regulatory role in gene transcription, methylation has been found associated with heterochromatin, suggesting a link to gene silencing[147]. Turnover of H4 methylation is much lower than acetylation[148,149]. Interestingly, while methylation appears to have a different biological role to acetylation, there appears to be little competition between these modifications on H4 [150]. However, similar to the interplay known on H3, the appearance of methylation and acetylation on H4 are linked. H3 methylation is known to change in response to

environmental exposure, and studies have shown that methylation can be the more dominant PTM when present before acetylation takes place, suggesting that for maximum effect each modification must be site specific and deposited in a temporally specific way[45,140]. Further studies reinforced these links by focusing on changes in these PTMs after treating cells with de-acetylase inhibitors. For example, it was shown that TSA treatment also alters H4 methylation state in addition to the level of acetylation, and that DNA hyper-methylation is a pre-requisite for histone de-acetylation[55,151].

While many compounds are now known to affect histone acetylation, the first in-depth studies focused on the effects of butyrate treatment[35,152-154]. Initially, it was shown that levels of acetylated H3 and H4 increased following butyrate treatment in HeLa cells, and that this accumulation was reversible upon withdrawal of treatment. This treatment was also shown to alter differentiation patterns in Friend erythroleukaemia cells, suggesting a possible link between histone modification and cell cycle progression[153,155]. Butyrate treatment was also shown to affect cell morphology and had varying effects on the activity of several enzymes, many of which are involved in metabolic pathways[152].

The acetylation levels of core histones are under the control of enzymes with opposing activities: histone de-acetylases (HDACs) and histone acetyl-transferases (HATs). Gene transcription is regulated through the action of these enzymes at the level of nucleosomal DNA packaging. Many histone de-acetylase inhibitors have now been described, typically short chain compounds such as butyrate and valproic acid, and hydroxamic acids such as trichostatin A. One hypothesis explaining their use as anti-cancer drugs is that they are able to reactivate genes silenced by DNA hyper-methylation at promoter sites. Treatment of cells with these compounds results in a characteristic accumulation of highly acetylated histone forms, and the associated changes in gene expression, cell cycle progression and apoptosis. There is now significant interest in the natural microbial product TSA, which was initially isolated from *Streptomyces hygroscopicus*. TSA is a specific and potent inhibitor of class 1 and class 2 histone de-acetylase enzymes[156-158].

In the present work, since naturally occurring modifications are known to occur at specific sites or combinations of sites, the order of lysine acetylation was initially investigated through TSA treatment to determine how modifications would appear through inhibition of de-acetylase enzymes. A study was also carried out to investigate the responses of different cell lines to TSA exposure. The principal aims of the work described in this chapter were to investigate the effects of the HDAC inhibitor TSA across multiple cell lines, each of which carries mutations which may alter the PTM profile, and to use mass spectrometric fragmentation techniques to determine the order in which lysine residues on the N-terminal tail of histone H4 are modified.

3.2 Methods

3.2.1 Cell Culture and TSA Treatment

To determine whether or not de-acetylase inhibition was specific to a particular cell line, multiple human derived cell lines were cultured with a fixed concentration of TSA of 50 nM. The aim of this initial study was to confirm that TSA treatment resulted in a characteristic and reproducible increase in modified histone H4 isoforms. Cell lines were cultured at 37 °C in an atmosphere of 5% CO_2. RPMI culture medium was supplemented with fetal calf serum and penicillin/streptavidin to retard microbial growth. Cells were removed from the culture medium at three time points before histone extraction was performed as described in section 2.5. The culture times were 1h, 3h and 6h, and two controls were included for each cell line; 1h and 6h di-methyl sulfoxide (DMSO) treatment.

3.2.2 Liquid Chromatography and Mass Spectrometry

Histone extracts were separated by LC using a Vydac C_{18} reverse phase column, prior to FT-ICR mass spectrometry. Each sample was separated over a 37 minute gradient using an Ultimate 3000 LC system (Dionex), which was coupled to the ESI inlet of the mass spectrometer. The gradient was as follows: Buffer A was 2% acetonitrile in 0.03% tri-fluroacetic acid (TFA) and Buffer B was 80% acetonitrile with 0.03% TFA. The gradient rose to 44% B over 5minutes, from 5 to 22 minutes to 49% B, and held at 49% for a further 5 minutes. At 27 minutes Buffer B was increased to 100% and held for 5 minutes, before Buffer A was increased to 100% and held for 5 minutes.

The data presented in this chapter was acquired on two FT-ICR mass spectrometers. Much of the data for the HDAC inhibitor study (for the HCT-116 cell line) was acquired on a Bruker Apex Qe mass spectrometer, while the data for all other cell lines and all of the tandem mass spectrometry work to identify the order of acetylation was carried out on a Bruker solariX mass spectrometer. The solariX instrument offered greater sensitivity and better CID and ECD performance when compared to the Apex Qe. Data was

acquired in broadband mode with a mass range of 500-3000 *m/z*. Each spectrum was the sum of 500 mass analyses whenever possible.

For fragmentation work histone fractions were collected manually from each run and stored on ice. Successful fragmentation involved selection of a high charge state precursor ion (typically 13^+ or greater) followed by adjustment of the CID and ECD settings. Precursor ions were isolated and ion accumulation times for CID were 1 second, with the collision voltage set to ~ 18 V. ECD was performed with extended ion accumulation times, typically 20 seconds. The dispenser cathode was set to a current of 1.7 nA and the ECD pulse length was set to ~ 0.06 seconds.

3.2.3 Data Analysis

Data was analyzed using DataAnalysis software (Bruker Daltonics), before being exported and plotted in Microcal Origin (v 6.0). Calculation of the level of acetylated species was performed using an in-house written program (written in Python), using the method described by Smith[159,160], modified to suit the work performed. Briefly, acetylation was quantified from the integrated ion abundances of modified species. Typically, the three most abundant charge states were used for this analysis. Each integrated ion abundance was then weighted according to the number of modified Lysine residues. These were then summed and divided by the total weighted ion abundance of all modified H4 species possible. The levels of acetylation are presented as a percentage (i.e. ((acetylation present)/(acetylation possible)) multiplied by 100).

3.3 Results

3.3.1 H4 Acetylation in Multiple Cell Lines

Each cell line used in this study was analyzed under similar conditions. Figure 3.3 below shows a total ion chromatogram of Histone H4. Figure 3.4 shows the MALDI-ToF spectrum generated from the same sample prior to chromatographic separation while Figure 3.5 shows an extracted ion chromatogram for histone h4 from HCT-116 cells (1h control sample) with the LC gradient overlaid. H4 eluted as a single peak separately from the other core histones. A total ion chromatogram showing the elution of all histones during a typical chromatographic run is presented in Figure 3.3 below. The broadband spectrum generated by summing across the eluted peak is shown in Figure 3.3 with an inset of the 7^+ charge state, while a MALDI-ToF spectrum is shown in Figure 3.4.

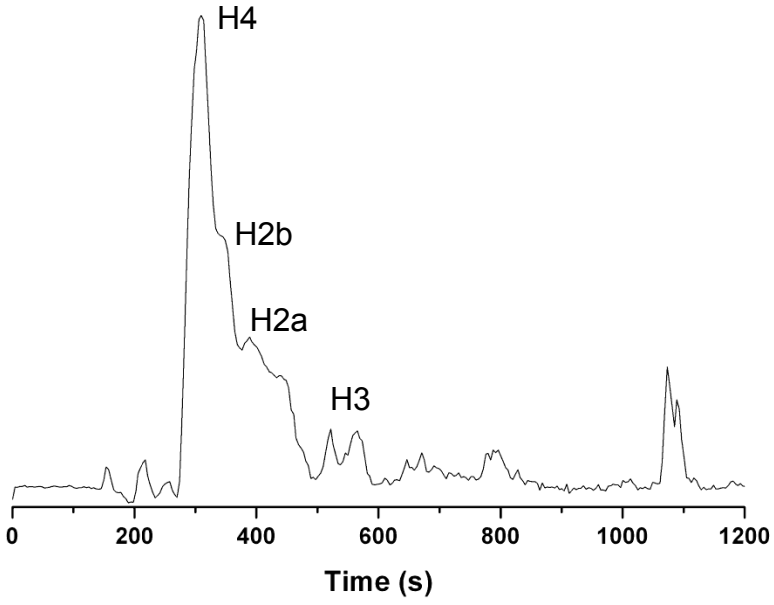

Figure 3.3: Total ion chromatogram of histone H4 from HCT-116 1h control cells. The peaks corresponding to the elution of the core histones are labelled..

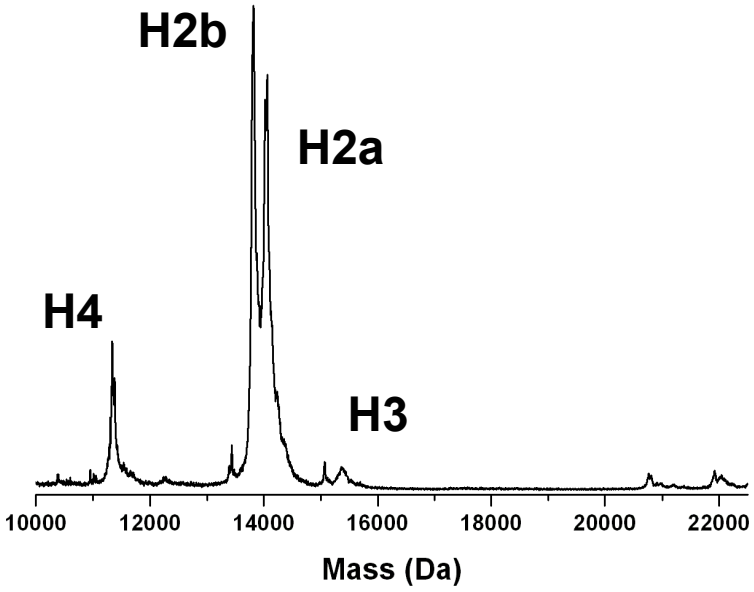

Figure 3.4: MALDI-ToF mass spectrum of core histones from HCT-116 cells after 1 hour DMSO treatment.

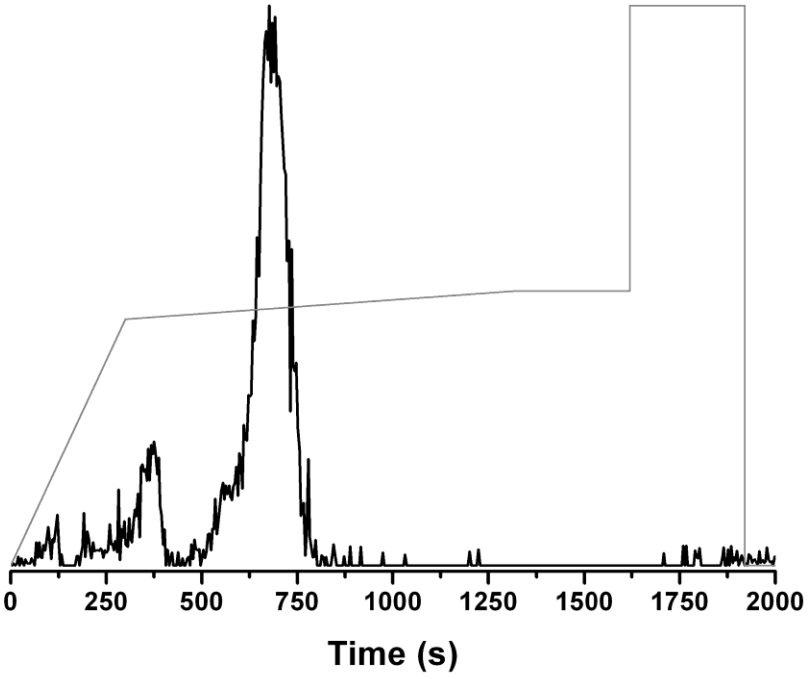

Figure 3.5: Extracted ion chromatogram of histone H4 from HCT-116 1h control cells. H4 eluted as a single peak over a time of roughly 200 seconds.

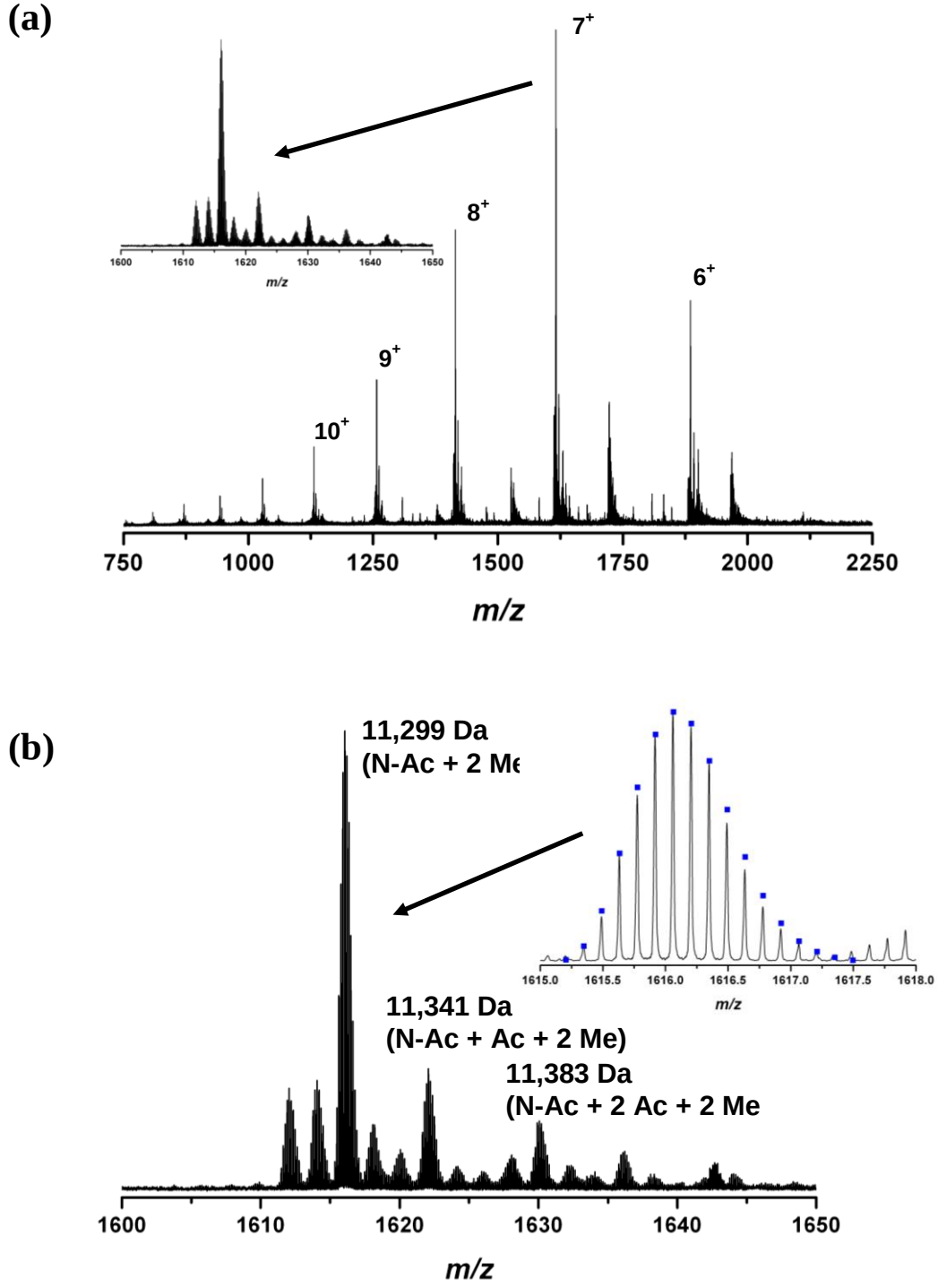

Figure 3.6: Mass spectrum of H4 from HCT-116 cells after 1h DMSO treatment. (a) broadband spectrum with inset of 7^+ charge state. (b) 7^+ charge state with inset of base peak corresponding to an intact mass of 11,299 Da. The post-translational modifications of three peaks are labelled where, (N-Ac) means N-terminal acetylation, (Ac) means acetylation and (Me) means methylation. A simulated isotope pattern is included (blue dots) corresponding to N-terminally acetylated di-methylated H4 (11,299 Da).

SDS-PAGE followed by Coomassie Brilliant Blue staining revealed bands corresponding in molecular weight to the core histones (data not shown). With their presence in the samples verified by electrophoresis, analysis was then performed by LC-MS. The gradient conditions used allowed elution of histone H4, with little contamination of other core histones with similar retention to the column stationary phase, permitting the generation of mass spectra of good quality. While the spectrum shown in Figure 3.6 (above) is of H4, the first observation of note is the presence of multiple species in a single charge state. This highlights an important feature of H4, it is rarely present in unmodified form, and as shown in subsequent figures, multiple modified forms are typically present. The next feature to note is the regular spacing between modified forms, which correspond to regular mass shifts. The most abundant peaks are shifted in mass by 42 Da, while the minor peaks are separated by 14 Da. A 42 Da mass shift is in agreement with the presence of an acetyl group, while a 14 Da mass shift corresponds to the presence of a methyl group; both modifications are known to occur on histone H4. In addition, the 42 Da mass shift could also correspond to the presence of three methyl groups (present on a single lysine, or distributed over one, two or three residues). Ultimately, the identity and location of these modifications can only be confirmed through fragmentation studies which were also performed.

In the untreated control cells, the dominant form of H4 corresponds in mass to the presence of a di-methylated species with a single acetyl group (with theoretical mass of 11,299.383 Da, and measured mass of 11,299.520 Da giving a mass measurement error of 12 ppm. The peaks of next highest abundance also correspond to di-methylated species, with varying numbers of acetyl groups, suggesting that methylation (in this case di-methylation) is a stable modification, while acetylation is more dynamic.

Table 3.2: Modified H4 isoforms and their theoretical masses. All masses were calculated using Bruker Daltonics Isotope simulation software and only mono-isotopic neutral masses are displayed. Unmodified H4 is defined as H4 sequence (Uniprot P62805) with N-terminal methionine removed, acetylated at serine 1 and di-methylated at lysine 20.

H4 Isoform	Theoretical Mass (Da)
H4	11,271.351
H4 + Me	11,285.367
H4 + 2Me	11,299.383
H4 + 3Me	11,313.398
H4 + Ac	11,313.362
H4 + Ac + Me	11,327.378
H4 + Ac + 2Me	11,341.393
H4 + Ac + 3Me	11,355.409
H4 + 2Ac	11,355.372
H4 + 2Ac + Me	11,369.388
H4 + 2Ac + 2Me	11,383.404
H4 + 2Ac + 3Me	11,397.419
H4 + 3Ac	11,397.383
H4 + 3Ac + Me	11,411.399
H4 + 3Ac + 2Me	11,425.414
H4 + 3Ac + 3Me	11,439.430
H4 + 4Ac	11,439.394
H4 + 4Ac + Me	11,453.409
H4 + 4Ac + 2Me	11,467.425
H4 + 4Ac + 3Me	11,481.441

Examination of the abundance of all peaks reveals that those corresponding to di-methylated H4 species dominate the spectra, while other methylated forms account for the minority of H4 species observed. This high proportion of di-methylated H4 species is in agreement with previous studies on H4 which describe the stable presence of di-methylation (at lysine 20).

To determine an effective concentration range of TSA to use in further studies, a dose response study was performed on HCT-116 cells. Cells were cultured in medium identical to that used in the time course study, with the exception that a range of TSA concentrations were added to the medium. The TSA concentrations used were 10, 100, 250 and 500 nM, and the cells were cultured for a fixed time of thirty minutes before histone extraction and subsequent LC-MS analysis. The results of the TSA dose response treatment are shown in Figure 3.7.

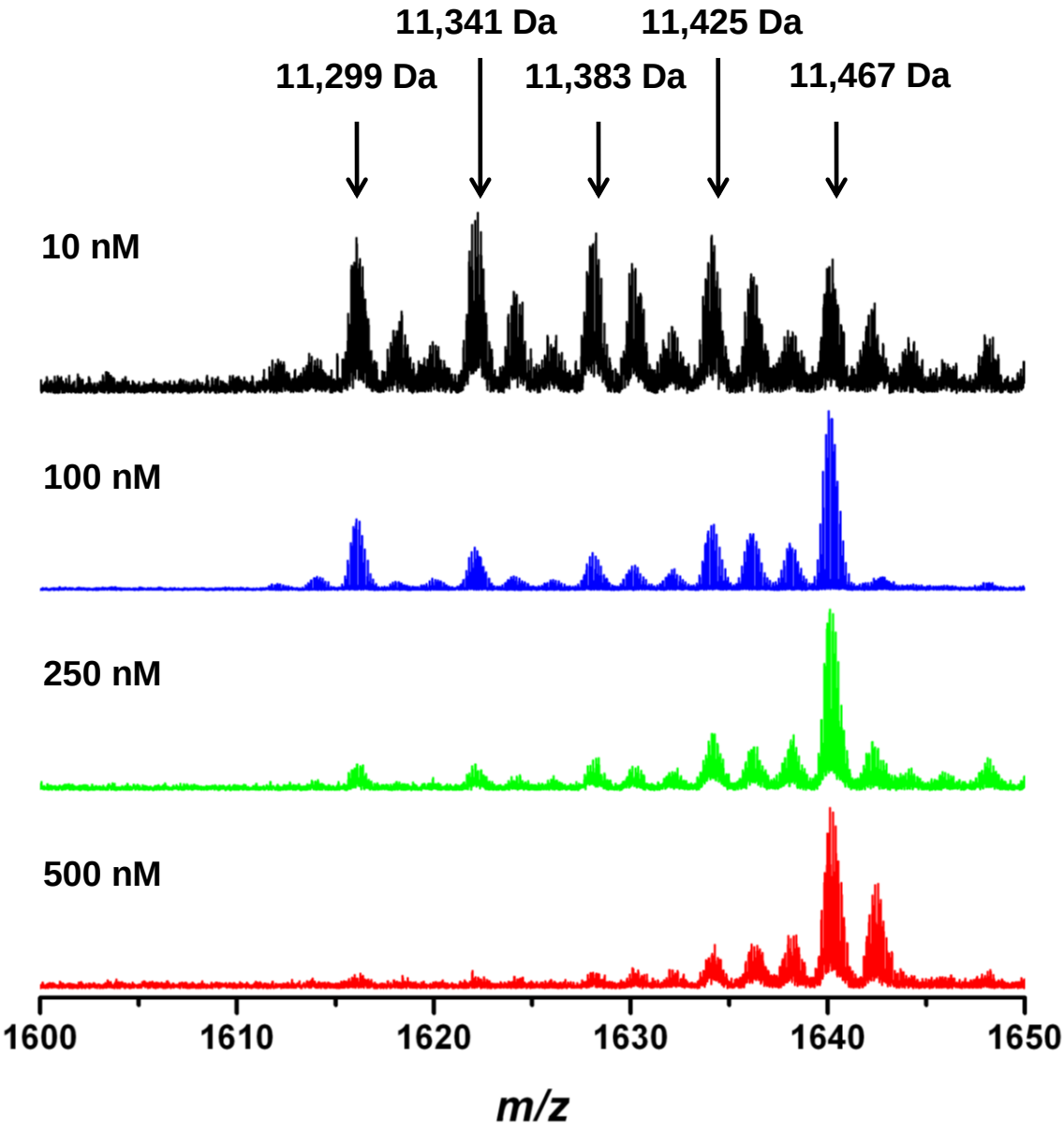

Figure 3.7: Dose response of HCT-116 cells after 30 minutes treatment to various TSA concentrations. The mass spectrum for the 7^+ charge state of the PTM profile is shown.

The results of the TSA dose response indicate the following: when present in concentrations as low as 10 nM, TSA has an inhibitory effect on histone de-acetylase enzymes, and these enzymes appear completely inhibited at a TSA concentration of 250 nM. Above a concentration of 250 nM, no further change in histone PTM profile is seen. It is clear from these results that above 250 nM TSA concentration, there is little further

effect on histone H4 acetylation level. The levels of acetylation calculated for the dose response treatment shown in Figure 3.4 were as follows; roughly 52% of N-terminal lysines were acetylated after the 10 nM treatment. At 100 nM this value rose to almost 61%. At 250 nM, the acetylation level was calculated at roughly 75% and the level of acetylation after 500 nM TSA treatment was 80%.

The effects of TSA time course treatment in HCT-116 cells are shown in Figure 3.8. The 50 nM treatment was applied for a range of times (between thirty minutes and six hours) before histone extraction. Figure 3.8 shows the mass spectrum for a single charge state of H4, the 7^+ charge, state following the various treatments. The masses of the multiple species in the spectra potentially correspond to modified forms of histone H4, listed in Table 3.2.

The TSA time course results demonstrate the effectiveness of TSA as a histone de-acetylase inhibitor. Analysis of the results reveals the following; although there is a shift in the abundance of modified H4 isoforms, the most dominant species still correspond in mass to di-methylated species. This finding confirms the suggestion that while TSA is effective in altering acetylation of H4, it has little effect on methylation state. The response to TSA treatment is also rapid, changes in acetylation state are seen after only thirty minutes of treatment with acetylation levels rising from 27% to 47%, and ultimately to 67% after 6 hours of TSA exposure. The control samples reveal that the changing acetylation state is a result of the TSA treatment, and not due to the culture conditions or the presence of di-methyl sulfoxide (added to the control samples as it was used as solvent for the TSA).

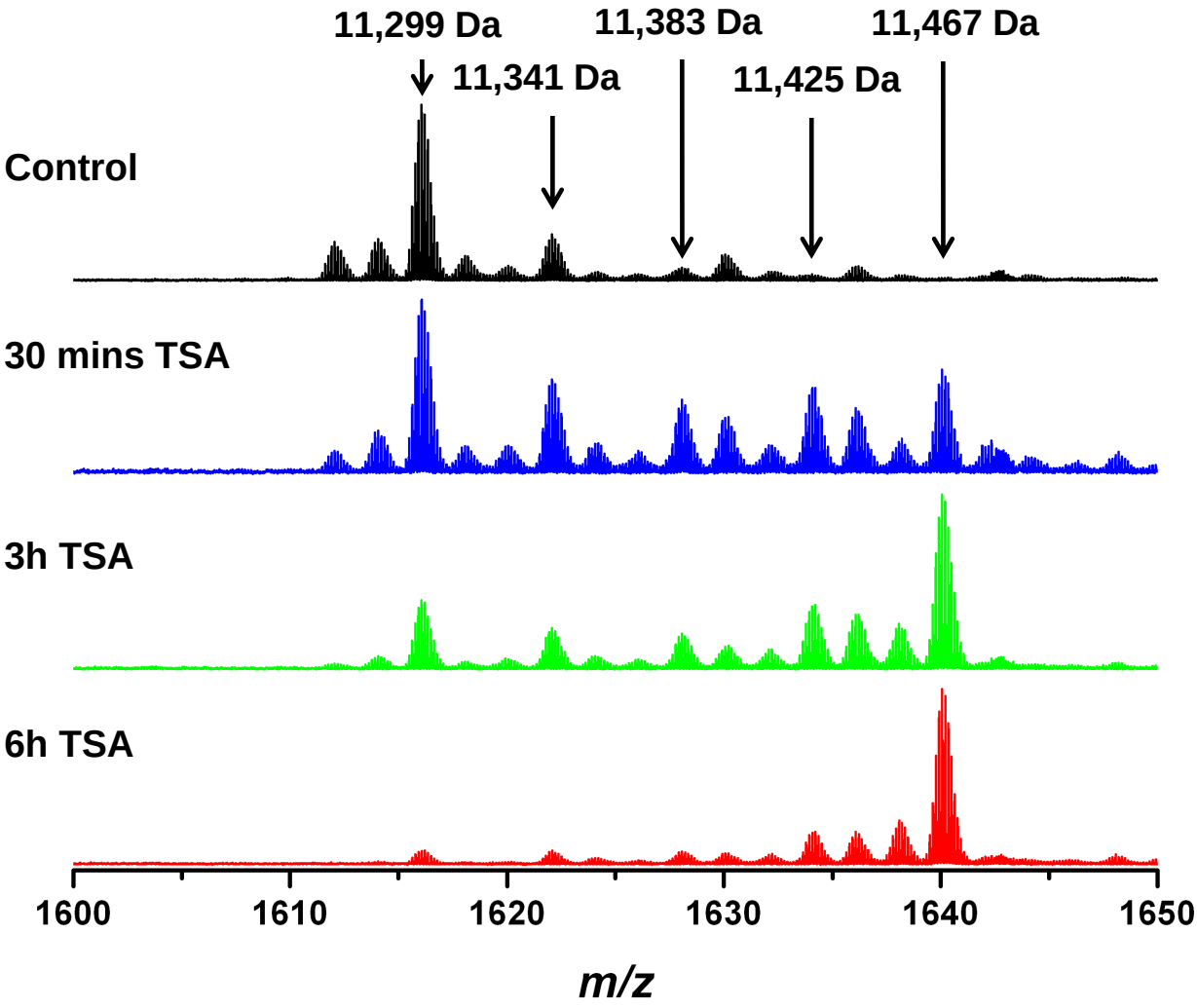

Figure 3.8: PTM profile in the mass spectrum for the 7^+ charge state of histone H4 from HCT-116 cells after 50 nM TSA treatment (30 mins, 3h and 6h). Untreated cells were included as control (cultured for 6h).

While the results demonstrate the efficacy of TSA as an HDACi in HCT-116 cells, they do not conclusively show that the action of TSA is universal across cell lines. To test whether or not TSA treatment would reproducibly result in the accumulation of acetylated forms of H4, multiple cell lines were treated with a fixed concentration of TSA (50 nM) for various time lengths before histone extraction. A brief description of the cell lines used is given in Chapter 2 (Section 2.2.1), however the cell lines used shared some common features. All were human derived, and all potentially carry genetic modifications which may play a role in affecting histone post-translational modification. Cell lines implicated in similar disease states (e.g. THP1 and OCI-AML3 are both linked to Acute Myeloid Leukemia) were derived from different patients.

The results of the cross cell line TSA time course study are shown in the following figures, Figures 3.9 to 3.14. In all of these figures the mass spectrum for the 7^+ charge state of histone H4 is shown to illustrate the PTM profile. The most striking aspect of the data generated is that while TSA is a potent inhibitor of de-acetylation in HCT-116 cells, this feature is not consistent across the cell lines chosen. The results of the OCI-AML3 TSA time course are shown in Figure 3.9. Acetylation in the control samples established a baseline level of roughly 23% (mean value of the two control samples). After one hour of treatment, acetylation rose to 34%, and increased to almost 46% after three hours. At six hours, acetylation is at a maximum of over 54%. The acetylation levels in the two control samples are in good agreement with each other, indicating that changes in acetylation are due to TSA treatment and not cell culture time. The acetylation seen in OCI-AML3 cells after TSA treatment is markedly different from that seen in HCT-116 cells, demonstrating that the cellular response to TSA is not universal across cell lines.

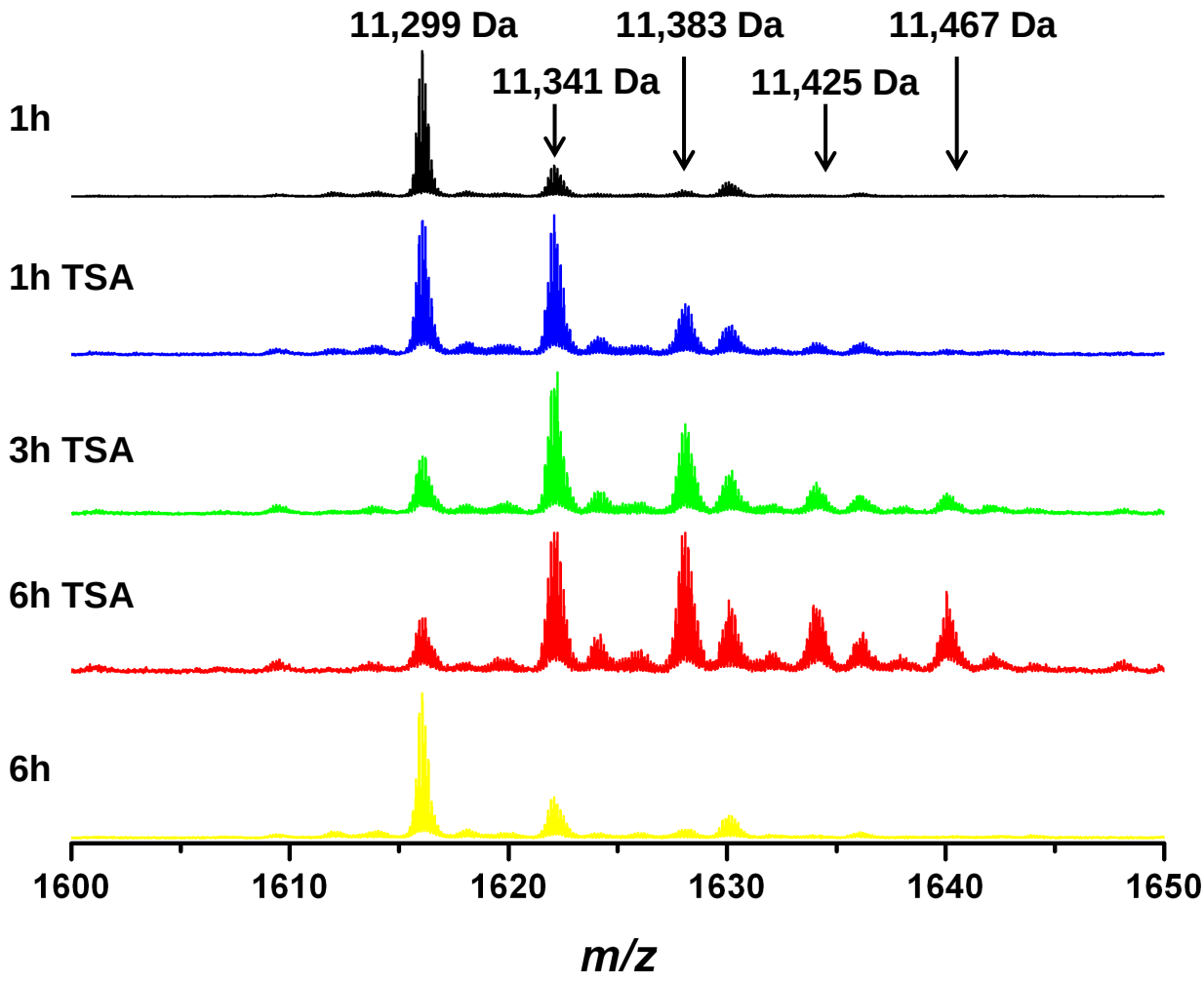

Figure 3.9: Response of OCI-AML3 cells to 50 nM TSA time course over 6 hours. The mass spectrum for the 7^+ charge state of the PTM profile is shown.

Treatment of the chosen cell lines with TSA did not result in a uniform acetylation profile, however, those that differed from the HCT-116 PTM profile displayed a similar distribution.

Figure 3.10 below shows the results of TSA time course treatment on K562 cells. In contrast with the results generated from HCT-116 cells, TSA treatment does not completely inhibit histone deacetylation. The data also reveals that in K562 cells, there is little change in acetylation levels after three hours treatment. Calculation of acetylation levels reveals that the occupation of acetylation sites sits at a baseline level of roughly

22% (the mean of the levels calculated from the two control samples). After one hour of treatment, acetylation rose to over 36%, and peaks at three hours at over 48%. At six hours of treatment, acetylation drops slightly to 45%. There is significant similarity in the acetylation of the two control samples, indicating that the different acetylation levels are a result of the TSA treatment, and not the length of time cells were cultured.

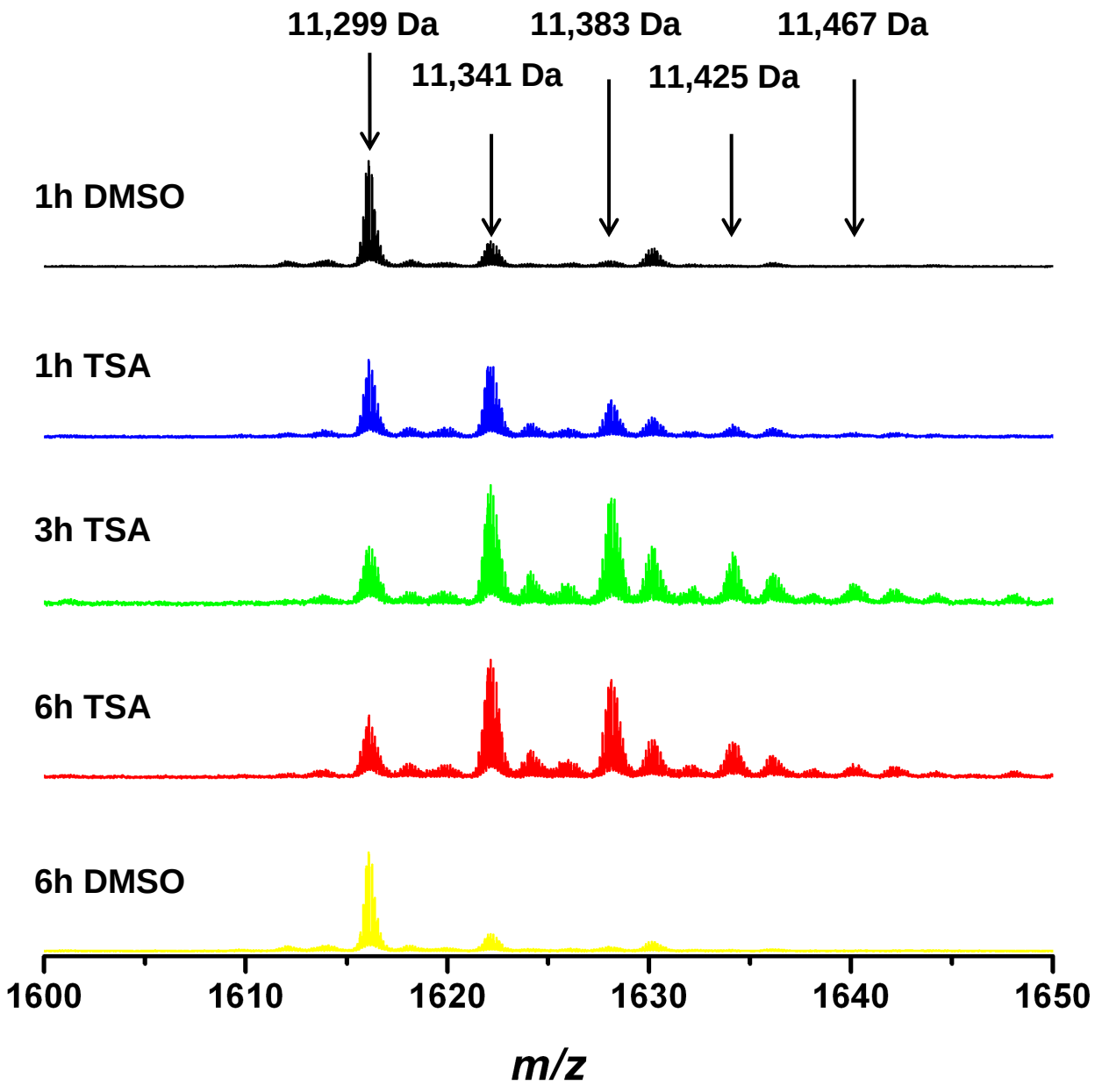

Figure 3.10: Response of K562 cell line to 50 nM TSA time course over 6 hours. The mass spectrum for the 7^+ charge state of the PTM profile is shown.

The results of the THP1 TSA time course treatment are shown in Figure 3.11 below.

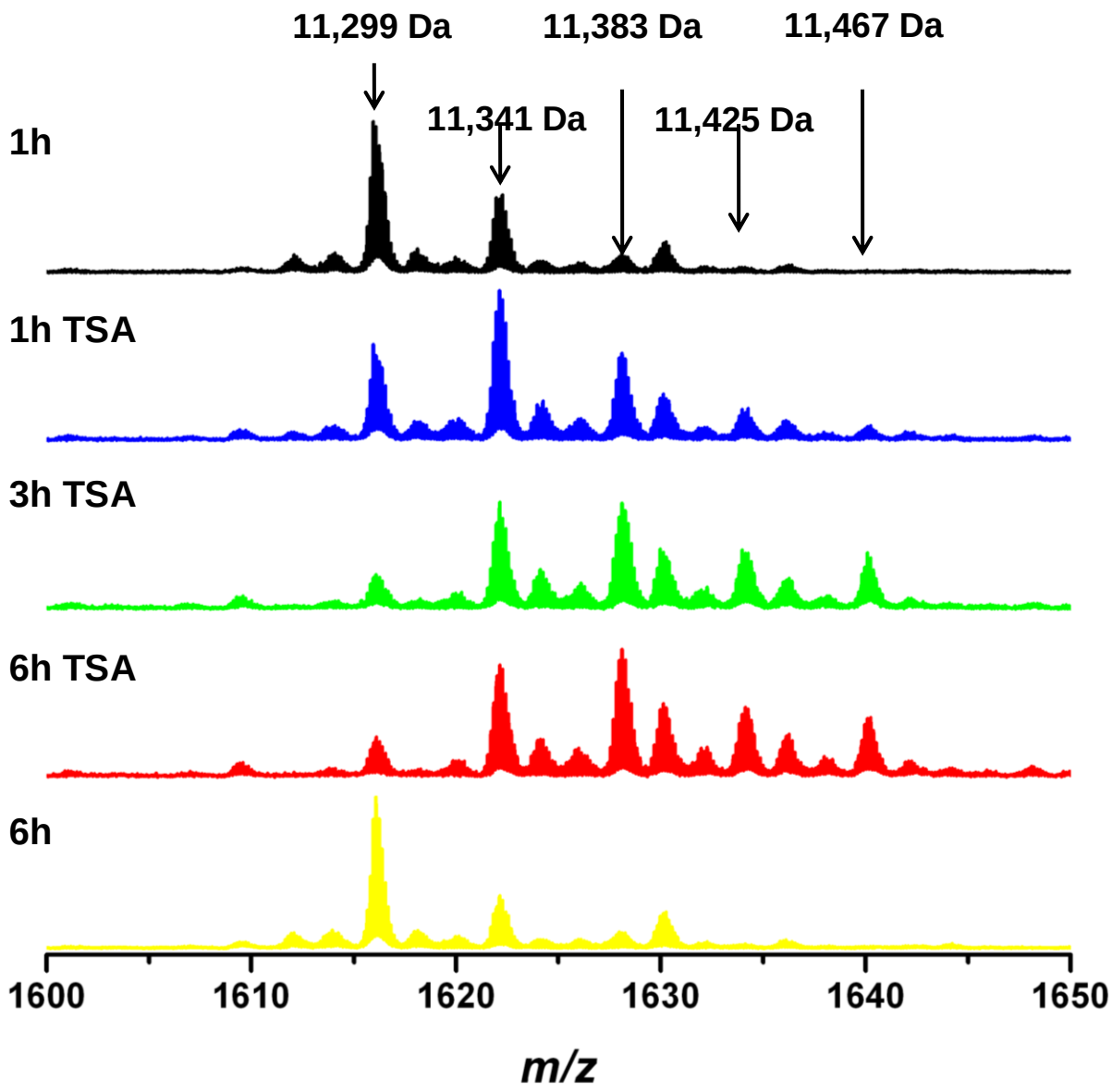

Figure 3.11: Response of THP1 cell line to 50 nM TSA treatment over 6 hours. The mass spectrum for the 7^+ charge state of the PTM profile is shown.

The baseline acetylation levels on the THP-1 cells are roughly 26% (generated from the values of the control samples). After one hour of TSA treatment, acetylation rose to over 41%, and reached 56% after three hours of treatment. After three further hours of treatment (at six hours), acetylation rose slightly to a maximum of over 57%. These

results are also in contrast to the results of TSA treatment on HCT-116 cells, again demonstrating that the effect of TSA as a de-acetylase inhibitor is not ubiquitous. There is good agreement in the acetylation levels of the control samples, indicating that changes in acetylation are due to the TSA treatment and not the length of cell culture time.

The results of the RAJ1 time course are shown in Figure 3.12 (below).

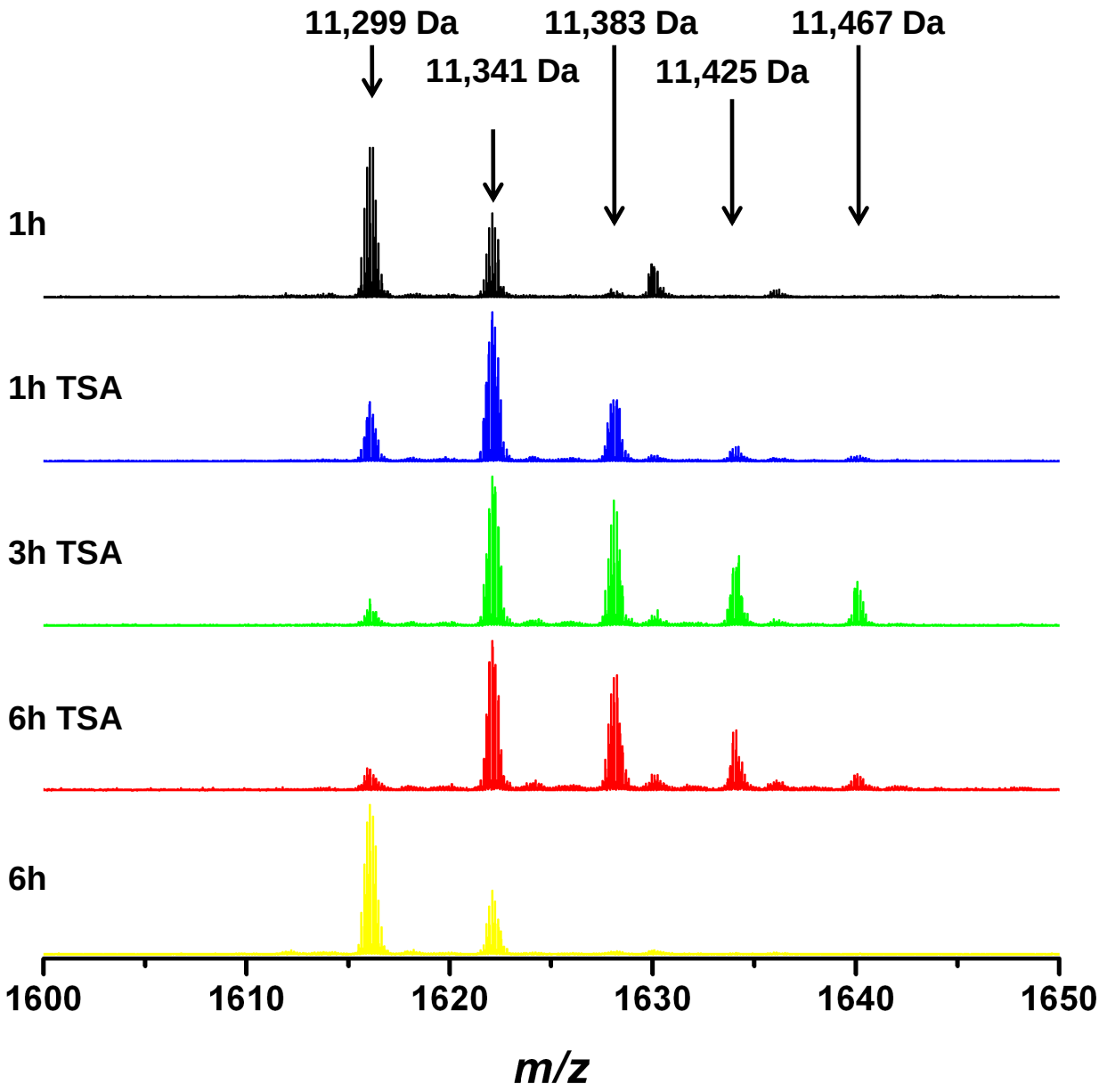

Figure 3.12: Response of RAJ1 cell line to 50 nM TSA time course over 6 hours. The mass spectrum for the 7^+ charge state of the PTM profile is shown.

The results of TSA treatment on RAJ1 cells further demonstrates that different cell lines respond to treatment differently. In comparison to other cell lines the baseline level of acetylation is slightly decreased at 20%. After one hour of TSA treatment acetylation rises to over 35%, and reaches its peak at over 51% at three hours treatment. By six hours, acetylation fell to 48%, and the six hour control sample displayed roughly 12% acetylation. The calculated standard deviations of the acetylation levels are low, all below 4%, showing good agreement from the data generated.

The results of TSA treatment on SN1 cells is shown in Figure 3.13 below. The control samples used to determine baseline acetylation levels are in good agreement with each other at roughly 10% each. After one hour TSA treatment, acetylation rose to almost 28%, and continued to rise to over 48% after three hours treatment. By six hours treatment, acetylation levels have reached their maximum at over 57%. The standard deviations of the calculated acetylation levels are low, all under 6%, indicating good agreement between the measured results.

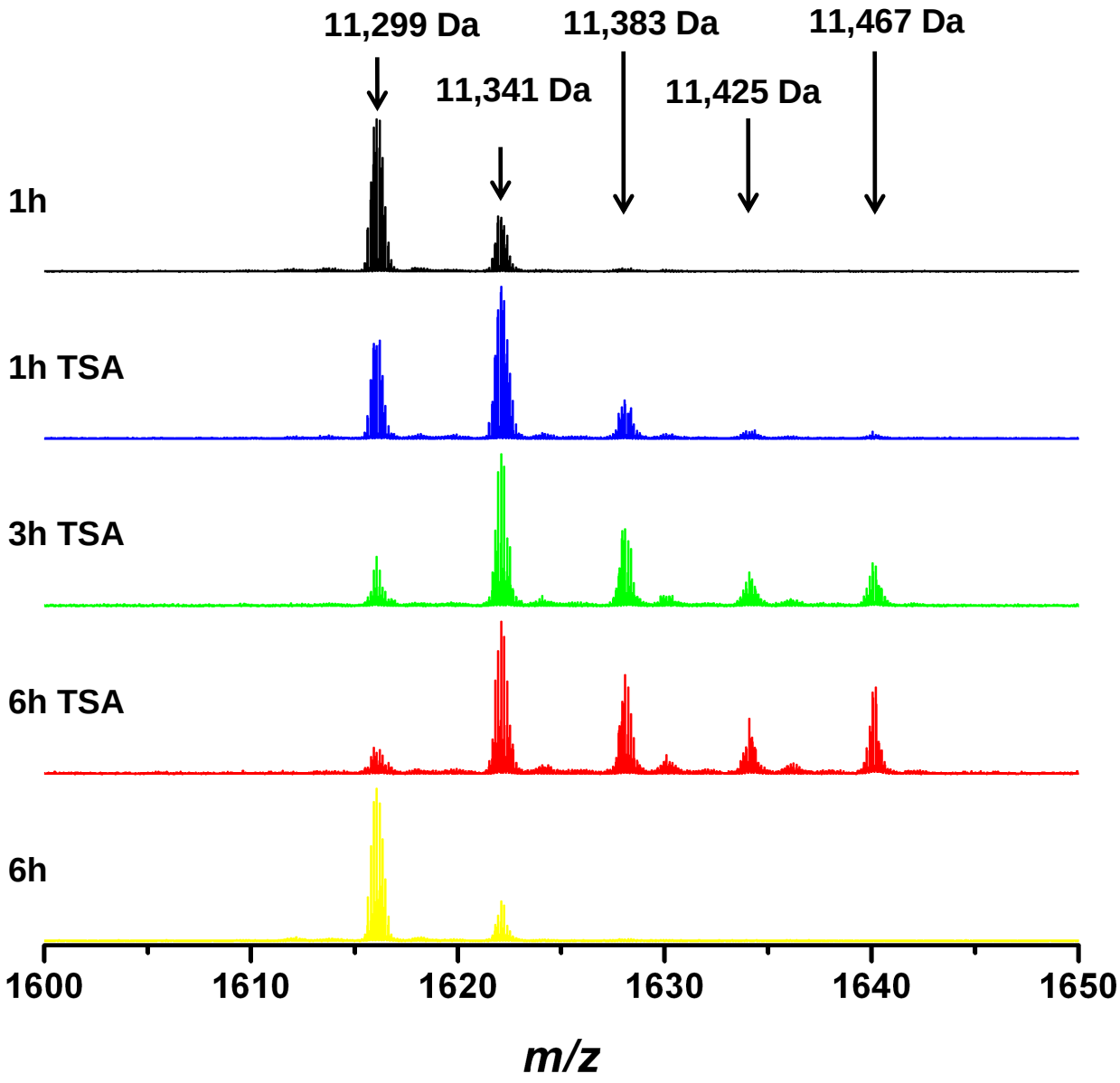

Figure 3.13: Response of SN1 cell line to 50 nM TSA time course over 6 hours. The mass spectrum for the 7^+ charge state of the PTM profile is shown.

The results of TSA treatment on MV411 cells is shown in Figure 3.14 below. Baseline acetylation, calculated from the control samples is low; at 12% after one hour, and at 11% after six hours of DMSO exposure. After one hour of TSA treatment acetylation rose to 28%, and continued to rise to 52% after three hours of treatment. After a further

three hours of TSA treatment (six hours), acetylation has reached a maximum of 54%. These results suggest that in this cell line, TSA treatment has little effect after three hours.

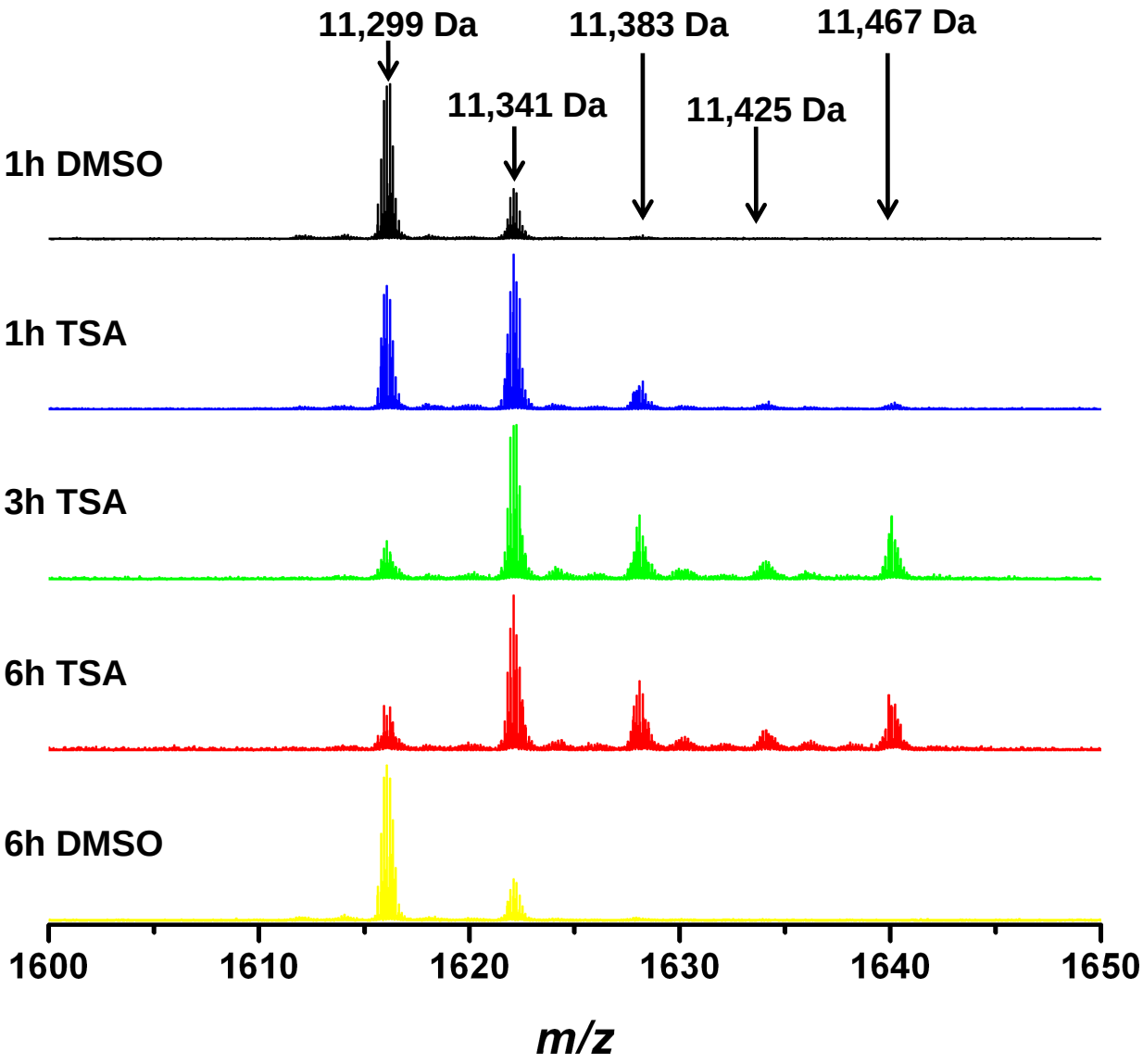

Figure 3.14: Response of MV411 cell line to 50 nM TSA time course over 6 hours. The mass spectrum for the 7^+ charge state of the PTM profile is shown.

The results of the TSA time course treatments demonstrate that the response to this de-acetylase inhibitor is similar across cell lines, but not identical. Each cell line displays an altered PTM profile after TSA treatment, but to varying levels. The different responses to the TSA time course are most likely a result of the gene mutations present in each cell

line. The majority of the cell lines tested exhibited a similar response to the TSA treatment; i.e. culture medium supplemented with TSA would result in an increase in acetylated histone H4 species, but full hyper-acetylation was never realized. The cells which displayed this response were all derived from various white blood cells and several are known to contain mutations which result in expression of fusion proteins. The only cell line in which full hyper-acetylation was achieved was the HCT-116 cell line which is derived from colo-rectal carcinoma.

3.3.2 Determination of the Order of Acetylation of Histone H4

In order to further investigate the response of different cell lines to HDACi treatment, histones were extracted from two of the previously utilized cell lines and after separation through HPLC, fractions of histone H4 were collected, re-infused into the mass spectrometer and subsequently fragmented by CID and ECD. The purpose of this investigation was to further characterize the changes induced by TSA treatment by focusing on the order of acetylation of the N-terminal lysine residues of H4, through comparing the results from two cell lines. To achieve this, TSA was administered as a dose response instead of a time course treatment. The cell lines chosen for the in depth study of H4 acetylation were HCT-116 and OCI-AML3. Two different cell lines were investigated in order to exclude the possibility of any variation in the acetylation order between cell lines. Cell cultures were exposed to TSA at the following concentrations: 50 nM, 100 nM, 250 nM and 500nM, for a period of one hour. The spectra presented below display the most extensive fragmentation data gathered.

3.3.2.1 HCT-116 Cell Line

At 50 nM, low levels of fragmentation were achieved on isolated modified forms of histone H4 from HCT-116 cells, most likely due to low quality of the extracted histone samples. This was potentially due to the extraction procedure, but a smaller cell culture (i.e. fewer cells) would also result in a low quality sample. As a result, little meaningful

data was gathered from several of the isolated species. Extensive fragmentation at this concentration was only achieved when a precursor of mass 11,467 Da was isolated and fragmented. The CID and ECD spectra of this precursor ion are shown in Figures 3.15 and 3.16 below, along with a combined fragment ion map (Figure 3.17) for this species of histone H4 generated from both the CID and ECD data.

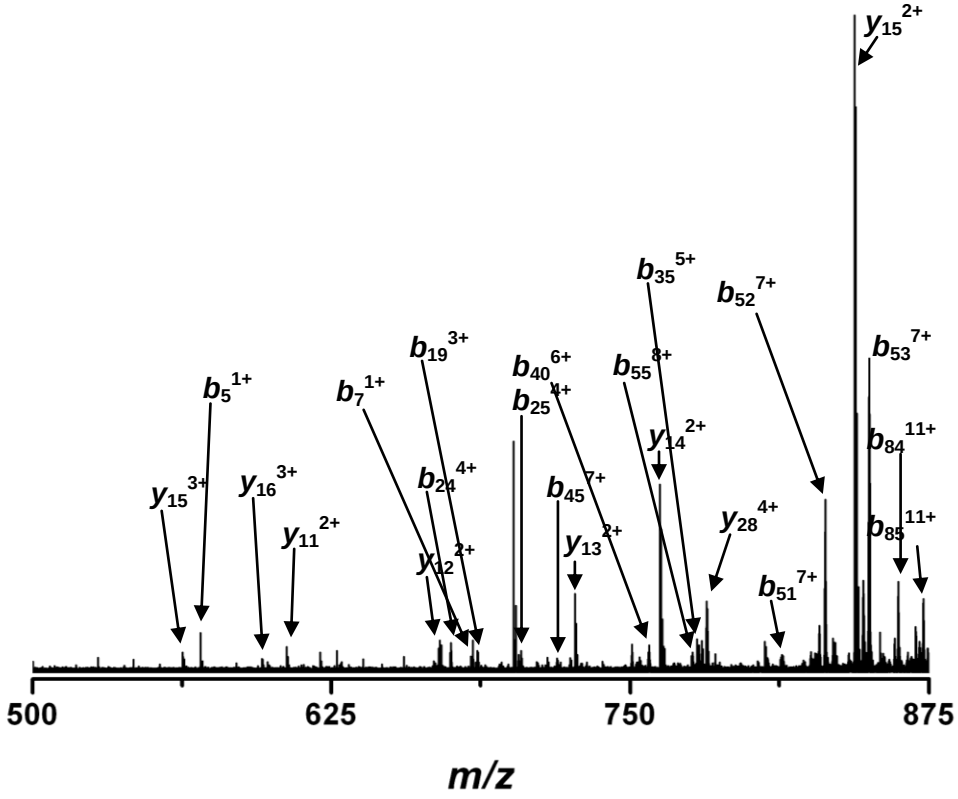

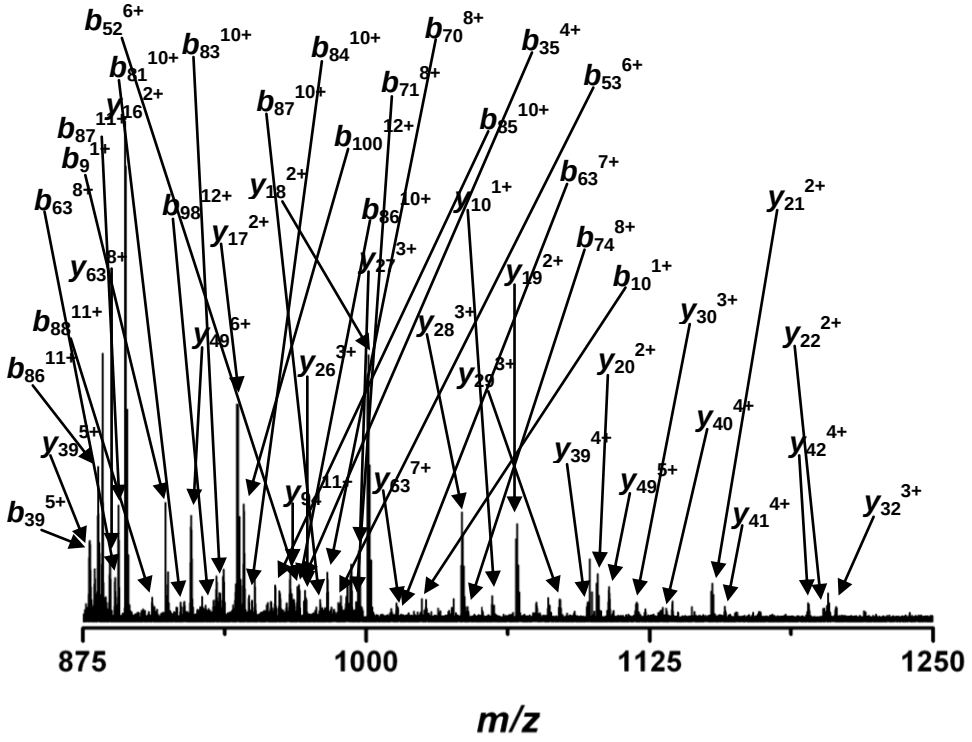

Figure 3.15: Top-down CID spectrum of histone H4 from TSA treated HCT-116 cells (50 nM) for the 13^{+} charge state from the precursor ion at 883.6 *m/z* . The complete list of the assigned fragment ions is attached as Appendix A1.

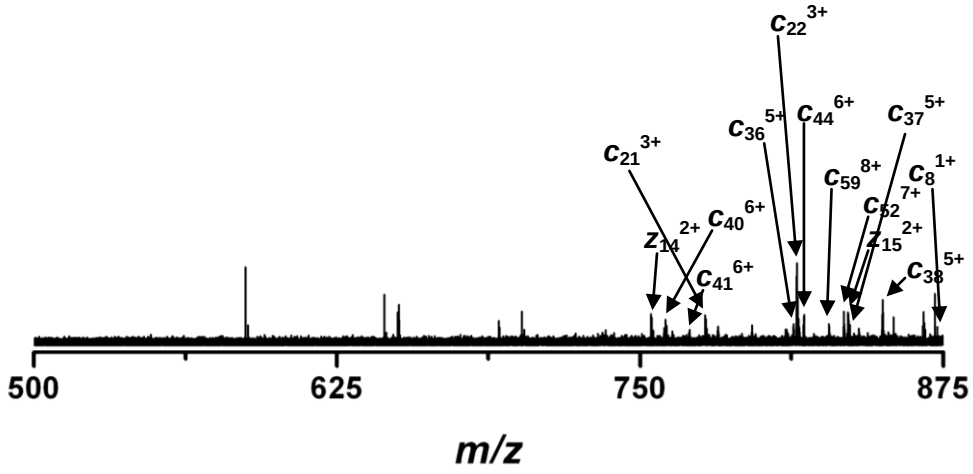

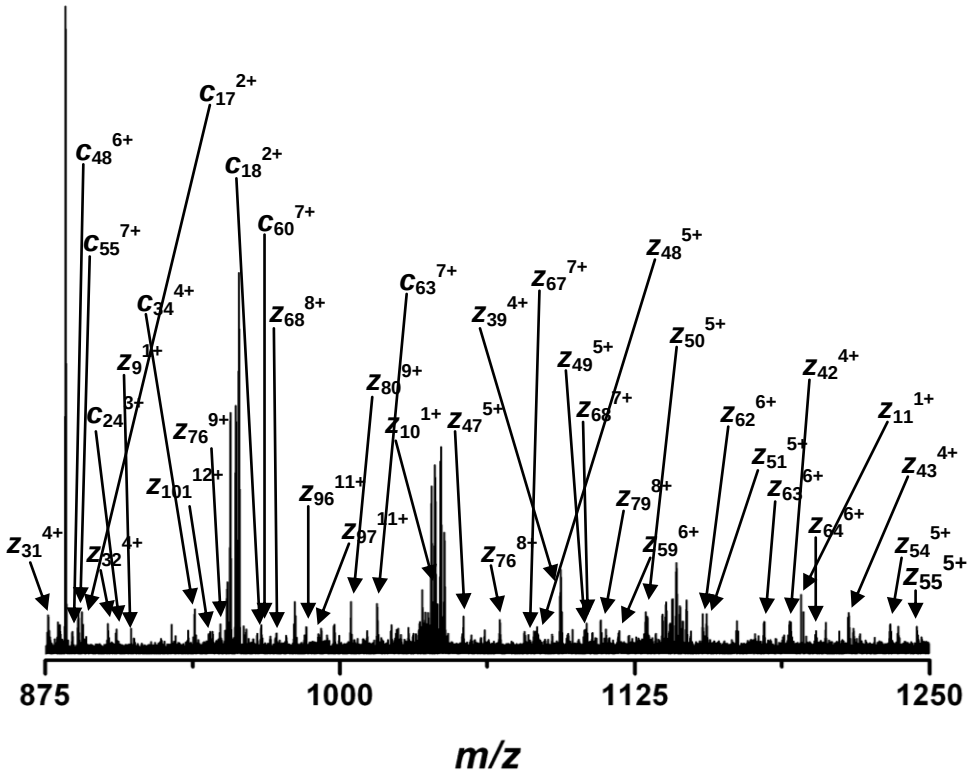

Figure 3.16: Top-down ECD spectrum of histone H4 from TSA treated HCT-116 cells (50 nM) for the 13^{+} charge state from the precursor ion at 883.6 *m/z*. A complete list of the assigned fragment ions is attached as Appendix A2.

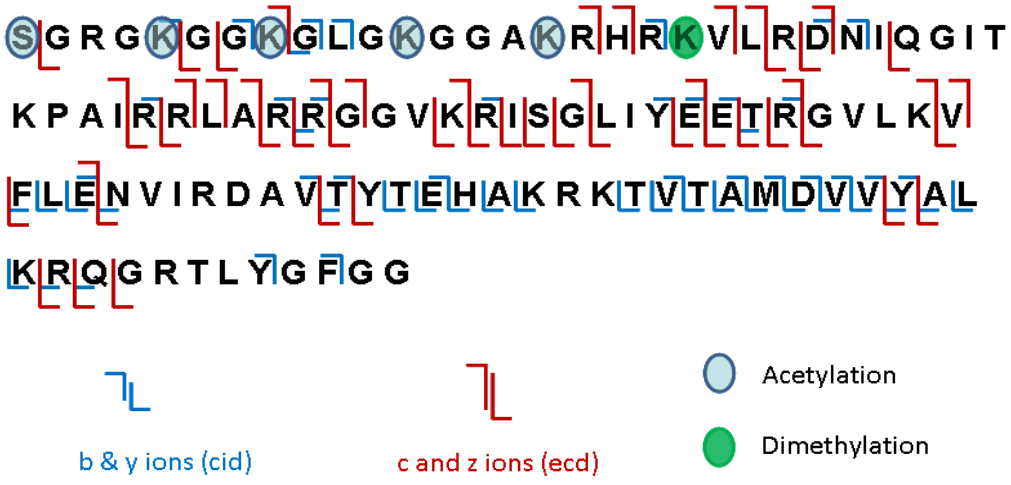

Figure 3.17: Fragment ion map of combined top-down CID and ECD of histone H4 from TSA treated HCT-116 cells (50 nM).

The fragment ion map confirmed acetylation of all N-terminal Lysine residues, along with di-methylation of lysine 20. The location of these modifications also reveals that H4 acetylation occurs exclusively in the N-terminal region, and not in the globular portion of the protein.

TSA treatment of HCT-116 cells at other concentrations provided more extensive sequence coverage. Figure 3.18 below, shows the CID spectrum obtained for the 13^{+} charge state of the modified H4 isoform (100 nM TSA treatment) from the precursor ion at 870.6 *m/*z, corresponding to an isoform with an intact mass of 11,299 Da with a fragment ion map (Figure 3.19)

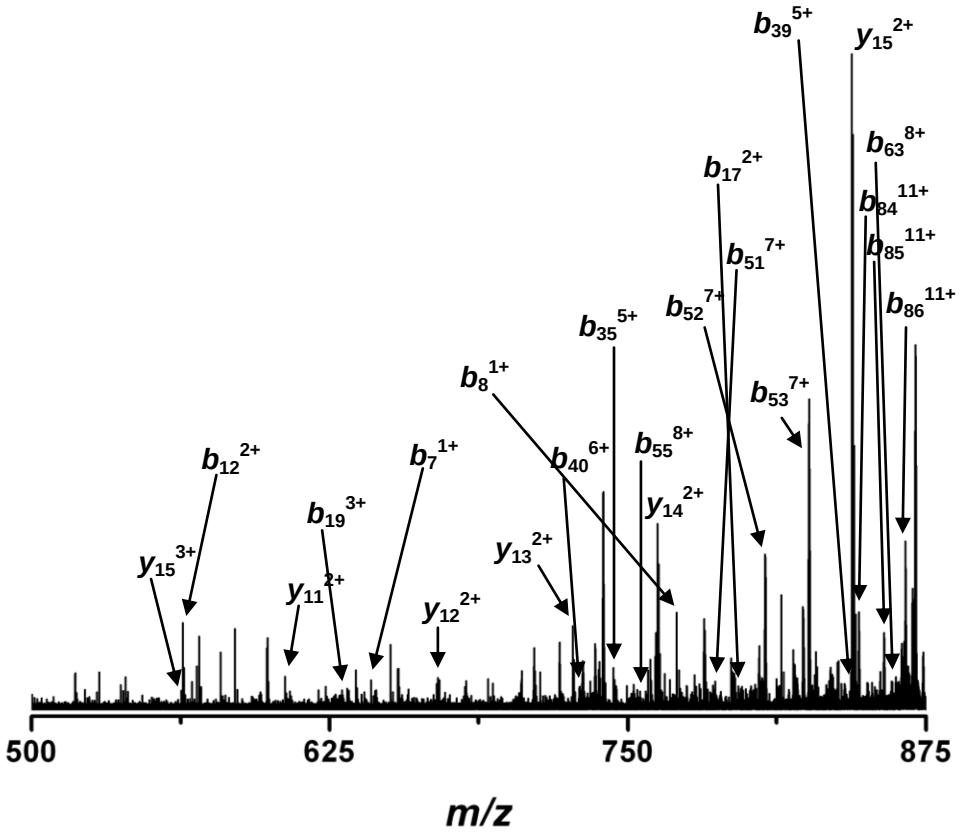

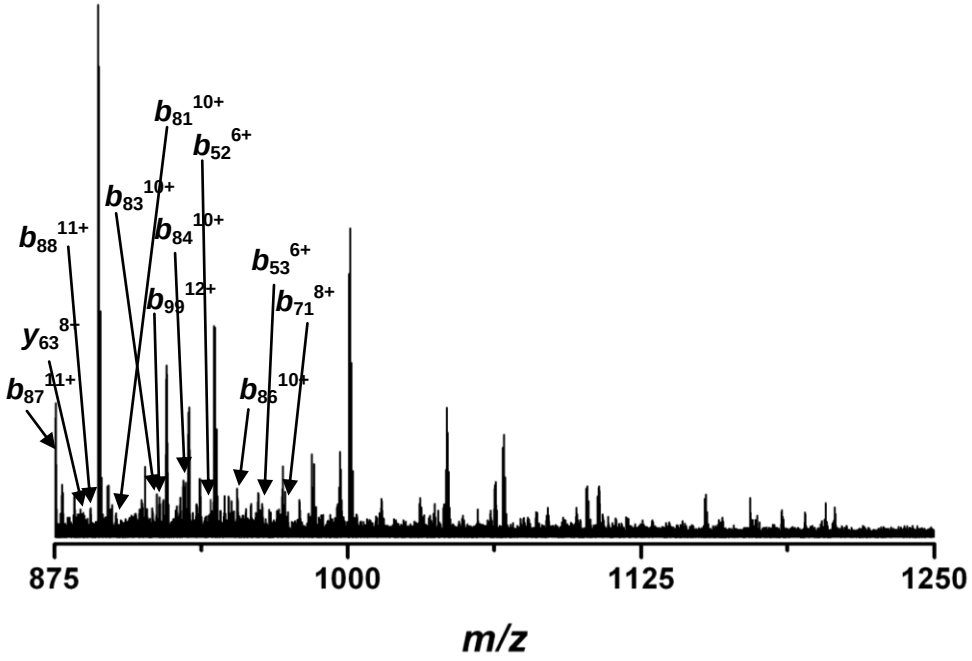

Figure 3.18: Top-down CID spectrum of histone H4 from TSA treated HCT-116 cells (100 nM) for the 13^{+} charge state from the precursor at 870.6 *m/z*. A complete list of the assigned fragment ions is attached as Appendix A3.

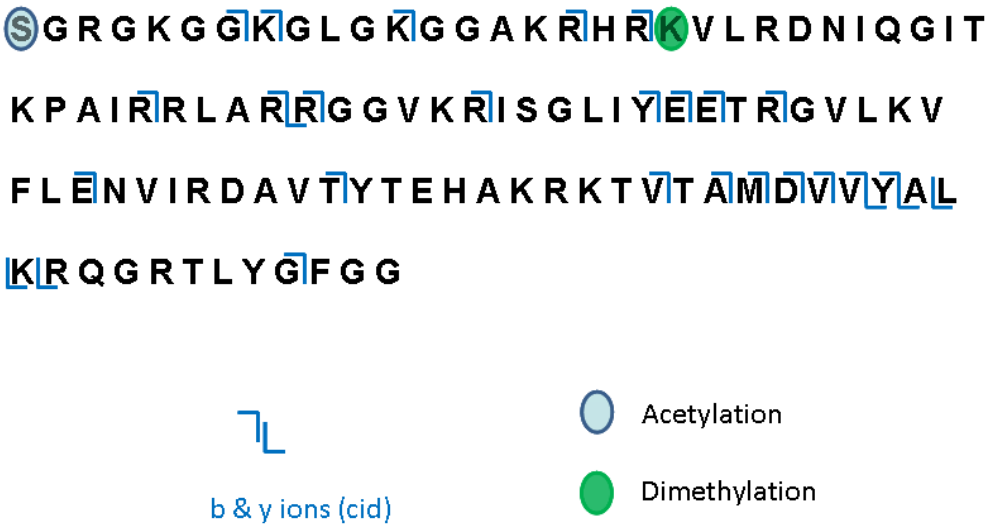

Figure 3.19: Fragment ion map top-down CID spectrum of histone H4 from TSA treated HCT-116 cells (100 nM) from the precursor at 870.6 *m/z*.

CID provided sufficient sequence coverage to assist in the localization of the PTMs present. The intact mass of the precursor suggests the presence of an acetyl group and di-methylation. The fragment ions enabled this acetyl group to be localized to within the

first seven amino acids, excluding all other lysine residues. The di-methylation is likely located at lysine 20 or a subsequent residue. At 100 nM TSA treatment, no further fragmentation was achieved using CID or ECD.

The CID spectrum of histone H4 from HCT-116 cells after 500 nM treatment exhibited good sequence coverage. The CID spectrum for the 13^{+} charge state of the precursor ion at 883.6 *m/*z, corresponding to an isoform with an intact mass of 11,467 Da is shown in Figure 3.20 below, with a fragment ion map (Figure 3.21).

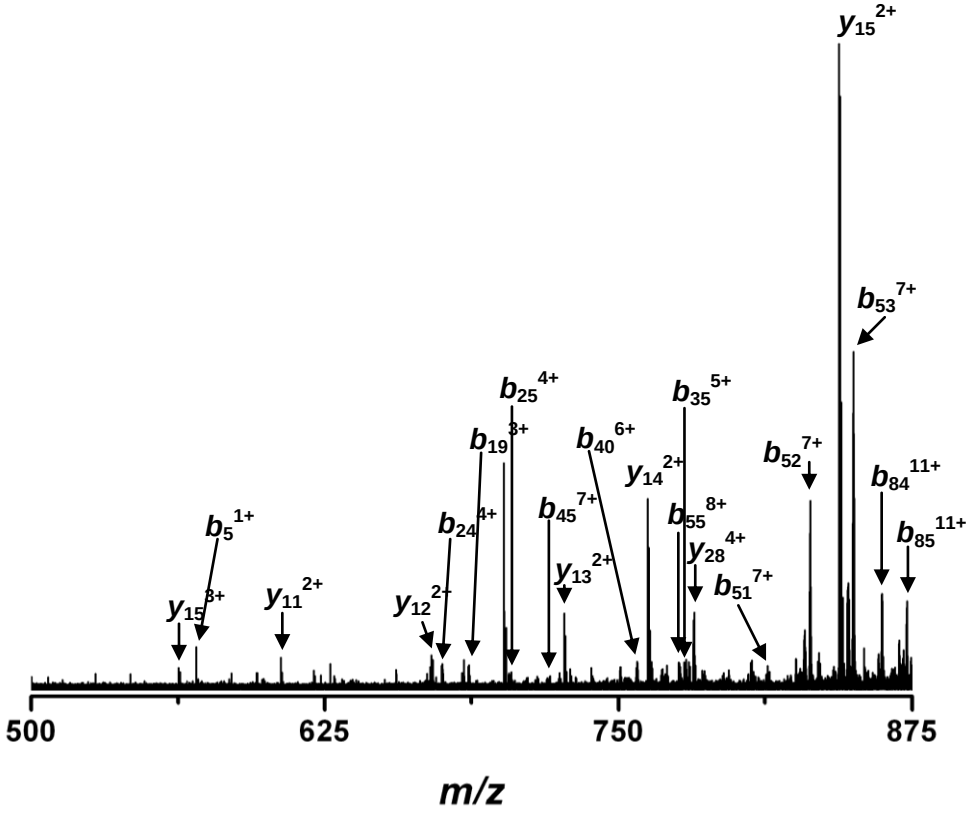

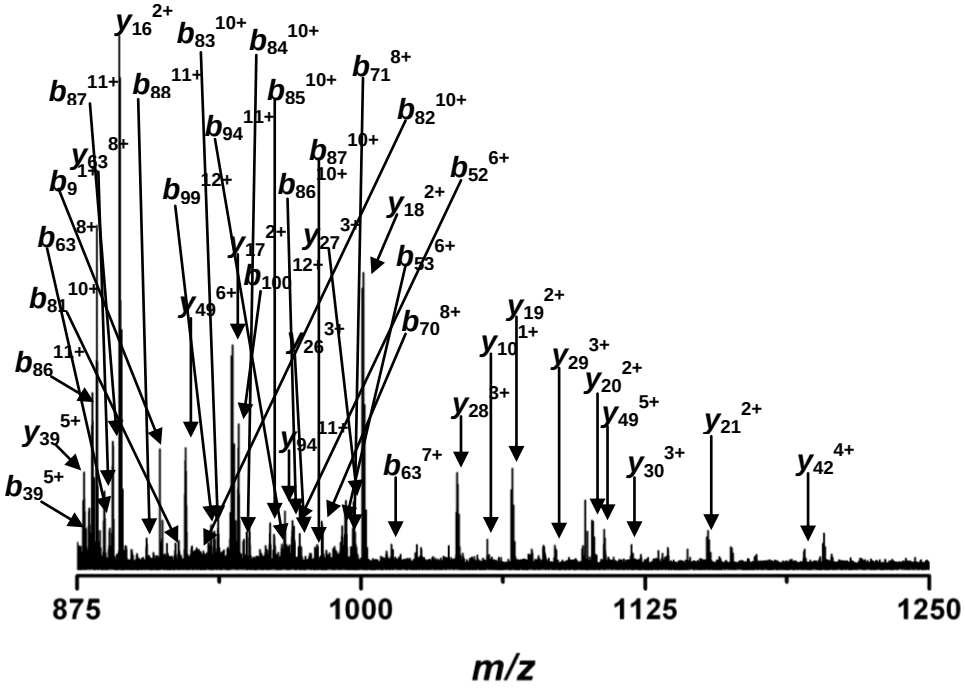

Figure 3.20: Top-down CID spectrum of histone H4 from TSA treated HCT-116 cells (500 nM) for the 13^{+} charge state from the precursor ion at 883.6 *m/z*. A complete list of the assigned fragment ions is attached as Appendix A4.

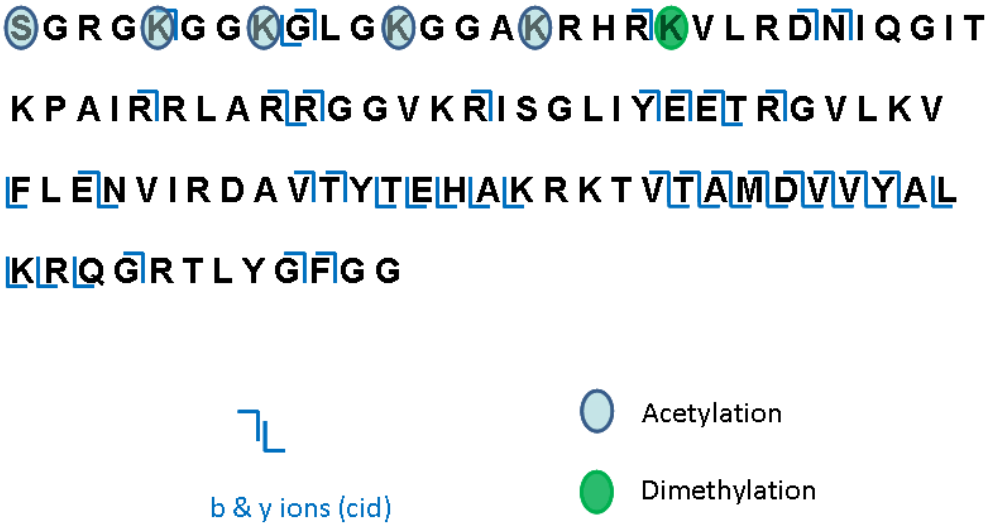

Figure 3.21: Fragment ion map of top-down CID spectrum of histone H4 from TSA treated HCT-116 cells (500 nM) for the precursor ion at 883.6 *m/z*.

The fragment ions observed after CID of the precursor at 883.6 *m/z* confirmed that this species was the fully hyper-acetylated form of histone H4, and that each acetyl group was located on an N-terminal lysine residue. The fragmentation data obtained using the HCT-

116 cell line provided only limited information on the acetylation order of histone H4. The cells from 250 nM TSA treatment provided no useful data, and each other concentration of TSA used yielded limited results. This was most likely a result of low protein yield from the extraction process.

3.3.2.2 OCI-AML3 Cell Line

Similar experiments performed on TSA treated OCI-AML3 cells yielded much more in depth results. Instrument settings and culture conditions were unchanged between the two cell lines, suggesting that the improved sequence coverage was largely due to a higher protein concentration in the samples. The spectra shown in Figures 3.22 and 3.23 below show the fragmentation data obtained for the 13^{+} charge state of histone H4 (after 50 nM treatment) following CID and ECD of the precursor ion at 870.6 *m/z* corresponding to an isoform with an intact mass 11,299 Da, along with a combined fragment ion map for this species of histone H4 generated from both the CID and ECD data (Figure 3.24).

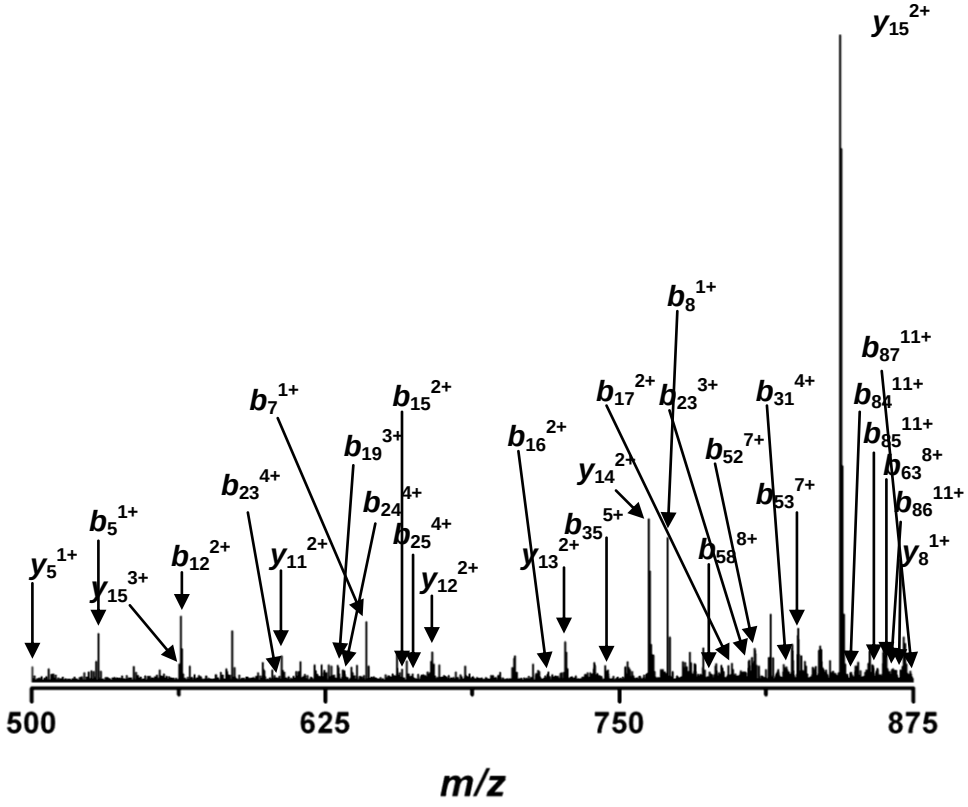

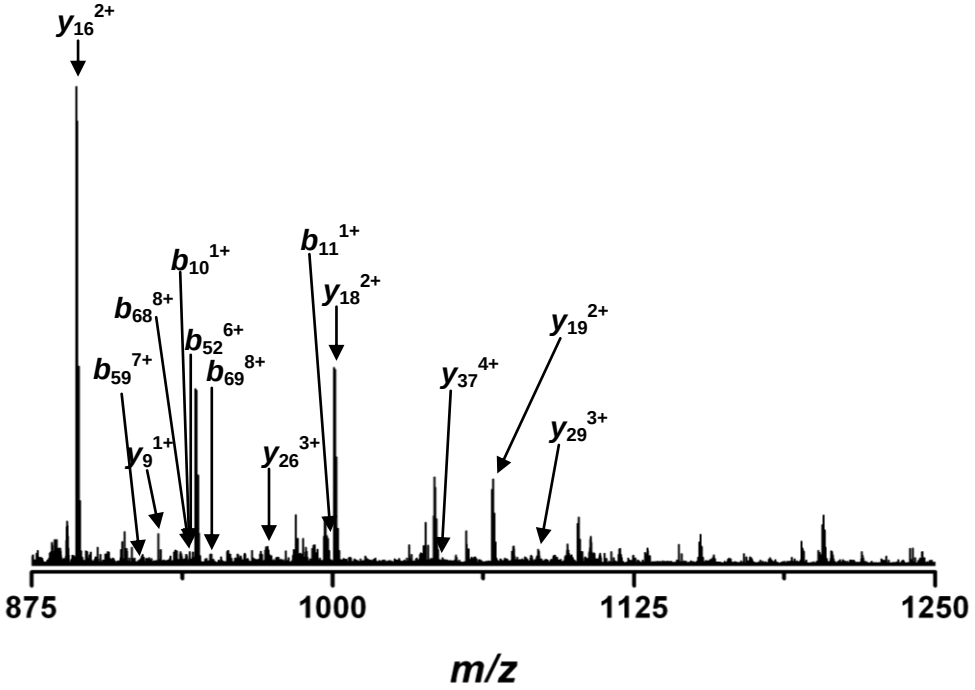

Figure 3.22: Top-down CID spectrum of histone H4 from TSA treated OCI-AML 3 cells (50 nM) for the 13^{+} charge state from the precursor ion at 870.6 *m/z*. A complete list of the assigned fragment ions is attached as Appendix A5.

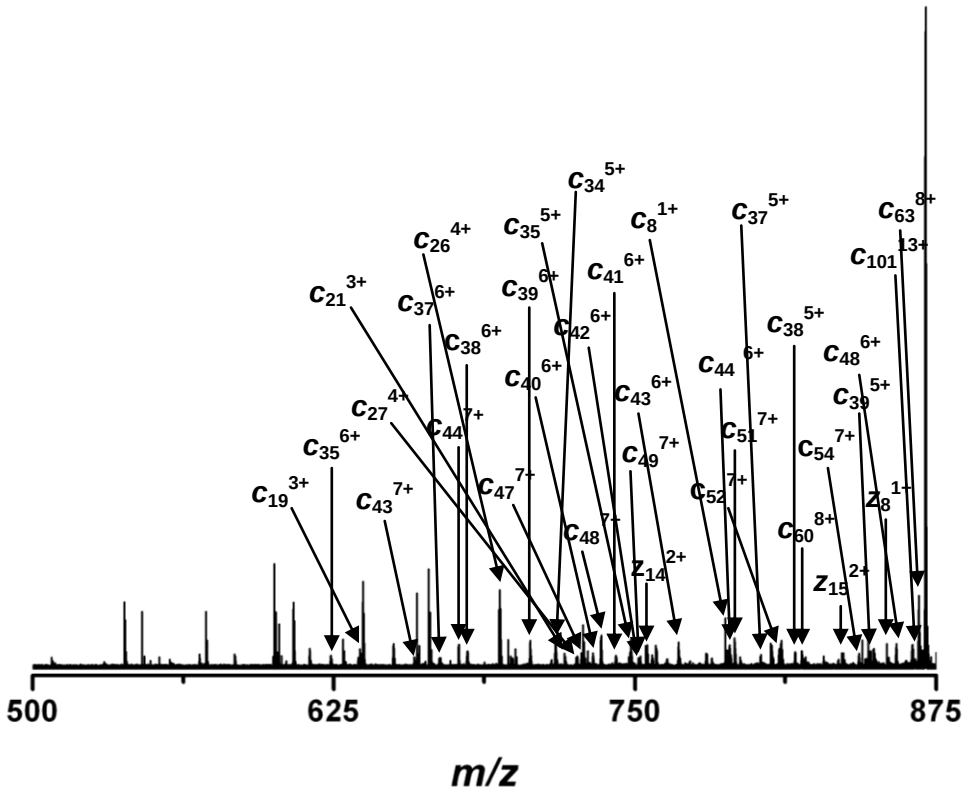

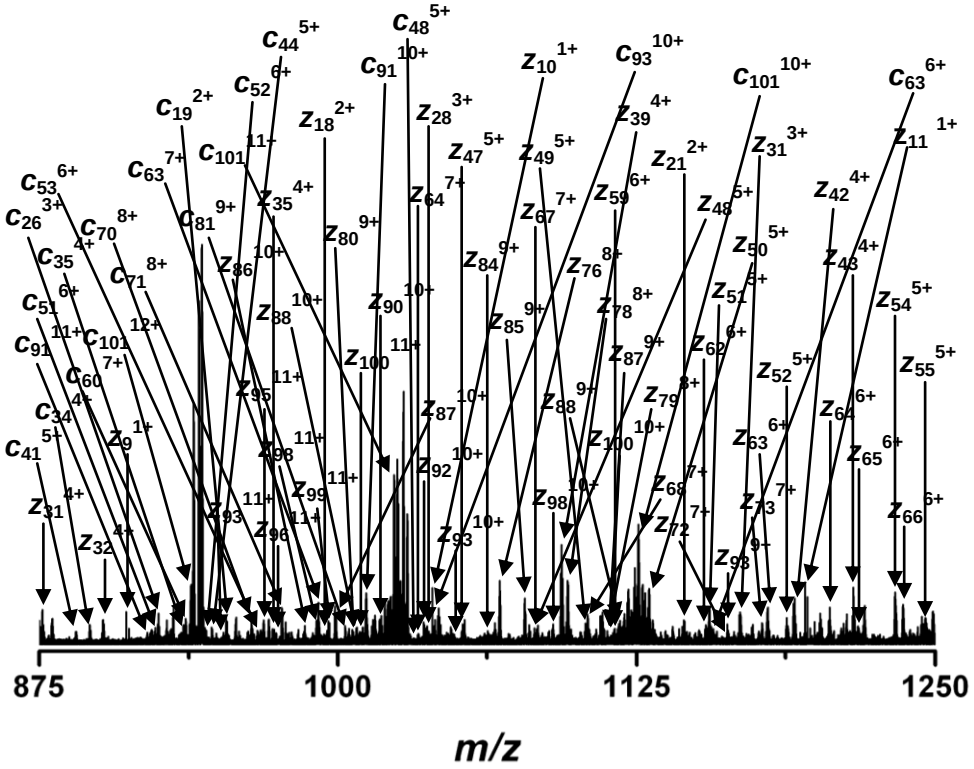

Figure 3.23: Top-down ECD spectrum of histone H4 from TSA treated OCI-AML3 cells (50 nM) for the 13^{+} charge state from the precursor ion at 870.6 *m/z*. A complete list of the assigned fragment ions is attached as Appendix A6

Figure 3.24: Fragment ion map of combined top-down CID and ECD of histone H4 from TSA treated OCI-AML3 cells (50 nM).

The fragmentation data enable the presence of a single acetyl group in this species to be conclusively localized to the N-terminal serine residue. The other modification present is the di-methyl group located at lysine 20, a common post-translational modification.

Figures 3.25 and 3.26 below show CID and ECD fragment spectra for the 13^{+} charge state of the modified form of histone H4 at 873.9 *m/z*. This precursor ion mass-to-charge ratio corresponds to an isoform with an intact mass of 11,341 Da, an increase in mass of 42 Daltons with respect to that of the precursor ion selected for fragmentation in the figures above.

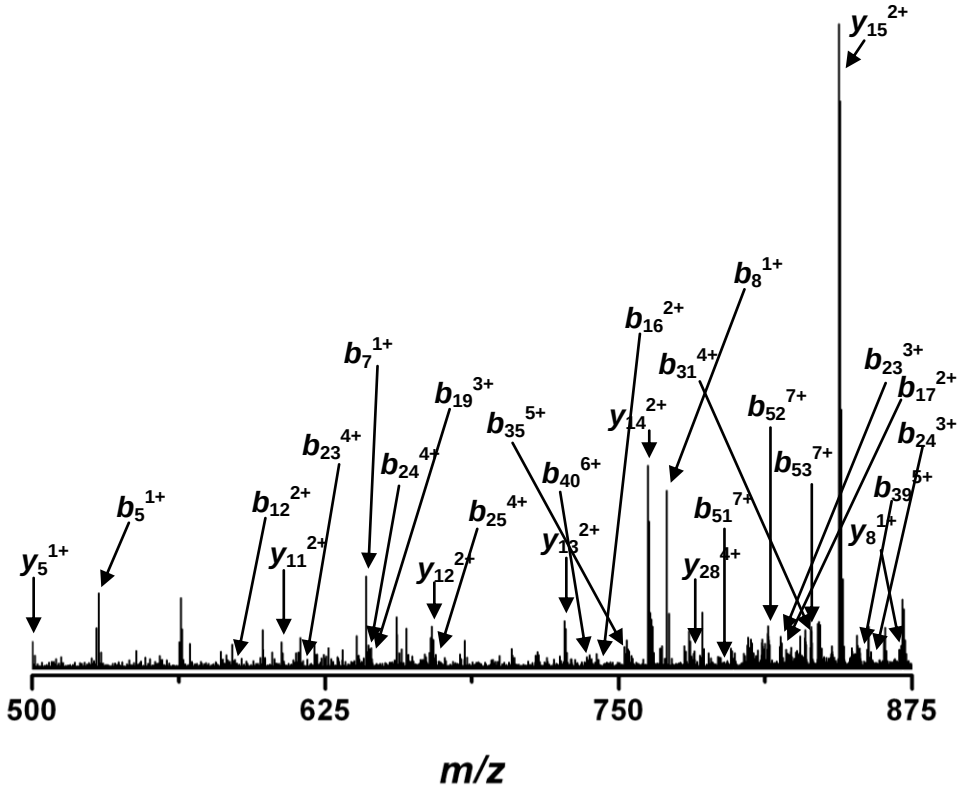

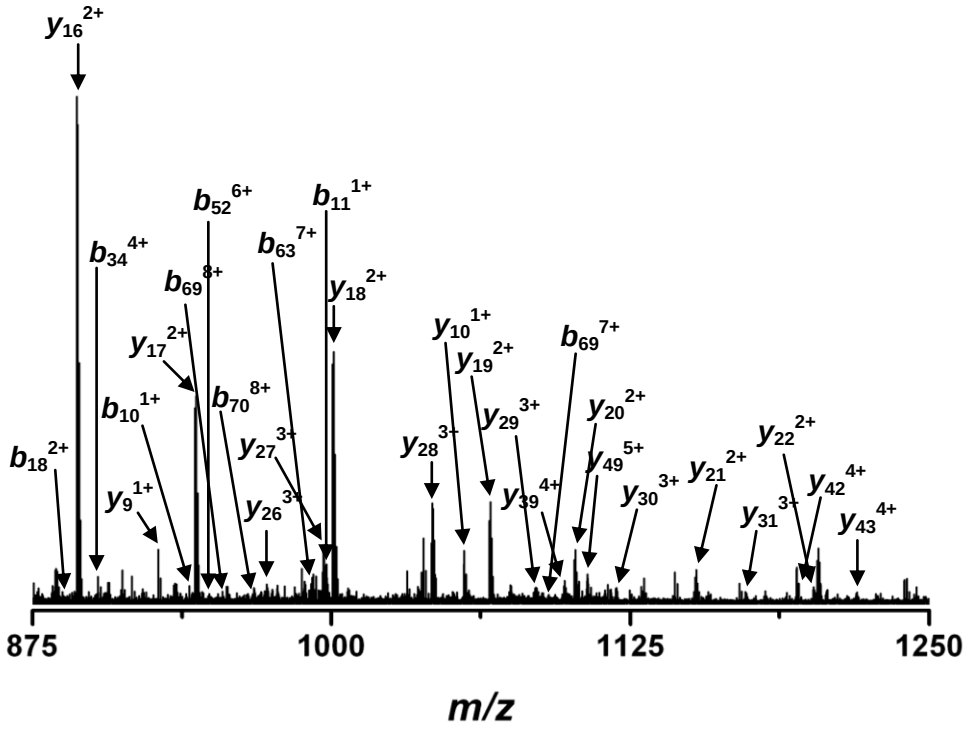

Figure 3.25: Top-down CID spectrum of histone H4 from TSA treated OCI-AML3 cells (50 nM) for the 13^+ charge state from the precursor ion at 873.9 *m/z*. A complete list of the assigned fragment ions is attached as Appendix A7.

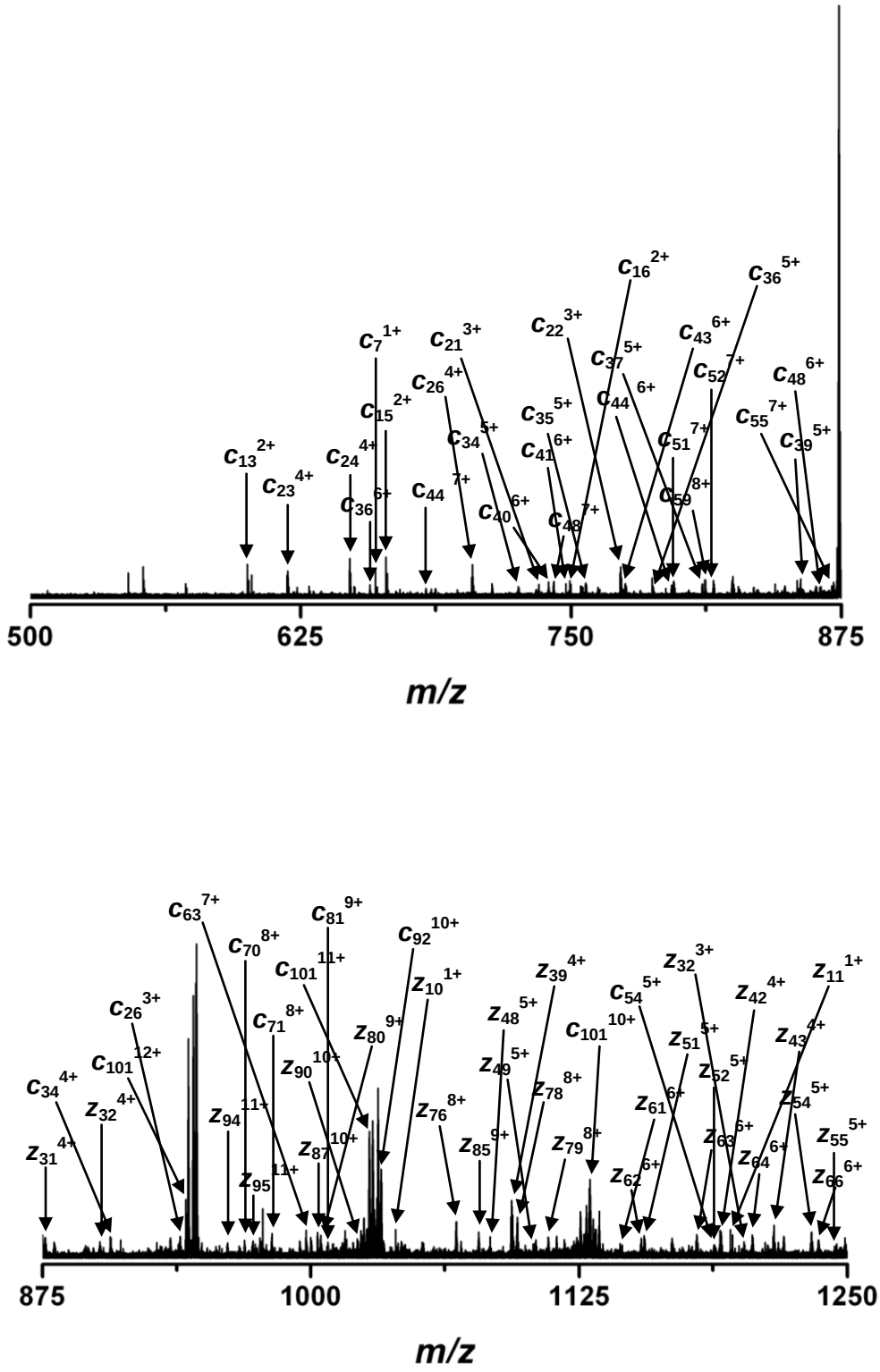

Figure 3.26: Top-down ECD spectrum of histone H4 from TSA treated OCI-AML3 cells (50 nM) for the 13^{+} charge state from the precursor ion at 873.9 *m/z*. A complete list of the assigned fragment ions is attached as Appendix A8.

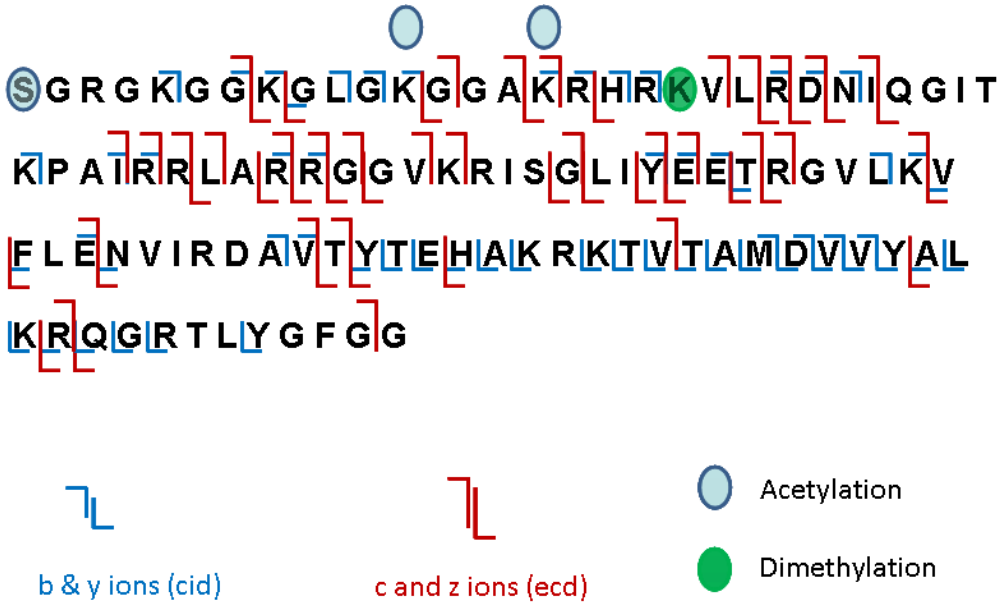

Figure 3.27: Fragment ion map of combined top-down CID and ECD of histone H4 from TSA treated OCI-AML3 cells (50 nM).

Both the CID and ECD spectra confirm the presence of the N-terminal acetylation, and di-methylation at lysine 20 (shown in Figure 3.27). In addition, the mass increase can be accounted for by the presence of a second acetyl group. However the position of this acetyl group cannot be identified with complete confidence. The CID data reveals that the PTM is located on lysine 12 while the ECD reveals the acetyl group is at lysine 16 (shown as blue circles above the lysine residues in Figure 3.27). The most likely explanation is that this modified form of H4 exists as a mixture of these two species.

CID was then performed on the 12^+ charge state of the modified form of H4 at 950.1 *m/z* (it was not possible to achieve clean isolation of the 13^+ charge state). This precursor ion mass-to-charge ratio corresponds to an isoform with an intact mass of 11,383 Da. The spectrum is shown in Figure 3.28 below, along with a fragment ion map (Figure 3.29).

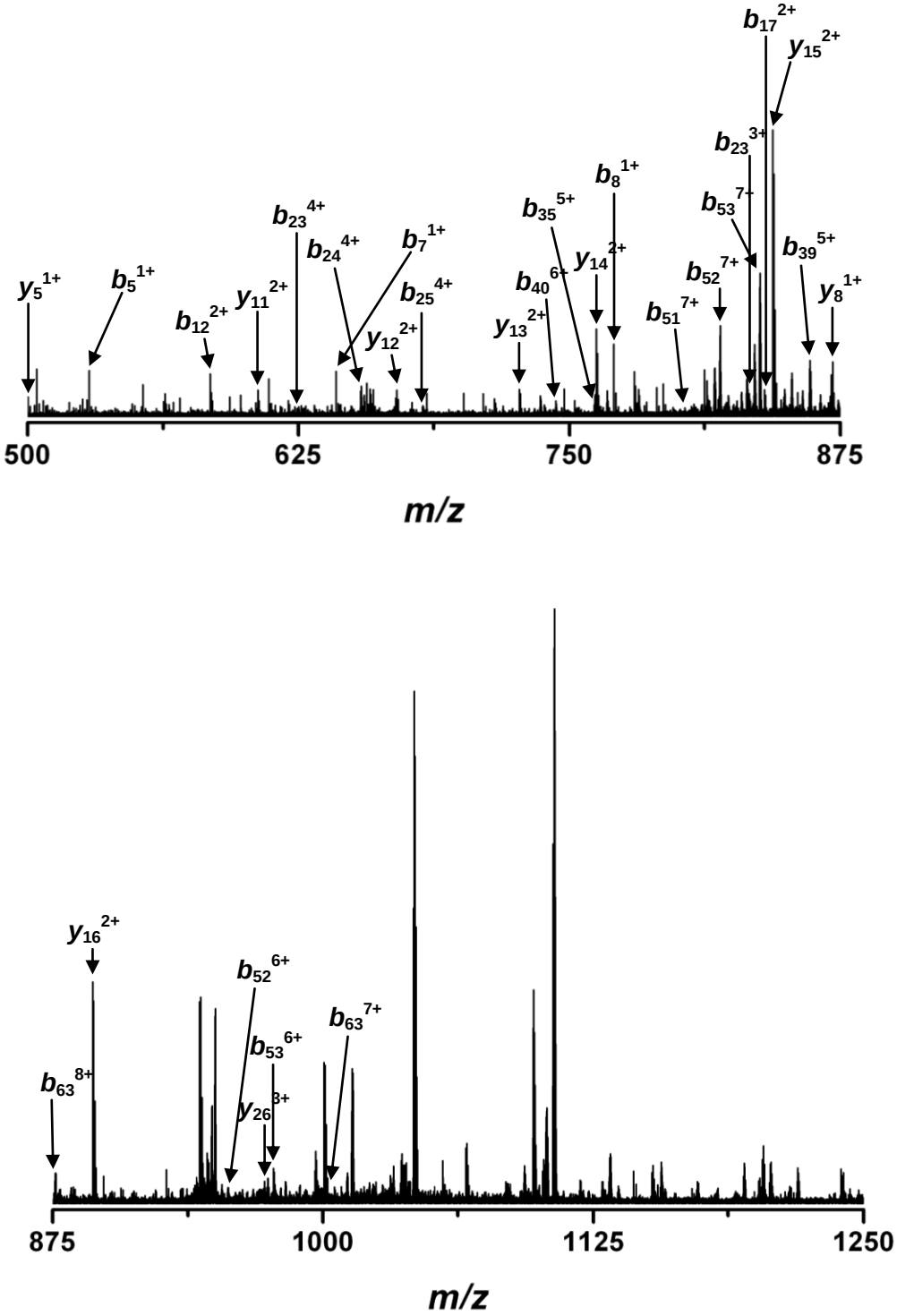

Figure 3.28: Top-down CID spectrum of histone H4 from TSA treated OCI-AML3 cells (50 nM) for the 12^+ charge state from the precursor ion at 950.1 *m/z*. A complete list of the assigned fragment ions is attached as Appendix A9

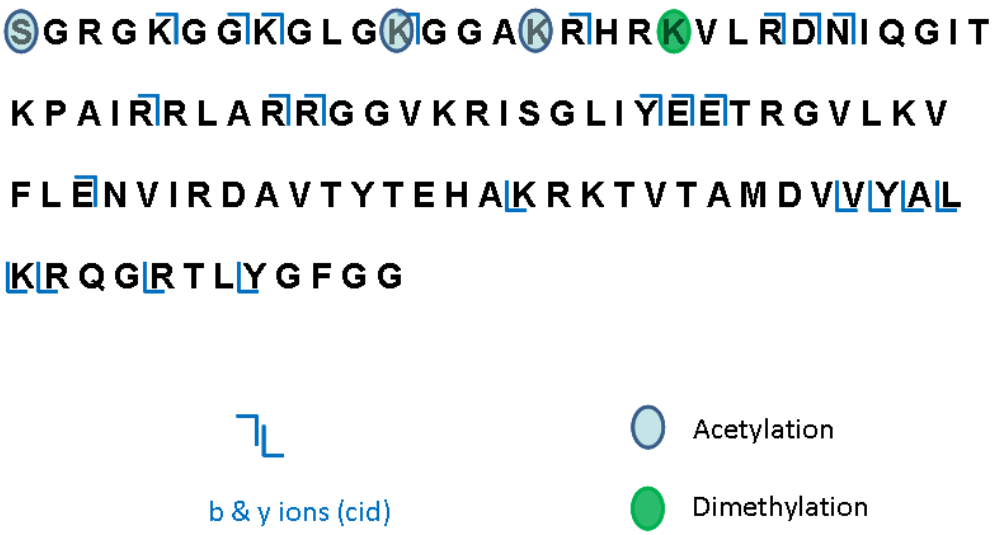

Figure 3.29: Fragment ion map of top-down CID of histone H4 from TSA treated OCI-AML3 cells (50 nM).

The fragmentation data shown in the figure above was sufficient to conclusively confirm that the first two sites of acetylation in histone H4 are lysines 16 and 12.

At 100 nM TSA treatment, low sequence coverage was achieved on the modified forms of H4. CID and ECD experiments were performed on the 13^{+} charge state of the precursor ion at 870.6 *m/z*, corresponding to an isoform with an intact mass of 11,299 Da, again confirming as for the 50 nM TSA treatment, that this is histone H4 carrying an N-terminal acetylation and a di-methylation at lysine 20.

Figures 3.30 and 3.31 below show CID and ECD spectra for the 13^{+} charge state of the precursor ion at 873.9 *m/z*, corresponding to an isoform with an intact mass of 11,341 Da, along with a combined fragment ion map (Figure 3.32).

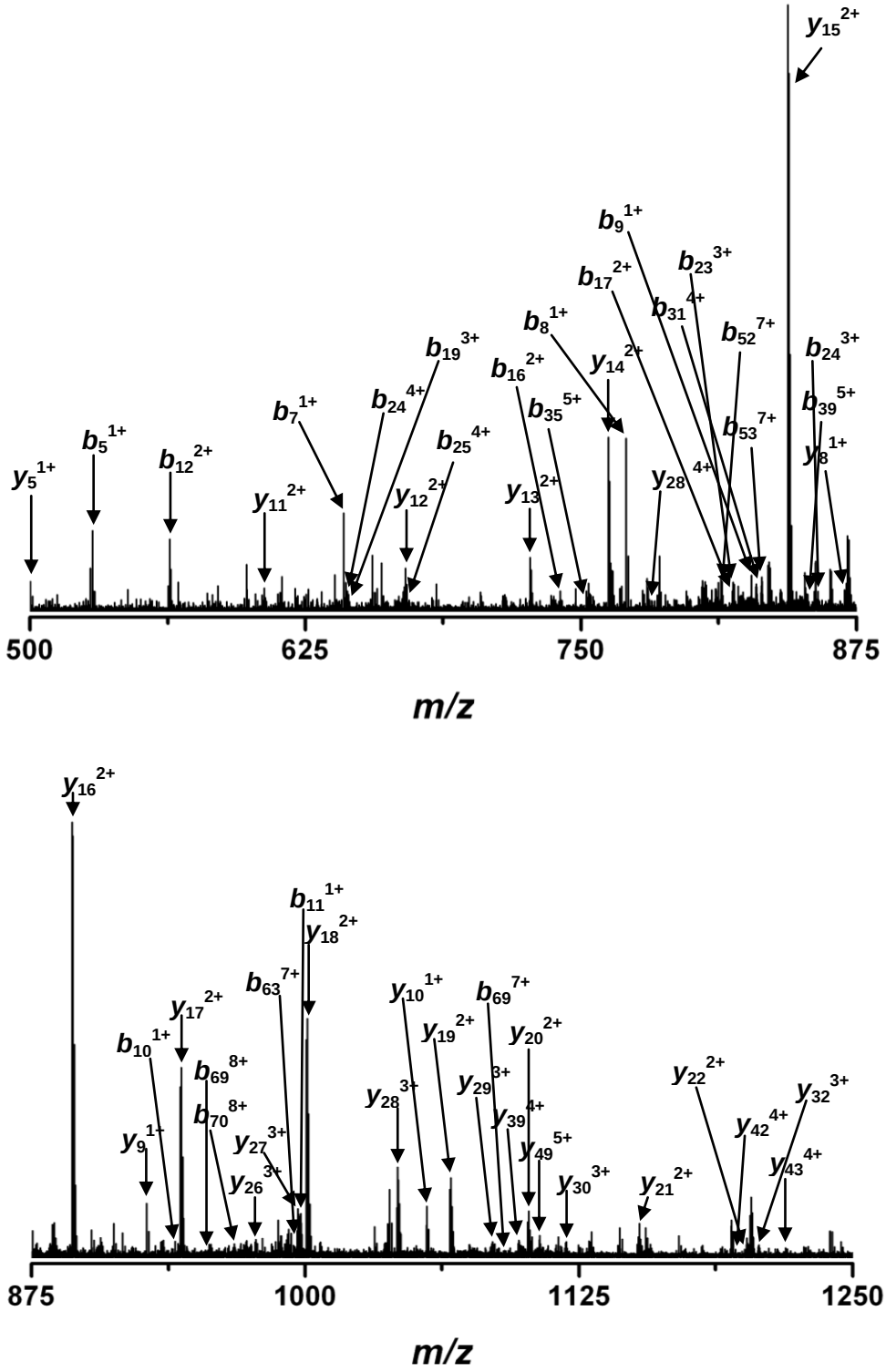

Figure 3.30: Top-down CID spectrum of histone H4 from TSA treated OCI-AML3 cells (100 nM) for the 13^{+} charge state from the precursor ion at 873.9 *m/z*. A complete list of the assigned fragment ions is attached as Appendix A10.

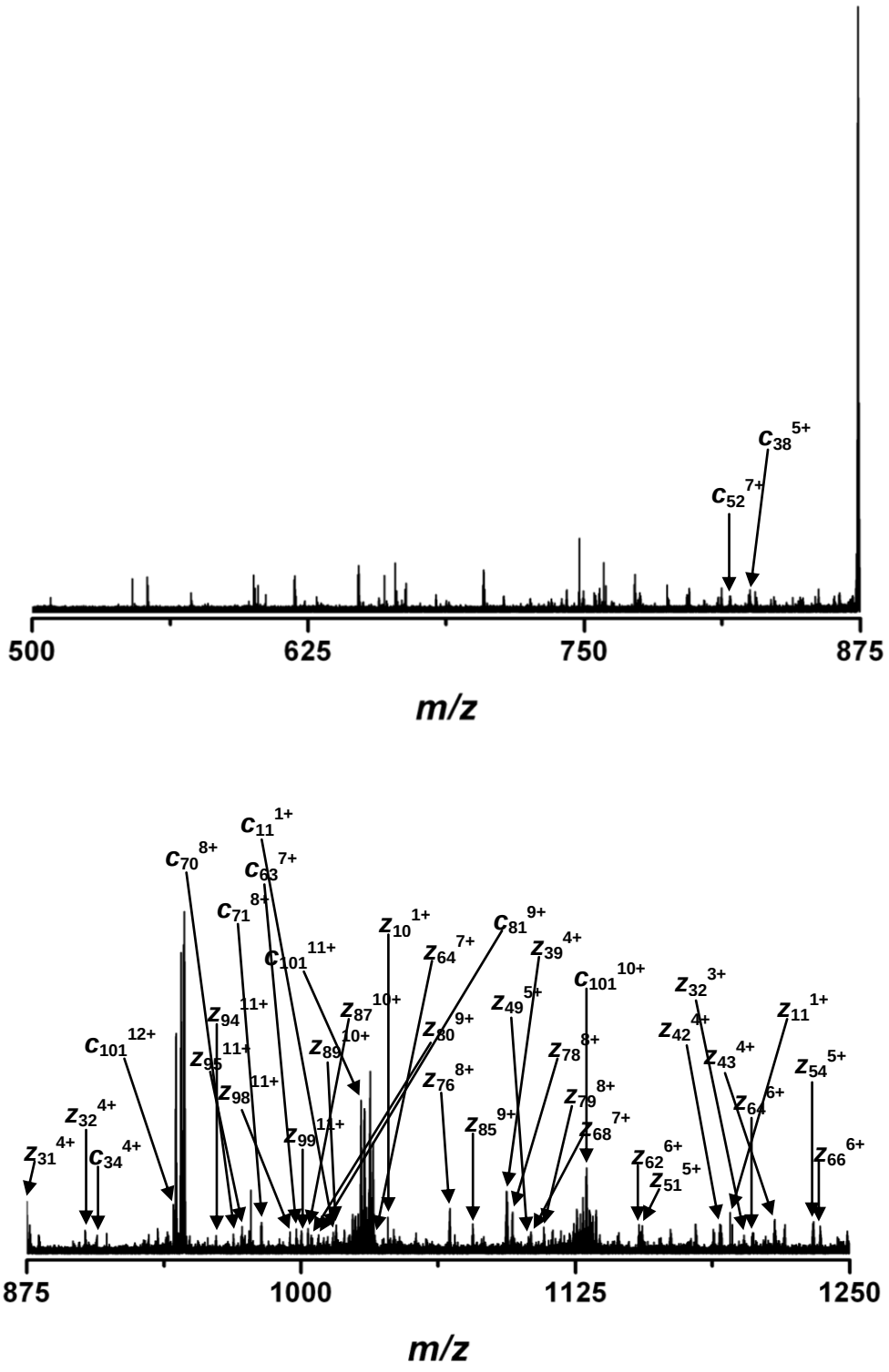

Figure 3.31: Top-down ECD spectrum of histone H4 from TSA treated OCI-AML3 cells (100 nM) for the 13^{+} charge state from the precursor ion at 873.9 *m/z*. A complete list of the assigned fragment ions is attached as Appendix A11.

Figure 3.32: Fragment ion map of combined top-down CID and ECD of histone H4 from TSA treated OCI-AML3 cells (100 nM).

As shown in the above figures, extensive sequence coverage was achieved using both fragmentation techniques. When combined, the data reveal no discrepancies in the localization of PTMs. This species of histone H4 ion is N-terminally acetylated, di-methylated at lysine 20 and acetylated at lysine 16, confirmed by both methods of fragmentation.

Attempts to perform fragmentation on the 12^+ charge state of the modified form of H4 at 950.1 *m/z*, corresponding to an isoform with an intact mass of 11,383 Da were of only limited success. After multiple attempts at isolation and fragmentation, low sequence coverage was achieved and only the N-terminal acetylation and di-methylation could be conclusively localized. The final species to be examined in the cells treated with 100 nM TSA was the 13^+ charge state for the precursor ion at 880.4 *m/z*. This precursor ion mass-to-charge ratio corresponds to an isoform with an intact mass of 11,425 Da. The results of the CID and ECD experiments performed are shown in the spectra below, Figures 3.33 and 3.34, along with a combined fragment ion map (Figure 3.35).

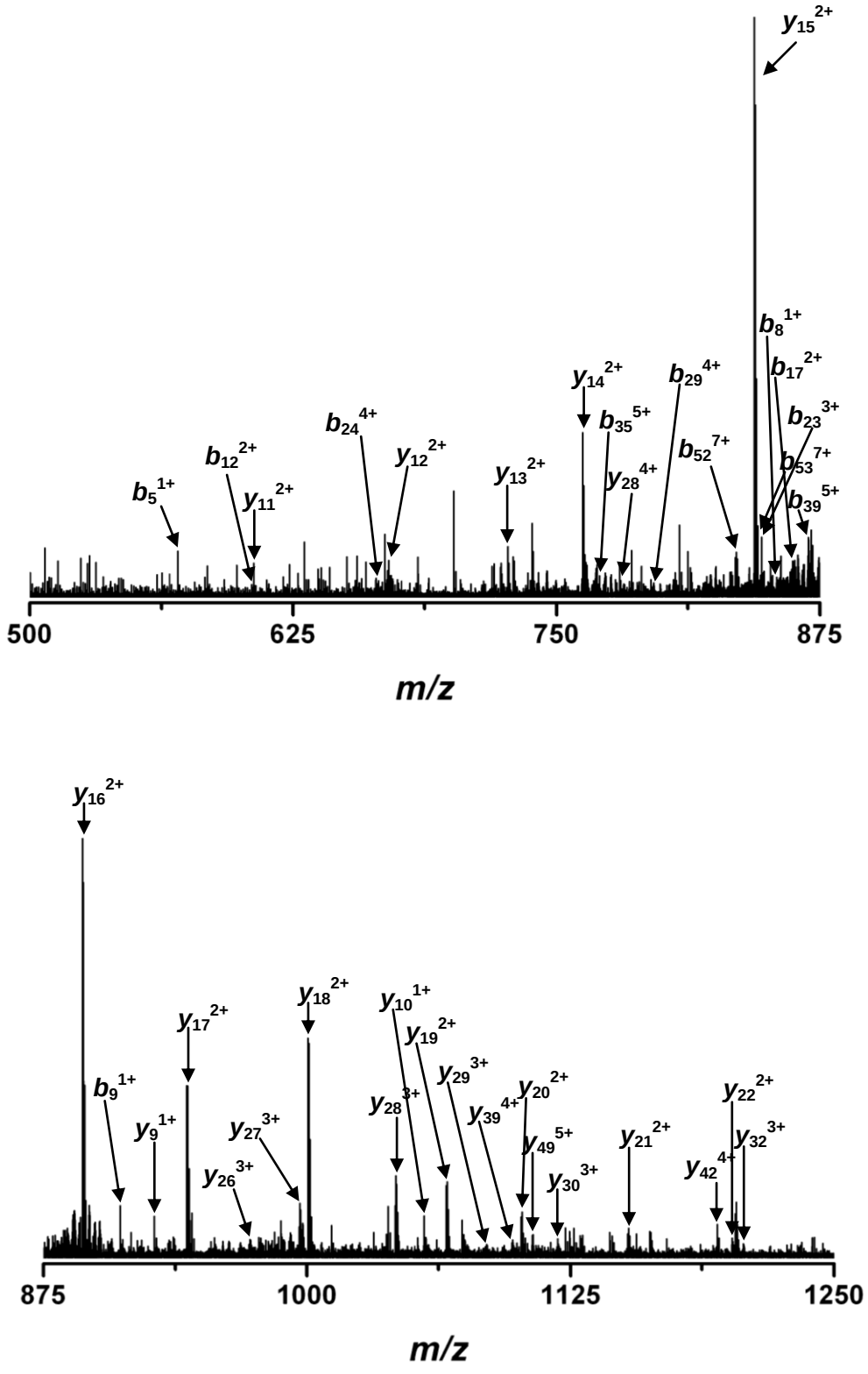

Figure 3.33: Top-down CID spectrum of histone H4 from TSA treated OCI-AML 3 cells (100 nM) for the 13^{+} charge state from the precursor ion at 880.4 *m/z*. A complete list of the assigned fragment ions is attached as Appendix A12.

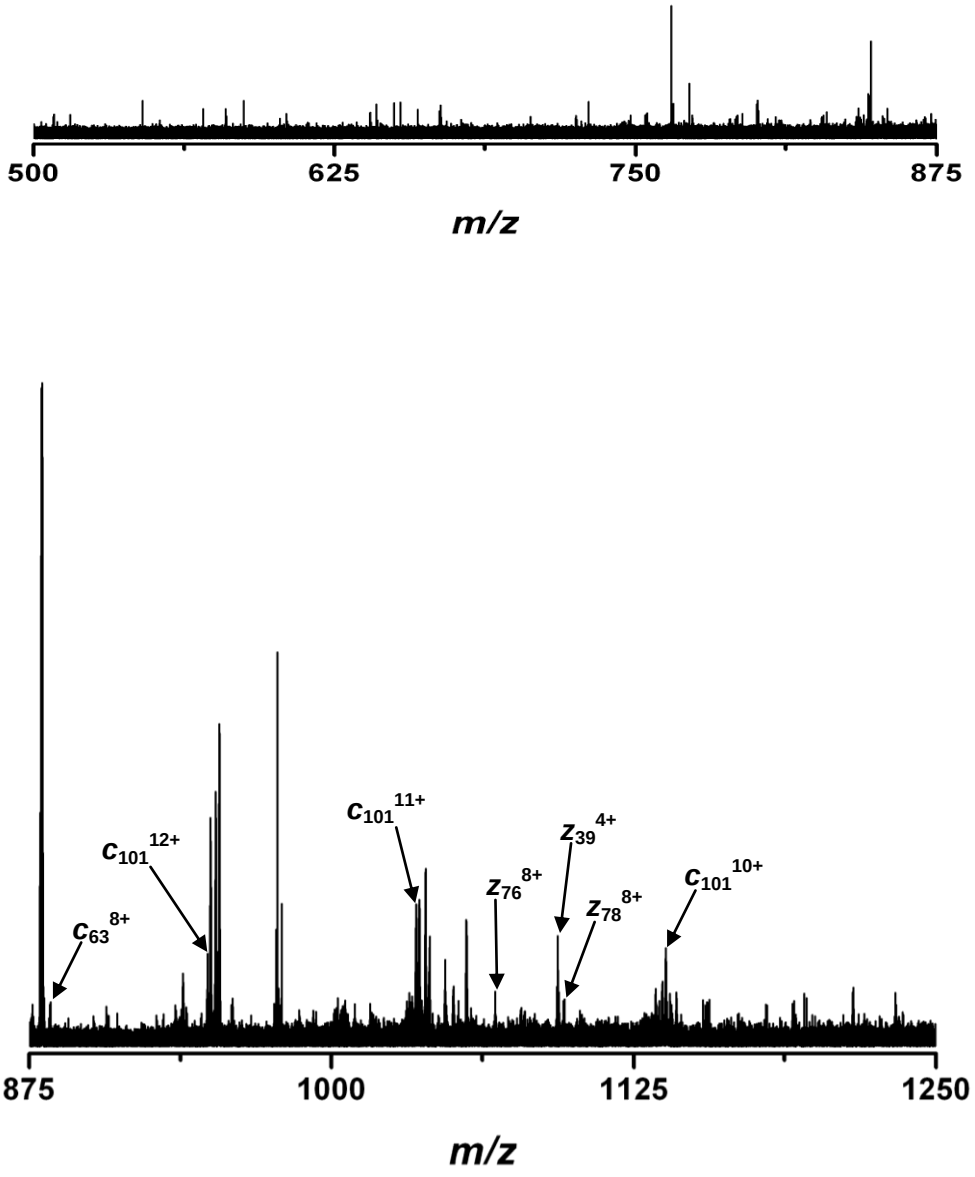

Figure 3.34: Top-down ECD spectrum of histone H4 from TSA treated OCI-AML 3 cells (100 nM) for the 13^{+} charge state from the precursor ion at 880.4 *m/z*. A complete list of the assigned fragment ions is attached as Appendix A13.

Figure 3.35: Fragment ion map of combined top-down CID and ECD of histone H4 from TSA treated OCI-AML 3 cells (100 nM).

The fragmentation data above shows that the N-terminal acetylation, and lysine 20 and lysine 16 modifications are as seen previously, while newer modifications are located on Lysine residues closer to the N-terminus, specifically the newly added acetyl groups are located at lysines 5 & 8.

Little meaningful data was gained through fragmentation of multiple H4 species after 250 nM TSA treatment. This is most likely due to low yield of histone proteins during the extraction process. Figure 3.36 below shows the only useful spectrum acquired. This is the CID spectrum of the 13^{+} charge state from the precursor ion at 873.9 *m/z*, corresponding to an isoform with an intact mass of 11,341 Da. A fragment ion map is presented in Figure 3.37.

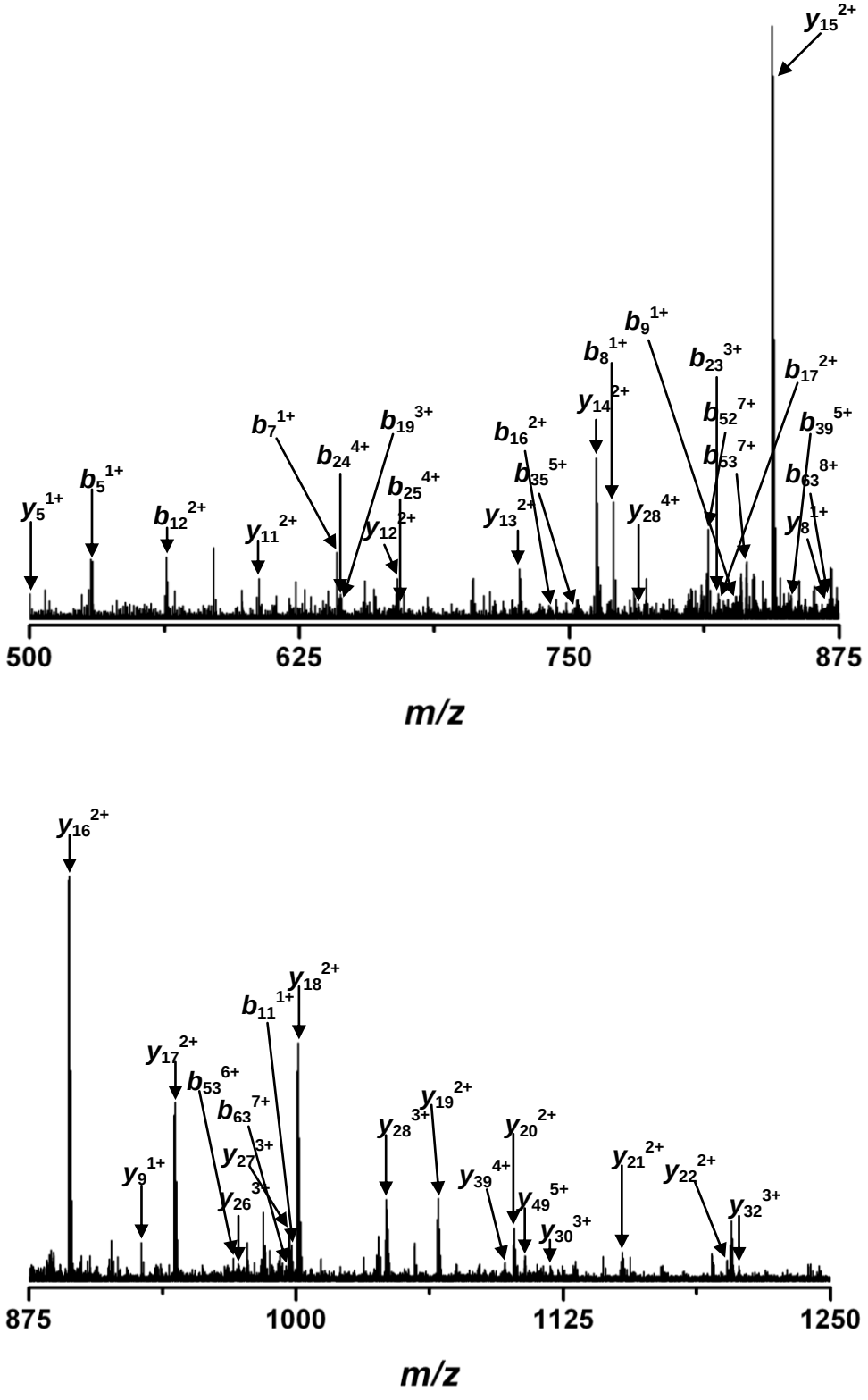

Figure 3.36: Top-down CID spectrum of histone H4 from TSA treated OCI-AML3 cells (250 nM) for the 13^{+} charge state from the precursor ion at 873.9 *m/z*. A complete list of the assigned fragment ions is attached as Appendix A14.

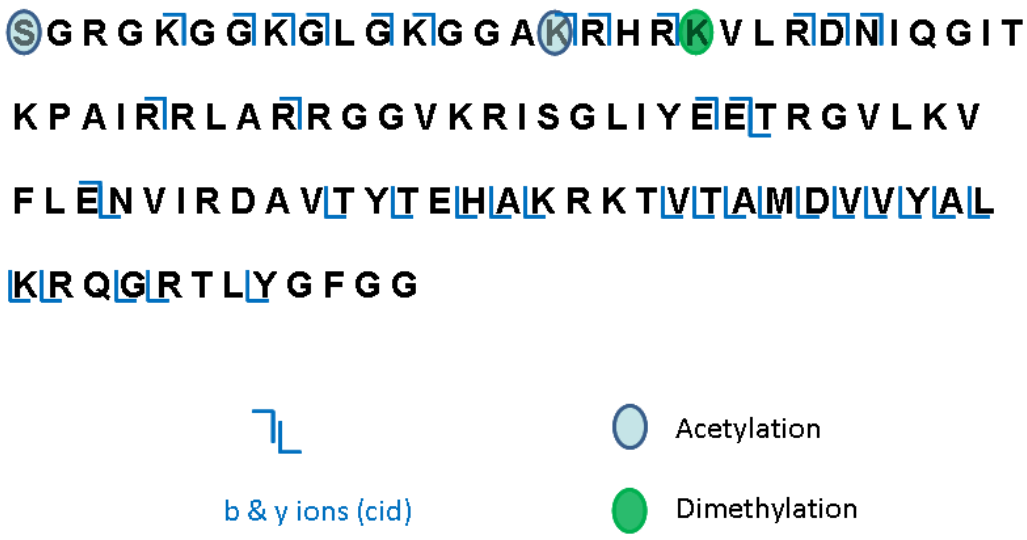

Figure 3.37: Fragment ion map of top-down CID of histone H4 from TSA treated OCI-AML3 cells (250 nM).

The fragment map shown above is in agreement with data presented earlier, in that the first lysine residue to be modified by acetylation is lysine 16. While the 250 nM TSA treatment provided little information, the next treatment and extraction carried out provided extensive sequence coverage of all ions fragmented by both CID and ECD. While the reasons for the improved results after 500 nM TSA treatment are unclear, they are most likely to do with more protein extracted during the procedure.

CID and ECD spectra of the 13^{+} charge state of H4 species at 873.9 *m/z*, corresponding to an isoform with an intact mass of 11,299 Da confirmed that this was the common form; acetylated at the N-terminus and di-methylated at lysine 20. The CID and ECD spectra are shown in Figures 3.38 and 3.39, together with a combined fragment ion map (Figure 3.40).

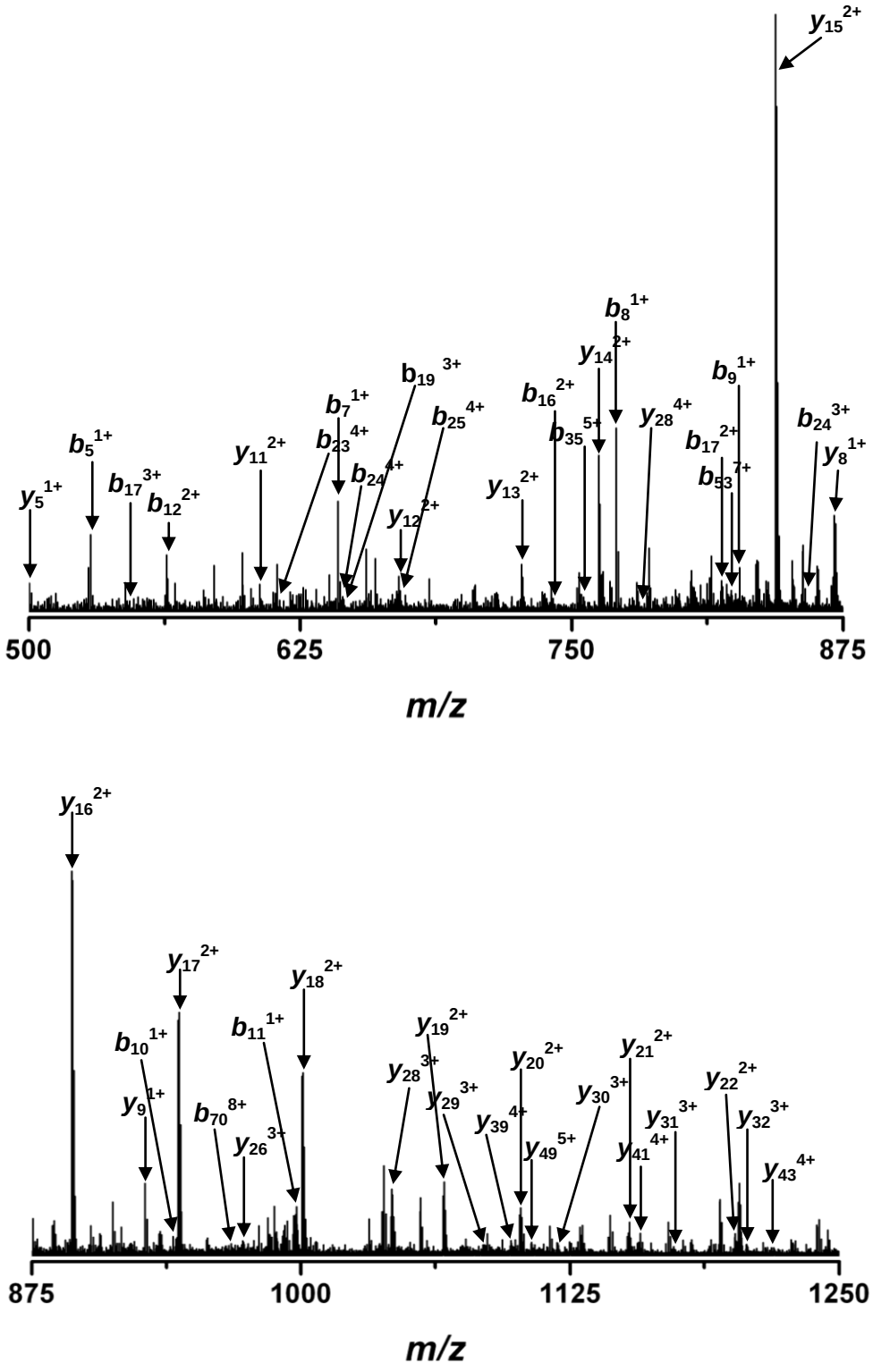

Figure 3.38: Top-down CID spectrum of histone H4 from TSA treated OCI-AML3 cells (500 nM) for the 13^{+} charge state from the precursor ion at 873.9 *m/z*. A complete list of the assigned fragment ions is attached as Appendix A15.

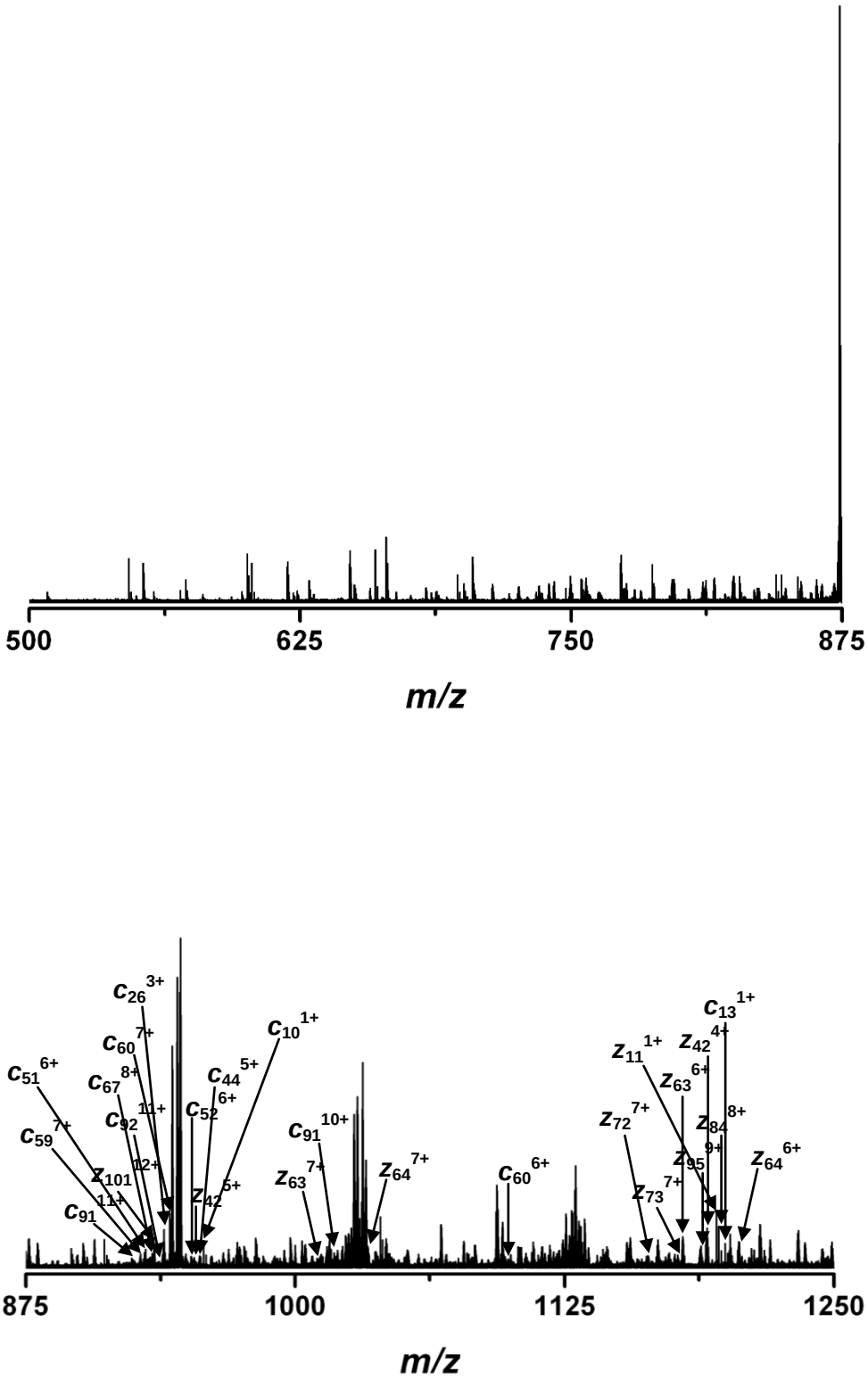

Figure 3.39: Top-down ECD spectrum of histone H4 from TSA treated OCI-AML3 cells (500 nM) for the 13^{+} charge state from the precursor ion at 873.9 *m/z*. A complete list of the assigned fragment ions is attached as Appendix A16.

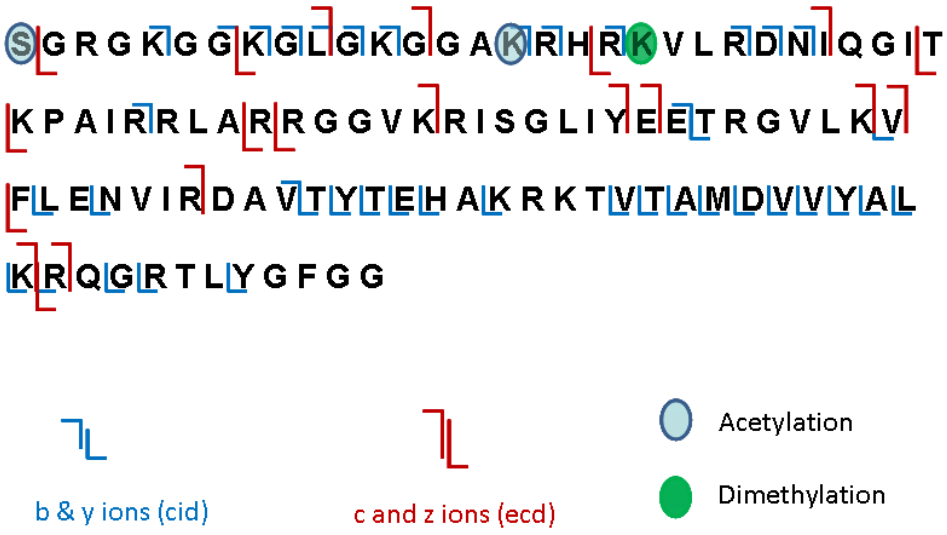

Figure 3.40: Fragment ion map of combined top-down CID and ECD of histone H4 from TSA treated OCI-AML3 cells (500 nM).

In agreement with similar data presented from other treatments, the first site of acetylation (excluding the N-terminal serine) is lysine 16. The data presented in the above figure showed no ambiguity in the location of the acetyl group, i.e. the ion fragmented above was not a mixture of modified H4 acetylated at lysines 12 and 16.

The next species investigated was the 13^{+} charge state for the precursor ion at 877.1 *m/z*, corresponding to an isoform with an intact mass of 11,383 Da. This intact mass corresponds to N-terminally acetylated and di-methylated H4 with a mass increase of 84 Da. CID and ECD spectra of this precursor ion are shown in Figures 3.41 and 3.42 below, with a combined fragment ion map (Figure 3.43).

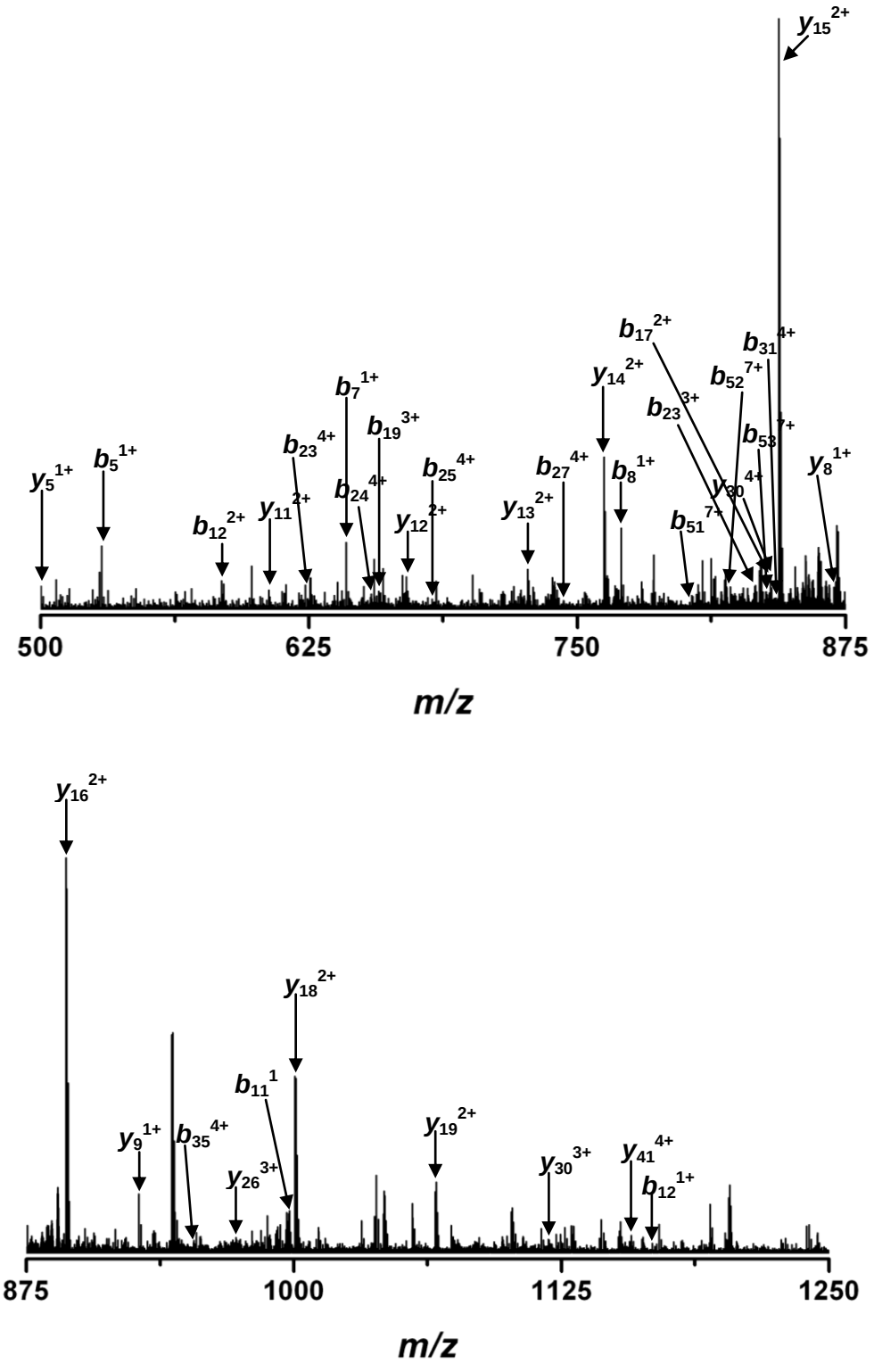

Figure 3.41: Top-down CID spectrum of histone H4 from TSA treated OCI-AML3 cells (500 nM) for the 13^{+} charge state of the precursor ion at 877.1 *m/z*. A complete list of the assigned fragment ions is attached as Appendix A17.

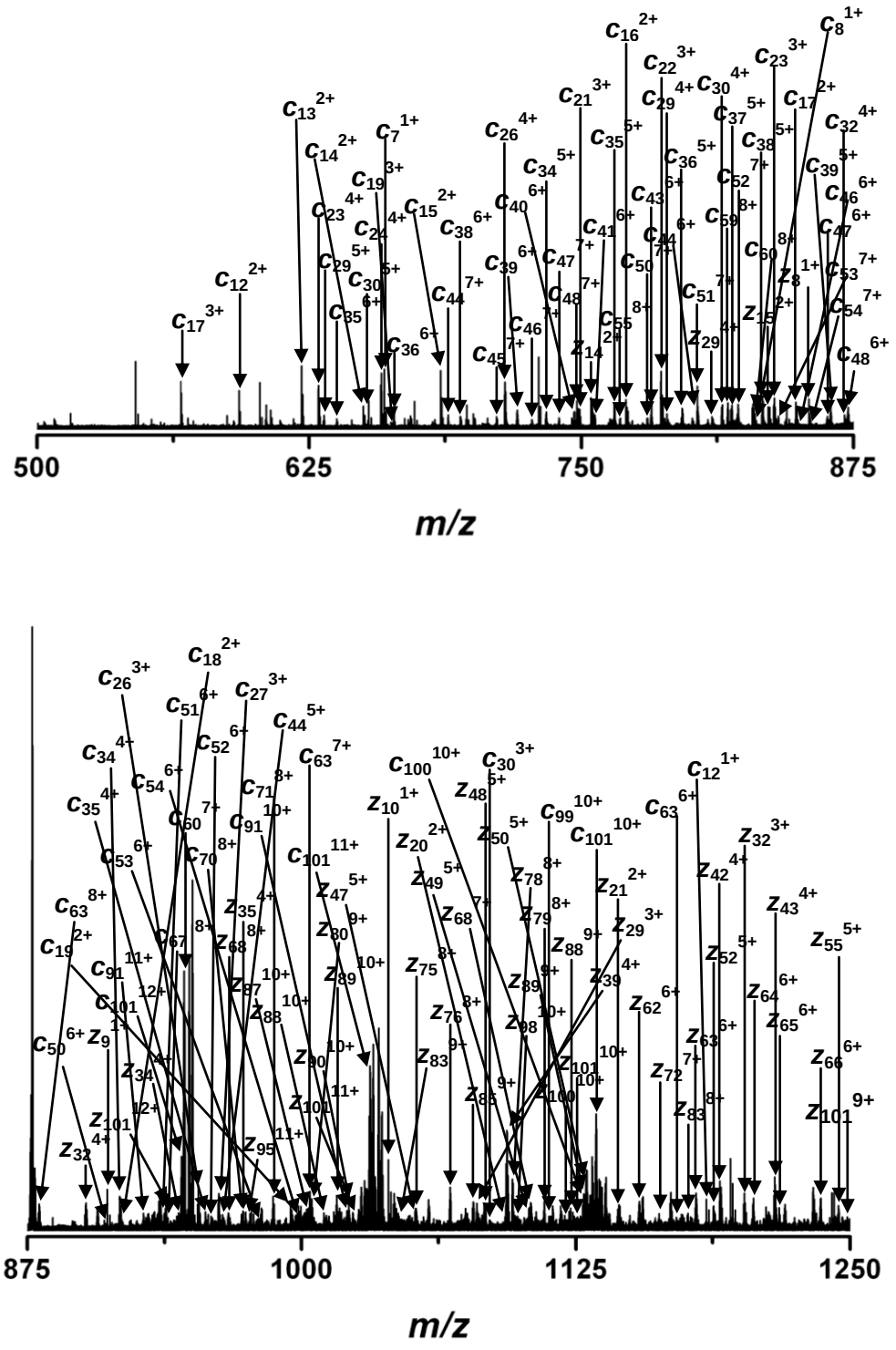

Figure 3.42: Top-down ECD spectrum of histone H4 from TSA treated OCI-AML3 cells (500 nM) for the 13^{+} charge state from the precursor ion at 877.1 *m/z*. A complete list of the assigned fragment ions is attached as Appendix A18.

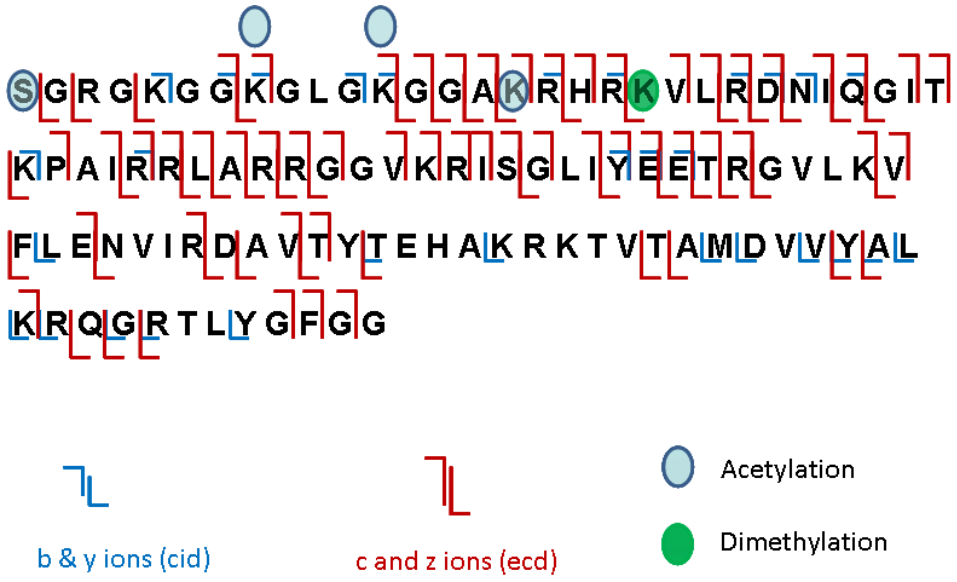

Figure 3.43: Fragment ion map of combined top-down CID and ECD of histone H4 from TSA treated OCI-AML3 cells (500 nM).

While the intact mass of this ion corresponded to N-terminally acetylated and di-methylated H4 with two additional acetyl groups, the location of one of these groups could not be identified conclusively from the fragmentation data. Acetylation was confirmed at lysine 16, and the data gathered suggest that the next acetyl group is located at either lysine 8 or lysine 12. CID data suggested that lysine 8 was acetylated whereas ECD data suggested that the seondary site of acetylation was lysine 12. Again, this implied that this isoform of H4 exists as a mixture of these possible combinations.

The next species to be examined was the 13^{+} charge state for the precursor ion at 880.4 *m/z*. The intact mass of 11,425 Da for this precursor ion corresponds to a mass increase of 126 Da over the unmodified form of H4. CID and ECD experiments were performed, and Figure 3.44 below shows the ECD spectrum obtained. While CID was successful, a low number of fragment ions were generated so this spectrum is not shown; however a combined fragment ion map is presented below the ECD spectrum (Figure 3.45).

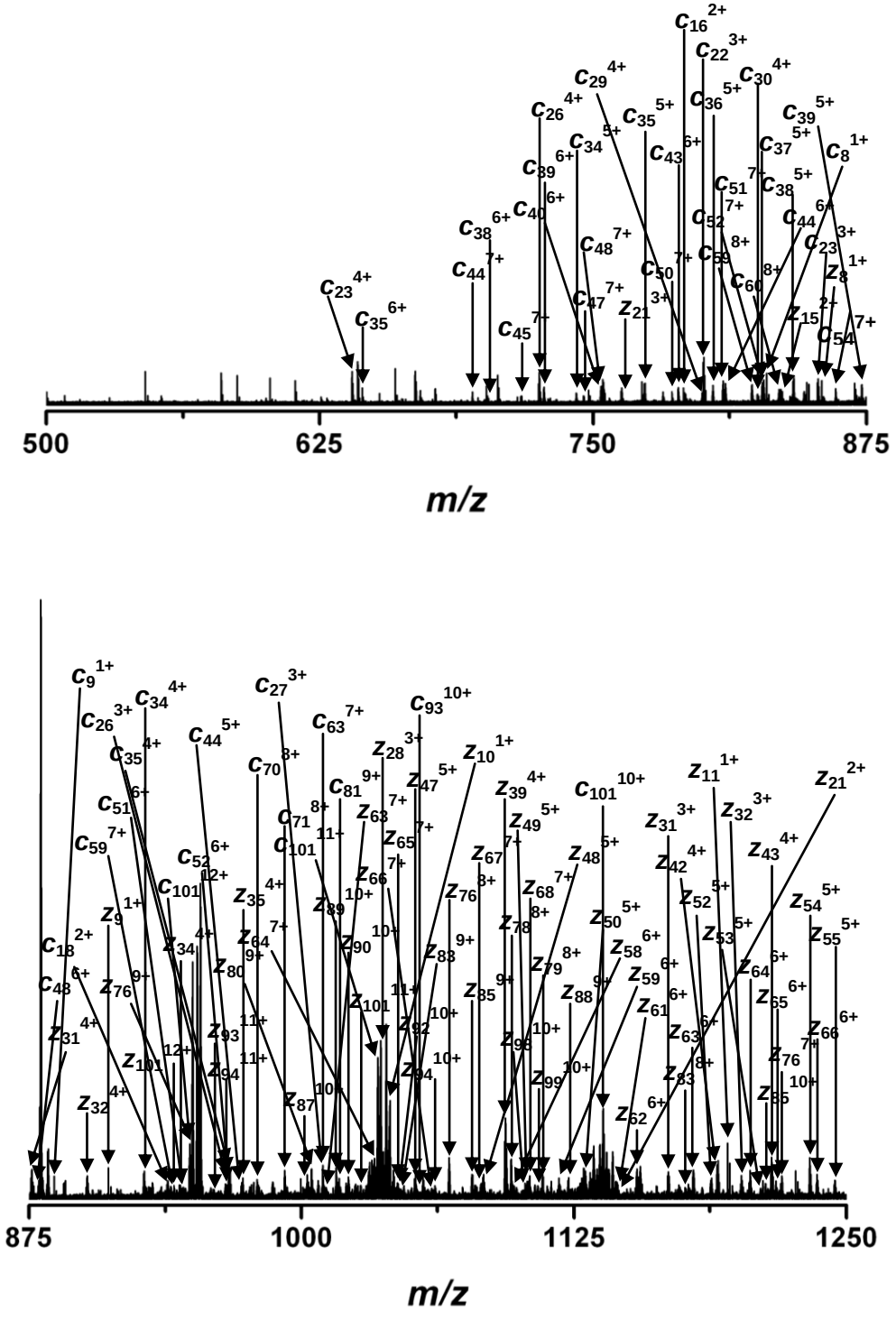

Figure 3.44: Top-down ECD spectrum of histone H4 from TSA treated OCI-AML3 cells (500 nM) for the 13^{+} charge state from the precursor ion at 880.4 *m/z*. A complete list of the assigned fragment ions is attached as Appendix A19.

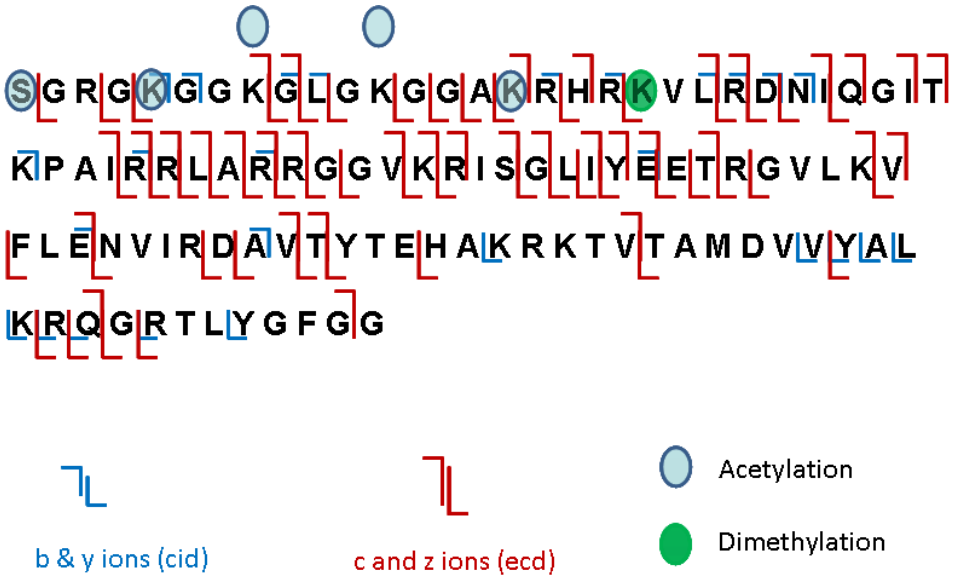

Figure 3.45: Fragment ion map of combined top-down CID and ECD spectrum of histone H4 from TSA treated OCI-AML3 cells (500 nM).

The fragmentation data confirmed acetylation at lysine 5 and lysine 16, while the position of the third acetylation could not be confirmed accurately; however its position can be narrowed down to either lysine 8 or lysine 12. Again, this suggests that modified forms of H4 exist as a mixture containing modifications at various sites.

The final species to be investigated from the 500 nM treated OCI-AML3 cell line was the 13^+ charge state for the precursor ion at 883.6 *m/z*. This precursor ion has an intact mass of 11,467 Da, which corresponds to a mass increase of 168 Da over the unmodified form of H4. CID and ECD spectra are shown in Figures 3.46 and 3.47 below along with a combined fragment ion map (Figure 3.48).

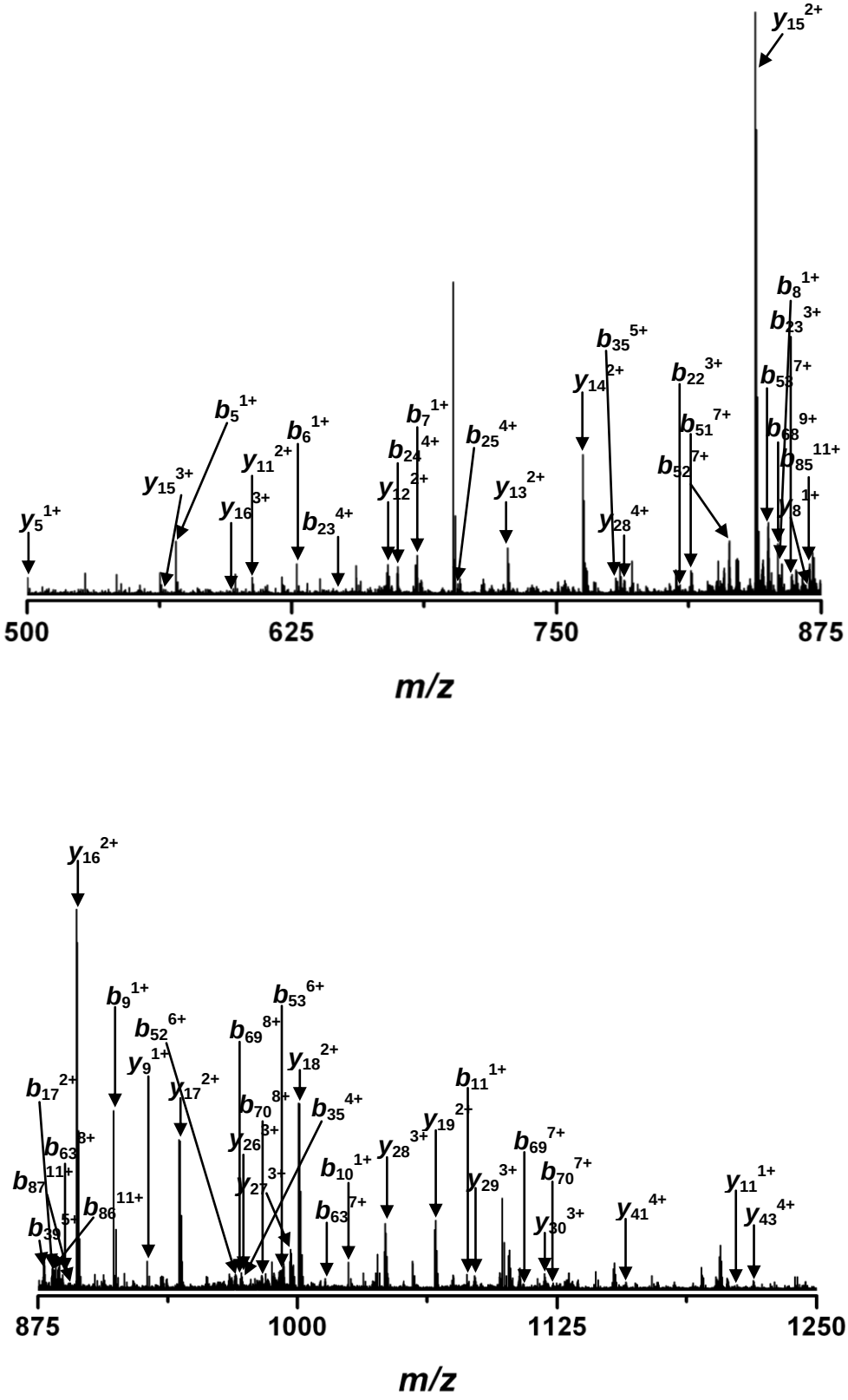

Figure 3.46: Top-down CID spectrum of histone H4 from TSA treated OCI-AML3 cells (500 nM) for the 13^{+} charge state from the precursor ion at 883.6 *m/z*. A complete list of the assigned fragment ions is attached as Appendix A20.

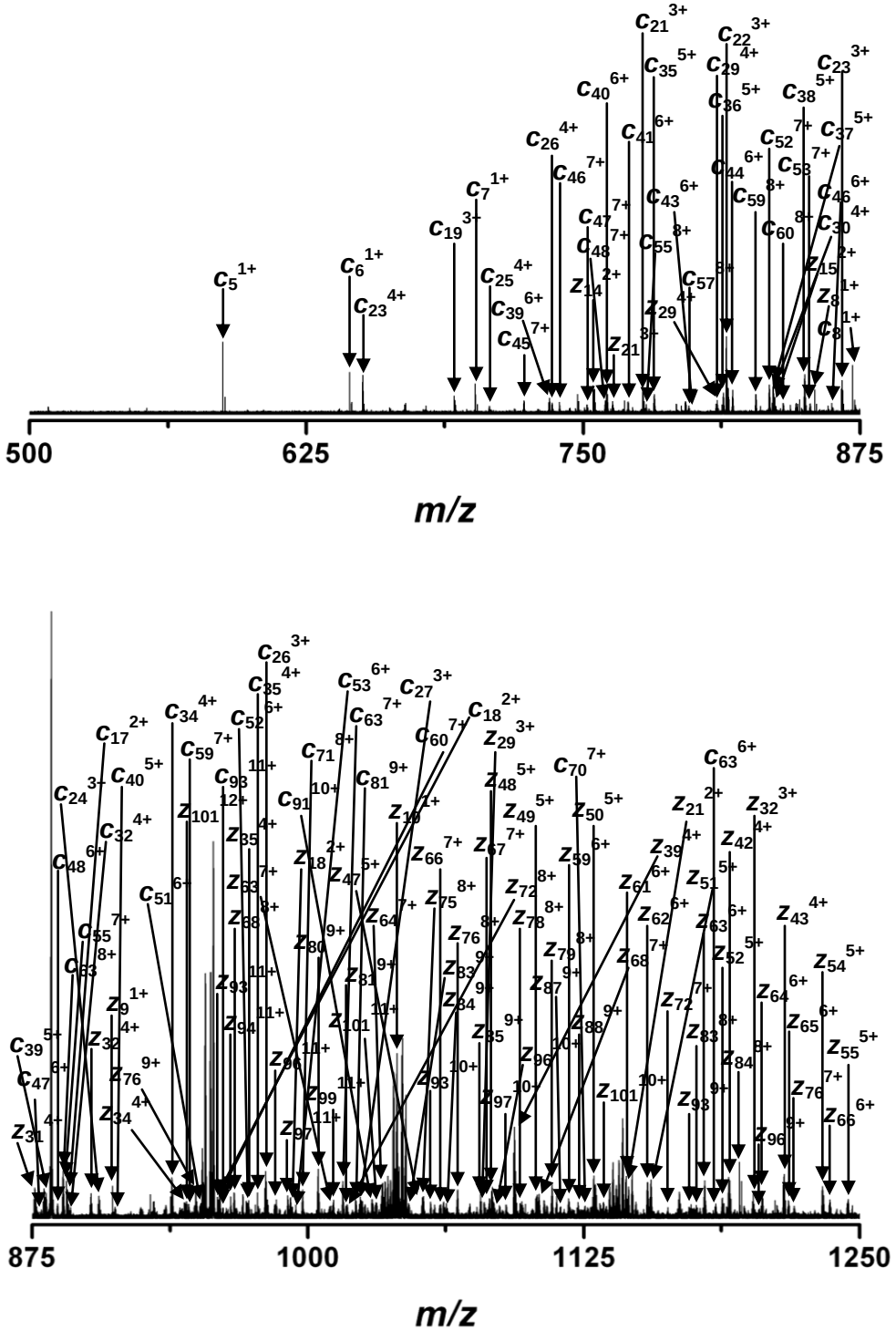

Figure 3.47: Top-down ECD spectrum of histone H4 from TSA treated OCI-AML3 cells (500 nM) for the 13^{+} charge state from the precursor ion at 883.6 *m/z*. A complete list of the assigned fragment ions is attached as Appendix A21.

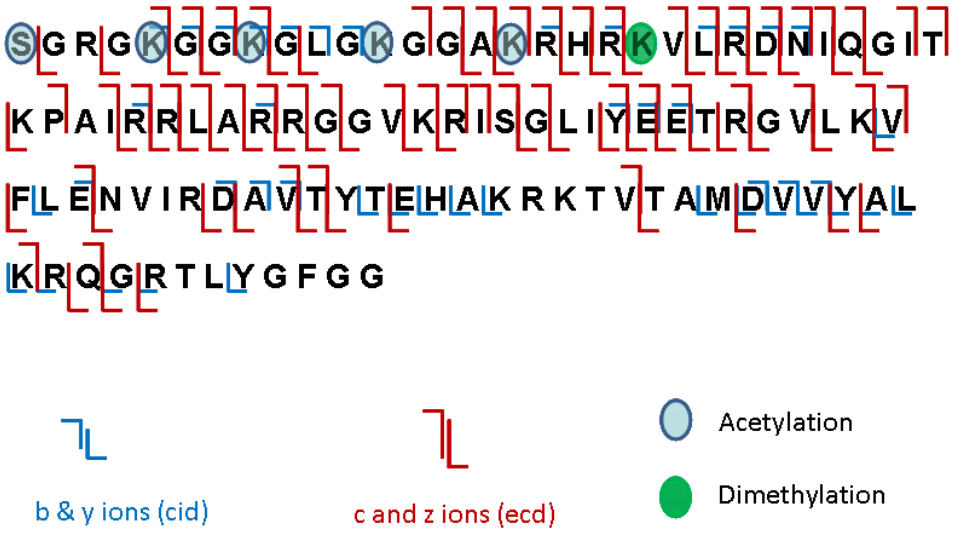

Figure 3.48: Fragment ion map of combined top-down CID and ECD of histone H4 from TSA treated OCI-AML3 cells (500 nM).

The extensive fragmentation achieved confirmed that all the modifications observed were located in the N-terminal region, and that no lysine residues after lysine 20 carried a PTM. The fragment ion map above shows clearly that post-translational acetylation of H4 occurs at lysines 5, 8, 12 and 16.

3.4 Conclusions

The data presented in Section 3.3.1 demonstrate that the response to the histone deacetylase inhibitor Trichostatin A is variable across cell lines. This is evident in the different ion abundances of modified H4 in each of the cell lines. This can potentially be explained by the nature of the mutations carried in each of the cell lines. Each cell line was derived from various cancerous tissues, and it is logical to assume that due to the altered growth rates of cancerous cells that different mechanisms are at play in regulating transcription. Since histone PTMs serve a pivotal role in gene expression, it follows that the response of such cells to deacetylase inhibitors would be variable.

The two cell lines chosen to investigate the order of acetylation of H4 displayed very different responses to TSA treatment. HCT-116 cells could reach full hyper-acetylation following TSA treatment, defining hyper-acetylation as the complete occupancy of all N-terminal lysine residues which could be modified with the addition of an acetyl group (this definition is necessary to exclude lysine 20 from the other four modifiable Lysine residues). A much lower proportion of OCI-AML3 cells reached full hyper-acetylation following TSA treatment, even after six hours. While CID and ECD fragmentation data on histone H4 extracted from OCI-AML3 cells yielded much useful information, less was obtained from HCT-116 cells, most likely due to low protein yield from the histone extraction procedure. From examination of the fragmentation spectra and the fragment ion maps presented above, the following conclusions can be drawn.

In HCT-116 cells, the histone isoform with an intact mass of 11,467 Da which corresponds to N-terminally acetylated and di-methylated H4 together with a mass increase of 168 Da, is the completely hyper-acetylated form with lysines 5, 8, 12 and 16 carrying acetyl groups. This was seen in the 50 nM and 500 nM treatments.

In OCI-AML3 cells, the histone isoform with an intact mass of 11,342 Da, which corresponded to N-terminally acetylated and di-methylated H4 with a mass increase of 42 Da was mono-acetylated, primarily at lysine 16. This was seen in spectra obtained from the 100 nM, 250 nM and 500 nM TSA treatments. The results from the 50 nM treated cells suggested that the acetyl group could be present on either lysine 16 or lysine 12. Fragments from the CID and ECD spectra confirmed the presence of both modified forms suggesting that mono-acetylated H4 could exist as a mixture.

The histone isoform with an intact mass of 11,383 Da, corresponding to N-terminally acetylated and di-methylated H4 together with a mass increase of 84 Da, had two additional acetyl groups. In OCI-AML3 cells treated with 50 nM TSA the acetyl groups were mapped to lysine 16 and lysine 12. In cells treated with 500 nM TSA the acetyl groups were mapped to lysine 16 and either lysine 12 or lysine 8.

The histone isoform with an intact mass of 11,425 Da, corresponding to N-terminally acetylated and di-methylated H4 together with a mass increase of 126 Da, had three additional acetyl groups. In OCI-AML3 cells treated with 100 nM TSA the acetyl groups were mapped to lysine 12, lysine 8 and lysine 5. In cells treated with 500 nM TSA the acetyl groups were mapped to lysine 16, lysine 5 and either lysine 8 or lysine 12. Fragments observed confirmed the presence of the modification at both these sites suggesting that H4 carrying this number of PTMs could exist as a mixture of these modified forms.

Similar to results gathered from HCT-116 cells, the histone isoform with an intact mass of 11,467 Da was tetra-acetylated H4, with each N-terminal lysine residue carrying an acetyl group. This was seen in OCI-AML3 cells after 500 nM TSA treatment.

From the data presented it is possible to suggest an order to the preferred site of H4 acetylation, based on the occurrence of the modification at each lysine residue. Lysine acetylation of histone H4 initially begins at lysine 16. This is followed by acetylation at lysine 12 or lysine 8. Lysine 5 is the last (and least observed) site of acetylation. This is shown in Figure 3.33 below. These results are in good agreement with work performed previously which employed middle-down or bottom–up mass spectrometry approaches[150,161-163].

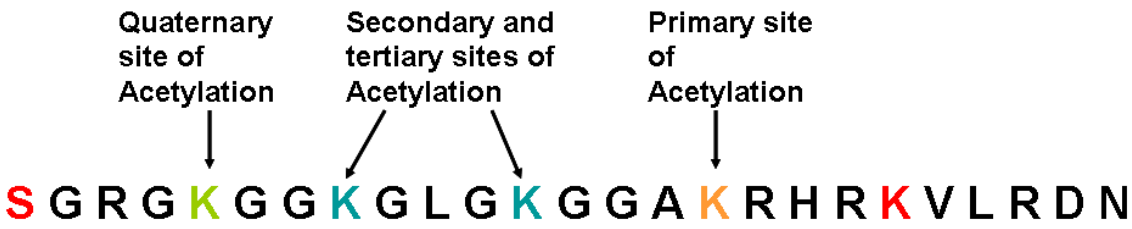

Figure 3.49: Sequence of N-terminal region of H4. Lysine residues with PTMs affected by TSA are highlighted and labeled in order of observed modifications.

3.5 Future Work

While the present study has provided a good indication of the order of acetylation, future work could focus on determining whether or not the site of modification is dependent on the presence of other PTMs close to the residue of interest. This work could begin with investigating histone H4 acetylation in the absence of the di-methyl group located at lysine 20, and using the methods employed here (treatment with a de-acetylase inhibitor and top-down FT-ICR MS). The modifications present at each N-terminal lysine could then be characterized.

In addition, this work could be extended to the other histone protein known to be extensively decorated by acetylation, histone H3. However, the study of histone H3 would be more challenging due to the large number of methyl groups known to modify arginine residues. Nevertheless, a better understanding of the combinations of post-translational modifications would increase the body of knowledge linking PTMs to specific biological functions.

Chapter 4

The Role of Lactic Acid as a Histone De-acetylase Inhibitor

Chapter 4 describes a study carried out to investigate the effects of lactic acid exposure to the acetylation profile of histone H4. An introduction is given which includes a brief description of how lactic acid is formed during energy metabolism in eukaryotes, along with the methods used in the work and results generated. A summary and suggestions for future work are provided at the end of the chapter.

4.1 Introduction

Energy metabolism in eukaryotes can broadly be split into three stages: glycolysis, the citric acid cycle and oxidative phosphorylation. The first stage, glycolysis, involves the uptake of glucose (the preferred source of energy) into the cell and its conversion to the end product pyruvic acid[164]. Pyruvic acid enters the citric acid cycle, and through a series of reactions, adenosine tri-phosphate (ATP, the molecule which serves as the body's energy currency) is generated. Following the citric acid cycle, oxidative phosphorylation converts products of the citric acid cycle into water and carbon dioxide using a series of reactions which function as an electron transport chain. Water and carbon dioxide are the ultimate products of metabolism and their formation signals the complete metabolism of a glucose molecule. A single glucose molecule can yield up to 36 molecules of ATP[165] and Figure 4.1 below is a representation of glycolysis (a) and the citric acid cycle (b).

(a)

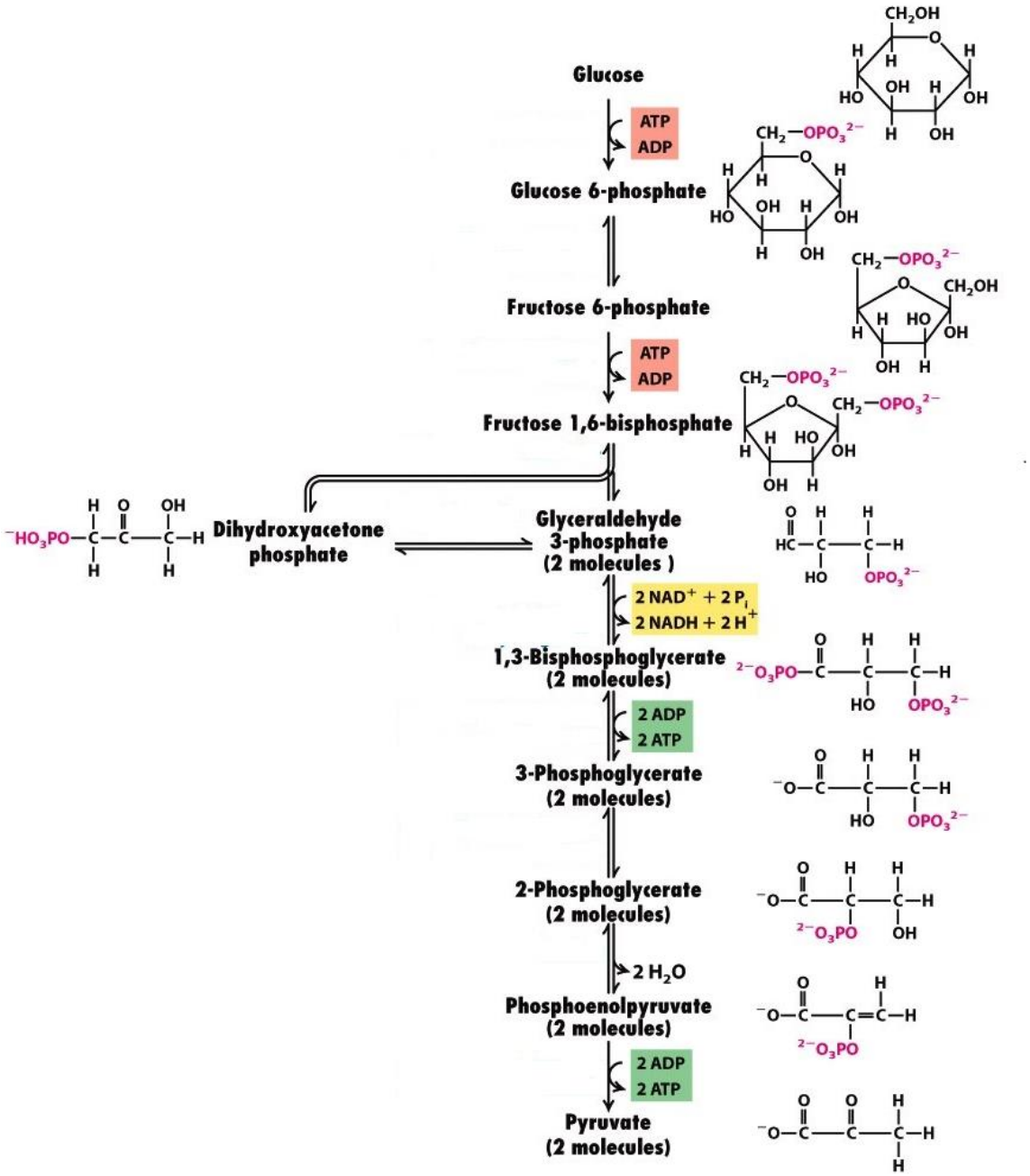
Glucose
ATP
ADP
Glucose 6-phosphate
Fructose 6-phosphate
ATP
ADP
Fructose 1,6-bisphosphate
Dihydroxyacetone phosphate
Glyceraldehyde 3-phosphate (2 molecules)
2 NAD+ + 2 Pi
2 NADH + 2 H+
1,3-Bisphosphoglycerate (2 molecules)
2 ADP
2 ATP
3-Phosphoglycerate (2 molecules)
2-Phosphoglycerate (2 molecules)
2 H2O
Phosphoenolpyruvate (2 molecules)
2 ADP
2 ATP
Pyruvate (2 molecules)

(b)

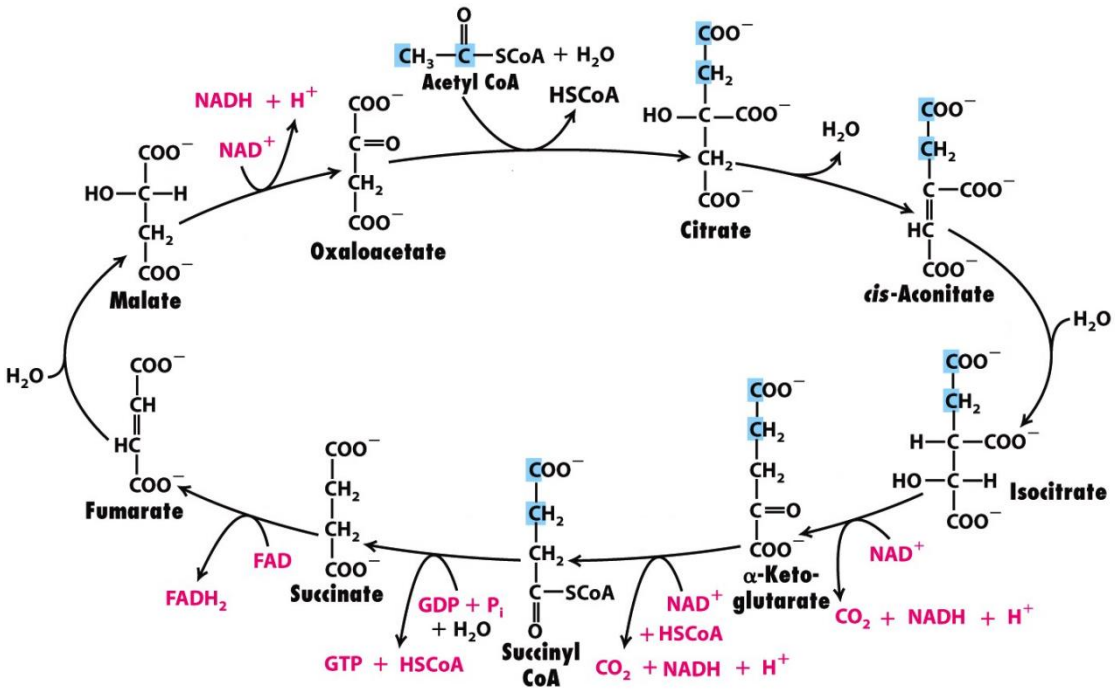

Figure 4.1: Overview of (a) glycolysis and (b) the citric acid cycle. Figures adapted from Lodish *et al*[166].

Entry into each of the stages is dependent on the availability of the correct substrates e.g. glycolysis begins with the six carbon sugar glucose, but not with its isomer fructose. Regulating the availability of several such substrates are enzymes responsible for the inter-conversion of various isomers[167]. Glucose is sourced from the diet, however the citric acid cycle begins with the three carbon keto-acid, pyruvic acid. Under aerobic conditions, this is the end product of glycolysis, but under anaerobic conditions i.e. when oxygen is present in limited amounts, glycolysis favours the formation of lactic acid, which can be reversibly converted into pyruvic acid by the enzyme lactate de-hydrogenase. Figure 4.2 below shows the inter-conversion of these molecules.

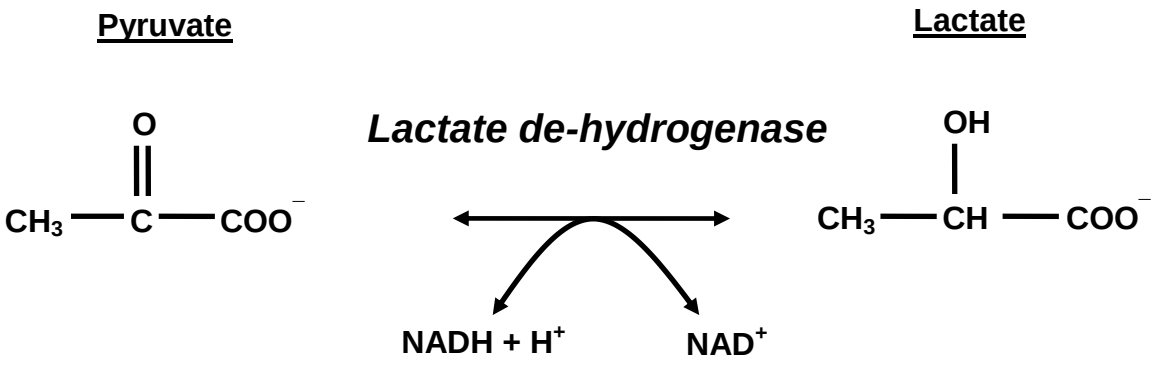

Figure 4.2: Reversible conversion of pyruvate to lactate by the enzyme lactate de-hydrogenase. Figure adapted from Stryer [168].

During intense exercise, when insufficient oxygen is present for glycolysis to proceed as normal, lactic acid becomes the main end product, rising to levels of 55.9 mM. These levels return to normal (around 2.8 mM) once sufficient oxygen is available[169]. It has been shown previously that pyruvate and butyrate have an effect on the acetylation of histone H4[153,155,170], however little concrete evidence exists showing whether or not lactate can affect histone acetylation. The relevance of considering the role of lactic acid as a histone de-acetylase inhibitor becomes apparent when considering the metabolism of cells which undergo altered growth rates; i.e. cells which have become cancerous. Replicating cells can be split broadly into three groups depending on growth rates and entry/exit of stages of the cell cycle. Cells can be classed as non-tumourigenic, tumourigenic or metastatic. While the majority of cells fall into the non-tumourigenic group, tumourigenic cells (which are pre-cancerous) are known to metabolise energy through different pathways.

During respiration in healthy cells, lactate concentration is roughly ten times that of pyruvate[169]. Otto Warburg reported in 1926 that tumourigenic cells relied heavily on glycolysis to generate ATP, while the citric acid cycle and oxidative phosphorylation were used to a much lesser extent. This observation was manifested as an increase in the amount of lactic acid in the presence of oxygen, a result of the conversion of pyruvic acid into lactic acid by the enzyme lactate de-hydrogenase[171]. This phenomenon, noted by Warburg, and has come to be known as the Warburg effect[172,173]. While it is still

unknown if the Warburg effect is a cause or a result of tumourigenesis, the increase in glucose consumption and the elevated levels of lactic acid in cancerous cells is now well known[174,175].

The work performed in the previous chapter serves as a starting point for the material presented here.

The effect of lactate as a histone de-acetylase inhibitor was tested against the activity of two histone modifying enzymes; histone de-acetylases one and two (HDAC 1 and HDAC 2). The HCT-116 cell line was shown to be sensitive to histone de-acetylase inhibitors, as such it was deemed suitable for the work described here. Cells were cultured and supplemented with lactate, histones extracted and LCMS performed to investigate whether lactate could alter the acetylation of histone H4.

The aims of this study were as follows:

- To determine if lactate, a by-product of glycolytic metabolism, could affect histone H4 acetylation.
- To quantify by mass spectrometry, any changes in the acetylation pattern of histone H4.

4.2 Methods

4.2.1 Cell Culture and Lactate Treatment

HCT-116 cells were cultured as described previously and split into four groups; two groups received a supplement of histone de-acetylase 1 (HDAC 1) at 5 and 10 units, and the other two groups supplemented with HDAC 2. The cells were divided further according to HDACi treatment. Lactate (as sodium lactate) was added to the culture medium in either L- or D- form at a final concentration of 100 mM. As negative control, sodium chloride was added to one group (100 mM) and as positive control TSA was added to another (100 nM). The treatment was carried out as a time course, with exposure lasting thirty minutes, three hours or six hours. After each of these periods cells were washed briefly in PBS before histone extraction was carried out (as described in section 2.2.3). A workflow of the experiment is shown in Figure 4.3 below.

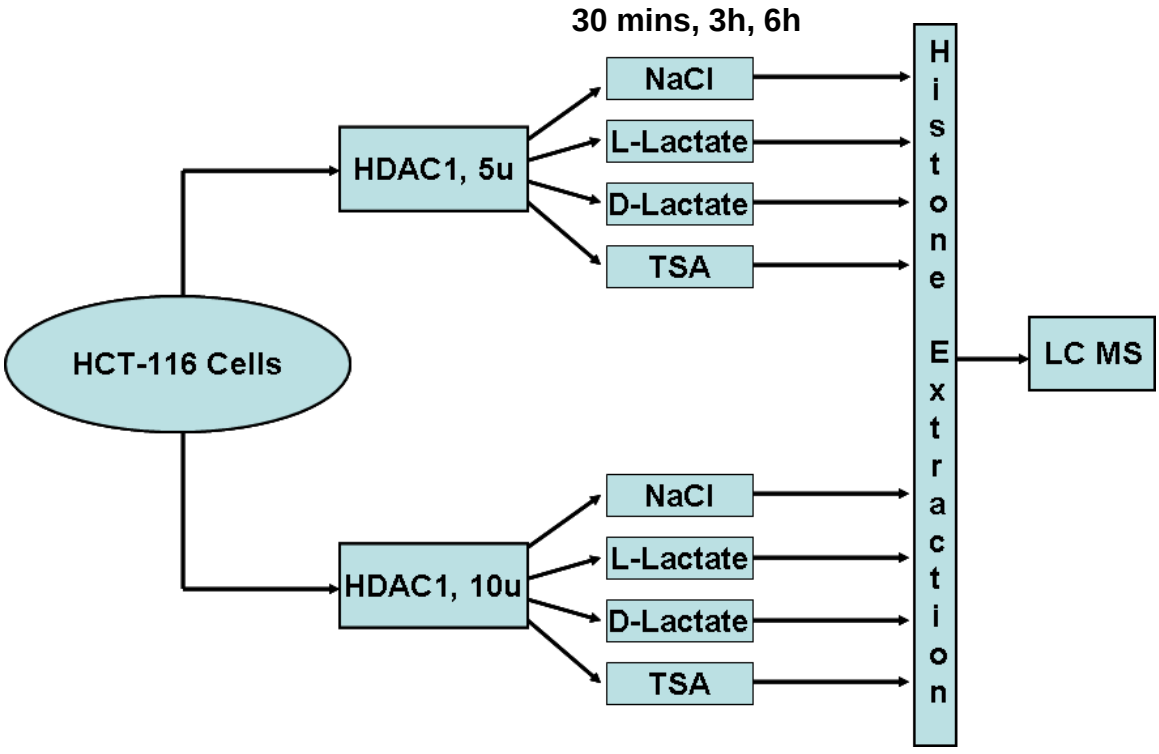

Figure 4.3: Workflow of experiment to determine if lactate can affect histone acetylation. The steps shown above were repeated for cells receiving HDAC2 treatment.

4.2.2 Liquid Chromatography and Mass Spectrometry

LC-MS was performed with a Dionex Ultimate 3000 system coupled to a Bruker Daltonics Apex Qe FT-ICR mass spectrometer equipped with either a 9.4 T or a 12 T superconducting magnet. Data was acquired in broadband mode with an ion accumulation time of roughly 1 second. Each spectrum acquired was the sum of 2 mass analyses.

4.2.3 Data Analysis

Data was analysed using Compass DataAnalysis software (Bruker) and ion abundances were calculated using in house software (written in Python), using a modified version of the method described by Smith *et al* [159,160]. Briefly, acetylation was quantified from the integrated ion abundances of modified species at the three highest abundance charge states. Each integrated ion abundance was then weighted according to the number of modified lysine residues. These were then summed and divided by the total weighted ion abundance of all modified H4 species possible. The levels of acetylation are presented as a percentage (i.e. ((acetylation present)/(acetylation possible)) multiplied by 100). All spectra were exported as simple ASCII files and plotted using Microcal Origin (version 6.0).

4.2.4 Statistical Analysis

Statistical analysis of data was performed using Minitab Statistical Software, Version 16 (Minitab Inc). Ion abundance data was manually entered into Minitab and the on-board statistical analysis functions were used to perform either paired t-tests or analysis of variance. A p- value of <0.05 indicated a difference between the data being compared (i.e. acceptance of the null hypothesis where a change in acetylation level was the result of the treatment administered to the cells) while a p- value >0.05 was interpreted as there being no statistical difference between data sets (i.e. acceptance of the alternative hypothesis).

4.3 Results

4.3.1 HDAC 1 Treatment

The LC-MS spectra shown in Figure 4.4 below display the 9^+ charge state of histone H4 extracted from HCT-116. Cells were treated with 5 units HDAC 1 and either sodium chloride, L-lactate, D-lactate or TSA (shown in different colours) for thirty minutes.

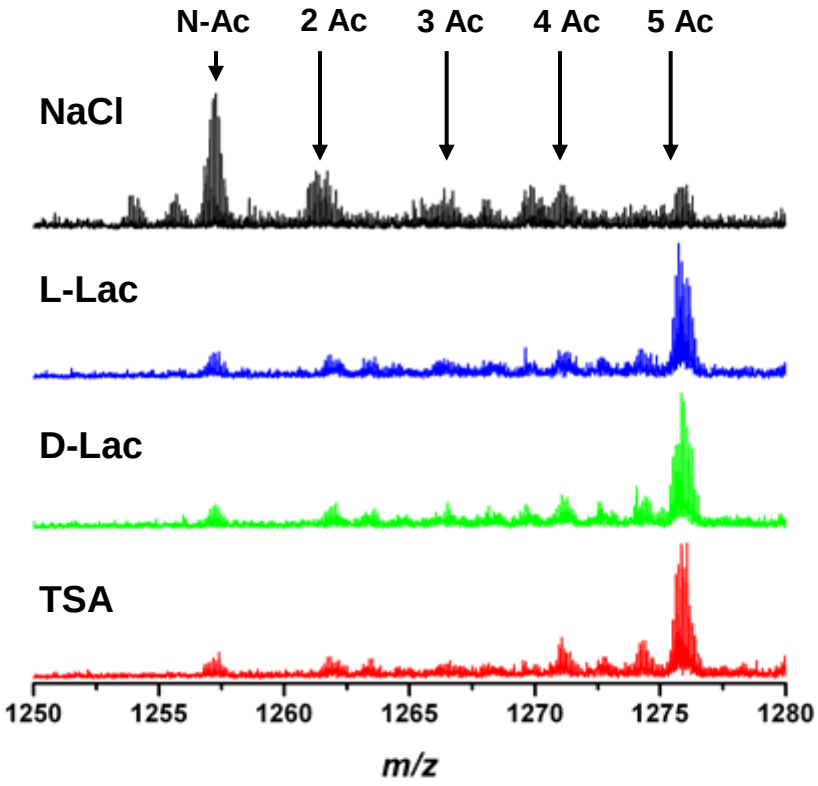

Figure 4.4: LC-MS spectra for the 9^+ charge state of histone H4 after 30 minutes treatment with L- or D-lactate (blue and green respectively). NaCl (black) and TSA (red) were included as negative and positive controls respectively. The di-methylated peaks are labelled and numbered in order of acetylation state where (N-Ac) means N-terminally acetylated and (2 Ac) means two acetyl groups are present etc.

As would be expected for the NaCl treatment, little change is seen in the amount of acetylation. The L-lactate treatment proved an effective histone deacetylase inhibitor (HDACi), as did the D-lactate treatment. TSA is a known inhibitor of histone de-acetylation and this treatment resulted in the expected rise in abundance of acetylated species. The level of acetylation calculated for the NaCl treatment was 37%. L-lactate, D-lactate and TSA all inhibited de-acetylation to a similar extent with acetylation values

of 73%, 75% and 74% respectively. The standard deviations from these values (calculated from the three highest abundance charge states) were all under 5%, giving good confidence in the results.

The LC-MS spectra shown in Figure 4.5 below display the 9^+ charge state of histone H4, with similar treatments to those described above, except that the treatments were applied for three hours. Similar to Figure 4.4 above, the colours used in the spectra represent the various treatments.

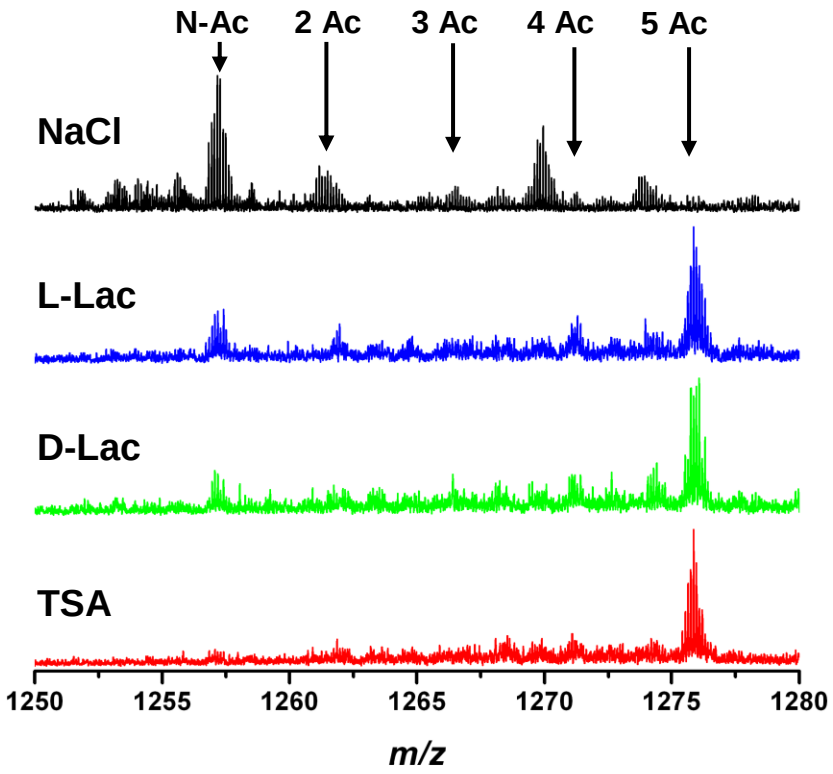

Figure 4.5: LC-MS spectra for the 9^+ charge state of histone H4 after 3 hours treatment with L- or D-lactate (blue and green respectively). NaCl (black) and TSA (red) were included as negative and positive controls respectively. The di-methylated peaks are labelled and numbered in order of acetylation state where (N-Ac) means N-terminally acetylated and (2 Ac) means two acetyl groups are present etc.

Changes in the level of acetylation start to appear after three hours treatment time. The level of acetylation in the NaCl treated cells rose, visible as the peaks at roughly 1270 *m/z* and 1274 *m/z*, an unexpected observation as sodium chloride is not known to affect

histone acetylation. Contrary to this, and somewhat expected, the levels of acetylation in the three other treatments fell. Acetylation in the L-lactate cells fell to 63%, D-lactate treated cells fell to 66% and acetylation of TSA treated cells fell to 66%. The maximum standard deviation from these values was 5.81% (TSA treatment), again giving good confidence in the results. The extension of treatment time resulted in a drop in acetylation for all treatments (except NaCl) which is most likely a result of the various treatments being matabolised by the cells.

The LC-MS spectra shown in Figure 4.6 below show the 9^+ charge state of histone H4 after six hours treatment with the same four compounds.

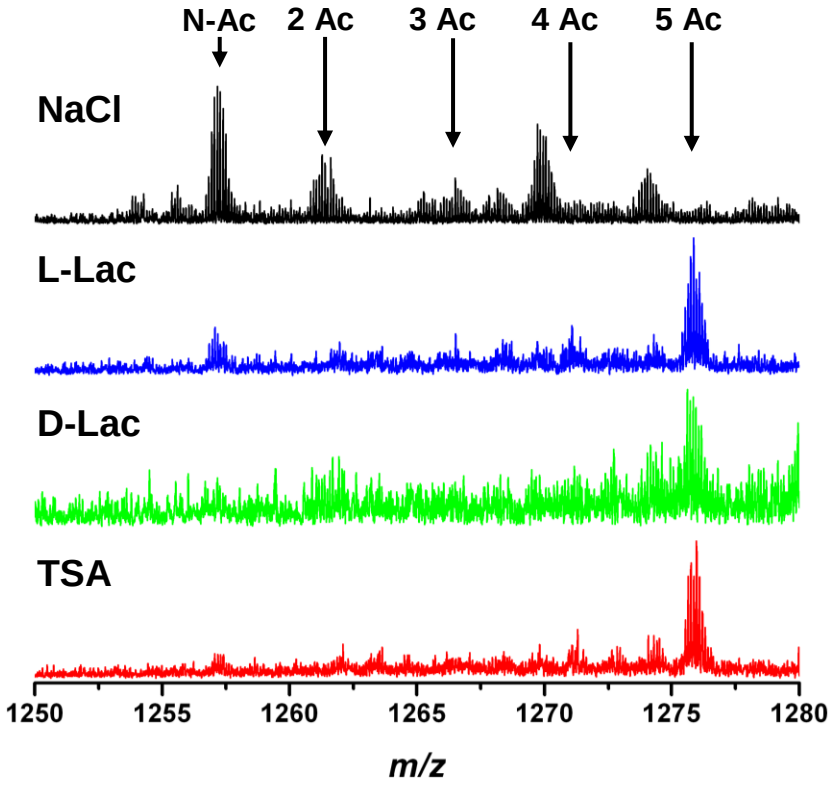

Figure 4.6: LC-MS spectra for the 9^+ charge state of histone H4 after 6 hours treatment with L- or D-lactate (blue and green respectively). NaCl (black) and TSA (red) were included as negative and positive controls respectively. The di-methylated peaks are labelled and numbered in order of acetylation state where (N-Ac) means N-terminally acetylated and (2 Ac) means two acetyl groups are present etc.

After six hours treatment there was little change in acetylation levels when compared to the results of the three hour treatment. Acetylation in the NaCl treated cells rose slightly to 47%. Acetylation in the other treatments remained stable; 63% for the L-lactate treatment, 68% for the D-lactate treatment and 72% for the TSA treatment. The standard deviations from these values were all below 6% (D-lactate treatment), again giving good confidence in the results. The results are summarised in Figure 4.7 below.

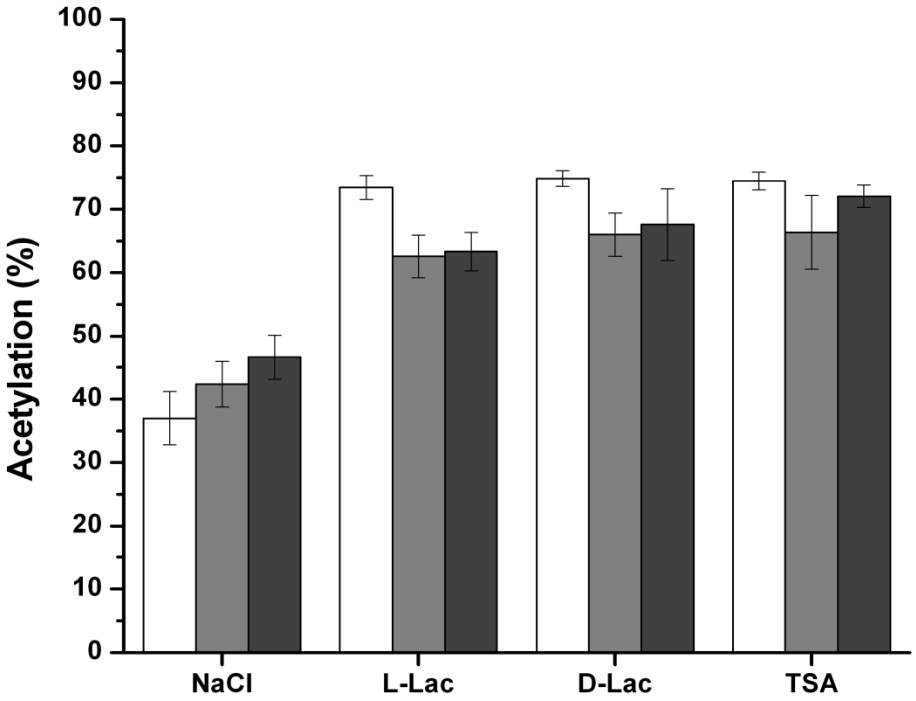

Figure 4.7: Graph showing the combined results of all treatments over the three time periods for cells supplemented with 5 units HDAC 1; 30 minutes (white), 3 hours (light grey) and 6 hours (dark grey).

The NaCl control treatment exhibited consistently lower acetylation than all other treatments after each time period. The other treatments each displayed a similar pattern in acetylation, specifically that acetylation would reach a maximum value after thirty minutes treatment and this would subsequently drop and stabilise over the following six hours.

The following spectra show the results of treatment with the four compounds over similar time periods, however, in this case cells were supplemented with 10 units HDAC 1 instead of 5 units. Figure 4.8 below displays the results of the thirty minute treatment.

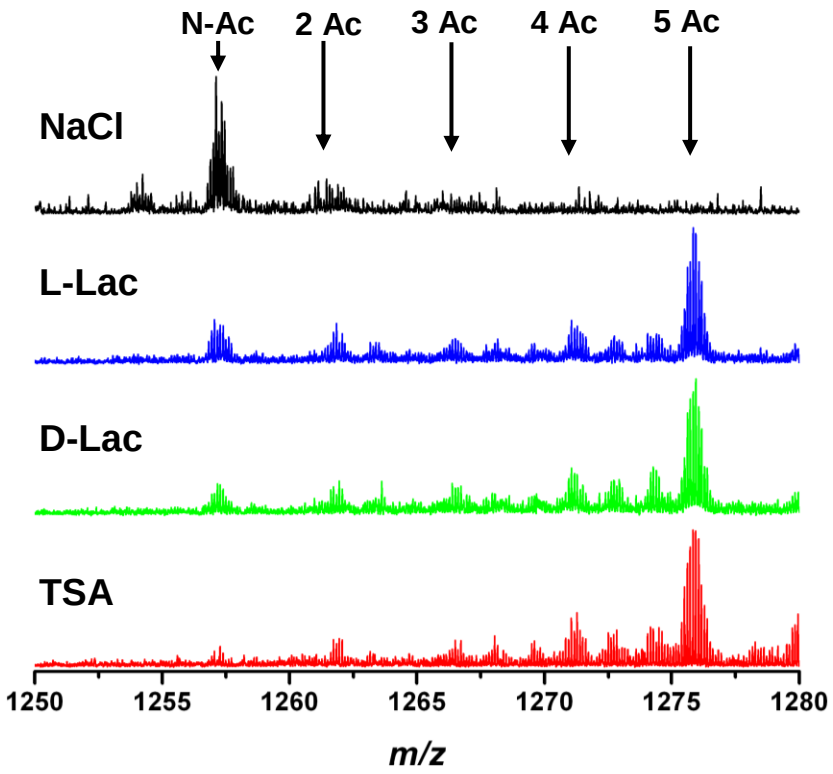

Figure 4.8: LC-MS spectra for the 9^+ charge state of histone H4 after 30 minutes treatment with L- or D-lactate (blue and green respectively). NaCl (black) and TSA (red) were included as negative and positive controls respectively. The di-methylated peaks are labelled and numbered in order of acetylation state where (N-Ac) means N-terminally acetylated and (2 Ac) means two acetyl groups are present etc.

As found in the earlier experiments involving supplementation with 5 units of HDAC 1, acetylation of the NaCl treated cells was low at 38%. Acetylation after all other treatments was higher; 74% (L-lactate), 78% (D-lactate) and 61% (TSA). Standard deviations were all below 8% (NaCl) with the other values typically around 4%. While the effect of the lactate treatments still show that L- and D-lactate are inhibitors of histone de-acetylation, the effect of the TSA treatment is reduced when compared to the corresponding data following supplementation with 5 units of HDAC 1. This could be a

result of the increased amount of HDAC1 supplemented to the cells. However, it is also possible that this result is partly due to the charge states chosen for the calculation performed. The similarity in the increased levels of acetylation of the lactate treated samples when compared to the data for supplementation with 5 units of HDAC 1 suggest this may be the case.

Figure 4.9 below shows the results of the three hour treatment.

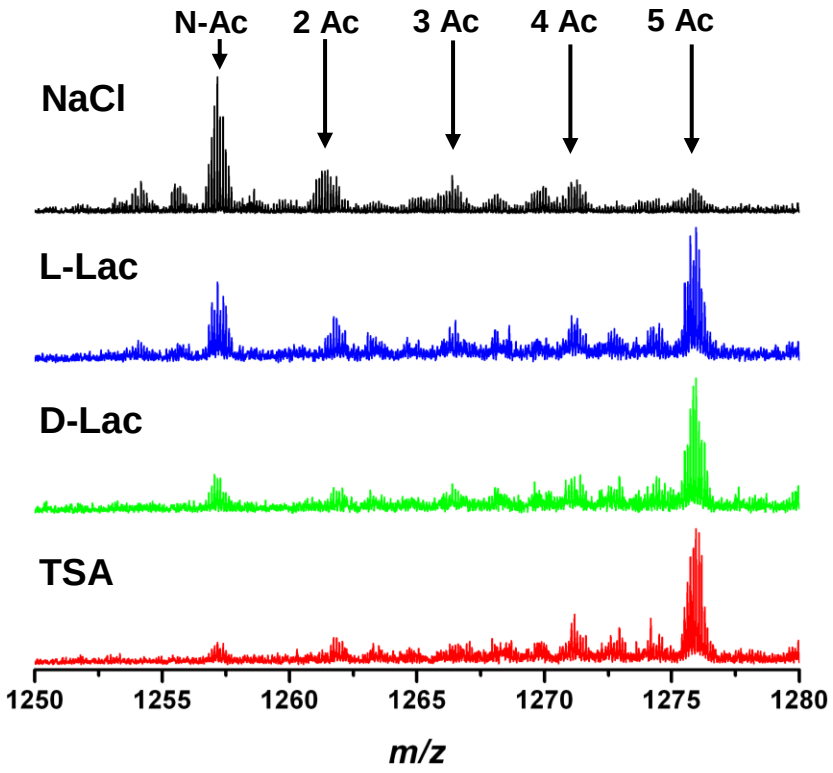

Figure 4.9: LC-MS spectra for the 9^+ charge state of histone H4 after 3 hours treatment with L- or D-lactate (blue and green respectively). NaCl (black) and TSA (red) were included as negative and positive controls respectively. The di-methylated peaks are labelled and numbered in order of acetylation state where (N-Ac) means N-terminally acetylated and (2 Ac) means two acetyl groups are present etc.

Acetylation in the NaCl treated cells rose slightly to 43%, similar to the results seen for the same time course following supplementation with 5 units of HDAC 1. Acetylation in the lactate treated cells dropped to 66% (L-lactate) and 69% (D-lactate), while this value rose in the TSA treated cells (81%). The values calculated for the L- and D-lactate

treated cells were simiar to those observed earlier for the same time course, again indicating that after three hours treatment the inhibitory effect of the lactate was reduced potentially due to metabolism of the treatment. The increase in value calculated for the TSA treatment is likely a better indication of the true level of acetylation when compared to the thirty minute time course. This can be confirmed to an extent by the low standard deviations from the calculated values, all of which were under 4% (TSA).

Figure 4.10 below displays the results of the six hour treatments.

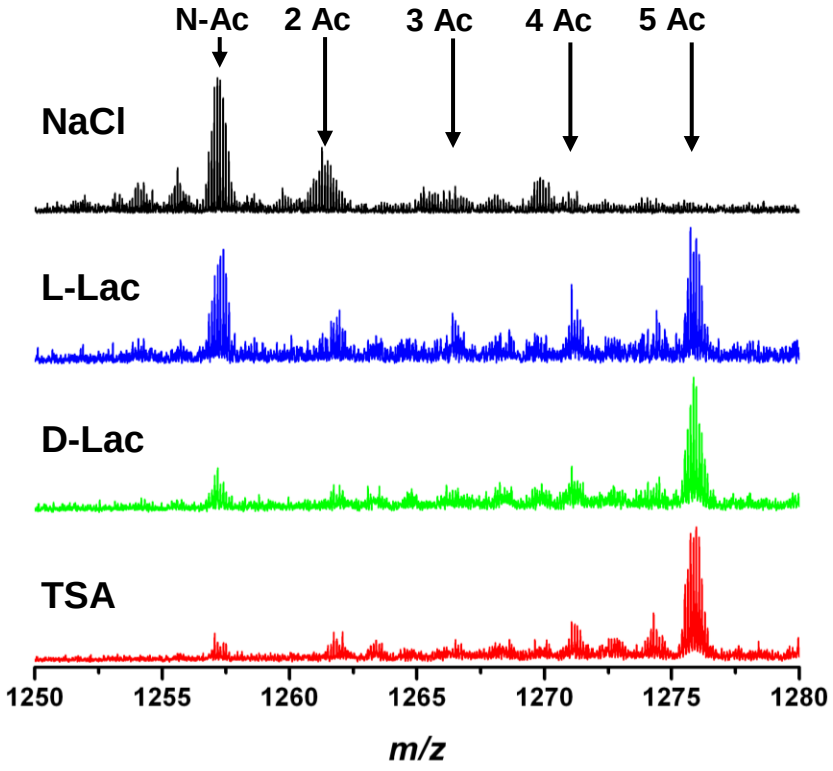

Figure 4.10: LC-MS spectra for the 9^{+} charge state of histone H4 after 6 hours treatment with L- or D-lactate (blue and green respectively). NaCl (black) and TSA (red) were included as negative and positive controls respectively. The di-methylated peaks are labelled and numbered in order of acetylation state where (N-Ac) means N-terminally acetylated and (2 Ac) means two acetyl groups are present etc.

Differences were apparent when compared to previous spectra. Acetylation in the NaCl treatment remained fairly stable at a value of 40%. A drop in acetylation for the L-lactate treatment can be seen by the emergence of the peak at ~1257 *m/z*, indicating an increase

in the N-terminally acetylated di-methylated form of H4. The level of acetylation for the L-lactate treatment was calculated as 60%. Acetylation after six hours with the other treatments (D-lactate and TSA) remained elevated with values of 76% and 81% respectively. All standard deviations were low with a maximum value of 5% (NaCl) giving good confidence with the results. Similar to the data for supplementation with 5 units of HDAC 1, acetylation levels fell after three hours for the L-lactate treatment, however, in this case the level of acetylation continued to fall after six hours. These results are summarised in Figure 4.11 below.

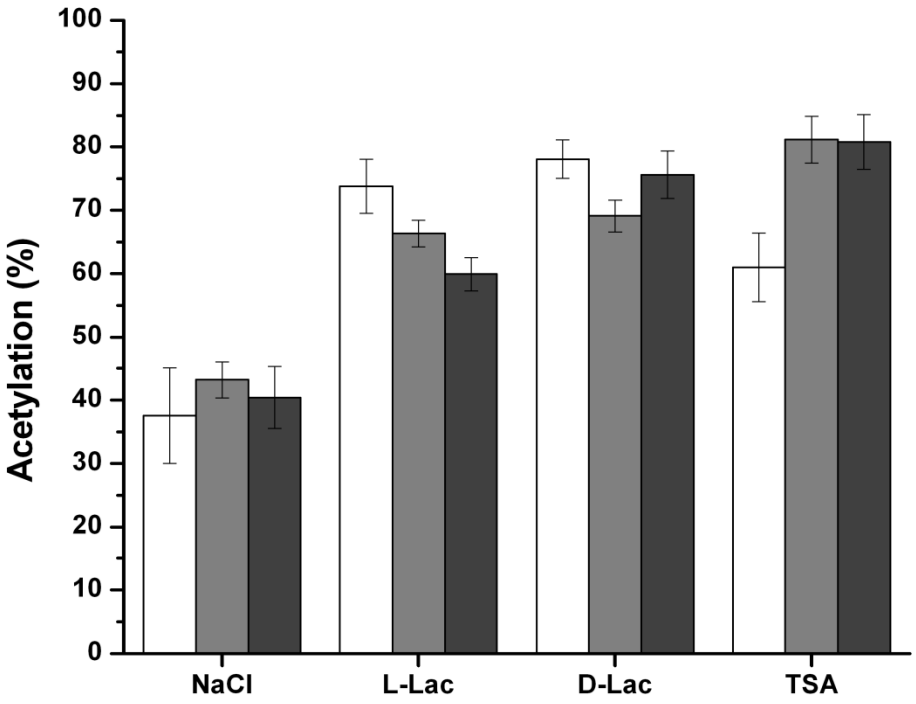

Figure 4.11: Graph showing the combined results of all treatments over the three time periods for cells supplemented with 10 units of HDAC 1; 30 minutes (white), 3 hours (light grey) and 6 hours (dark grey).

With the exception of the anomalous thirty minute TSA treatment, the following trends were observed in the data above; the treatments had their maximum inhibitory effect after thirty minutes. After three hours and six hours, acetylation after TSA treatment was high with little variation in value. At all treatment times D-lactate was a more potent inhibitor

of HDAC 1 activity than L-lactate, however L-lactate did inhibit HDAC 1 activity when compared to the NaCl control treatment. The similarity and lack of variation in acetylation after NaCl treatment gave an indication of the base level of acetylation expected in untreated cells, which was visible in all LC-MS spectra as the base peak at ~ 1257 *m/z*. As shown through fragmentation work in the previous chapter, this peak represents H4 which carries an N-terminal acetylation and di-methylation at lysine 20.

4.3.2 HDAC 2 Treatment

The following data were acquired as described previously, with the exception that instead of supplementing cells with HDAC 1, HDAC 2 was used. Any difference in results could then be attributed to a change in the inhibitory effect of the treatments with respect to the de-acetylase enzyme chosen. Figure 4.12 below shows the results of the various treatments after thirty minutes exposure to each of the compounds after cells were supplemented with 5 units of HDAC 2.

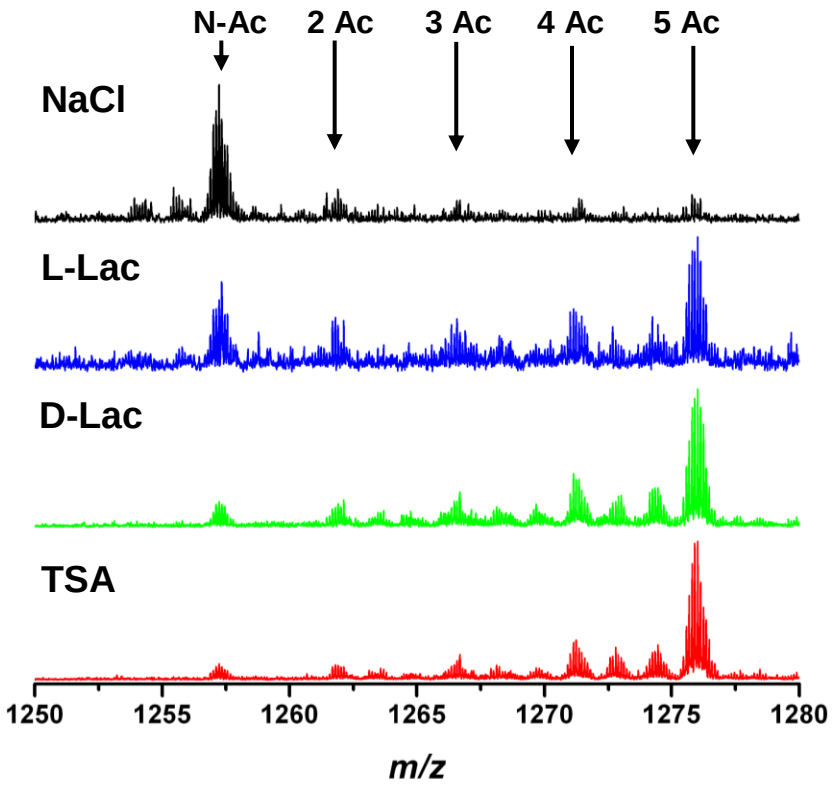

Figure 4.12: LC-MS spectra for the 9^+ charge state of histone H4 after 30 minutes treatment with L- or D-lactate (blue and green respectively) after cells were supplemented with 5 units of HDAC 2. NaCl (black) and TSA (red) were included as negative and positive controls respectively. The di-methylated peaks are labelled and numbered in order of acetylation state where (N-Ac) means N-terminally acetylated and (2 Ac) means two acetyl groups are present etc.

NaCl treatment had little effect in acetylation level with a value of 31%. L- and D-lactate, and TSA treatment resulted in an increase in acetylation of H4 with values of 60%, 80% and 82% respectively. The standard deviations from these values were all consistently low with a maximum value of 4% (NaCl). These results compare well with the data from the earlier experiments using supplementation with 5 units of HDAC 1, which gave similar results after thirty minutes. Figure 4.13 below shows the levels of acetylation after three hours treatment with each of the compounds.

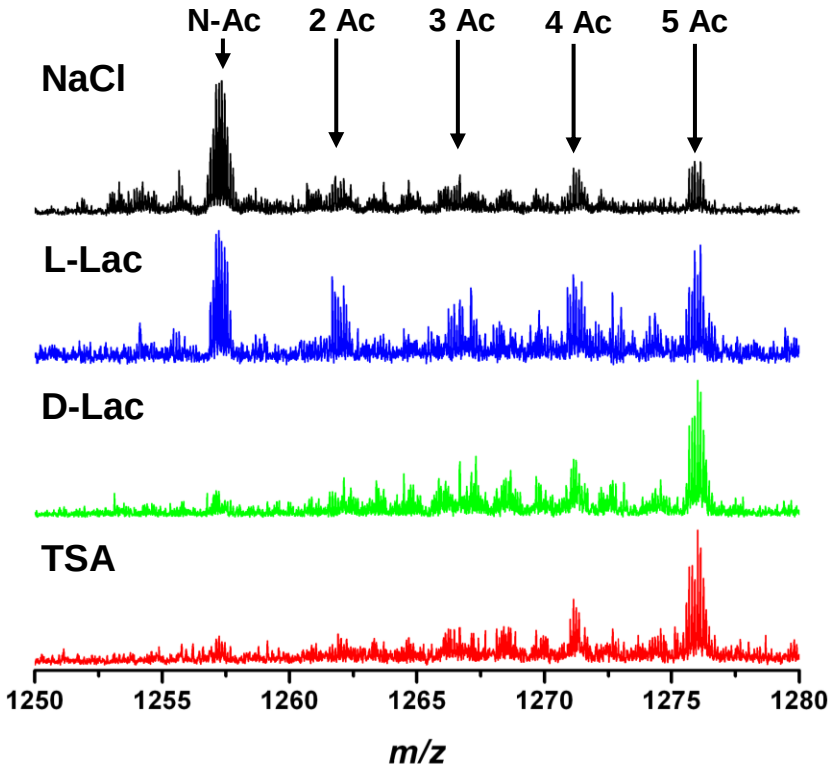

Figure 4.13: LC-MS spectra for the 9^{+} charge state of histone H4 after 3 hours treatment with L- or D-lactate (blue and green respectively) after cells were supplemented with 5 units of HDAC 2. NaCl (black) and TSA (red) were included as negative and positive controls respectively. The di-methylated peaks are labelled and numbered in order of acetylation state where (N-Ac) means N-terminally acetylated and (2 Ac) means two acetyl groups are present etc.

After three hours a more significant change in acetylation was observed in all treatments, except for NaCl which rose slightly to 38%. Acetylation in the L-lactate treated cells dropped to 55%, with the D-lactate and TSA treatments also showing a drop in acetylation with values of 66% and 72% respectively. Standard deviations from these values were all low with a maximum of 5% (NaCl) giving good confidence in the results. Such a significant drop in acetylation was most likely a result of metabolism of each of the treatments. Figure 4.14 below displays the results of the six hour treatment with each of the compounds.

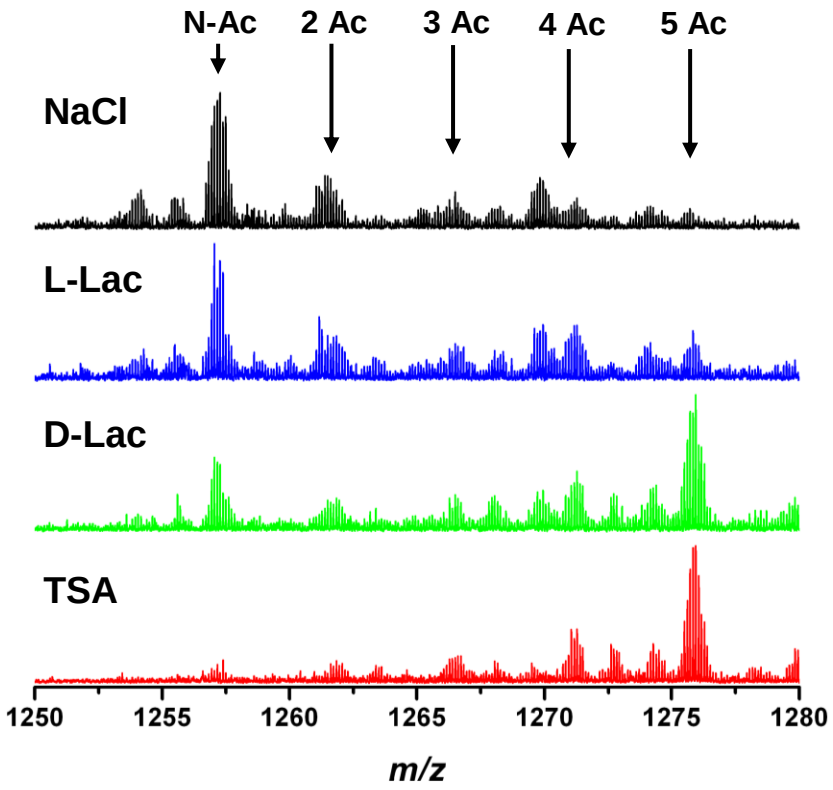

Figure 4.14: LC-MS spectra for the 9^+ charge state of histone H4 after 6 hours treatment with L- or D-lactate (blue and green respectively) after cells were supplemented with 5 units of HDAC 2. NaCl (black) and TSA (red) were included as negative and positive controls respectively. The di-methylated peaks are labelled and numbered in order of acetylation state where (N-Ac) means N-terminally acetylated and (2 Ac) means two acetyl groups are present etc.

After six hours treatment, acetylation in the NaCl treated cells remained stable at 39%. Acetylation in all other treatments dropped. Acetylation in the L-lactate treated cells fell to 45%, in the D-lactate treated cells this value was 59% and only a slight drop was observed in the TSA treated cells with a final value of 69%. There was greater variation in the standard deviation for these values in the six hour treatment, with the largest from the NaCl treated cells (8%). All others were below 6% giving good confidence in the results. The larger standard deviation in the NaCl treatment was most likely a result of the charge states chosen for the calculation used to quantify the level of acetylation. Figure 4.15 below summarises the results of the experiments following supplementation with 5 units of HDAC 2.

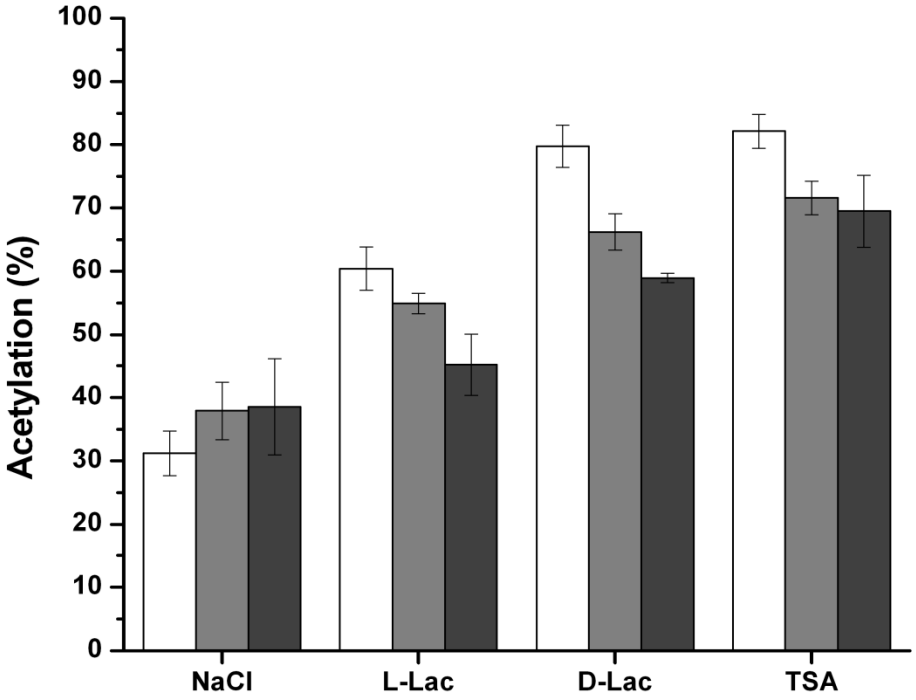

Figure 4.15: Graph showing the combined results of all treatments over the three time periods for cells supplemented with 5 units of HDAC 2; 30 minutes (white), 3 hours (light grey) and 6 hours (dark grey).

Comparing this data with that shown in Figure 4.7 (supplementation with 5 units of HDAC 1), the following observations can be made: L-lactate is a more potent inhibitor of HDAC 1 than HDAC 2. This was true for all three treatment times. At three hours and six hours the level of acetylation in the L-lactate treated cells continued to drop in the HDAC 2 treated cells, while it remained stable in the HDAC 1 treated cells. D-lactate and TSA are more potent inhibitors of the two HDAC enzymes used than L-lactate, with H4 hyper-acetylation evident at all time periods. NaCl has little effect as a histone de-acetylase inhibitor with acetylation values consistent across all time periods, which were slightly elevated when compared to the results presented in Chapter 3.

The following LC-MS spectra display the 9^{+} charge state of histone H4 from cells treated with the same four compounds, the only change being that cells were supplemented with 10 units of HDAC 2. Figure 4.16 below shows the results of the thirty minute treatment.

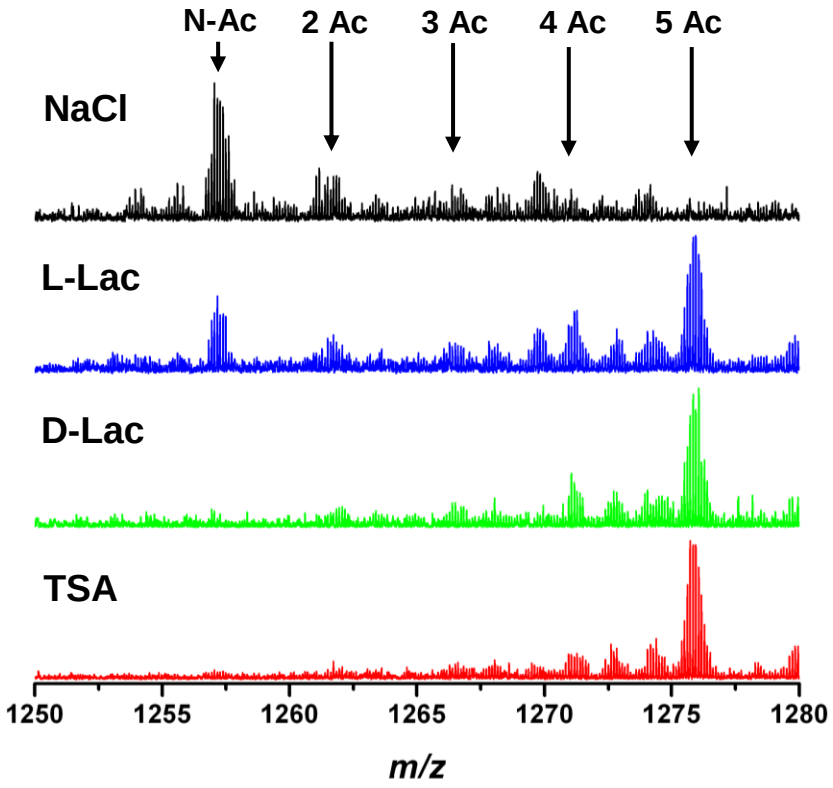

Figure 4.16: LC-MS spectra for the 9^+ charge state of histone H4 after 30 minutes treatment with L- or D-lactate (blue and green respectively) after cells were supplemented with 10 units of HDAC 2. NaCl (black) and TSA (red) were included as negative and positive controls respectively. The di-methylated peaks are labelled and numbered in order of acetylation state where (N-Ac) means N-terminally acetylated and (2 Ac) means two acetyl groups are present etc.

As with all previous HDAC treatments, the level of acetylation in the NaCl treated cells was low at 41%. Acetylation was elevated in the remaining three samples; 58% in the L-lactate treated cells, 64% in the D-lactate treated cells and 71% in the TSA treated cells. The standard deviations for these values were higher than in other treatments, but also consistent with each other, with values in the range of 7% to 9%. This variation could potentially be accounted for by the charge states chosen for the calculation.

Figure 4.17 below shows the results of the three hour treatment with each of the compounds.

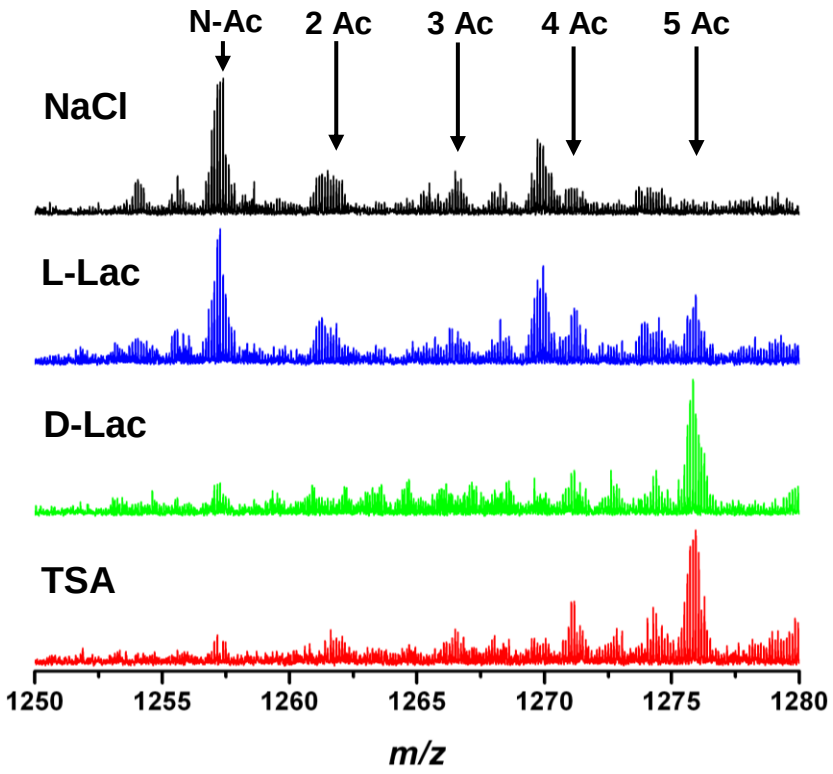

Figure 4.17: LC-MS spectra for the 9^+ charge state of histone H4 after 3 hours treatment with L- or D-lactate (blue and green respectively) after cells were supplemented with 10 units of HDAC 2. NaCl (black) and TSA (red) were included as negative and positive controls respectively. The di-methylated peaks are labelled and numbered in order of acetylation state where (N-Ac) means N-terminally acetylated and (2 Ac) means two acetyl groups are present etc.

Acetylation was low in the NaCl treated cells with a value of 42%. When compared to Figure 4.16 (30 minute treatment), acetylation was reduced in the other three samples. The L-lactate treated cells were acetylated to 49%, the D-lactate treated cells to 60% and the TSA treated cells to 61%. Standard deviations were low with a maximum of 7% (TSA treatment) giving good confidence in the results.

The final samples investigated were as above, but given a six hour treatment with each of the compounds. The results are shown in Figure 4.18 below.

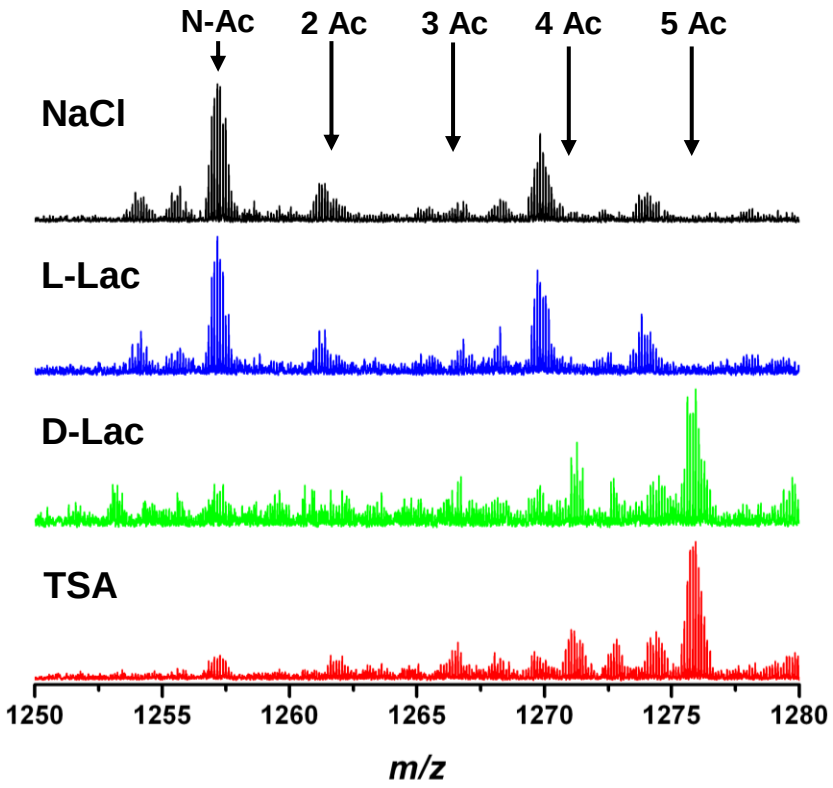

Figure 4.18: LC-MS spectra for the 9^+ charge state of histone H4 after 6 hours treatment with L- or D-lactate (blue and green respectively) after cells were supplemented with 10 units of HDAC 2. NaCl (black) and TSA (red) were included as negative and positive controls respectively. The di-methylated peaks are labelled and numbered in order of acetylation state where (N-Ac) means N-terminally acetylated and (2 Ac) means two acetyl groups are present etc.

With the exception of the TSA treated cells, acetylation fell in each of the samples after six hours treatment. Acetylation dropped slightly to 38% in the NaCl treated cells, this value fell by a greater amount in cells treated with L-lactate to 43% and acetylation again dropped slightly in the D-lactate treated cells to 58%. In the TSA treated cells, acetylation rose to 65%, an increase of over 4%. Standard deviations from these values ranged from 5% (L-lactate) to 8% (NaCl). This variation could be a result of the charge states chosen for the calculation performed.

Figure 4.19 below summarises the results of these experiments following supplementation with 10 units of HDAC 2.

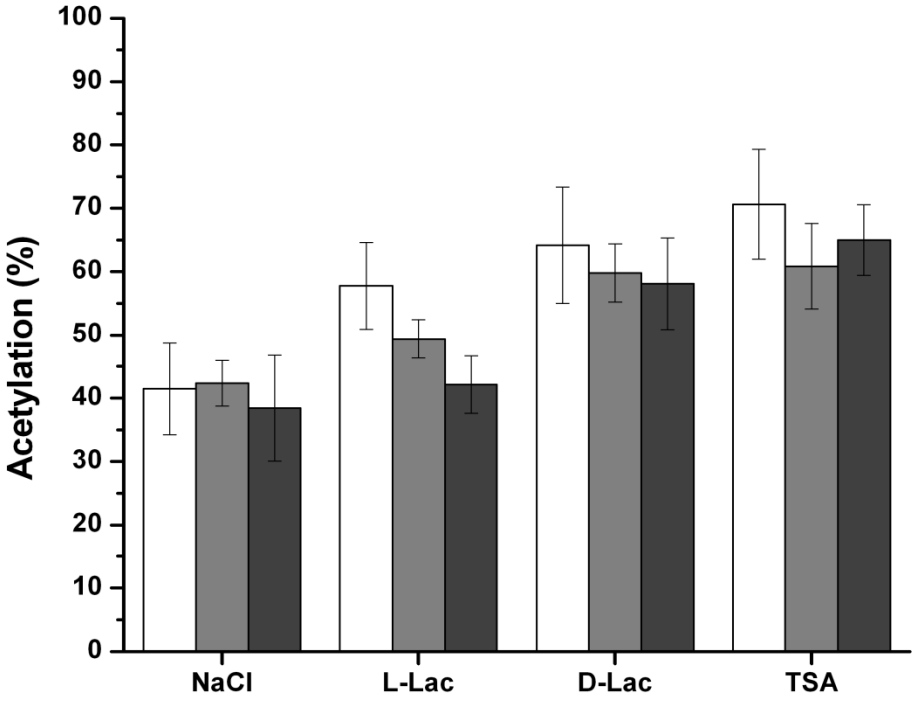

Figure 4.19: Graph showing the combined results of all treatments over the three time periods for cells supplemented with 10 units of HDAC 2; 30 minutes (white), 3 hours (light grey) and 6 hours (dark grey).

The following observations can be made regarding this data. Since there is little change in the acetylation level of NaCl treated cells across all time periods, NaCl served as a good negative control, providing confidence in the changes in acetylation seen in the lactate treated samples. The change in acetylation due to the addition of L-lactate is consistent with the hypothesis that L-lactate is an inhibitor of histone de-acetylase 2, and that its inhibitory effect reached its maximum shortly after administration to the cells. This inhibitory effect then decreases with prolonged treatment time. D-lactate is also an inhibitor of histone de-acetylase 2 activity, and similar to L-lactate its maximum effect is seen shortly after administration. In contrast to L-lactate, the inhibitory effect of D-lactate decreases to a lesser extent with increasing time leading to a more prolonged state

of hyper-acetylation. TSA, as expected, is an effective inhibitor of histone de-acetylase 2 activity with a maximum effect seen after thirty minutes treatment. Similar to D-lactate, the inhibitory effect of TSA decreased by a lesser extent with increasing time.

4.4 Conclusions

The combined results from these experiments demonstrate that when supplemented with either HDAC 1 or HDAC 2, the base level of acetylation in HCT-116 cells is roughly 37%. This is evident in all NaCl treated cells over all time periods tested. NaCl is not known to inhibit histone de-acetylase activity giving confidence that this is the base acetylation level. However, it is noteworthy that this base level of acetylation is higher than seen in completely untreated cells (data presented in Section 3.3.1).

L-lactate is observed to be an inhibitor of both HDAC 1 and HDAC 2 activity. The effect of L-lactate reaches its maximum soon after administration, and decreases thereafter. L-lactate is a more potent inhibitor of HDAC 1 than HDAC 2, with lower levels of acetylation observed when cells are supplemented with HDAC 1 compared to HDAC 2.

D-lactate is also observed to be an inhibitor of HDAC 1 and HDAC 2 activity. The inhibitory effect of D-lactate is greater than that of L-lactate. This is observed to be the case for cells supplemented with either HDAC 1 or HDAC 2. The inhibitory effect also diminishes over time, similar to L-lactate treated cells.

To test that a statistical difference exists in the data presented above, analysis of variance (ANOVA) was performed on the results used to generate Figures 4.7, 4.11, 4.15 and 4.19 (the graphs which summarise the data presented in the spectra). ANOVA was performed on each of the treatments against the mean acetylation value (with the standard deviation). In each case tested the p- value generated was 0.001 or lower indicating a difference in the results of each of the treatments. When ANOVA was performed by comparing treatment time with acetylation level the p- value generated was $p = 0.525$, indicating that no significant changes in acetylation were due to changes in treatment time.

The data presented above demonstrate that lactic acid is able to affect the acetylation profile of histone H4. The established links between histone post-translational modification and gene expression lend credence to the hypothesis that histone PTMs could potentially account for the increase in expression of genes associated with glycolysis[176-178]. This is of interest when considering the Warburg effect and its links to the metabolism of cancerous cells. Malignant cells are known to generate most of their energy through glycolysis, and fail to utilise the citric acid cycle and oxidative phosphorylation. It has been hypothesised that this is a result of malignant cells shutting down mitochondria (where the citric acid cycle takes place) through various mechanisms including a lack of essential intermediates[179]. The increase in glycolysis and resulting increase in pyruvic acid would lead to an increase in intra-cellular lactic acid concentration. The data presented in this chapter has demonstrated that lactate has an inhibitory effect on histone de-acetylase enzymes; this inhibitory effect is not likely due to any pH changes associated with increased lactic acid concentration since the data show that D-lactate (which would cause a similar change in pH to L-lactate) is a more potent inhibitor of histone de-acetylase enzymes than L-lactate. In the examples presented above the inhibitory effect is temporary since the cell line chosen is not known to have reduced mitochondrial activity. As such, mechanisms exist for the metabolism of the supplemented L-lactate which resulted in a brief increase in acetylated forms of histone H4. In vivo , where mitochondrial function may be impaired the effect would last longer. In contrast, D-lactate is not easily metabolised by the cells which is visible as the longer lasting effects of the D-lactate treatment.

This inhibition would manifest as an increase in acetylated forms of histone H4 with the associated DNA more accessible to transcription factors. The steps described above suggest a self perpetuating cycle where the altered histone PTM profile increases gene expression and cell proliferation. This hypothesis is in agreement with the data presented here which shows that lactic acid can inhibit histone de-acetylase enzymes, leading to a greater abundance of hyper-acetylated H4, linked to an increase in gene expression[180].

4.5 Future work

Future work could expand on this study, beginning with testing the inhibitory effect of L-lactate on other histone de-acetylase enzymes. Of the 18 known histone de-acetylases, HDAC 1 and HDAC 2 are hydrolase enzymes which do not depend on the presence of NAD^+/NADH to exert their action[137]. A similar experimental procedure to that described above could be performed, substituting other HDAC enzymes and determining if any changes to acetylation occur. This would help determine how broad the inhibitory effect of L-lactate is across the de-acetylase enzymes.

Chapter 5

The Post-translational Modification of Histone H4 as a Result of Rett Syndrome

This chapter deals with the subject of histone post translational modifications when looking at a specific biological condition, in this case Rett syndrome. An introduction is given which contains a detailed description of Rett syndrome and provides a background to the work undertaken. The methods used are described, and the results of the work carried out are provided, along with a discussion of the results and possible directions of future work.

5.1 Introduction

Rett syndrome is a neurological condition affecting ~ 1 in 15,000 births[181]. The condition is more prevalent in females, a consequence of the many mutations known to cause the syndrome being located on the X chromosome[182]. Since females have two X chromosomes, a level of redundancy exists in the genetic information carried within each, resulting in the majority of sufferers being female in gender[183]. Mutations occurring in the X chromosome in males typically result in early termination of the fetus[184]. The condition was first described by Andreas Rett in 1966[185,186], a medical doctor who noted patterns in the behaviour of several of his patients. The characteristic behaviours he noted included reduced speech and motor abilities, coupled with hand-wringing movements, now a well recognized symptom of the condition[187]. Interestingly, he found little correlation between those who suffered from the condition and a genetic family link, suggesting that transmission of the condition did not follow classic Mendelian laws. It is now known that most cases of Rett syndrome occur sporadically, making prediction of the occurrence of cases extremely difficult[188]. To date there is no screening method for Rett syndrome, so potential sufferers can not be identified early. Diagnosis is made through observation of symptoms, followed by monitoring of suspected cases for several

months (typically six to twelve months) before cases are confirmed[189]. While there is no suitable early detection method, there is some level of treatment available to patients with Rett syndrome[190].

In 1999 the cause of Rett syndrome was identified; a mutation localized to a specific gene on the X chromosome[184]. The gene encoded a protein which was found to bind methylated DNA[191]. Methyl DNA binding proteins are divided into four groups; the mutation specific to Rett syndrome effecting methyl CpG binding protein-2 (MeCP2)[192]. MeCP2 has been ascribed several molecular functions, one of which is a role in remodelling chromatin complexes. However, the mechanisms underlying this function are not well understood. One theory suggests that the specificity of MeCP2 for binding methylated DNA allows it to serve as a marker for other chromatin remodelling enzymes[193-195]. Studies on genetically engineered mice have provided important clues to the function of MeCP2. Deletion of the MeCP2 gene has resulted in a Rett-like condition, while tissue wide neuronal expression of MeCP2 can resurrect some of the lost functions[196,197]. These studies strengthen the belief that Rett syndrome is a neural condition. However, there is still debate over whether it is a neuro-degenerative or a neuro-developmental disorder[198]. While many who suffer from the illness do not carry deletions of the MeCP2 gene, numerous studies have shown that mutations of the gene can result in Rett syndrome.

The MeCP2 protein contains three major domains which are responsible for its activity; a methyl binding domain, a transcriptional repression domain and a C-terminal domain[199,200]. The functions of the C-terminal region are not well understood, but mapping of MeCP2 mutations has shown that the majority occur at or close to either of the first domains. Figure 5.1 below displays the three domains along with the locations of the most commonly seen mutations and their frequency.

While MeCP2 is thought to have several functions, it is of interest from an epigenetic perspective as it serves as a bridge between the two main avenues of epigenetic control; DNA methylation and chromatin structure[201]. Previous studies have attempted to identify

if alteration of MeCP2 (whether by deletion or mutation) can result in changes to histone post-translational modification. While changes were found, results were often in

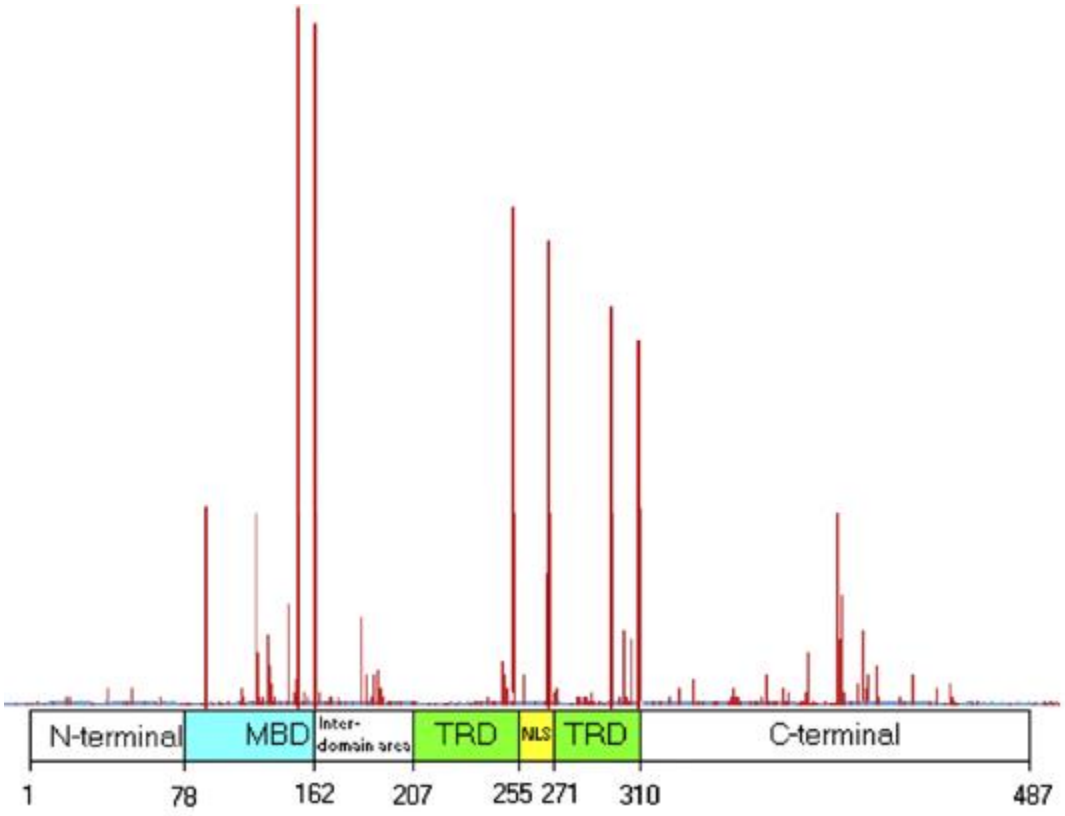

Figure 5.1: MeCP2 mutations known to cause Rett syndrome and their locations on the MeCP2 gene[202].

contradiction to other studies leading to some confusion over how MeCP2 can affect histone PTMs[203-206]. With this as a starting point, the aims of the work described in this chapter were as follows:

to identify if MeCP2 deletion can result in changes to the PTM profile of histone H4;
to characterise any observed changes in histone H4 PTM profile, and to investigate the possibility of using an altered PTM profile as a diagnostic marker for MeCP2 mutation.

5.2 Methods

5.2.1 Tissue Sampling and Protein Extraction

The experiments described in this chapter did not require cell culture as a source of histone proteins; instead the protein extraction was carried out on primary animal tissue, specifically whole mouse brain. The differences in procedure for histone extraction from cell cultures compared to using a tissue composed of multiple cell types presented several challenges which were addressed by modifying the acid extraction technique as described below. The pooled mouse brain samples were supplied by the research group of professor Adrian Bird of the Wellcome Trust Centre for Cell Biology (at the University of Edinburgh) and were the combined histone extracts of six mouse brains in each sample, with mice varying in age from six weeks to eighteen weeks. The single mouse brains used in the latter part of this work were donated by the Bird research group, however the histone extraction procedure was performed at the Scottish Instrumentation and Resource Centre for Advanced Measurement Science. All animals were reared and sacrificed at the University of Edinburgh

Whole mouse brain was kept frozen until homogenization. At the start of the procedure the brains were allowed to defrost completely at room temperature before homogenization in specially prepared buffer (PBS with 0.2 M H_2SO_4 in H_2O, 100 % TCA with 50 mM HCl in H_2O and added spermidine). Brains were placed in individual test tubes with 3 ml buffer and homogenized on a Potter S homogenizer at 1100 rpm for 7 strokes. The homogenate was transferred onto a 1 ml cushion of buffer in an SW-60 centrifuge tube and was then ultra-centrifuged at 27,600 rpm for 40 minutes at 4 °C. A spatula was used to remove the fatty plug and the lysate was decanted, the tubes were then inverted and allowed to drip dry on ice. The nuclei were resuspended in 1 ml PBS with sodium butyrate and centrifuged at 400 *g* for 5 minutes at 4 °C. The supernatant was removed, the pellet washed in 0.5 ml PBS with sodium butyrate and centrifuged again at 400 *g* for 5 minutes at 4 °C. The supernatant was again removed and the pellet resuspended in 1 ml of 0.2 M H_2SO_4 and left to rotate for 1 hour at 4 °C in an Eppendorf

tube. After incubation with H_2SO_4, the Eppendorf tubes were centrifuged at 13,000 rpm for 30 minutes at 4°C. The supernatant was transferred to a clean eppendorf and TCA was added to 20 % volume (250 µl), this was mixed and incubated on ice for 30 minutes. After incubation the Eppendorf tubes were centrifuged at 13,000 rpm for 30 minutes at 4°C. The supernatant was discarded and the pellet washed with 1 ml 50 mM HCl in acetone for 90 minutes and rotated at 4 °C. They were then centrifuged at 13,000 rpm for 20 minutes at 4°C, the supernatant discarded and the pellet washed in pure acetone overnight at 4°C.

The following day the Eppendorf tubes were spun at 13,000 rpm for 30 minutes at 4°C, the supernatant discarded and pellets allowed to air dry at room temperature. Pellets were then resuspended in 100 µl H_2O ready for LC-MS analysis.

5.2.2 Liquid Chromatography and Mass Spectrometry

LC-MS was performed as described previously under the following conditions. A Vydac C_{18} column was used for sample separation, operated at 30°C with a flow rate of 50 µl min^{-1} using the following gradient. Solvent A was 98% H_2O with 0.03% TFA and 2% acetone, and solvent B was 80% acetone and 20% H_2O with 0.03% TFA. 10 µl of sample was loaded onto the column for each run and separated over a 37 minute linear gradient. The gradient rose to 44% B over 5minutes, from 5 to 22 minutes to 49% B, and held at 49% for a further 5 minutes. At 27 minutes Buffer B was increased to 100% and held for 5 minutes, before Buffer A was increased to 100% and held for 5 minutes. Histone fractions were collected manually from each run and stored on ice for subsequent fragmentation work.

CID and ECD were performed on each fraction collected. For fragmentation work, samples were directly infused into the mass spectrometer using a Tri-Versa Nanomate. Precursor ions were isolated and ion accumulation times for CID were 1 second. The collision voltage was set to ~ 18 V and each spectrum was the sum of 500 mass analyses. ECD was performed with extended ion accumulation times, typically 20 seconds. The dispenser cathode was set to a current of 1.7 nA and the ECD pulse length was set to

~0.06 seconds. Similar to the CID experiments, each spectrum was the sum of 500 mass analyses whenever possible. The instrument used for mass analysis was a Bruker Daltonics solariX FT-ICR equipped with a 12 Tesla superconducting magnet.

5.2.3 Data Analysis

Data were acquired in broadband mode with a mass range of 500-3000 *m/z*, and data was analyzed using DataAnalysis software (Bruker Daltonics), before being exported and plotted in Microcal Origin (v 6.0). Fragmentation spectra were analysed by searching fragment ion lists online using the ProSight PTM database.

5.3 Results

5.3.1 Top-Down Mass Spectrometry

5.3.1.1 Pooled Mouse Brain Samples

The initial study of the effects of MeCP2 deletion on histone PTM profile were conducted on pooled mouse brain samples. Figure 5.2 below displays the mass spectra acquired for the 15^+ charge state of histone H4 for both wild type (WT) and MeCP2 knockout (KO).

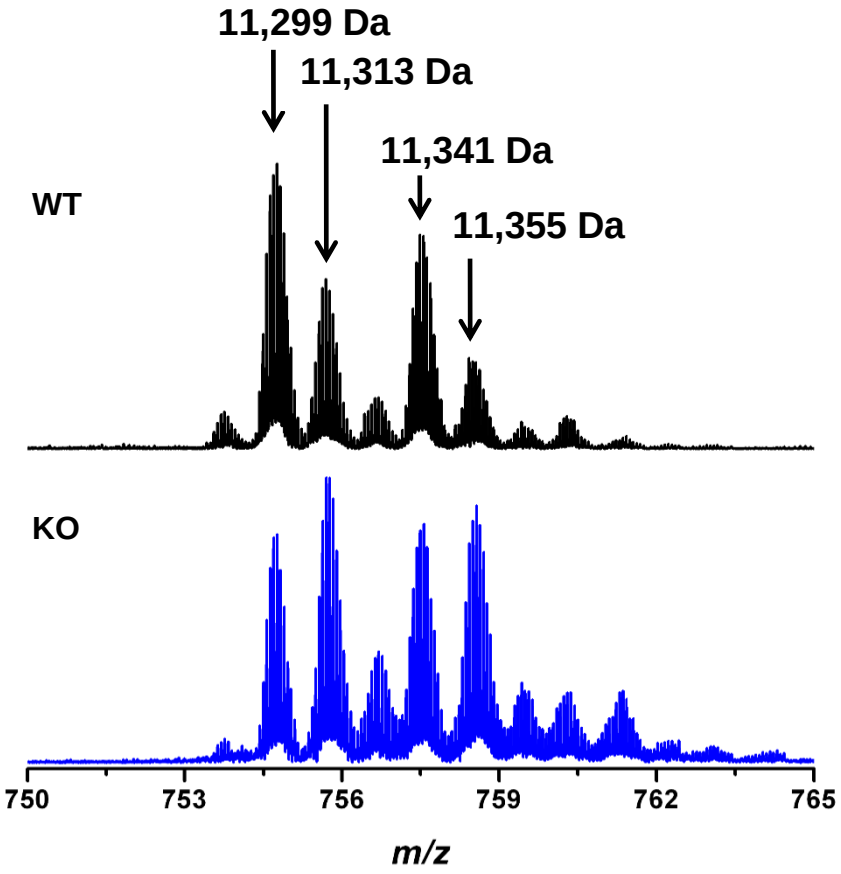

Figure 5.2: Mass spectra for the 15^+ charge state of histone H4 from WT (black) and MeCP2 knockout (blue) samples. The mono-isotopic intact masses of the four most abundant peaks are given.

The mass spectra display a clear difference in PTM profile between the two samples. To investigate this difference further, the various species were isolated and fragmented by

CID and ECD. The results of the fragmentation of the WT sample are shown in the following figures. Figure 5.3 below shows the mass spectrum for the 15^{+} charge state of histone H4 from the wild type sample, along with the ion species selected for fragmentation.

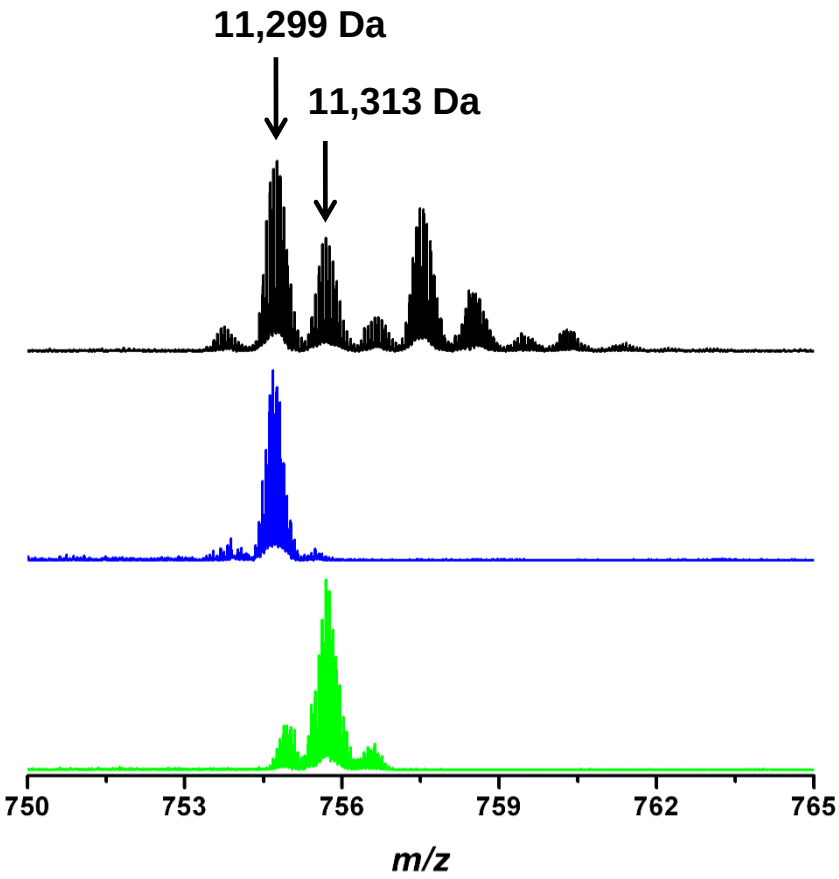

Figure 5.3: Mass spectrum for the 15^{+} charge state of histone H4 from pooled brain samples of wild type mice, along with ion species (indicated in blue and green) selected for fragmentation.

CID and ECD fragmentation was performed on both ion species. The CID fragmentation spectrum of the ion at 754 *m/z* (blue) is shown in Figure 5.4 below:

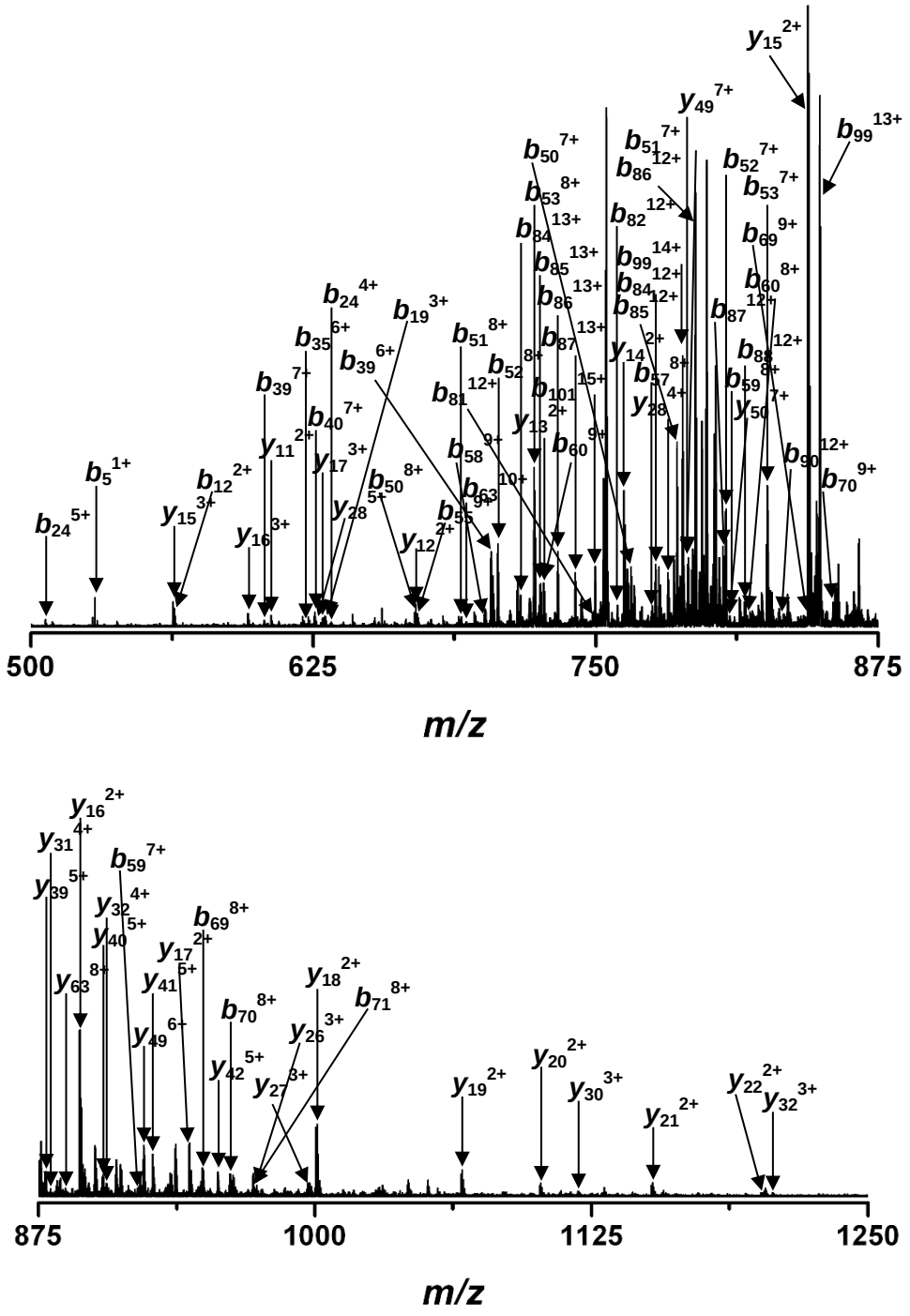

Figure 5.4: CID mass spectrum of ion at 754 *m/z* from WT pooled mouse brain samples. A complete list of the assigned fragment ions is attached as Appendix A22.

The ECD fragmentation spectrum for this ion at 754 *m/z* is shown in Figure 5.5 below, along with a combined fragment ion map for this species of histone H4 generated from both the CID and ECD data (Figure 5.6).

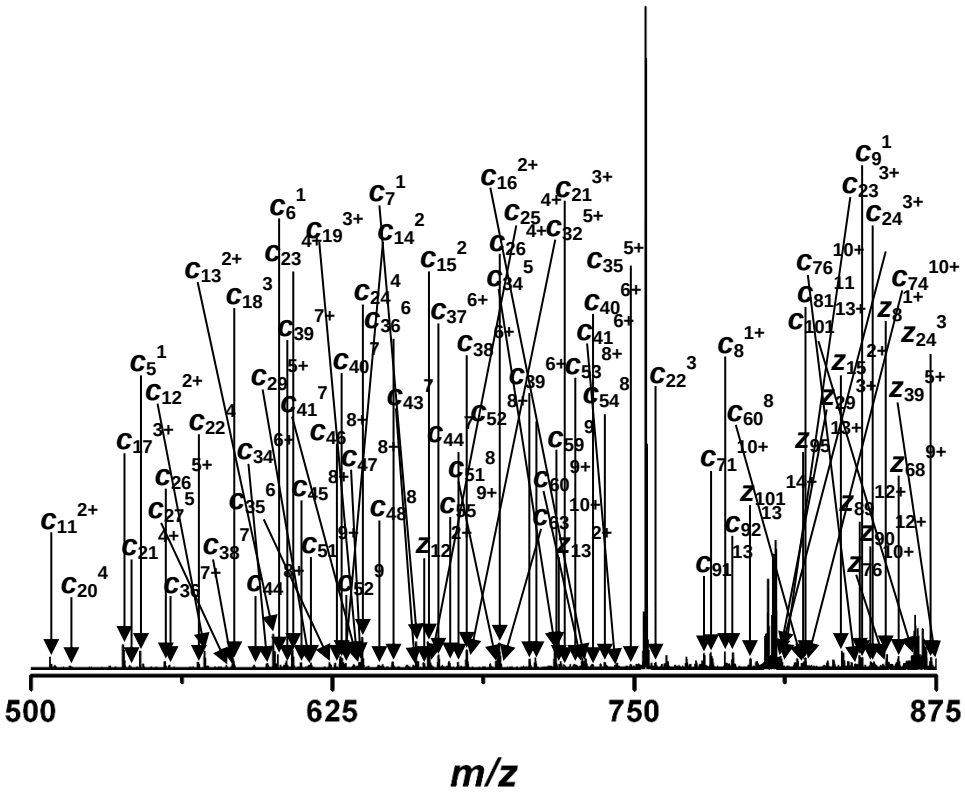

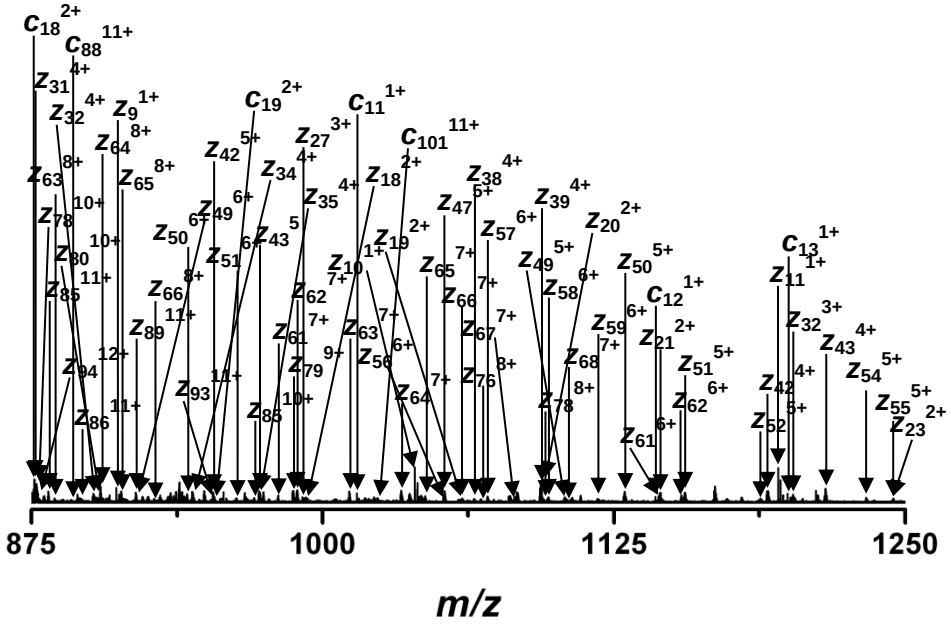

Figure 5.5: ECD fragmentation spectrum of ion at 754 *m/z*. A complete list of the assigned fragment ions is attached as Appendix A23.

Figure 5.6: Fragment ion map of combined CID and ECD spectra for the ion at 754 *m/z*.

As can be seen from the CID and ECD spectra, extensive fragmentation was achieved on the ion at 754 *m/z*. CID and ECD fragmentation both confirmed that this ion corresponded to histone H4 carrying an N-terminal acetylation and di-methylation at lysine 20.

The most pronounced difference in ion abundances between the WT and MeCP2 knockout samples was visible for the next ion species investigated, at 756 *m/z* (green). Figure 5.7 below displays the CID spectrum obtained from fragmentation of this ion.

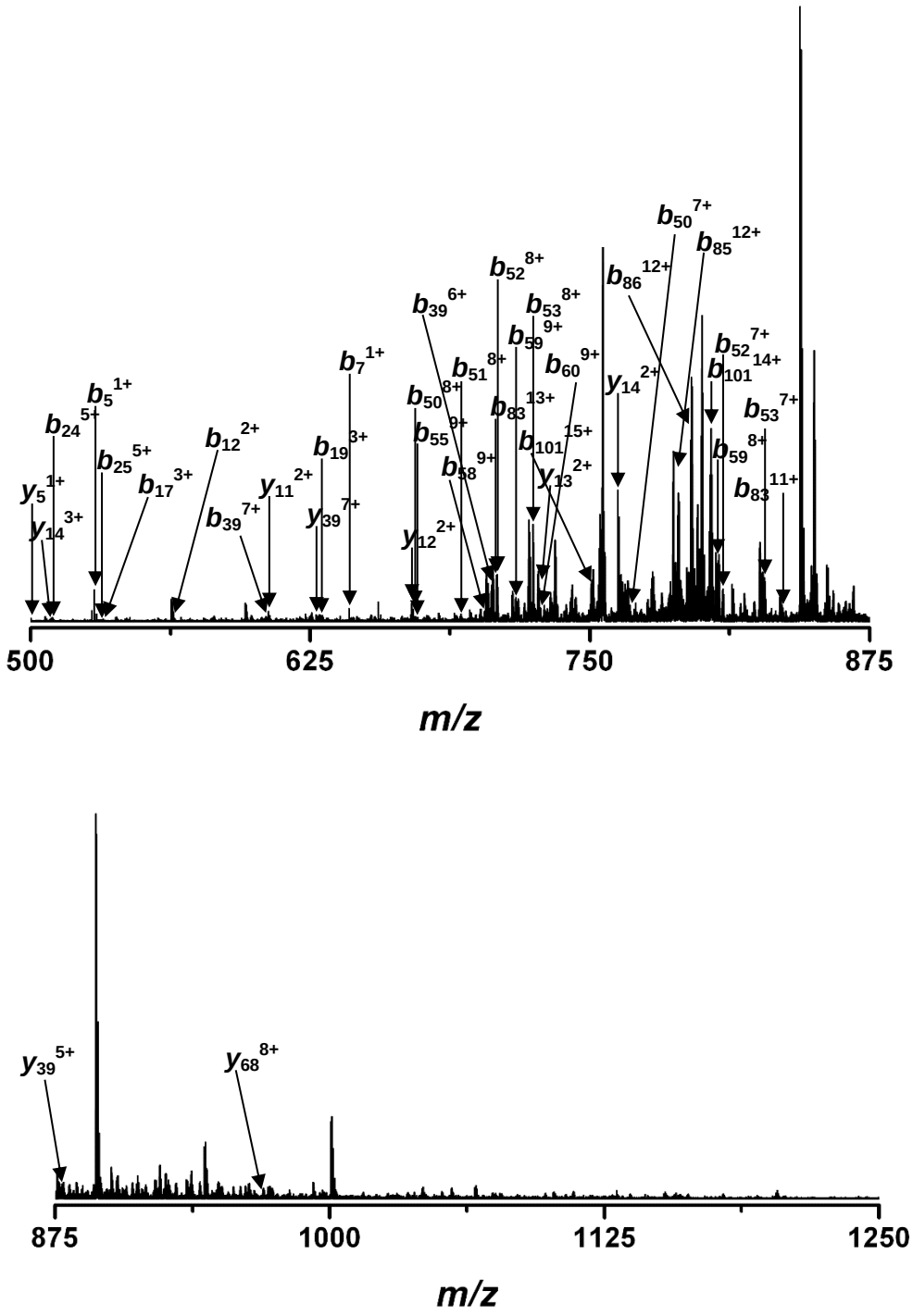

Figure 5.7: CID fragmentation spectrum of ion at 756 *m/z* from pooled WT brain sample. A complete list of the assigned fragment ions is attached as Appendix A24.

Figure 5.8 below shows the ECD spectrum for this ion at 756 *m/z* along with a combined fragment ion map for this species of histone H4 generated from both the CID and ECD data (Figure 5.9).

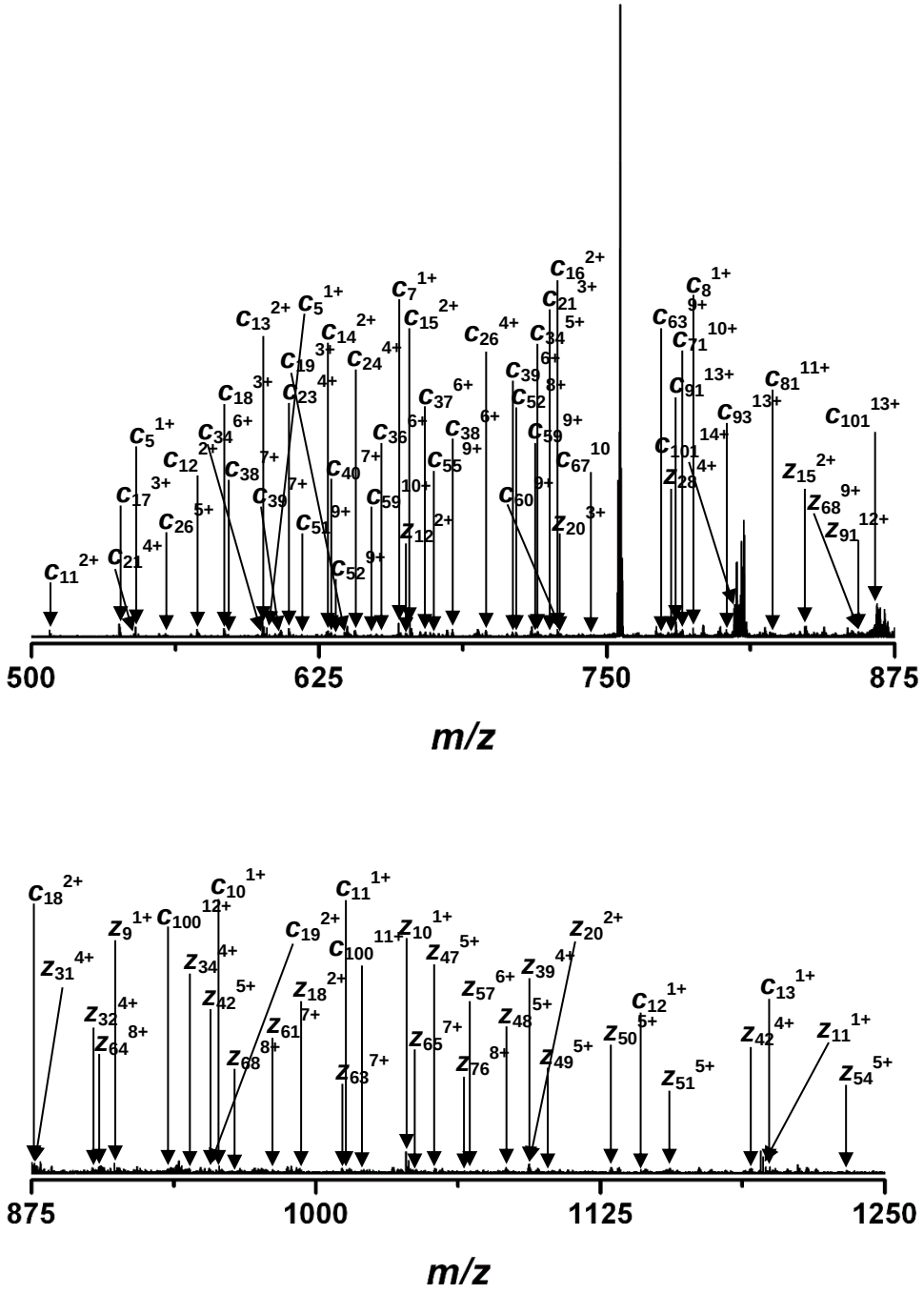

Figure 5.8: ECD spectrum of ion at 756 *m/z* from pooled WT mouse brain samples. A complete list of the assigned fragment ions is attached as Appendix A25.

Figure 5.9: Fragment ion map of combined CID and ECD spectra of the ion at 756 *m/z*.

The CID and ECD fragmentation data for this ion at 756 *m/z* confirmed that the observed increase in mass from that of the the ion at 754 *m/z* was due to tri-methylation at lysine 20. The level of fragmentation achieved, as displayed in the fragment ion map, provides strong evidence that this ion species at 756 *m/z* was not a heterogeneous mixture of modified forms of H4; i.e. H4 with the addition of a single methyl group at one of the N-terminal lysines, nor was it acetylated at lysine 20 which could have potentially accounted for the observed increase in mass.

Since there was a clear difference in the ion abundance for these ions at 754 *m/*z and 756 *m/*z between the wild type and MeCP2 knockout samples (see Figure 5.2), these ions were selected for isolation and fragmentation in the MeCP2 knockout samples. Figure 5.10 below shows the mass spectrum for the 15^{+} charge state from the knockout samples along with the ions isolated for subsequent fragmentation.

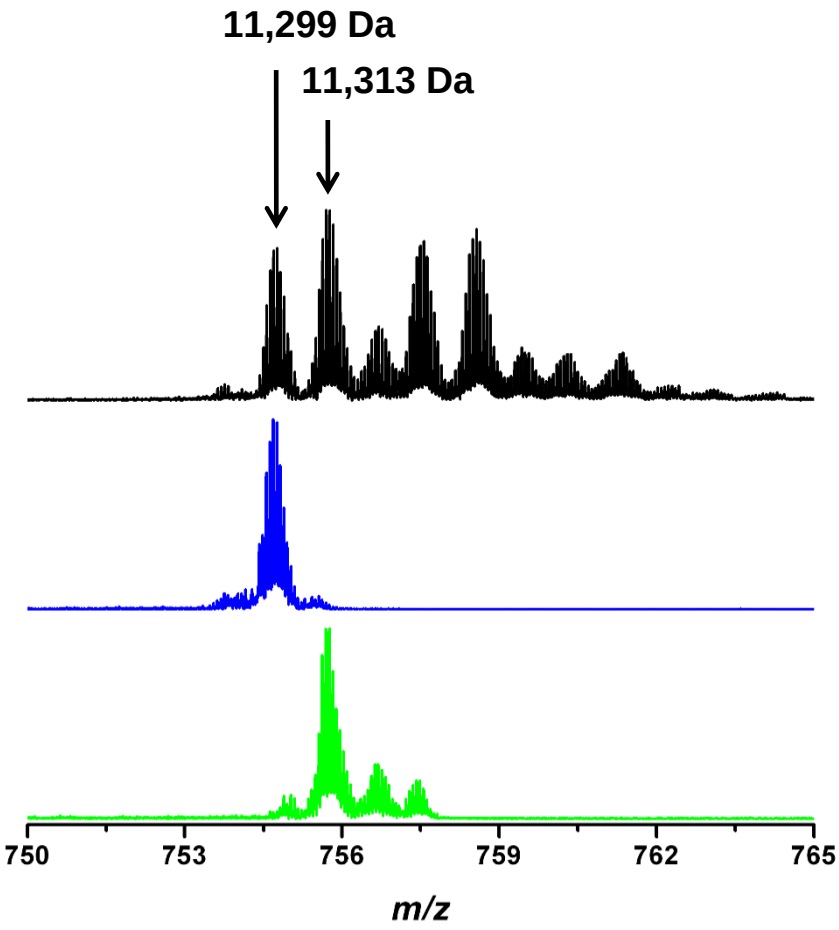

Figure 5.10: Mass spectrum for the 15^{+} charge state of histone H4 from pooled brain samples of MeCP2 knockout mice along with ion species (indicated in blue and green) isolated for fragmentation.

CID and ECD were performed on both ions selected; Figure 5.11 below shows the CID fragmentation spectrum obtained from the ion at 754 *m/z* (blue).

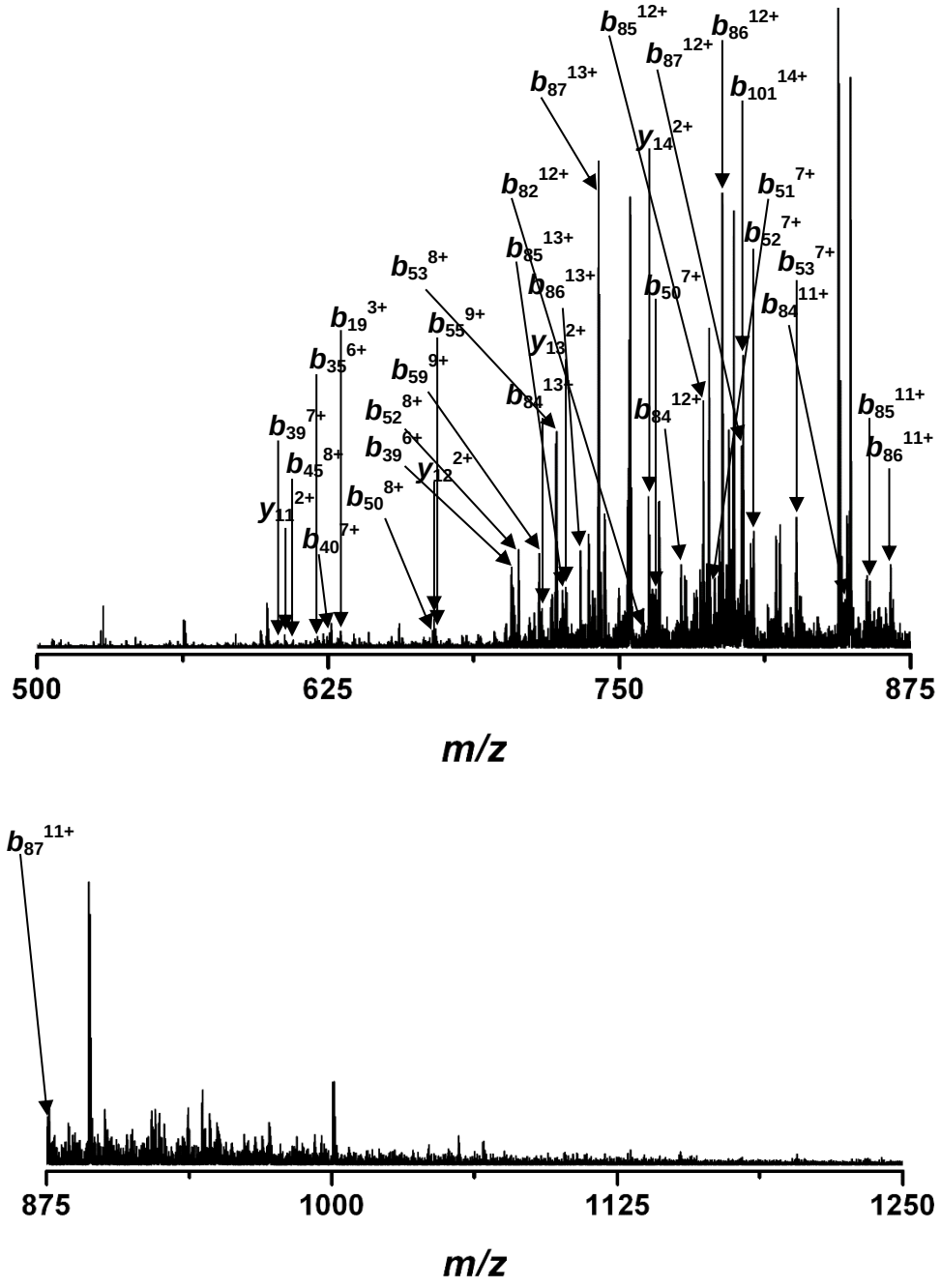

Figure 5.11: CID spectrum of ion at 754 *m/z* from pooled MeCP2 mouse brain samples. A complete list of the assigned fragment ions is attached as Appendix A26.

Figure 5.12 below shows the ECD spectrum acquired for the same ion, along with a combined fragment ion map for this species of histone H4 generated from both the CID and ECD data (Figure 5.13).

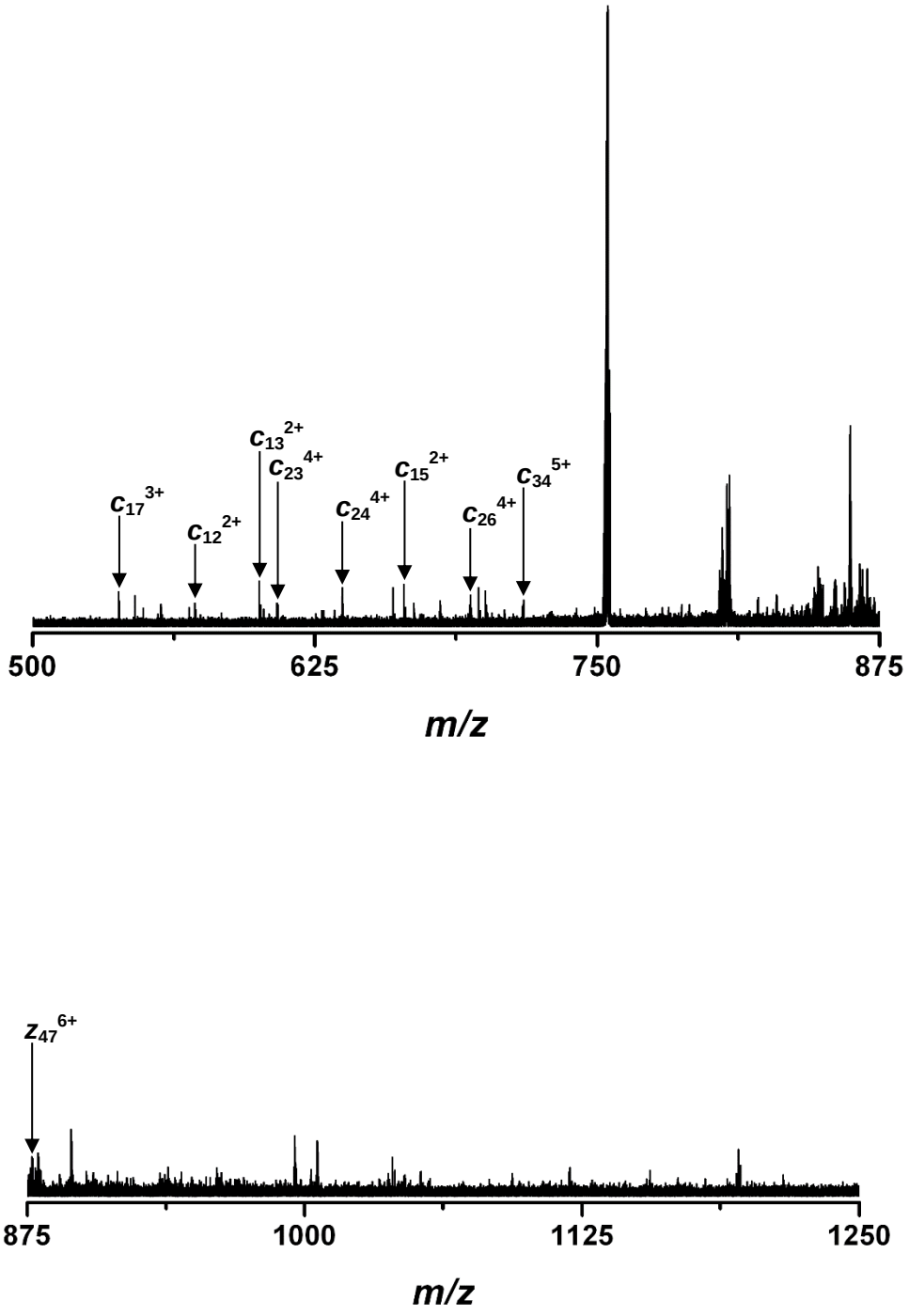

Figure 5.12: ECD spectrum of ion at 754 *m/z* from pooled MeCP2 knockout mouse brain samples. A complete list of the assigned fragment ions is attached as Appendix A27.

Figure 5.13: Fragment ion map of combined CID and ECD spectra for the ion at 754 *m/z*

While CID and ECD of the ion at 754 *m/z* from the MeCP2 knockout mice did not provide extensive sequence coverage, enough N-terminal fragments were generated to conclude that in the MeCP2 knockout mice, this ion species corresponded to the 'unmodified' form of histone H4, identical to that seen in the wild type mice.

CID and ECD experiments were then performed on the ion at 756 *m/z* (green) from the MeCP2 knockout mice. Figure 5.14, below, shows the CID spectrum acquired.

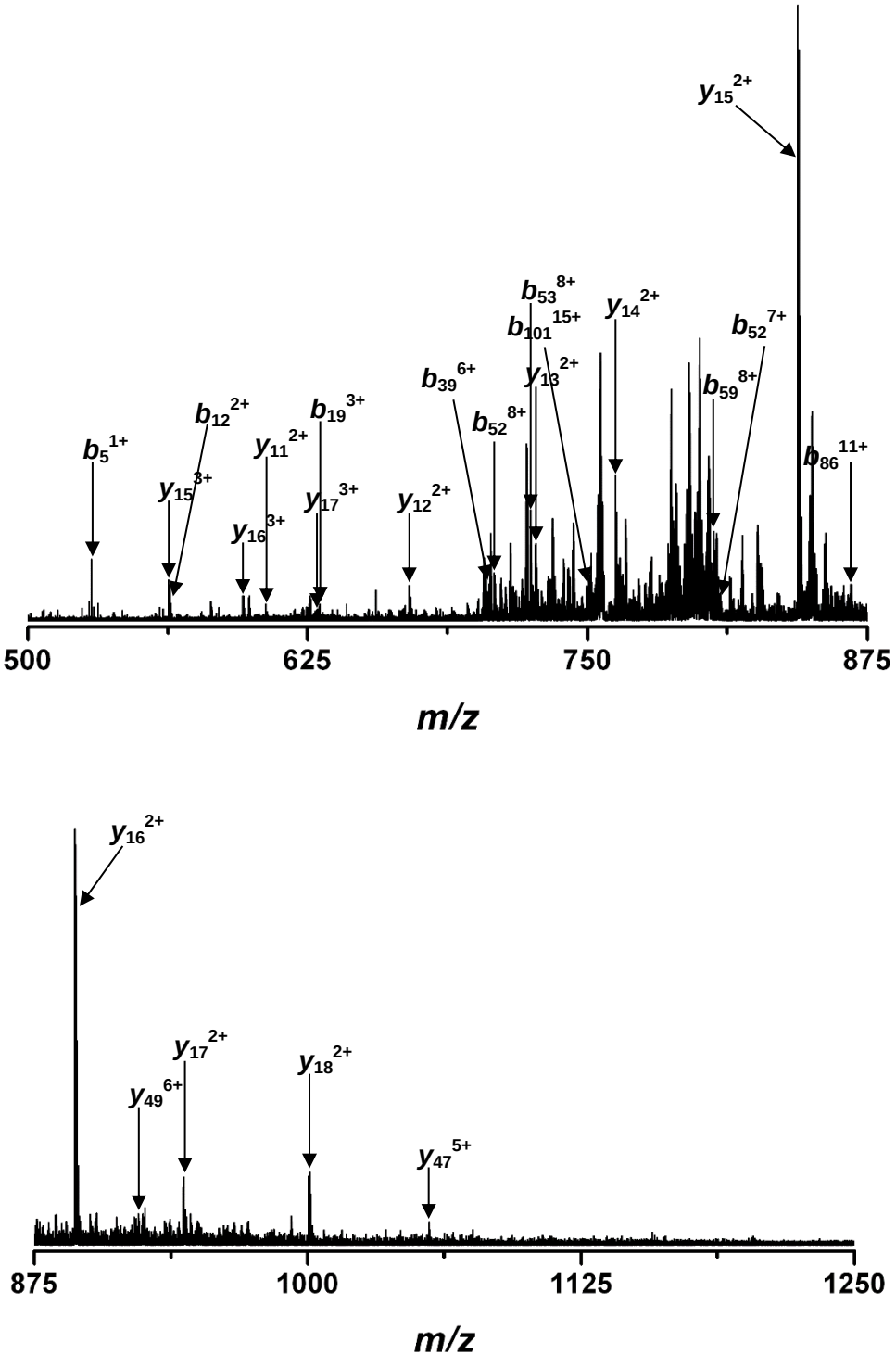

Figure 5.14: CID spectrum of ion at 756 *m/z* from pooled MeCP2 knockout mice brain samples. A complete list of the assigned fragment ions is attached as Appendix A28.

Figure 5.15 below shows the ECD spectrum obtained from the same ion along with a combined fragment ion map for this species of histone H4 generated from both the CID and ECD data (Figure 5.16).

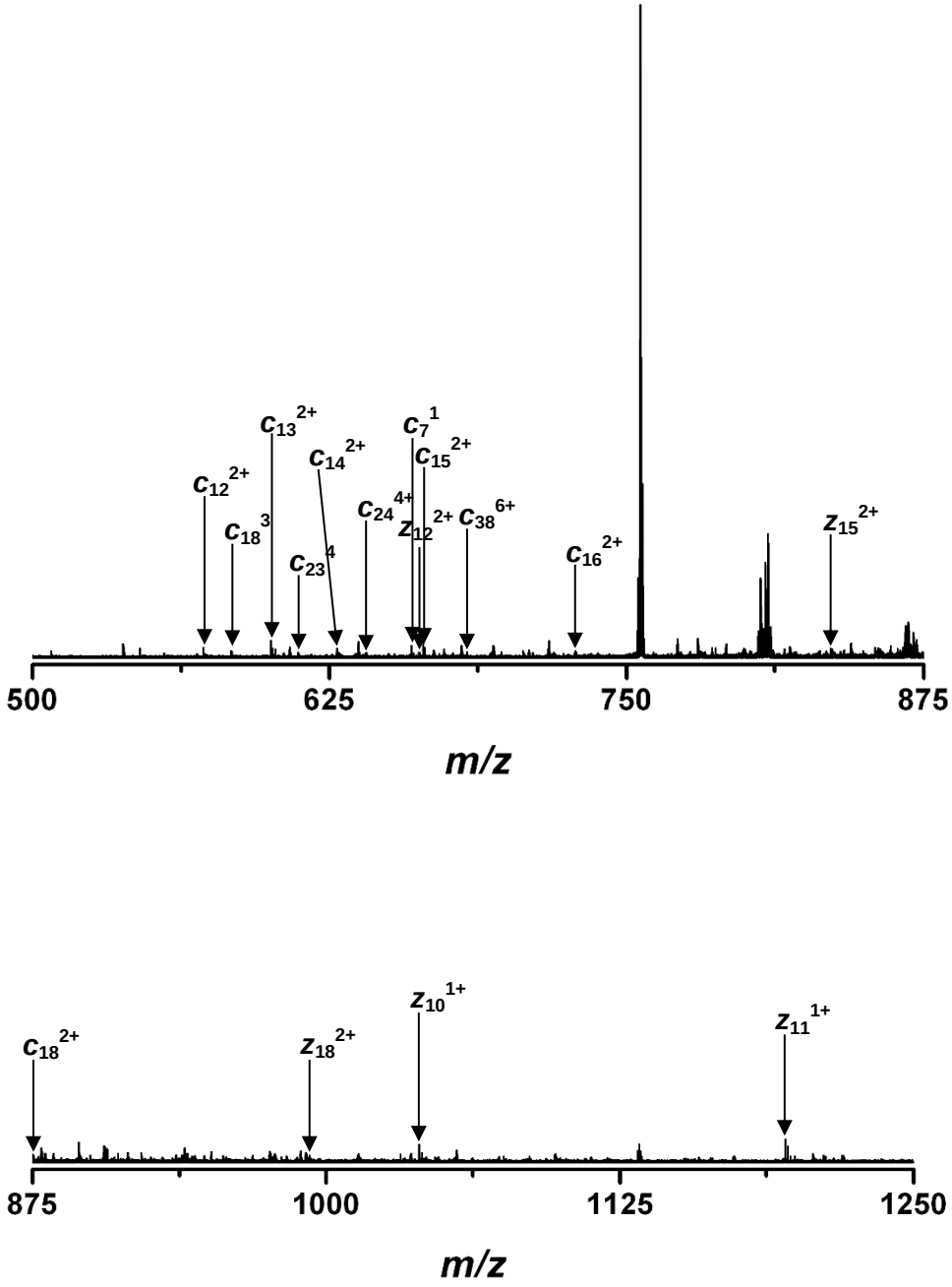

Figure 5.15: ECD spectrum of ion at 756 *m/z* from pooled MeCP2 knockout mice brain samples. A complete list of the assigned fragment ions is attached as Appendix A29.

Figure 5.16: Fragment ion map of combined CID and ECD spectra for the ion at 756 *m/z*.

Similar to the fragmentation experiments on the ion at 754 *m/z*, little fragmentation was achieved. However, enough N-terminal fragments were generated to conclude that the ion at 756 *m/z* from the MeCP2 knockout mice was the same as that from the wild type mice, i.e. that it was N-terminally acetylated histone H4 with a tri-methyl group at lysine 20.

5.3.1.2 Single Mouse Brain Samples

The results of the initial fragmentation studies on the pooled brain samples presented above suggested that MeCP2 mutation could possibly be linked to an altered PTM profile of histone H4, and more specifically correlated to an increase in tri-methylation at lysine 20. To investigate this possibility further, and to try and refine the hypothesis that MeCP2 mutation could result in altered histone post-translational modification, histone samples were harvested from the brains of single mice and analyzed individually. The symptoms of Rett syndrome are known to become apparent in affected mice weeks after birth, so two mice at an age of six weeks (one wild type and one MeCP2 knockout) were sacrificed for this investigation. While a potential obstacle to this study was the reduced amount of histone sample that could be extracted, the chance to eliminate any results that

were confounded by the mixed ages of the mice used in the pooled brain samples was considered an acceptable justification for the additional animal sacrifice.

Figure 5.17 below shows the mass spectrum for the 13^+ charge state of histone H4 from the wild type mouse brain sample, along with the ions chosen for isolation and fragmentation. CID and ECD experiments were performed on each ion species.

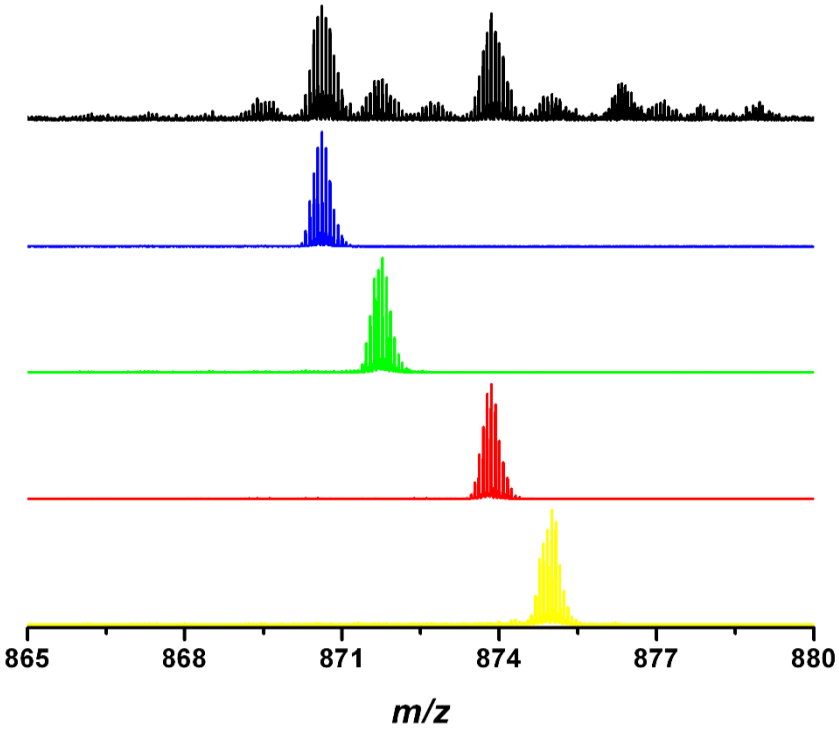

Figure 5.17: Mass spectrum for the 13^+ charge state of histone H4 from wild type whole mouse brain. The ion species chosen for subsequent fragmentation (indicated in blue, green, red and yellow) are shown in the layers underneath.

The mass spectrum for the 13^+ charge state of histone H4 from this wild type whole mouse brain sample had a similar PTM distribution to that of the pooled wild type mouse brain samples (Figure 5.3). In this case, sufficient amounts of H4 were extracted to allow fragmentation of four isolated ion species, and the isolation of each of these ions was superior to that achieved from the pooled brain samples. The CID spectrum of the ion at 870.6 *m/z* (blue) is shown in Figure 5.18 below.

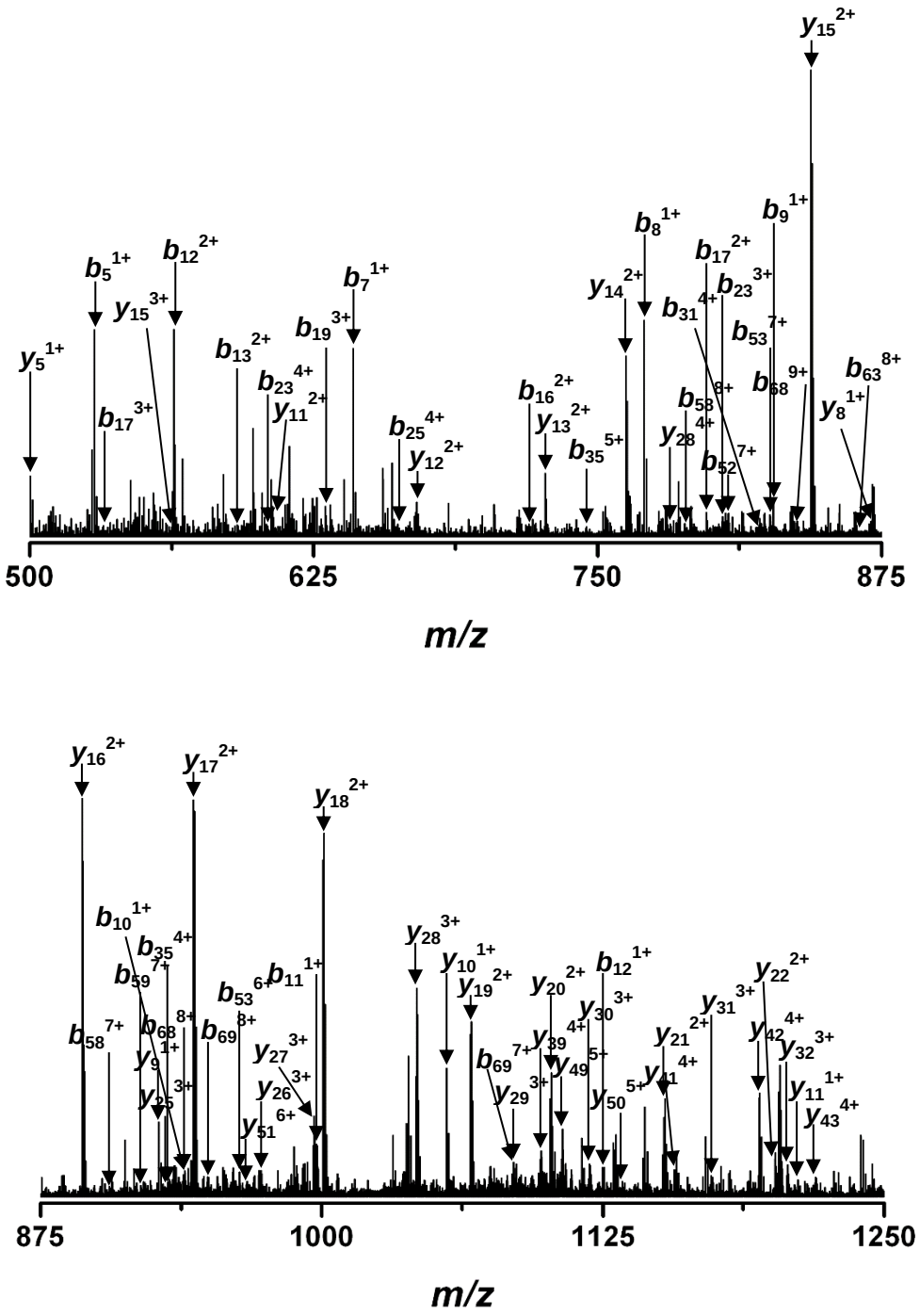

Figure 5.18: CID fragmentation spectrum of ion at 870.6 *m/z* from single wild type mouse brain sample. A complete list of the assigned fragment ions is attached as Appendix A30.

The ECD spectrum for this same ion species at 870.6 *m/z* is shown in Figure 5.19 below, along with a combined fragment ion map for this species of histone H4 generated from both the CID and ECD data (Figure 5.20).

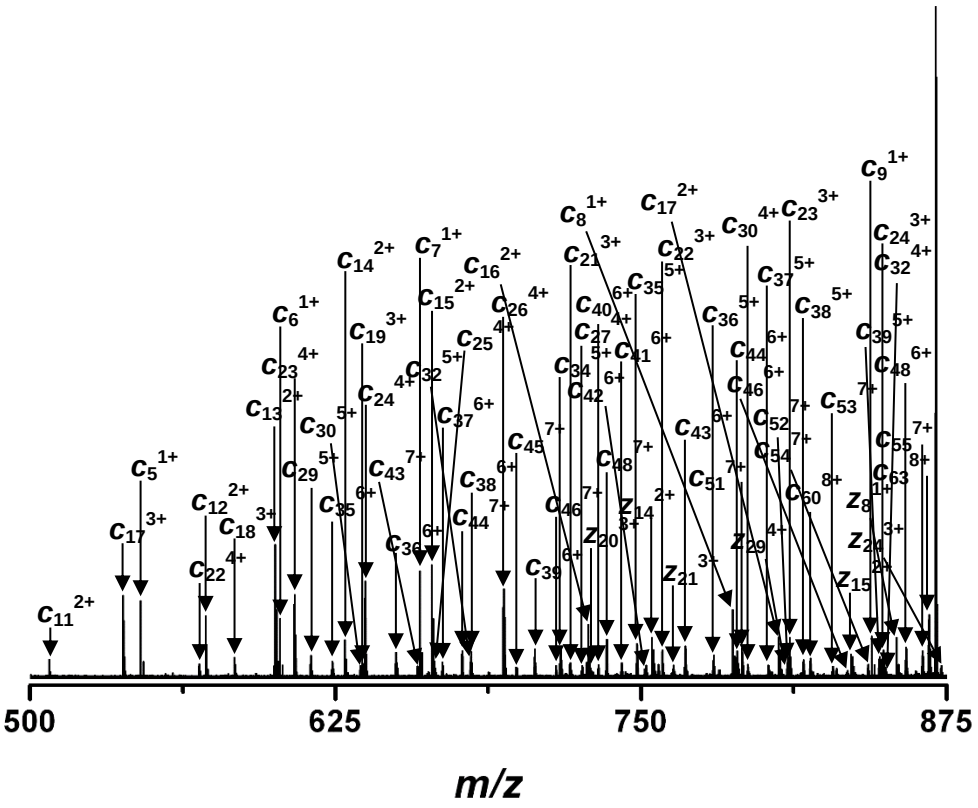

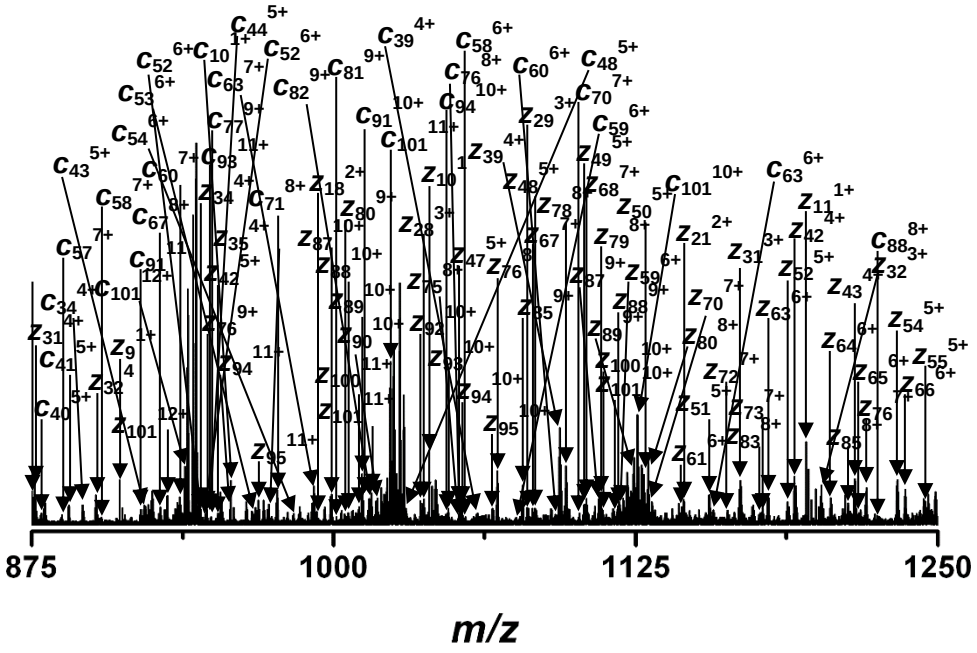

Figure 5.19: ECD fragmentation spectrum of ion at 870.6 *m/z* from wild type single mouse brain sample. A complete list of the assigned fragment ions is attached as Appendix A31

Figure 5.20: Fragment ion map of combined CID and ECD spectra for the ion at 870.6 *m/z*.

As can be seen from the combined fragment ion map, near complete sequence coverage was achieved after combining the results of the CID and ECD data. The identity of the ion at 870.6 *m/z* was confirmed as the 'unmodified' form of histone H4.

The next ion selected for fragmentation (green) had a mass-to-charge ratio of 871.8, which corresponded to an intact mass of 11,313 Da. The CID spectrum acquired from this ion is shown in Figure 5.21 below.

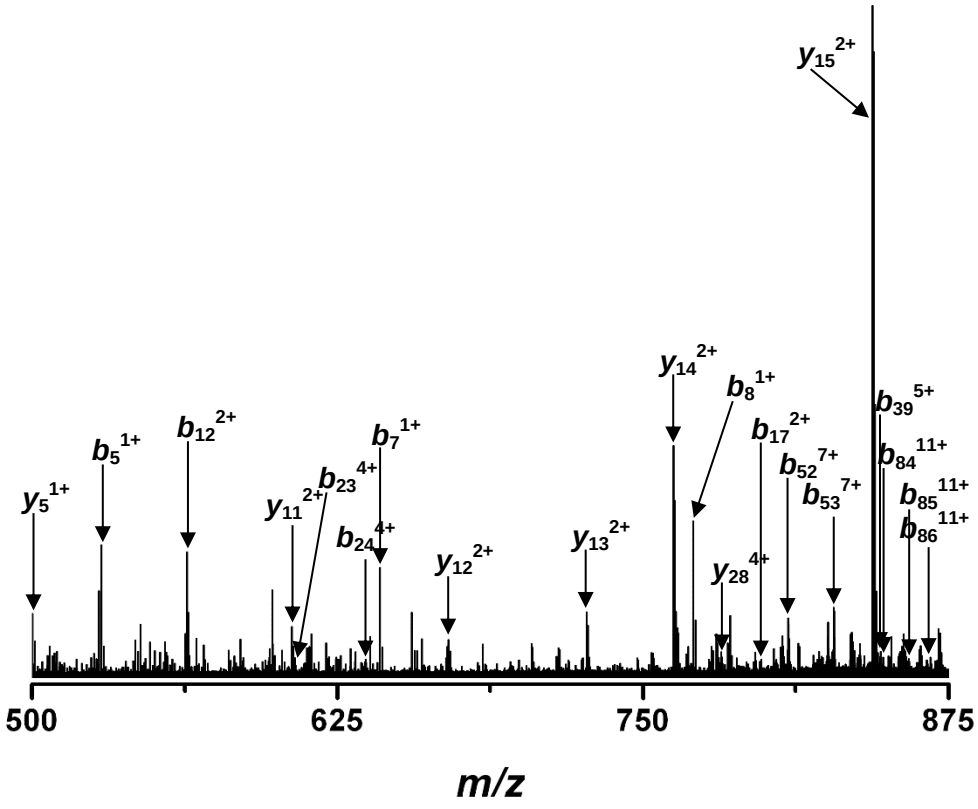

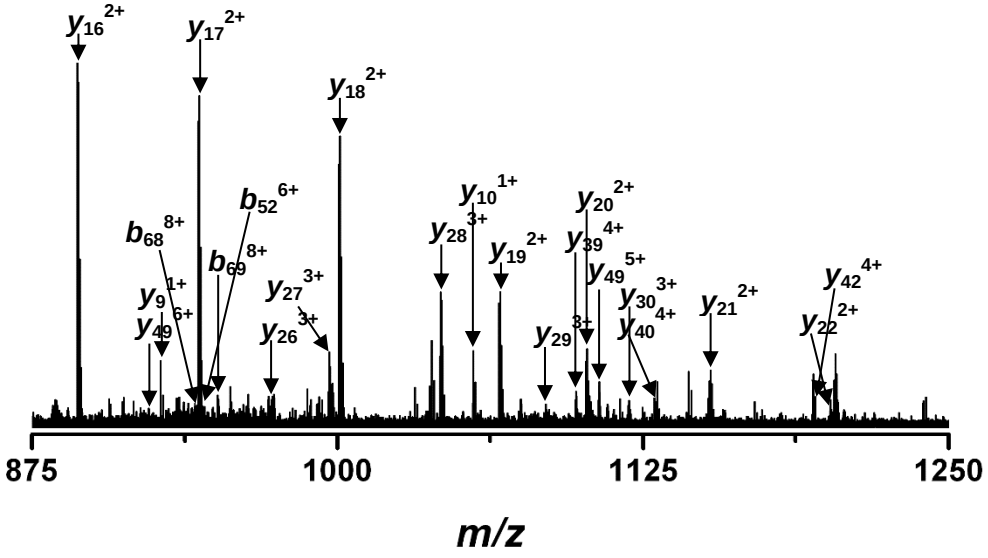

Figure 5.21: CID fragmentation spectrum of ion at 871.8 *m/z* from wild type single mouse brain sample. A complete list of the assigned fragment ions is attached as Appendix A32.

Figure 5.22 below, shows the ECD spectrum acquired from the same ion with a combined fragment ion map for this species of histone H4 generated from both the CID and ECD data (Figure 5.23).

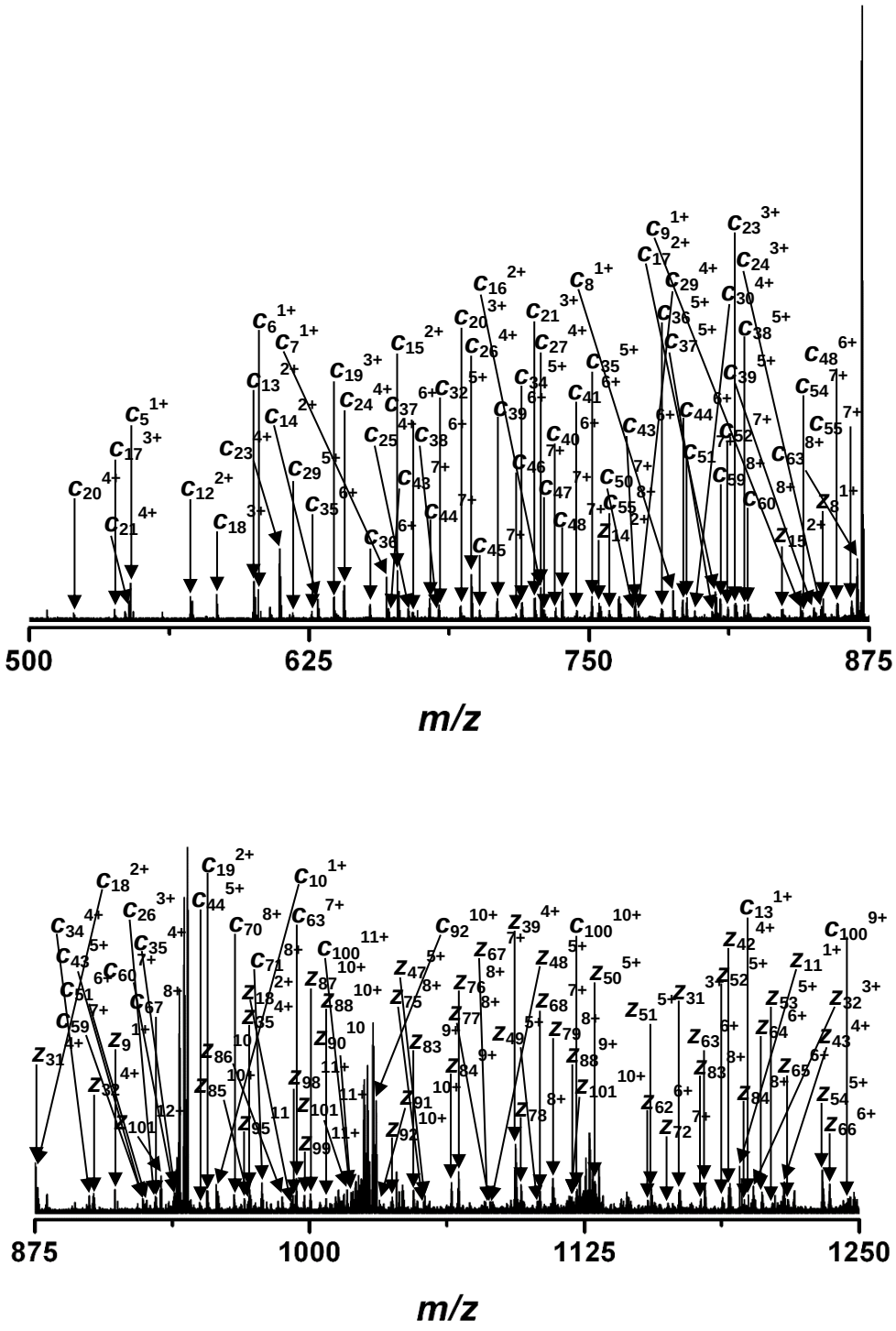

Figure 5.22: ECD fragmentation spectrum of ion at 871.8 *m/z* from wild type single mouse brain. A complete list of the assigned fragment ions is attached as Appendix A33.

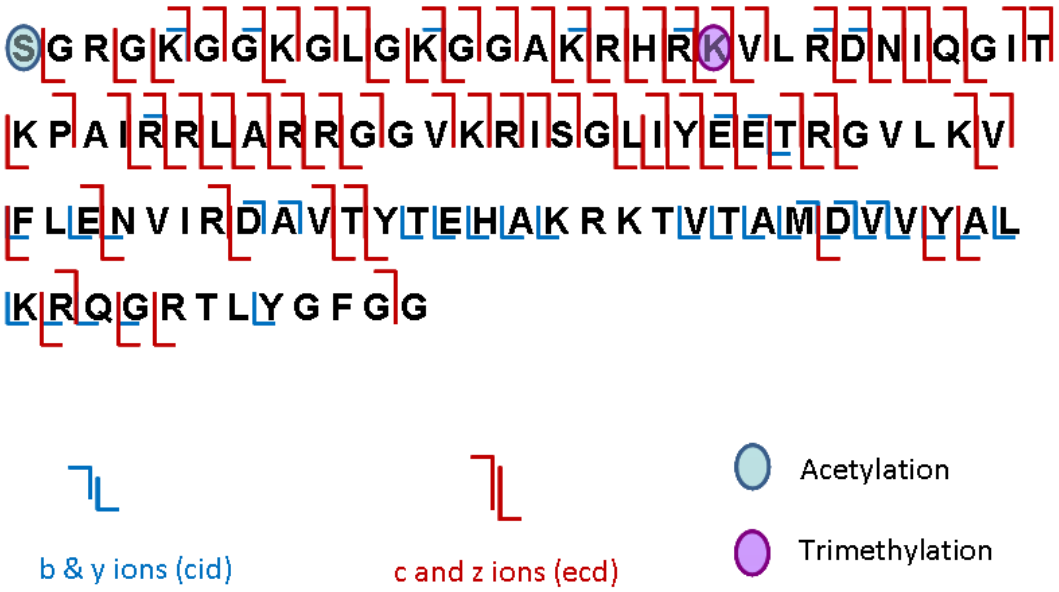

Figure 5.23: Fragment ion map of combined CID and ECD data for the ion at 871.8 *m/z*.

Similar to the fragment ion map shown in Figure 5.20, the combined fragment ion map above demonstrates that almost complete sequence coverage was achieved on the selected ion. The precursor ion had a mass increase of 14 Da compared to the unmodified form of histone H4. This mass increase was identified as being due to a tri-methylation at lysine 20 instead of the di-methylation more typically seen. Mass accuracy of each of the fragment ions was below 10 ppm, confirming that the mass increase was not due to acetylation of Lysine 20.

The next ion species selected for fragmentation was at 873.8 *m/z* (red). Figure 5.24 below shows the CID fragmentation spectrum for this ion.

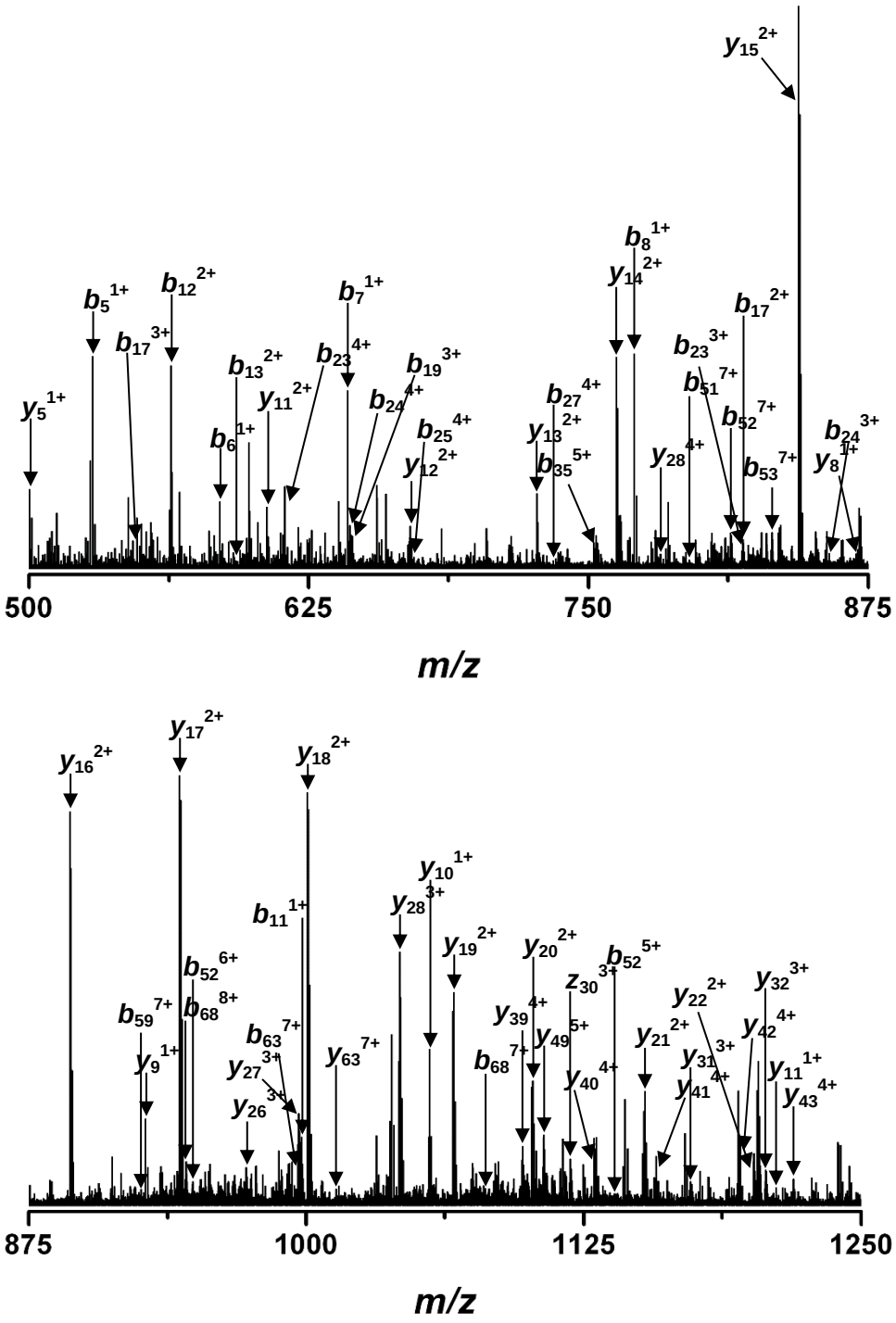

Figure 5.24: CID fragmentation spectrum of ion at 873.8 *m/z* from wild type single mouse brain sample. A complete list of the assigned fragment ions is attached as Appendix A34.

Figure 5.25 below shows the ECD spectrum gathered from the same ion with a combined fragment ion map for this species of histone H4 generated from both the CID and ECD data (Figure 5.26).

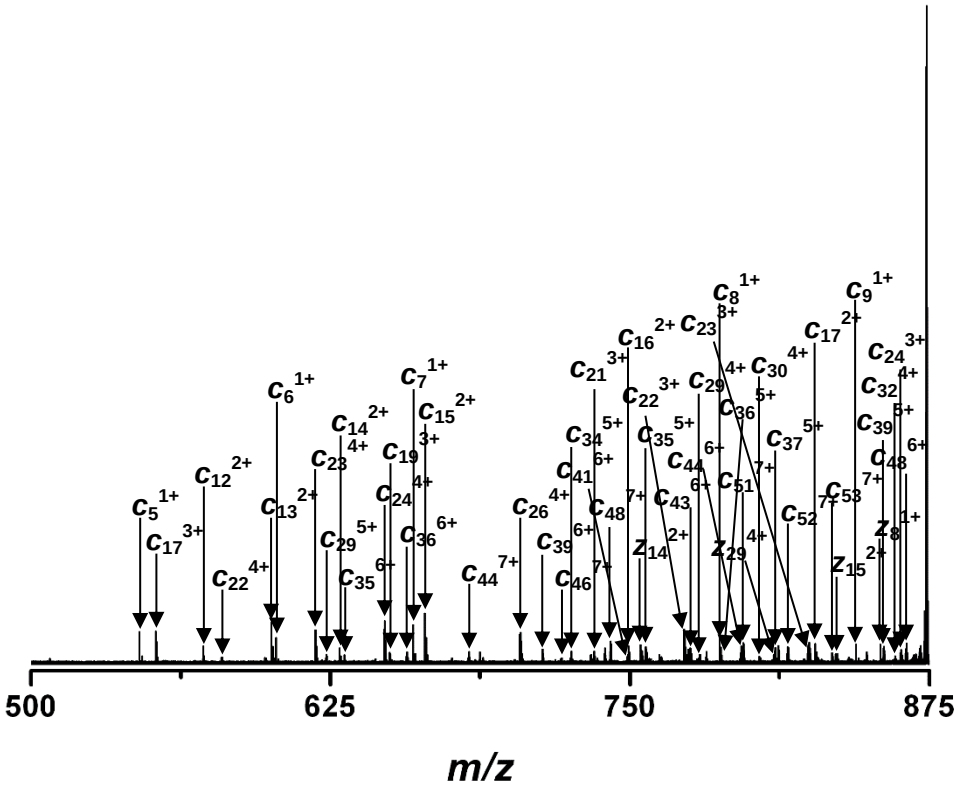

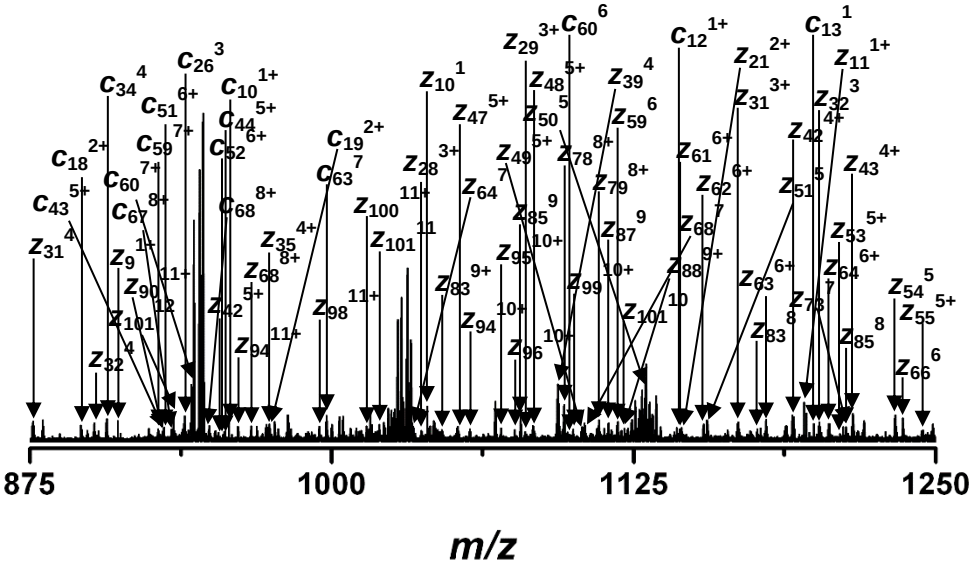

Figure 5.25: ECD spectrum of ion at 873.8 *m/z* from wild type single mouse brain. A complete list of the assigned fragment ions is attached as Appendix A35

Figure 5.26: Fragment ion map of combined CID and ECD data for the ion at 873.8 *m/z*.

The fragmentation data for this ion species at 873.8 *m/z* revealed that the mass increase of this ion above that of the normally observed form of histone H4 was due to the presence

of an acetyl group at lysine 16. No fragments corresponding to the acetylation of a different residue were found. This is in good agreement with the data presented in Chapter 3, in which the order of lysine acetylation in histone H4 was established.

The final ion selected for fragmentation was at 875.0 *m/z* (yellow). Figure 5.27 below shows the CID spectrum for this ion.

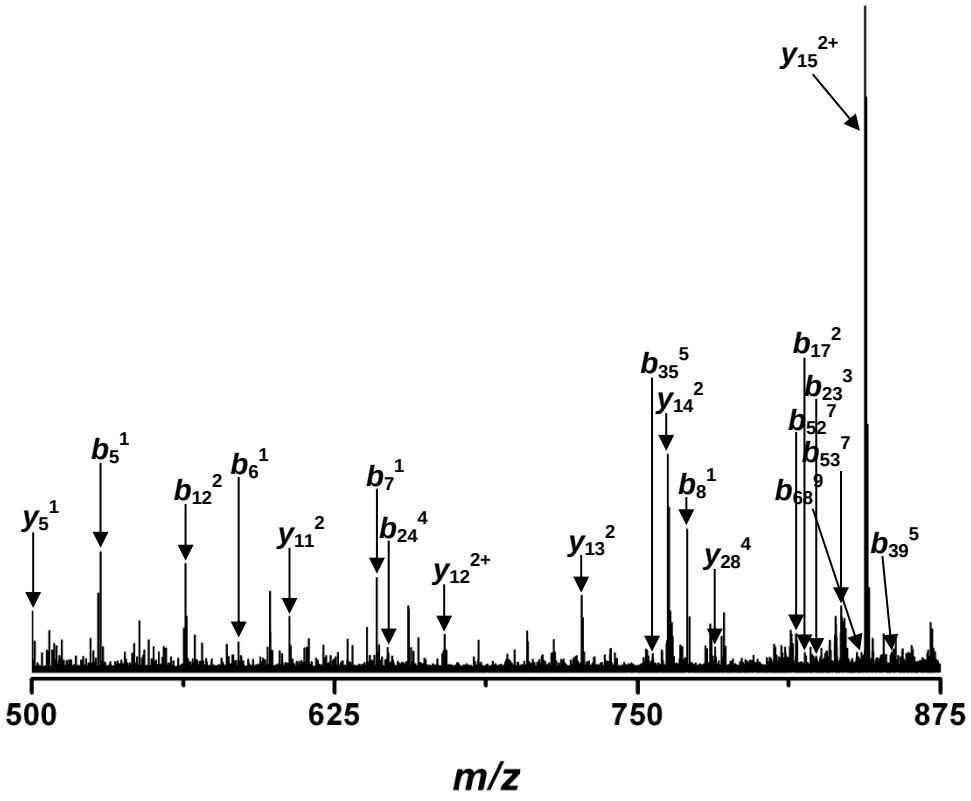

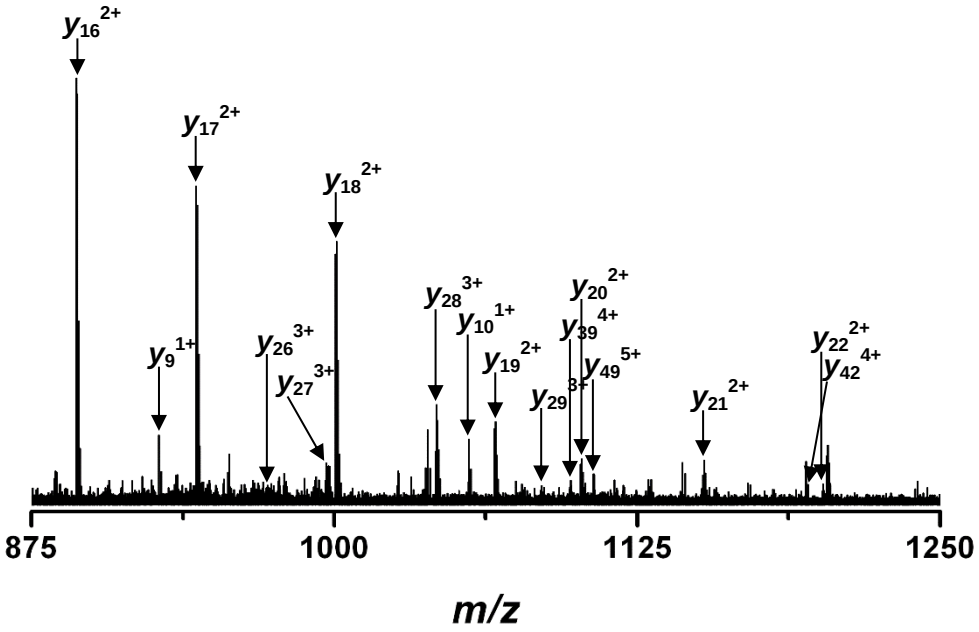

Figure 5.27: CID fragmentation spectrum of ion at 875.0 *m/z* from wild type single mouse brain sample. A complete list of the assigned fragment ions is attached as Appendix A36.

Figure 5.28 below shows the ECD spectrum acquired from the same ion along with a combined fragment ion map for this species of histone H4 generated from both the CID and ECD data (Figure 5.29).

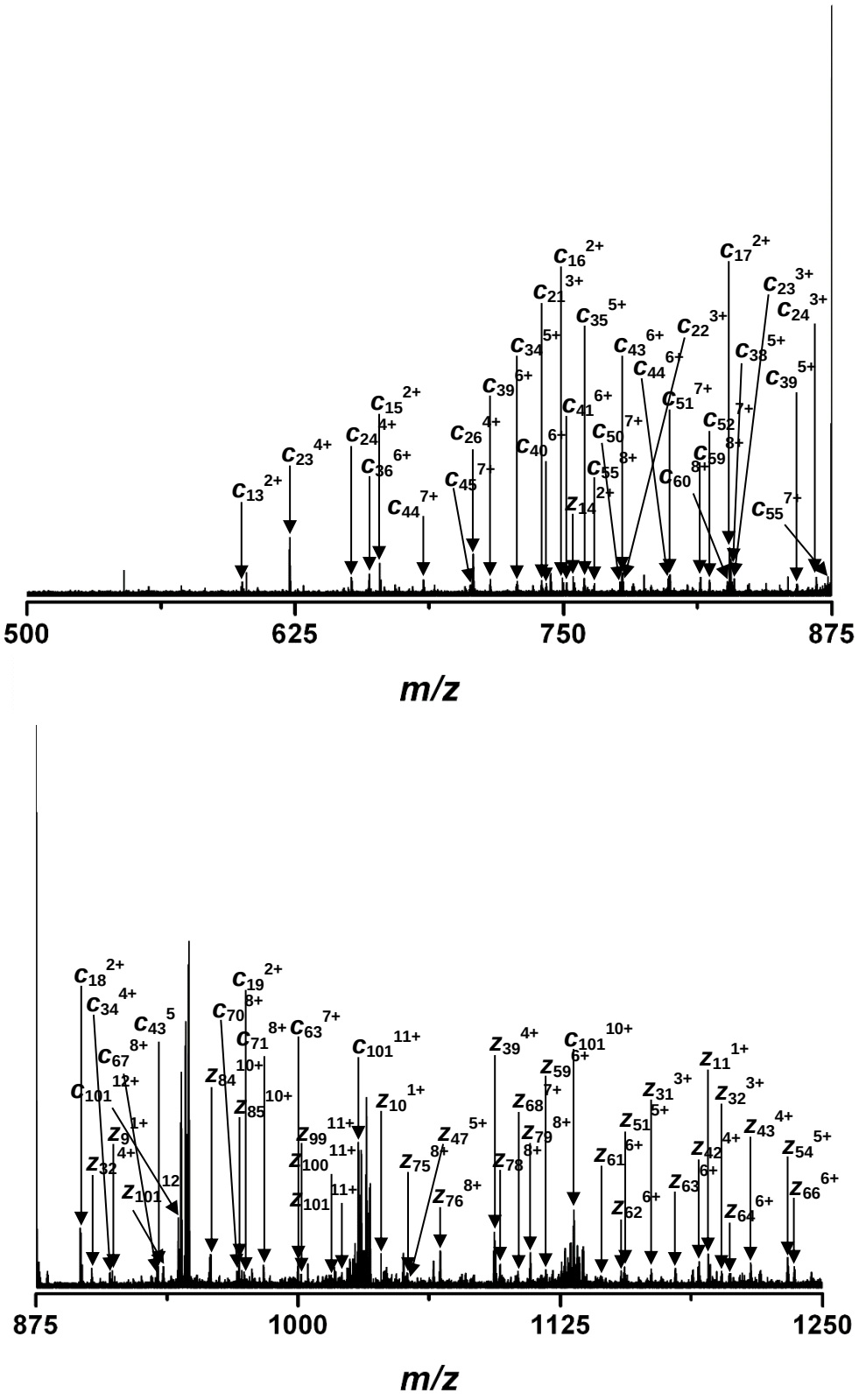

Figure 5.28: ECD spectrum of ion at 875.0 *m/z* from wild type single mouse brain. A complete list of the assigned fragment ions is attached as Appendix A37.

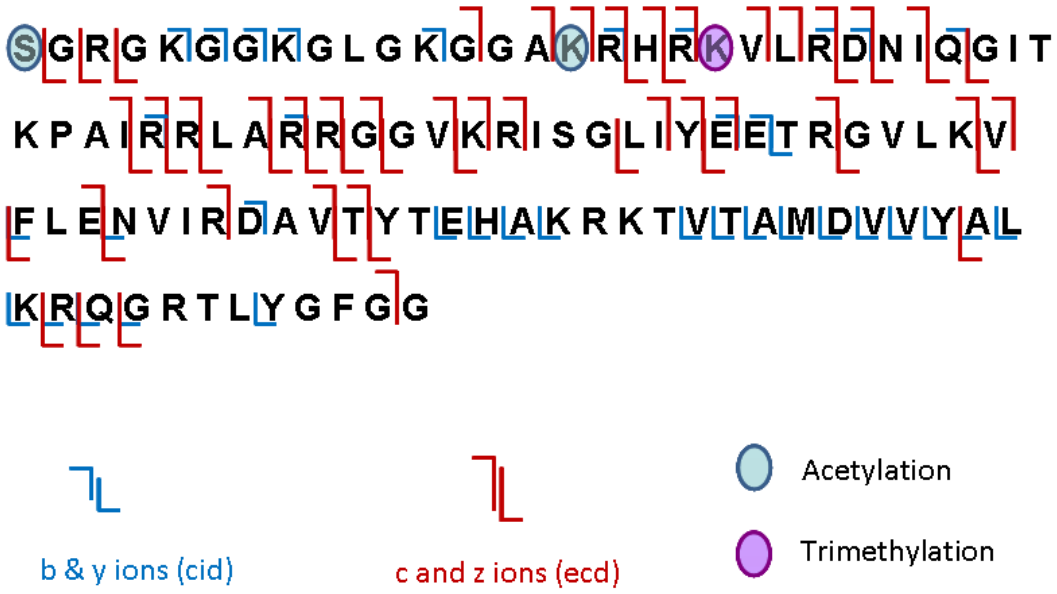

Figure 5.29: Fragment ion map of combined CID and ECD data for the ion at 875.0 *m/z*.

While less sequence coverage was achieved in fragmenting this ion, specifically in the N-terminal region, when the CID and ECD data were combined, the fragment ion map revealed that this ion was tri-methylated at lysine 20 and carried an acetyl group at lysine 16. Neither the CID or ECD data revealed the presence of ion species which would correspond to acetylation of a different lysine residue. In addition, the mass measurement error of all ions shown was below 10 ppm, giving confidence in the results.

The data presented above enabled the identification of four of the most abundant histone H4 isoforms from wild type whole mouse brain. Since the greatest change in PTM profile was seen among these modified forms of histone H4, the same series of experiments was carried out on whole mouse brain from MeCP2 knockout mice. A single mouse was sacrificed, its brain harvested and the histone extraction procedure was performed. In order to maximize the probability of observing an altered PTM profile, the mouse selected for sacrifice was six weeks of age, typically the latest age at which the effects of MeCP2 mutation are visible. Figure 5.30 below shows the mass spectrum for the 13^{+} charge state of histone H4 from the MeCP2 knockout mouse along with the ion species selected for fragmentation.

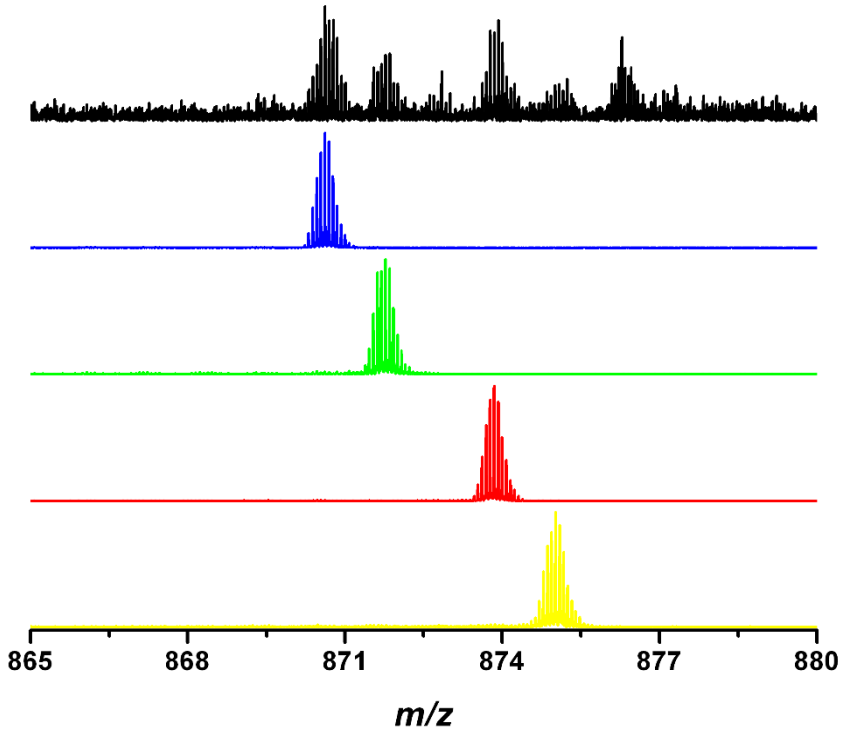

Figure 5.30: 13^{+} charge state of histone H4 from MeCP2 knockout whole mouse brain (black) with ions selected for subsequent fragmentation (indicated in blue, green, red and yellow).

Figure 5.31 below shows the spectrum generated from CID fragmentation of the ion at 870.6 *m/z* (blue).

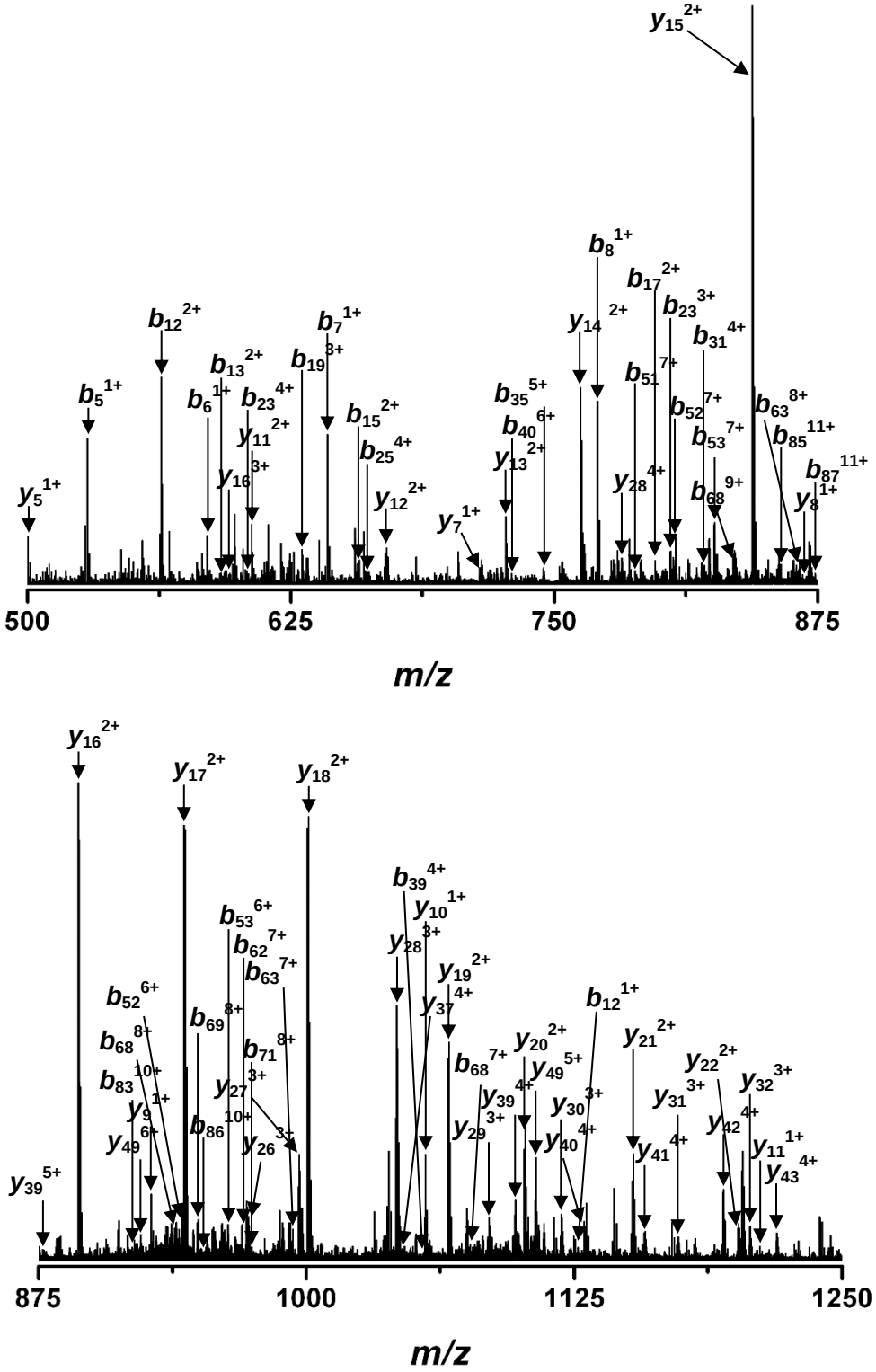

Figure 5.31: CID spectrum of ion at 870.6 *m/z* from MeCP2 knockout whole mouse brain. A complete list of the assigned fragment ions is attached as Appendix A38.

Figure 5.32 below shows the spectrum generated after ECD fragmentation of the same ion with a combined fragment ion map for this species of histone H4 generated from both the CID and ECD data (Figure 5.33).

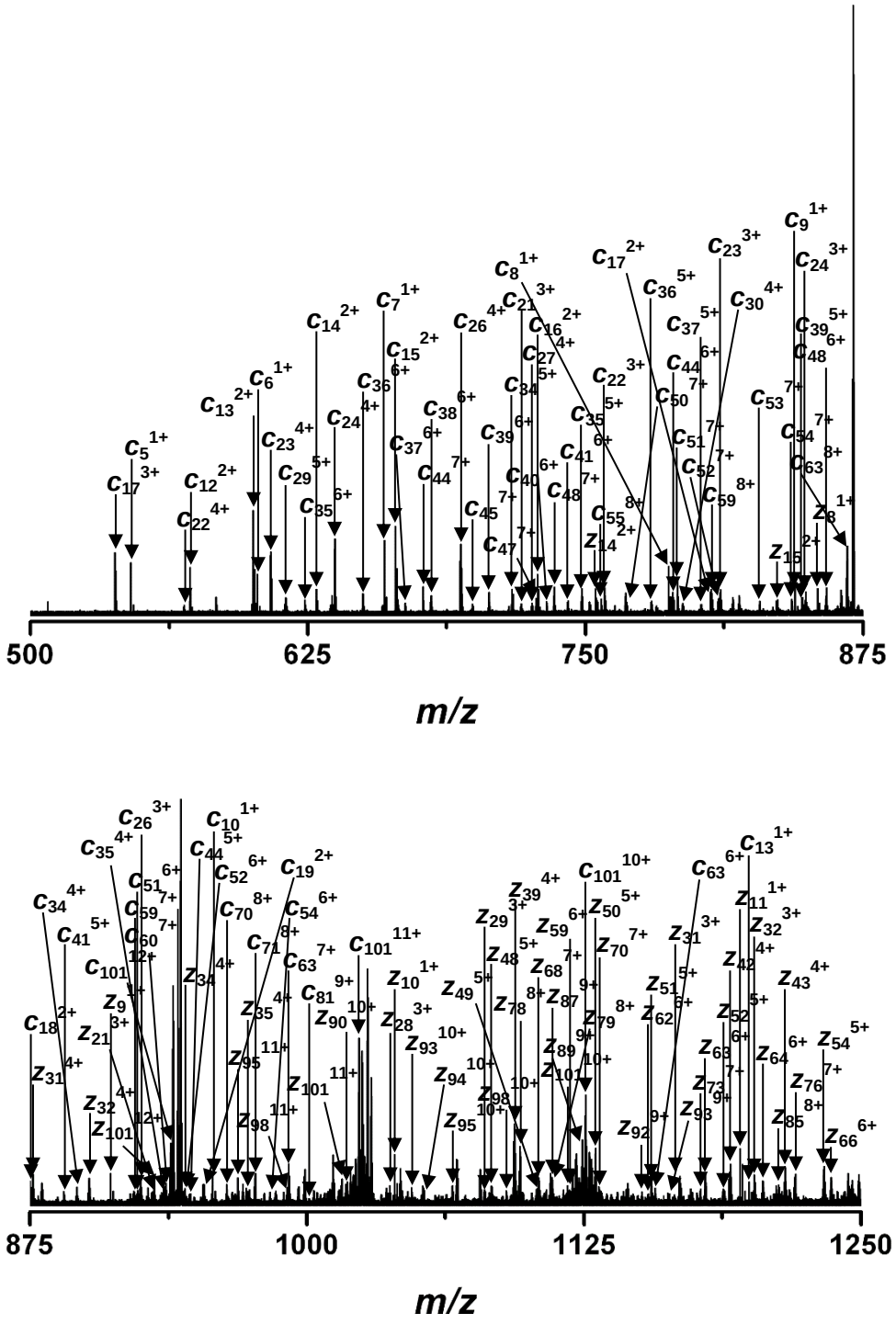

Figure 5.32: ECD spectrum of ion at 870.6 *m/z* from MeCP2 knockout whole mouse brain. A complete list of the assigned fragment ions is attached as Appendix A39.

Figure 5.33: Fragment ion map of combined CID and ECD data for the ion at 870.6 *m/z*.

The extensive sequence coverage confirmed that the ion at 870.6 *m/z* from the MeCP2 knockout mouse brain was the N-terminally acetylated histone H4, di-methylated at Lysine 20. The next ion selected for fragmentation was at 871.8 *m/z* (green) The CID spectrum acquired is shown in Figure 5.34 below.

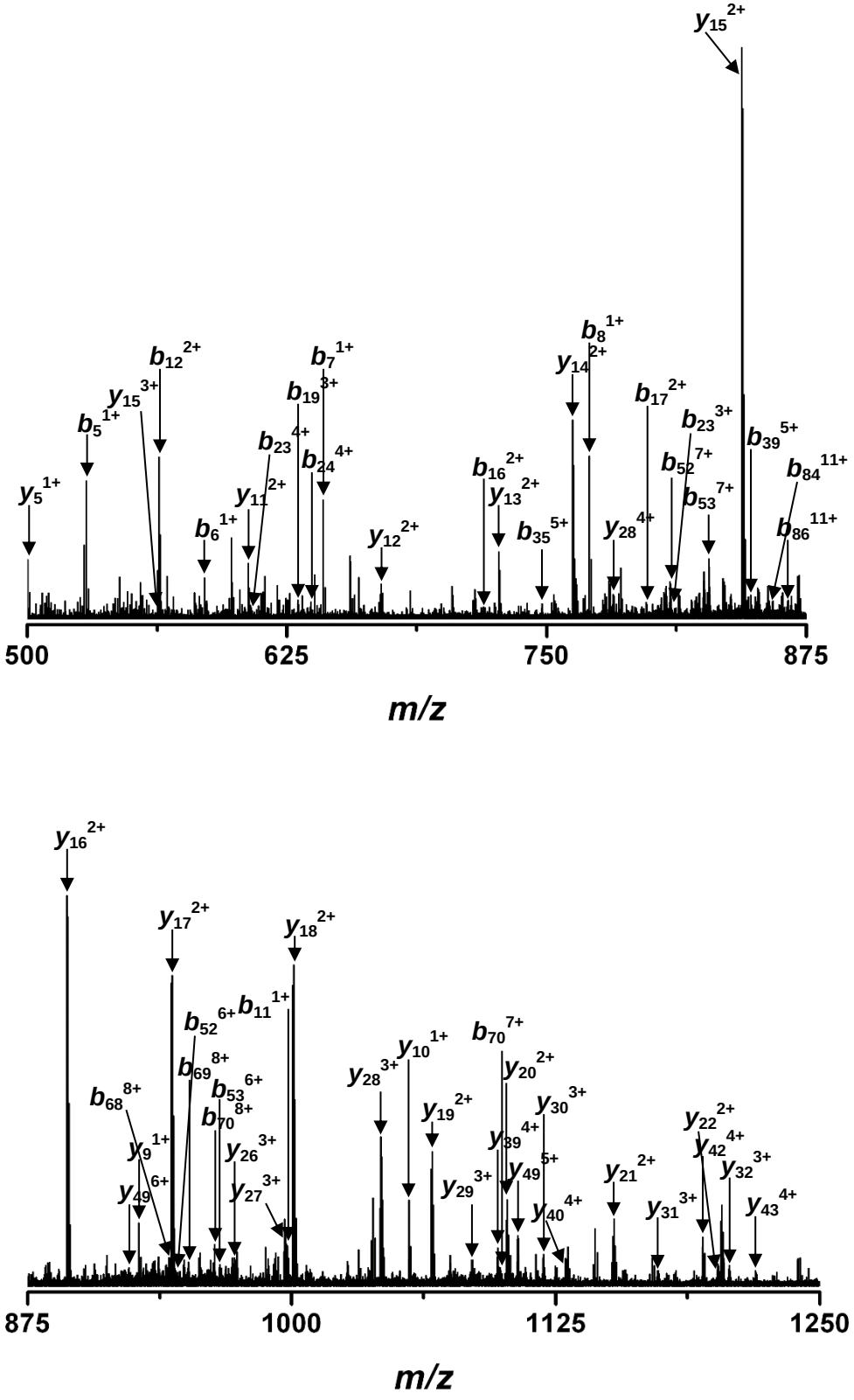

Figure 5.34: CID spectrum of ion at 871.8 *m/z* from MeCP2 knockout whole mouse brain. A complete list of the assigned fragment ions is attached as Appendix A40.

Figure 5.35 below shows the ECD spectrum generated from the same ion with a combined fragment ion map for this species of histone H4 generated from both the CID and ECD data (Figure 5.36).

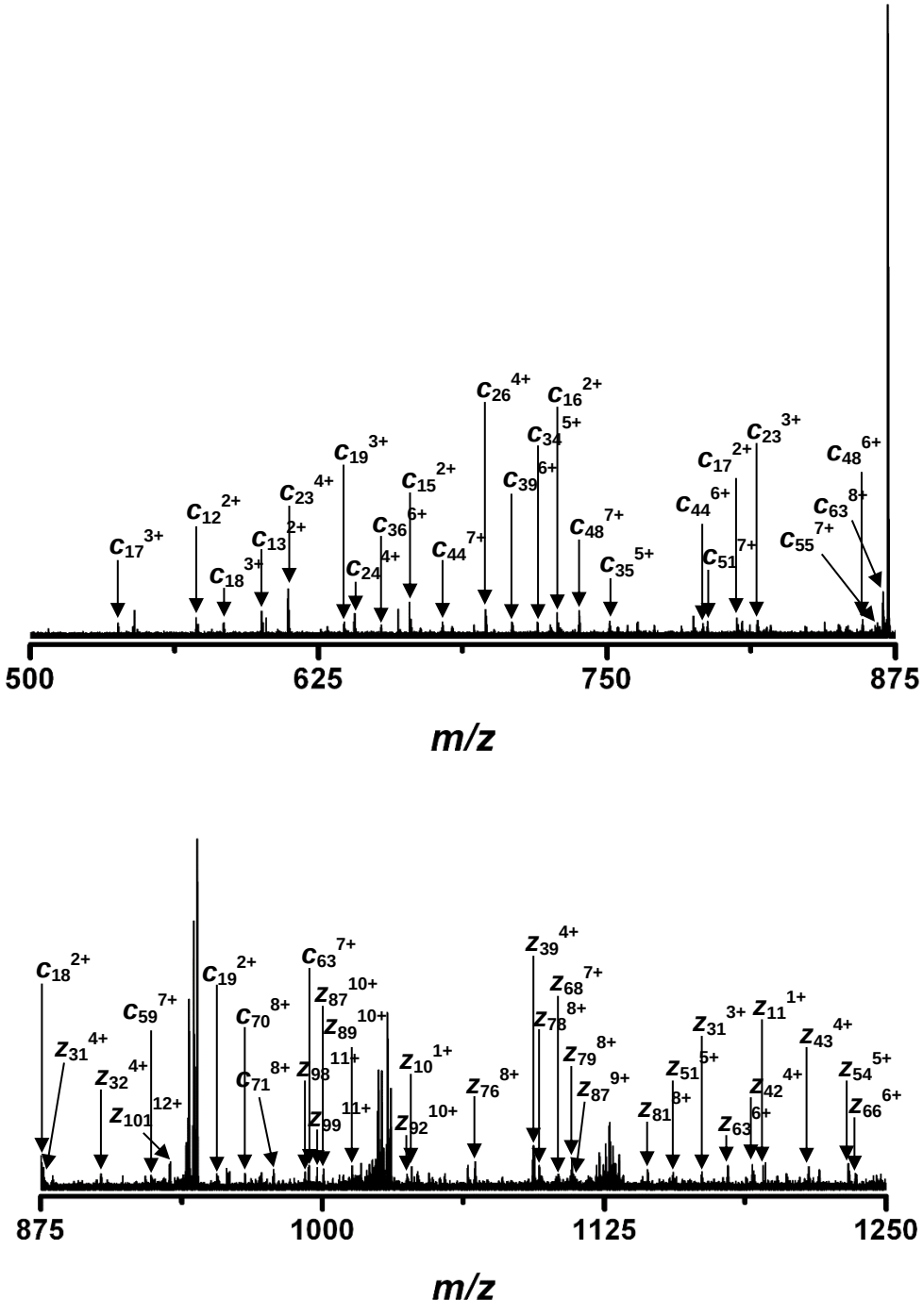

Figure 5.35: ECD spectrum of ion at 871.8 *m/z* from MeCP2 knockout whole mouse brain. A complete list of the assigned fragment ions is attached as Appendix A41.

Figure 5.36: Fragment ion map of combined CID and ECD data for the ion at 871.8 *m/z*.

The fragmentation data for this ion at 871.8 *m/z* confirmed that this ion species was N-terminally acetylated histone H4 tri-methylated at lysine 20. These PTMs were identical to those observed in the fragmentation spectra for the ion species at 871.8 *m/z* from the wild type mice sample.

The ion at 873.8 *m/z* (red) was next chosen for fragmentation. Figure 5.37 below shows the CID spectrum acquired.

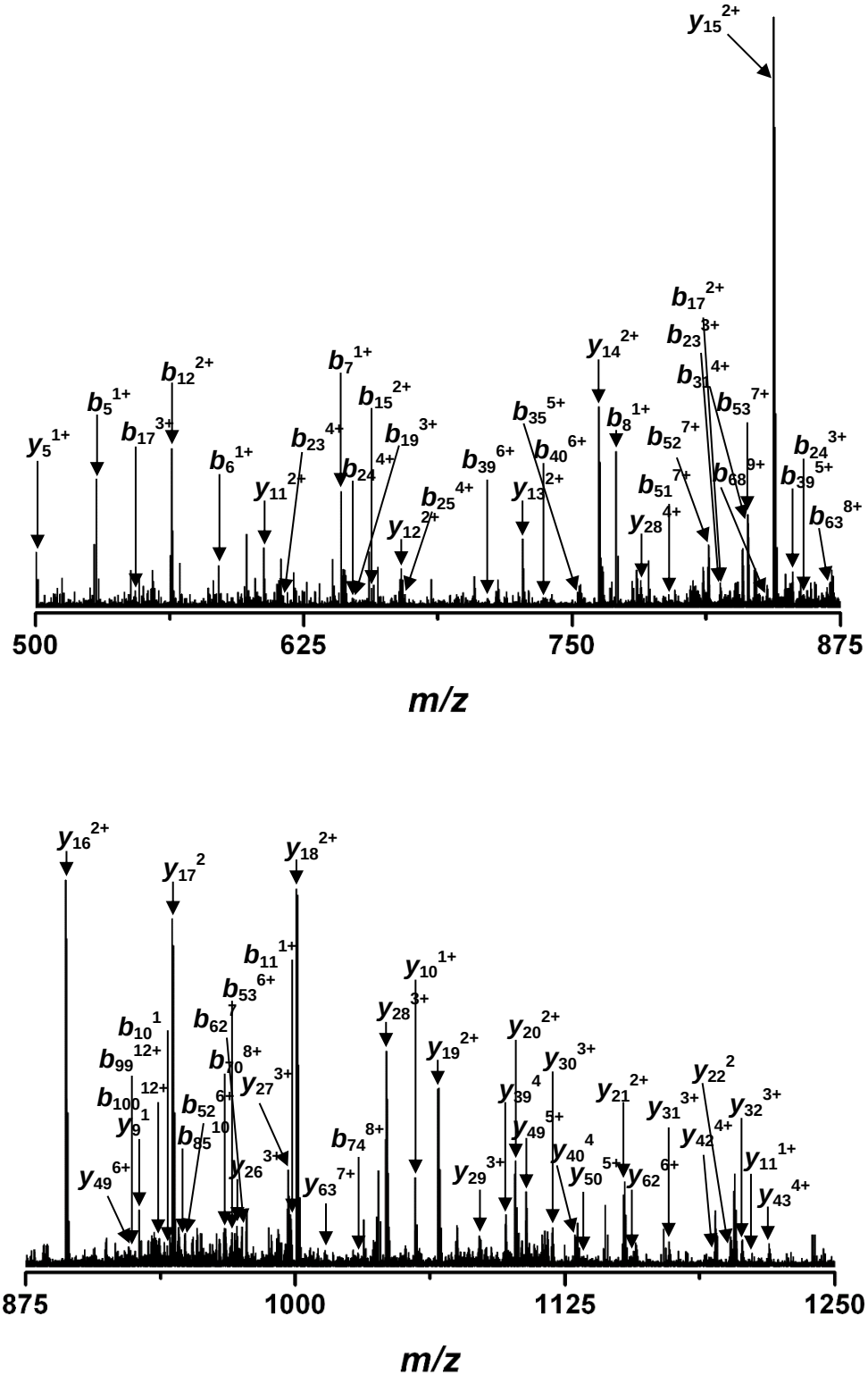

Figure 5.37: CID spectrum of ion at 873.8 *m/z* from MeCP2 knockout whole mouse brain. A complete list of the assigned fragment ions is attached as Appendix A42.

The ECD spectrum acquired is shown in Figure 5.38 below, along with a combined fragment ion map for this species of histone H4 generated from both the CID and ECD data (Figure 5.39).

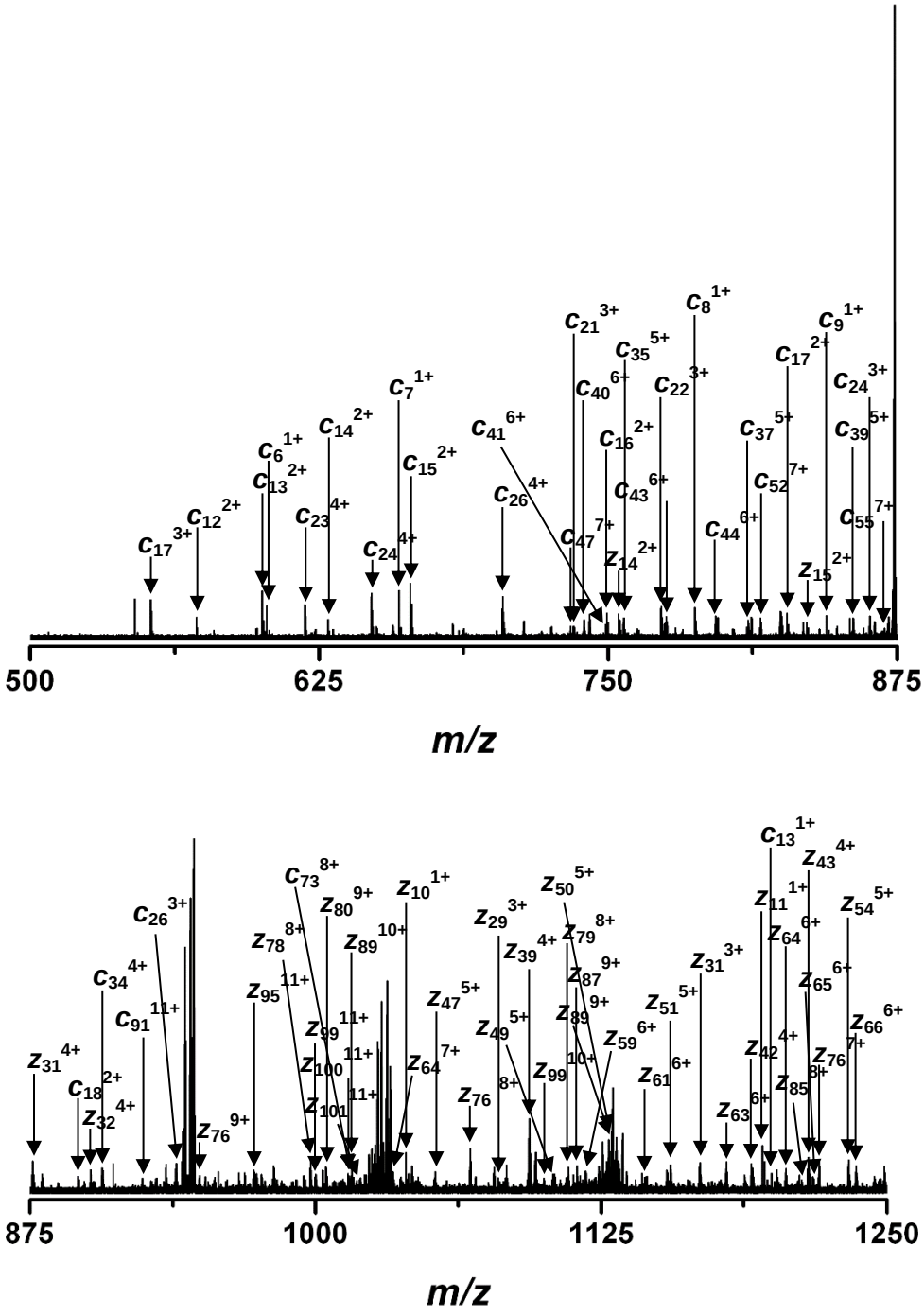

Figure 5.38: ECD fragmentation spectrum of ion at 873.8 *m/z* from MeCP2 knockout whole mouse brain. A complete list of the assigned fragment ions is attached as Appendix A43.

Figure 5.39: Fragment ion map of combined CID and ECD data for the ion at 873.8 *m/z*.

Examination of the fragmentation data revealed that this ion species corresponded to histone H4 with an acetyl group at lysine 16. The fragmentation data for the ion at 873.8 *m/z* from the wild type mouse brain sample confirmed the presence of the same PTMs.

The final ion selected for fragmentation was at 875.0 *m/z* (yellow). The CID spectrum gathered from this ion is shown in Figure 5.40 below.

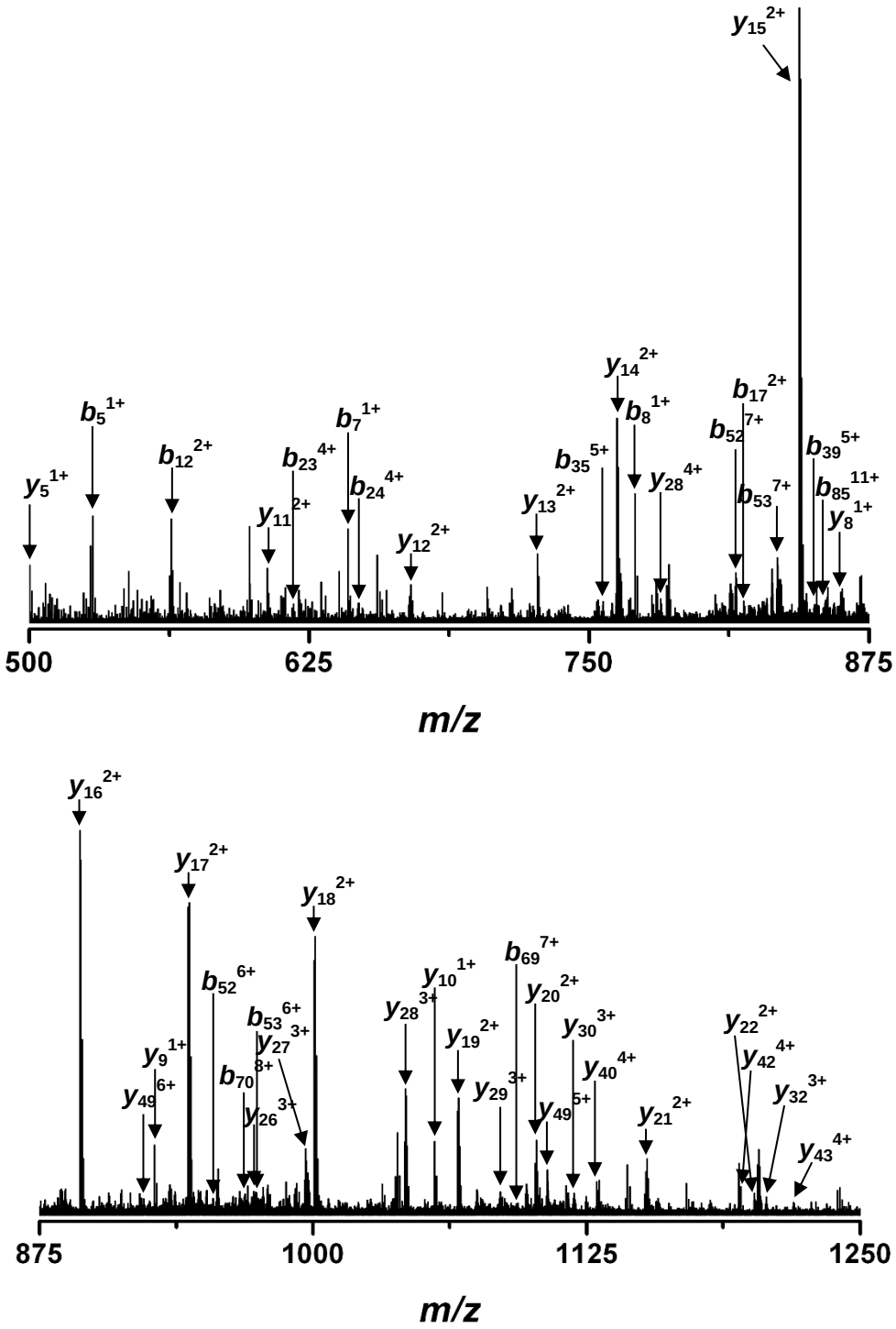

Figure 5.40: CID spectrum of ion at 875.0 *m/z* from MeCP2 knockout whole mouse brain. A complete list of the assigned fragment ions is attached as Appendix A44.

Figure 5.41 below shows the ECD spectrum acquired for the same ion along with a combined fragment ion map for this species of histone H4 generated from both the CID and ECD data (Figure 5.42).

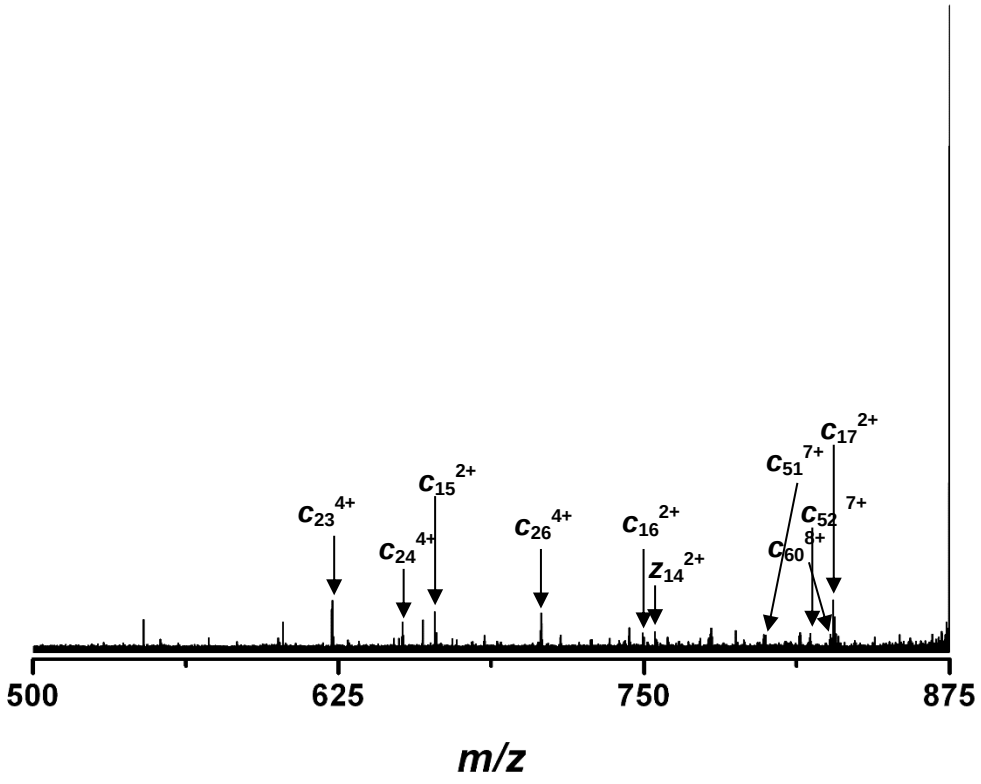

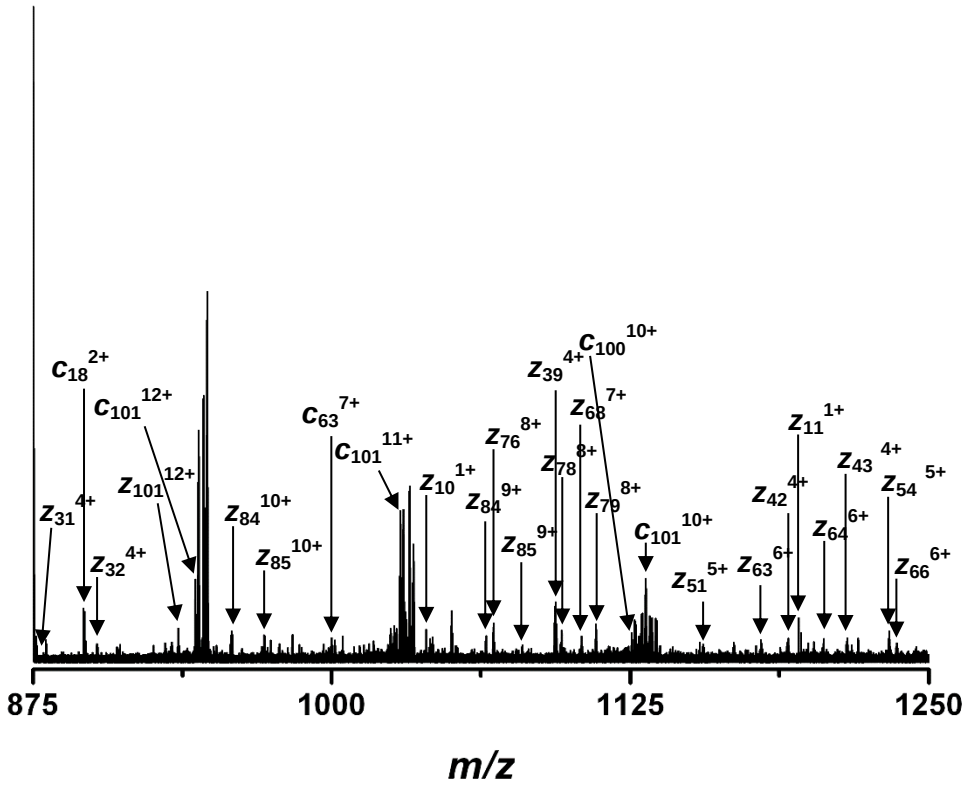

Figure 5.41: ECD spectrum of ion at 875.0 *m/z* from MeCP2 knockout whole mouse brain. A complete list of the assigned fragment ions is attached as Appendix A45.

Figure 5.42: Fragment ion map of combined CID and ECD data for the ion at 875.0 *m/z*.

Although ECD of this ion was not effective in fragmenting the N-terminal region, enough fragments were generated to confirm that this species was N-terminally acetylated histone H4 carrying a tri-methyl group at lysine 20 and an additional acetyl group at lysine 16, identical to the PTMs identified from the fragmentation data for ion species at 875.0 *m/z* from the wild type mouse brain sample.

5.3.2 Middle-Down Mass Spectrometry

The data presented above confirmed that the modified histone forms seen in the two samples of single mouse brain, wild type and MeCP2 knockout, were identical in their post-translational modifications. However, the relative abundance of these modified forms was different between the two samples.

In the spectra for the precursor ions where the fragmentation data had confirmed the presence of a di-methyl group at lysine 20 there were no other fragment ions to suggest the presence of other modified forms in the sample. However, the spectra for those precursor ions where the fragmentation data had confirmed the presence of a tri-methylation at lysine 20 (i.e. ions at 871.8 *m/z* and 875.0 *m/z*) each revealed fragments corresponding to di-methylation at lysine 20. The degree of mass isolation obtained for these precursor ions, shown in Figure 5.17 (WT) and Figure 5.30 (KO), suggested that only a single species was isolated. In an attempt to account for the presence of fragments containing di-methylated lysine from the tri-methylated precursor ion, the fragmentation spectra were closely examined for the presence of mono-methylated lysine species. The presence of a lysine bearing a single methyl group, in addition to the di-methyl group at lysine 20 would account for the mass difference of each ion. However, in each case no fragments exhibiting a mass increase consistent with mono-methylated lysine were found. The fragment ion spectra presented above were all examined for the presence of ions which serve as markers for specific modified forms of histone H4, however none of the previously documented marker ions were found[207-209].

In order to exclude the possibility that di-methylated precursor ions were present at low abundance within the mass isolation window of the tri-methylated ion species selected for fragmentation, the WT single mouse brain sample of histone H4 was analyzed by middle-down mass spectrometry. Endoproteinase Asp-N was selected to cleave histone H4 as it would provide an intact N-terminal region bearing all modifiable lysine residues. Figure 5.43 below shows the cleavage site of endoproteinases Asp-N and the resulting N-terminal fragment.

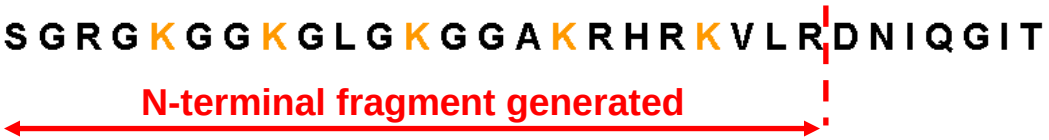

Figure 5.43: Amino acids 1-30 of histone H4 (after removal of initial methionine). The cleavage site of endoproteinase Asp-N is shown in red with resulting N-terminal fragment. Lysines known to be post-translationally modified are highlighted.

The broadband spectrum of histone H4 after digestion with Asp-N is shown in Figure 5.44 below.

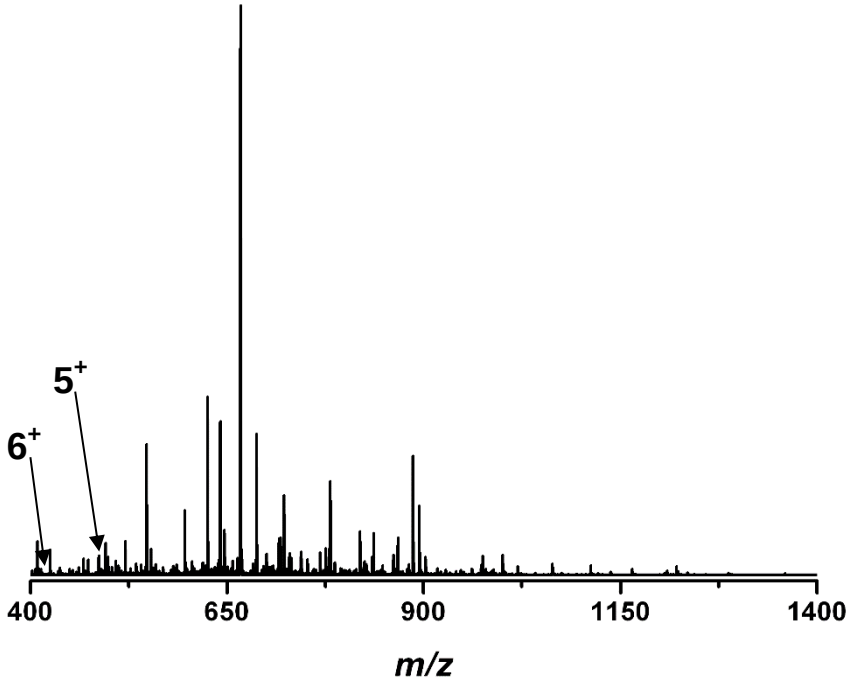

Figure 5.44: Broadband spectrum of histone H4 after enzymatic digestion with endoproteinase Asp-N with 5+ and 6+ charge states of the tri-methylated peptide labelled.

The *m/z* values of the 5^+ and 6^+ charge states of the tri-methylated N-terminal fragment precursor ions were calculated and each was selected for CID and ECD fragmentation. Figure 5.45 below shows the mass spectrum for the 5^+ charge state of this precursor ion following mass isolation, with a simulated isotope pattern overlaid.

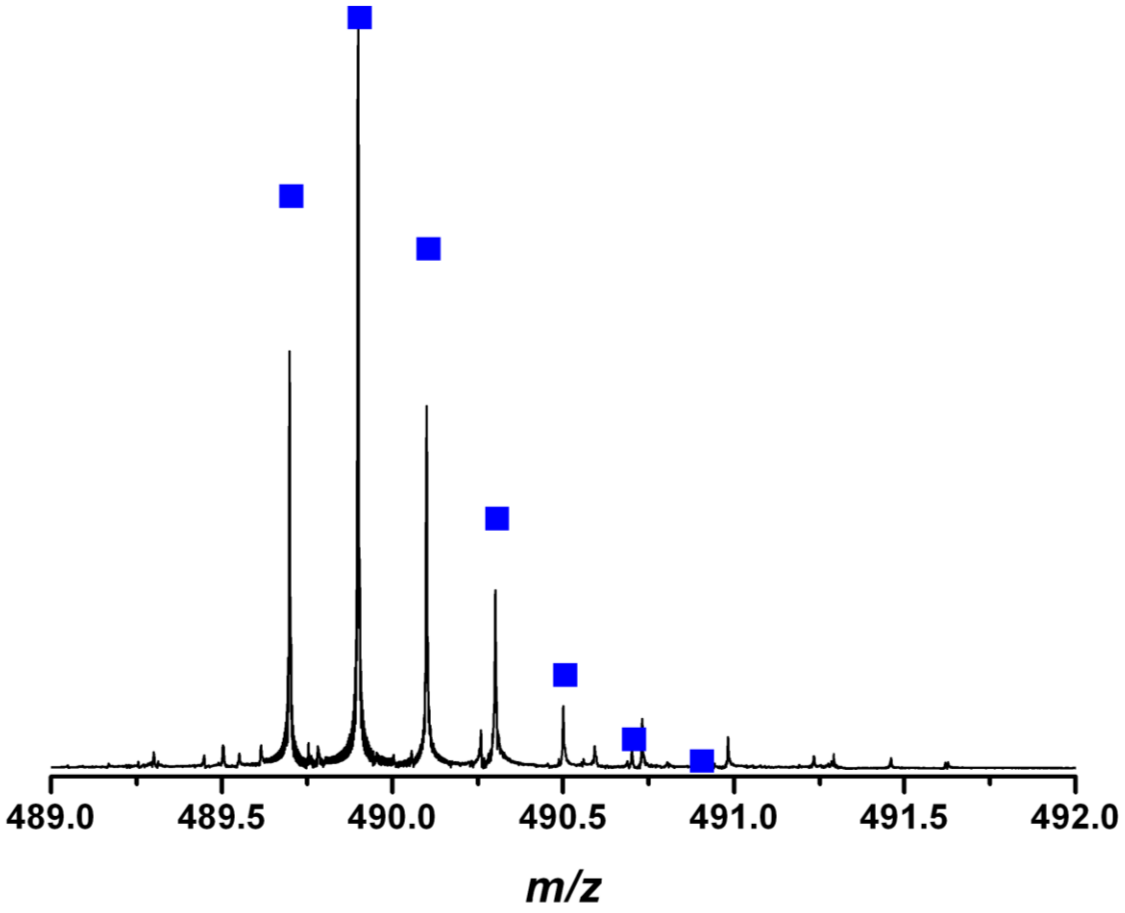

Figure 5.45: Mass spectrum for the 5^+ charge state of tri-methylated N-terminal region of histone H4 after digestion with Asp-N. An isotope simulation is overlaid (blue squares). The ion had an intact mass of 2,443 Da.

The simulated isotope pattern and the isolation achieved suggested that the only species present was the tri-methylated form of the N-terminal region. Figure 5.46 below shows the spectrum generated after fragmentation by CID.

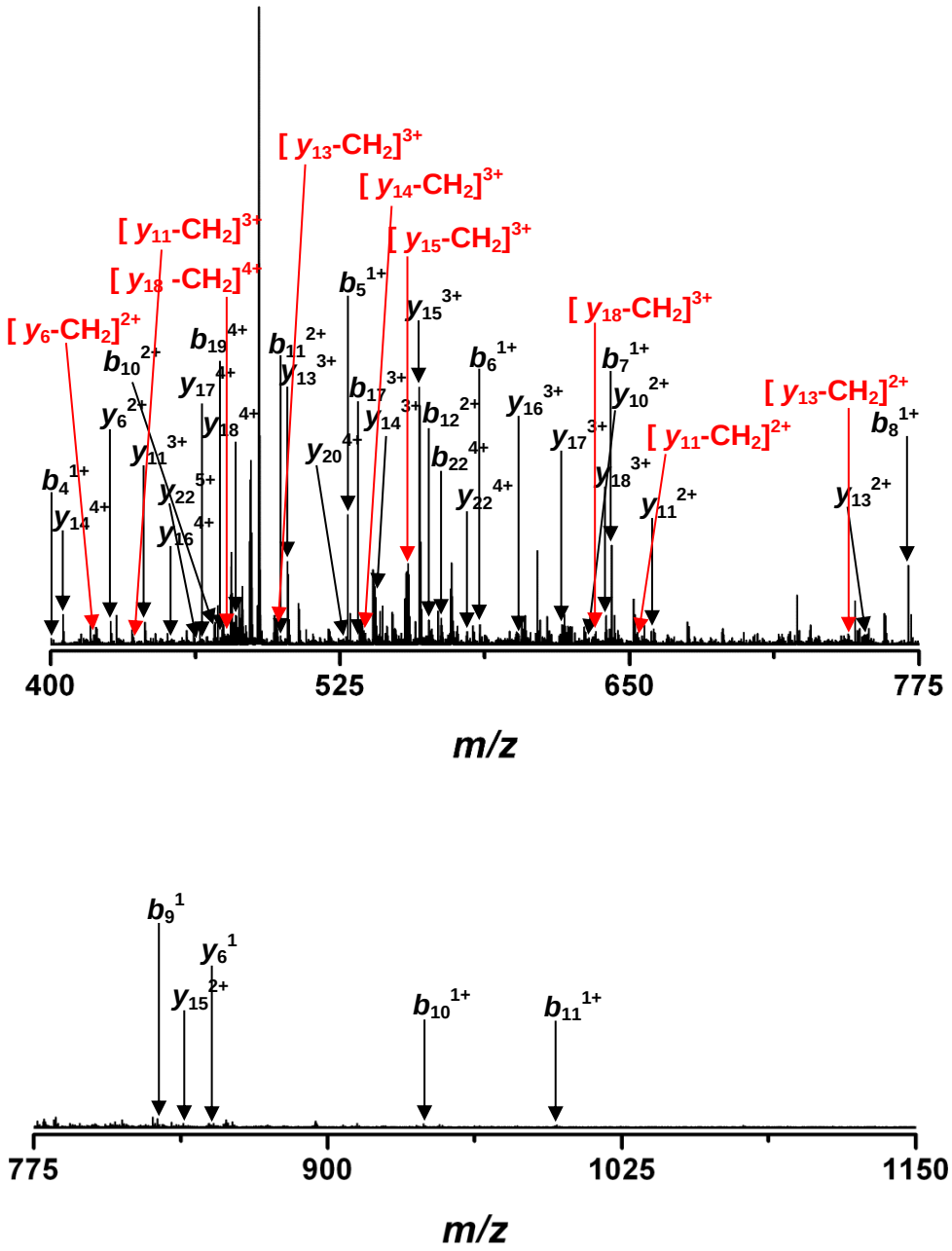

Figure 5.46: CID spectrum of 5^+ charge state of tri-methylated N-terminal region of histone H4 at 490 *m/z* after digestion with Asp-N. Fragments corresponding to di-methylated species are shown in red. A complete list of the assigned fragment ions is attached as Appendix A46.

Figure 5.47 below shows the corresponding ECD spectrum acquired after fragmentation of the isolated tri-methylated histone H4 N-terminal precursor ion with a combined fragment ion map generated from both the CID and ECD data.

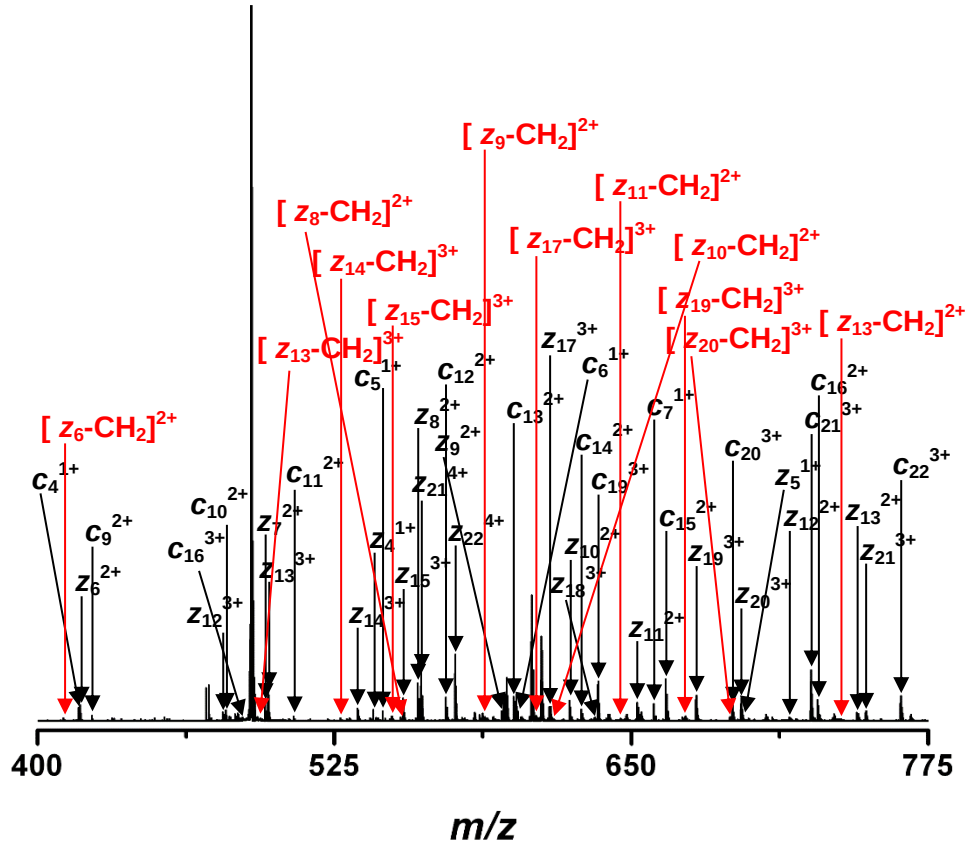
[z9-CH2]2+
[z11-CH2]2+
[z8-CH2]2+
[z17-CH2]3+
[z10-CH2]2+
[z14-CH2]3+
[z19-CH2]3+
[z15-CH2]3+
[z13-CH2]2+
[z20-CH2]3+
[z13-CH2]3+
[z6-CH2]2+
400
525
650
775
m/z

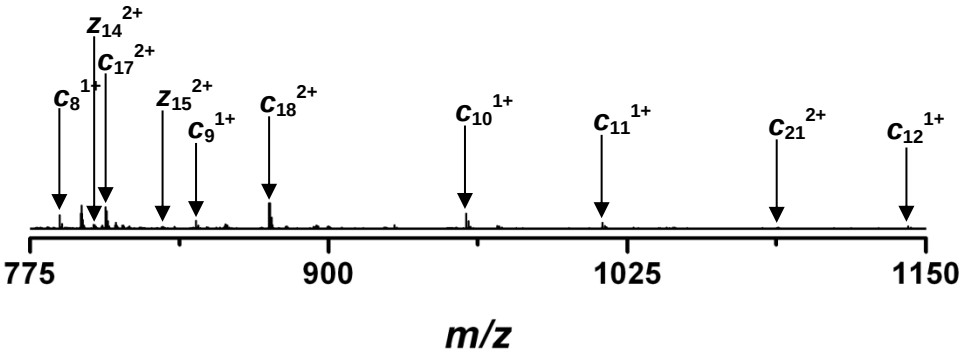
775
900
1025
1150
m/z

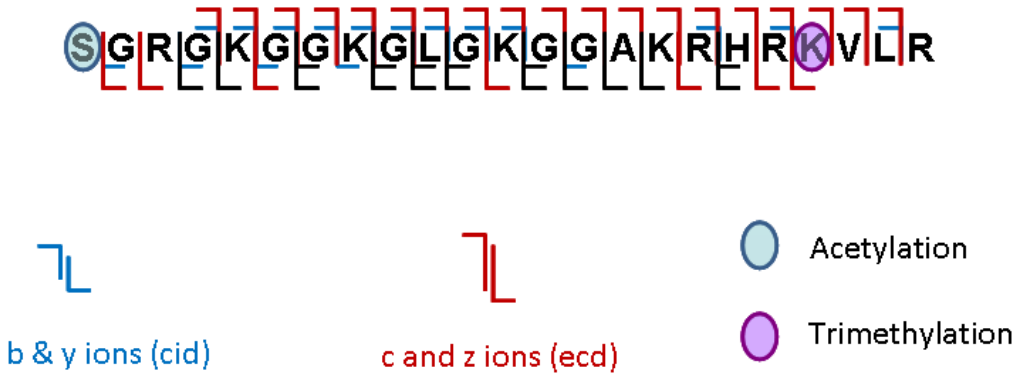

Figure 5.47: ECD spectrum of 5^+ charge state of tri-methylated N-terminal region of histone H4 at 490 *m/z* after digestion with Asp-N. A combined fragment ion map is given at the bottom of the figure. Fragments corresponding to di-methylated species are shown in red and fragments confirming the presence of di- and tri-methylated species in the fragment ion map are shown in black. A complete list of the assigned fragment ions is attached as Appendix A47.

Fragments corresponding to the di-methylated form of the histone H4 N-terminal region were observed in the CID and ECD spectra of the 5^+ charge state. To determine if these fragments were the result of poor precursor isolation of the 5^+ charge state, the 6^+ charge state of the tri-methylated N-terminal region of histone H4 was also isolated as the precursor ion and subjected to fragmentation by CID and ECD. Figure 5.48 below shows the mass spectrum for the 6^+ charge state of this precursor ion following mass isolation, with a simulated isotope pattern overlaid.

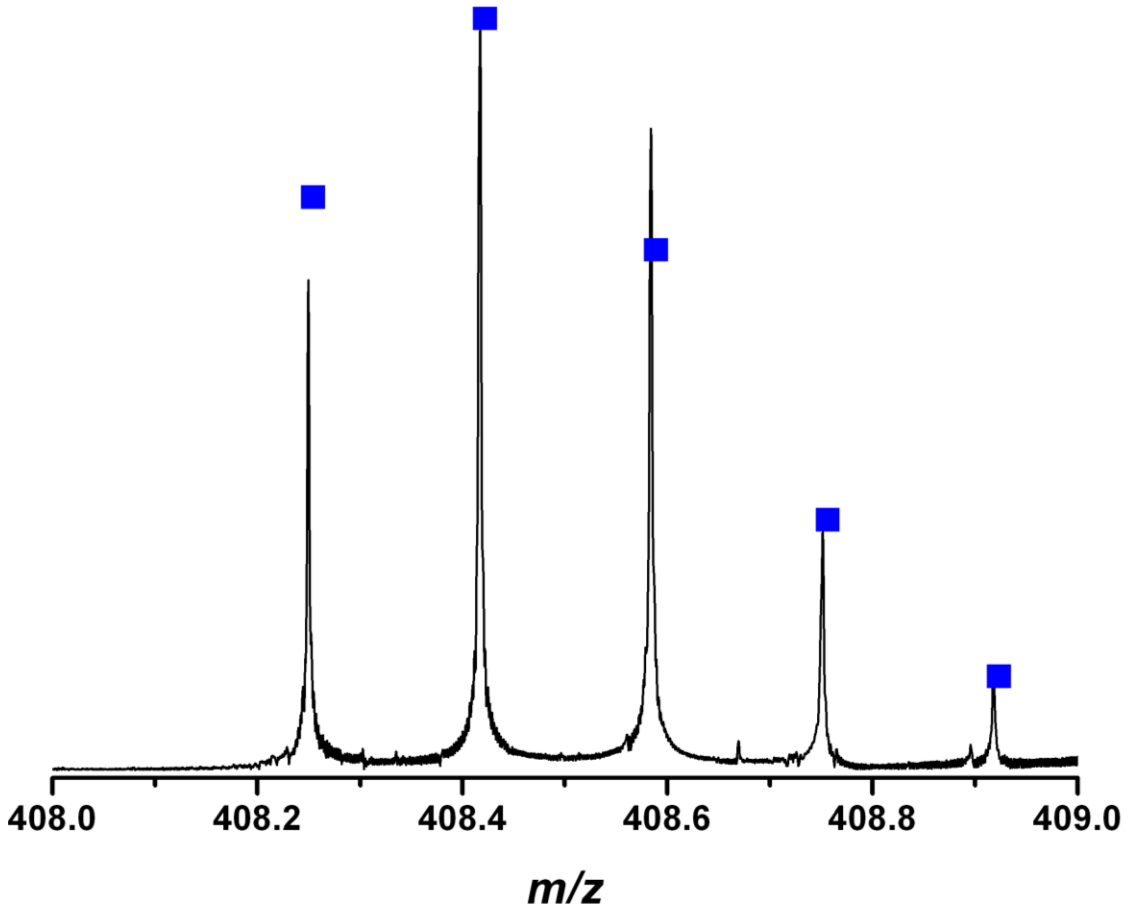

Figure 5.48: 6^+ charge state of tri-methylated N-terminal region of histone H4 after digestion with Asp-N, with isotope simulation overlaid (blue squares).

As was the case for the 5^+ charge state, the excellent level of mass isolation achieved suggested that the only ions proceeding to fragmentation were tri-methylated H4 precursors. Figure 5.49 below shows the CID spectrum acquired from the 6^+ charge state of the tri-methylated precursor.

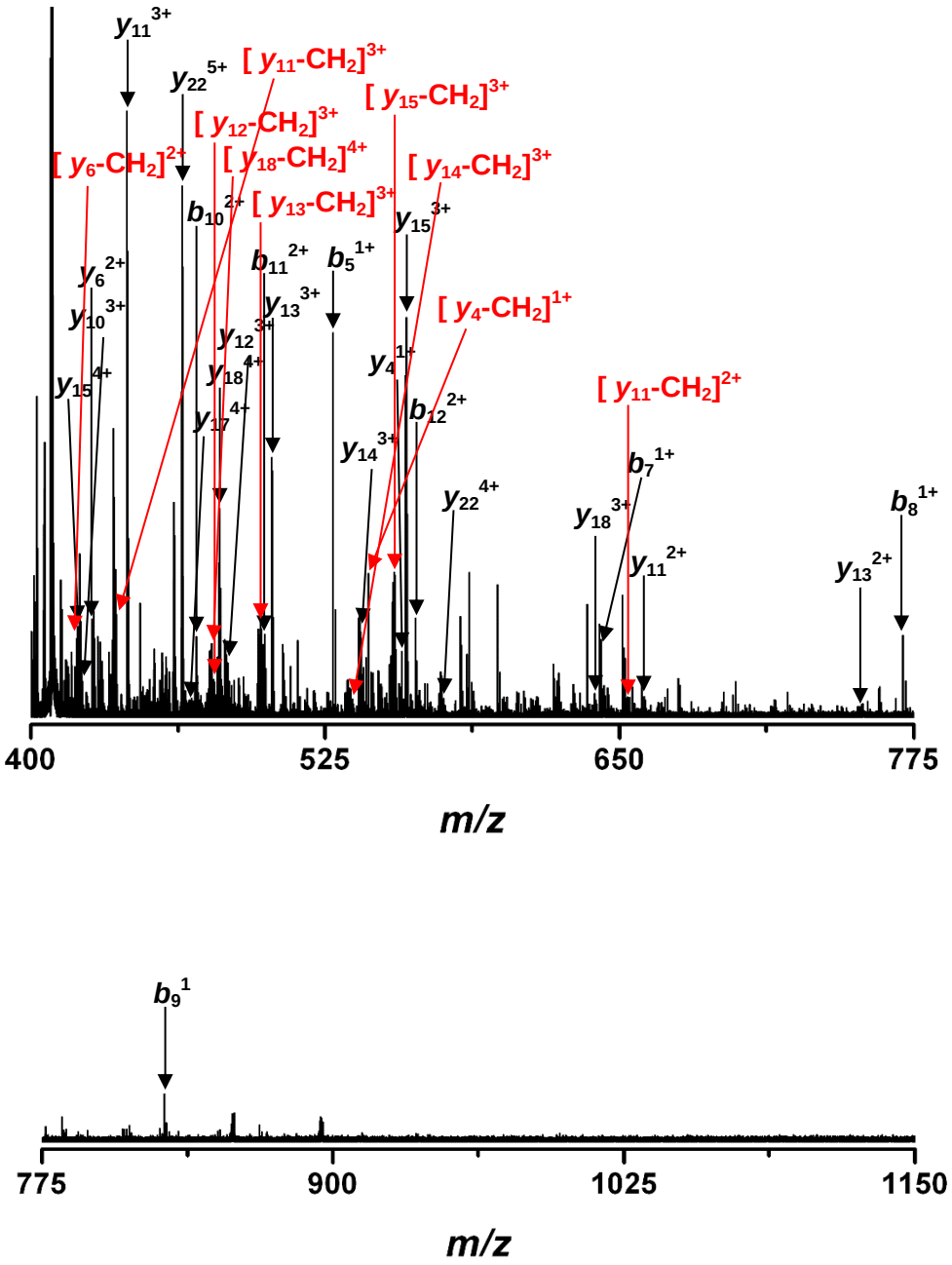

Figure 5.49: CID spectrum of 6^+ charge state of tri-methylated N-terminal region of histone H4 at 408 *m/z* after digestion with Asp-N. Fragments corresponding to di-methylated species are shown in red. A complete list of the assigned fragment ions is attached as Appendix A48.

Figure 5.50 below shows the spectrum acquired after ECD of the same ion with a combined fragment ion map generated from both the CID and ECD data.

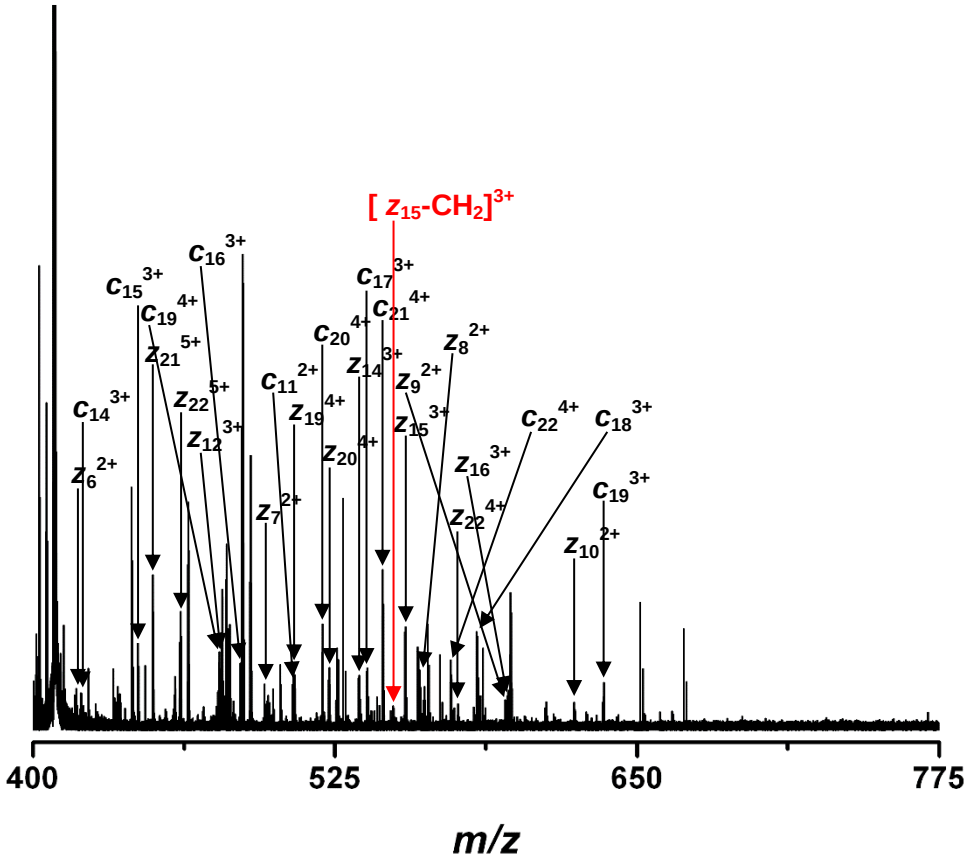
[z15-CH2]3+
c16 3+
c15 3+
c19 4+
z21 5+
c17 3+
c21 4+
c20 4+
z8 2+
z14 3+
c11 2+
z9 2+
z22 5+
z19 4+
z15 3+
c14 3+
z12 3+
c22 4+
c18 3+
z20 4+
z16 3+
z6 2+
c19 3+
z7 2+
z22 4+
z10 2+
400
525
650
775
m/z

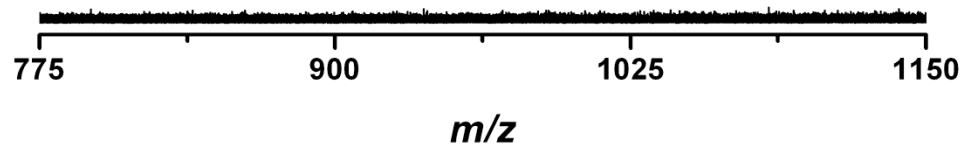
775
900
1025
1150
m/z

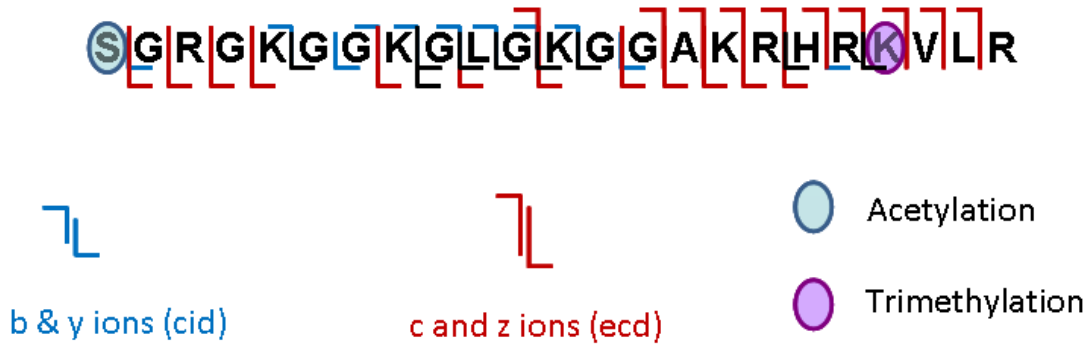

Figure 5.50: ECD spectrum of 6^+ charge state of tri-methylated N-terminal region of histone H4 at 408 *m/z* after digestion with Asp-N. A combined fragment ion map is given at the bottom of the figure. Fragments corresponding to di-methylated species are shown in red and fragments confirming the presence of di- and tri-methylated species in the fragment ion map are shown in black. A complete list of the assigned fragment ions is attached as Appendix A49.

Fragmentation of the 6^+ charge state of the tri-methylated N-terminal fragment revealed the presence of di-methylated fragments, with the di-methyl group located at lysine 20. Di-methylated fragments were observed in both CID and ECD spectra.

To determine if the source of the di-methylated fragment ions was from a di-methylated precursor ion, isolated and fragment alongside the tri-methylated precursor, the abundance of the fragment ions was quantitatively compared to the abundance of the isolated precursor ions. This quantitative comparison was based on the fragment ion relative ratios (FIRR), a technique in use to analyze the components of heterogeneous mixtures and which is particularly suitable for application to histone PTMs[210]. As an example, if a tri-methylated precursor ion was isolated which consisted of a mixture of ions carrying a tri-methyl group at a single residue or a di-and mono-methyl group at two residues, although having the same intact mass, then the abundance of di- and mono-methyl product ions should reflect the proportion of these ions present in the isolated precursor. Figure 5.51 below shows the isolation that was achieved when selecting the ion at 756 *m/z*, corresponding to the 15^+ charge state of histone H4 for fragmentation from the pooled MeCP2 knockout mouse brain sample (previously shown in Figure 5.10).

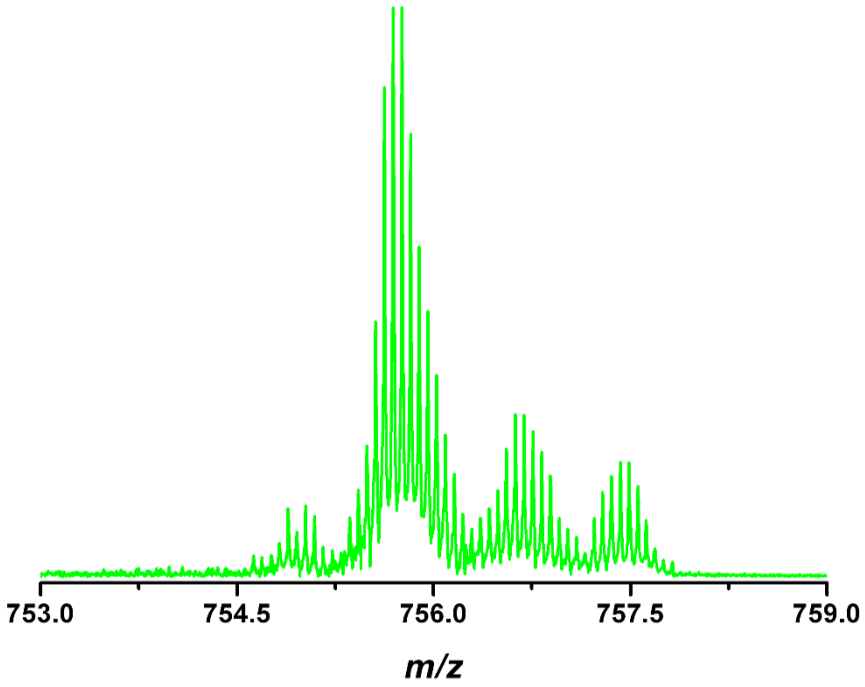

Figure 5.51: Isolation of ion at 756 *m/z* corresponding to 15^+ charge state of histone H4 from MeCP2 knockout pooled mouse brain sample.

Quantitation was carried out by integration of the area under the signal peaks and normalizing by this value to give a percentage abundance of each isoform in the isolation window. In the above spectrum, mono-methylated histone H4 (756.6 *m/z*) accounted for roughly 20 % of the ions detected. Di-methylated H4 (755.0 *m/z* and 757.4 *m/z*) accounted for roughly 17 % of the detected signal while tri-methylated H4 (755.7 *m/z*) accounted for over 60 % of the ions detected. If the di-methylated precursor ions were the source of the di-methylated product ions observed in the CID and ECD spectra, their relative abundances should be similar to that of the precursor ions; in this case roughly 4:1 (tri-methylated : di-methylated). Figure 5.52 below shows an expanded region of the CID spectrum corresponding to the precursor isolation of the ion at 756 *m/z* as shown in the figure above, which is focused over a narrow range where only two b_{53} product ions are visible.

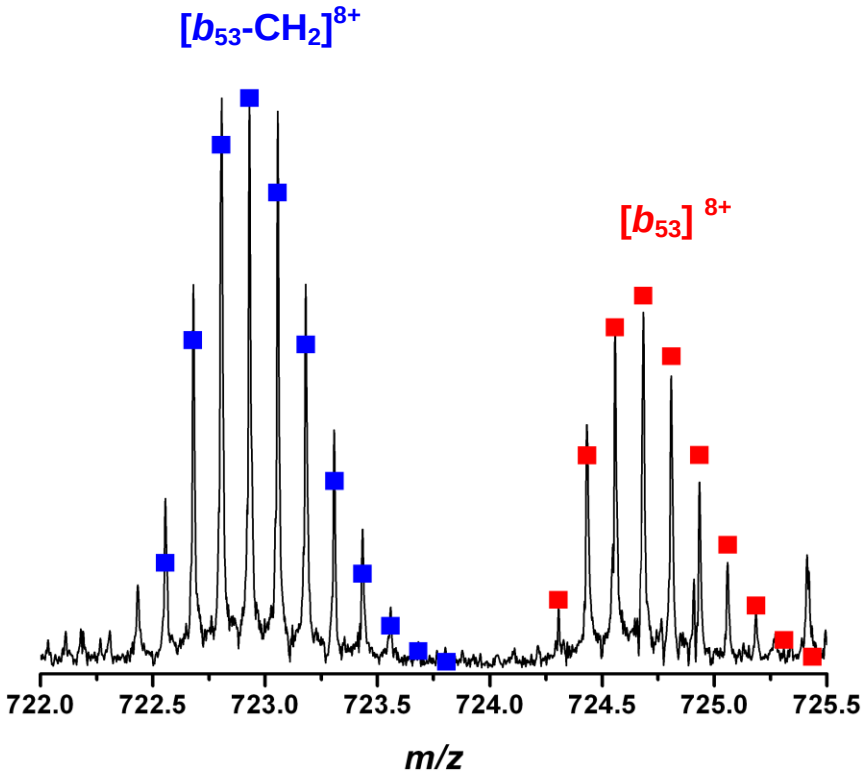

Figure 5.52: Expanded view of CID spectrum focusing on b_{53} product ions observed in MeCP2 knockout pooled mouse brain sample. Isotope simulations are overlaid for the tri-methylated product ion (red squares) and di-methylated product ion (blue squares).

This region of the spectrum contains two fragment ions, both corresponding to modified forms of b_{53}. The red isotope simulation overlaid is that of a tri-methylated b_{53} ion while the blue simulation is that of the di-methylated ion, and the relative abundance of each is roughly 60 % : 40 % (di-methylated : tri-methylated). This ratio does not match the results expected from the ratio of the precursor ions seen in Figure 5.51, suggesting that the di-methylated product ions could not all have originated from the di-methylated precursor ions.

Further confirmation can be found by examination of Figure 5.48 above which showed the degree of mass isolation achieved for the 6^+ charge state of the ion corresponding in mass to the tri-methylated N-terminal region of histone H4 after digestion with endoproteinases Asp-N. The ECD fragmentation spectrum (Figure 5.50) revealed that a

di-methylated product ion (z_{15}) was present. Figure 5.53 below shows an expanded view of the ECD fragmentation spectrum showing this z_{15} product ion together with the corresponding tri-methylated z_{15} product ion.

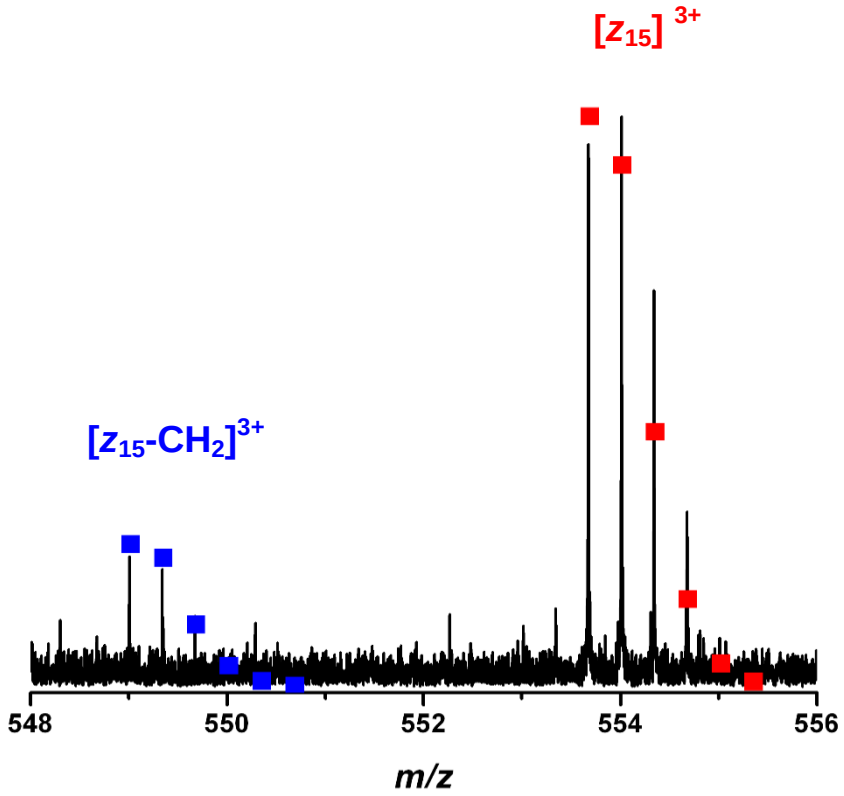

Figure 5.53: Expanded view of ECD spectrum of 6^+ charge state of tri-methylated N-terminal region of histone H4 from WT pooled mouse brain after digestion with Asp-N focusing on z_{15} product ions. Isotope simulations are overlaid for tri-methylated product ions (red squares) and di-methylated product ions (blue squares).

Although no other ions were detected in the isolation of the tri-methylated precursor, di-methylated product ions were observed after fragmentation. In each case where fragmentation was performed on a tri-methylated ion, di-methylated product ions were detected, and their presence cannot be accounted for.

This observation can potentially shed some light on the contradicting results of previous work which focused on changes to histone H4 PTM profile due to MeCP2 mutation.

5.4 Conclusions

The results presented in Section 5.3 show that in a mouse model, MeCP2 mutation has an effect on the PTM profile of histone H4. This was demonstrated in pooled and single mouse brain samples by top-down and middle-down mass spectrometry. These changes can potentially be explained by the known function of MeCP2 as a protein which binds to methylated DNA. Several DNA binding proteins are known to affect histone PTM profile through the recruitment of histone modifying enzymes, thus creating an altered PTM profile. While an increase in the abundance of acetylated histone H4 was observed, hyper-acetylation was not seen in any of the samples investigated, suggesting a limit to the ability of MeCP2 mutation to result in increased acetylation of histone H4.

In a mouse model, the PTM profile of histone H4 is similar to that observed in cells grown in culture (results shown in Chapter 3), and likely follow a similar order to the addition of post-translational modifications. A difference is visible in the PTM profile of histone H4 for wild type mice when compared to MeCP2 knockout. This difference has been characterized as an increase in the abundance of tri-methylated histone H4, with the tri-methyl group located at lysine 20. This difference is evident in pooled brain samples and in samples generated from a single mouse brain. Tri-methylation of histone H4, a modification known to accumulate in ageing tissues, serves as an indicator of transcriptional repression; an observation which is in agreement with earlier hypotheses about the biological function of this PTM[211,212].

Unlike cells grown in culture, the results presented above suggest that histone H4 extracted from a primary tissue source exists as a heterogeneous mixture to a much lesser extent. The fragmentation data did not suggest that modified species of H4 exist as a mixture with the modifications present at multiple lysine residues. The interpretation of fragmentation spectra of tri-methylated histone H4 can be complicated due to the

observation that di-methylated fragment ions can be present in the product ion spectra, even if they are absent during precursor isolation. This leads to a hypothesis that the tri-methylation at lysine 20 could be an inherently unstable modification, such that after the input of energy (during the fragmentation event), the loss of a methylene group occurs leading to the detection of a di-methylated product ion. Di-methylated product ions were detected after CID and ECD fragmentation of wild type and MeCP2 knockout samples by top-down and middle-down mass spectrometry.

5.5 Future Work

While the results presented have revealed that MeCP2 mutation (in this case deletion) have resulted in an increase in tri-methylated histone H4, future work could focus on whether or not this effect is present in all neural cell types. The work above was performed on whole brain samples, however neural tissue is known to be composed primarily of two cell types; neurons and glia. In the brain, glia are present at roughly twice the number of neurons, so an extension to this work could begin by separation of each cell type from the whole brain (of wild type and MeCP2 knockout), followed by histone extraction and mass spectrometry. This work could also confirm the results of a previous study which estimated the relative amount of MeCP2 in whole brain samples[213].

In addition, the present study has focused only on MeCP2 deletion (for the reason that deletion of the gene would most likely result in more severe symptoms). As well as focusing on the analysis of histone H4 from single cell types, investigation into the effects of MeCP2 mutation, i.e. mutations leading to truncated forms of the protein could reveal how changes to specific regions of the MeCP2 protein result in altered histone PTMs.

References

1 Crick, F. CENTRAL DOGMA OF MOLECULAR BIOLOGY. *Nature* **227**, 561-&, doi:10.1038/227561a0 (1970).

2 Watson, J. D. & Crick, F. H. C. MOLECULAR STRUCTURE OF NUCLEIC ACIDS - A STRUCTURE FOR DEOXYRIBOSE NUCLEIC ACID. *Nature* **171**, 737-738, doi:10.1038/171737a0 (1953).

3 Ghosh, A. & Bansal, M. A glossary of DNA structures from A to Z. *Acta Crystallographica Section D-Biological Crystallography* **59**, 620-626, doi:10.1107/s0907444903003251 (2003).

4 Schlissel, M. S. Regulating antigen-receptor gene assembly. *Nature Reviews Immunology* **3**, 890-899, doi:10.1038/nri1225 (2003).

5 Razin, A. & Cedar, H. DISTRIBUTION OF 5-METHYLCYTOSINE IN CHROMATIN. *Proceedings of the National Academy of Sciences of the United States of America* **74**, 2725-2728, doi:10.1073/pnas.74.7.2725 (1977).

6 Razin, A. & Riggs, A. D. DNA METHYLATION AND GENE-FUNCTION. *Science* **210**, 604-610, doi:10.1126/science.6254144 (1980).

7 Razin, A. CpG methylation, chromatin structure and gene silencing - a three-way connection. *Embo Journal* **17**, 4905-4908, doi:10.1093/emboj/17.17.4905 (1998).

8 Razin, A. & Shemer, R. Epigenetic control of gene expression. *Results and problems in cell differentiation* **25**, 189-204 (1999).

9 Keshet, I., Liemanhurwitz, J. & Cedar, H. DNA METHYLATION AFFECTS THE FORMATION OF ACTIVE CHROMATIN. *Cell* **44**, 535-543, doi:10.1016/0092-8674(86)90263-1 (1986).

10 Bird, A. THE ESSENTIALS OF DNA METHYLATION. *Cell* **70**, 5-8, doi:10.1016/0092-8674(92)90526-i (1992).

11 Tate, P. H. & Bird, A. P. Effects of DNA methylation on DNA-binding proteins and gene expression. *Current opinion in genetics & development* **3**, 226-231, doi:10.1016/0959-437x(93)90027-m (1993).

12 Jones, P. L. *et al.* Methylated DNA and MeCP2 recruit histone deacetylase to repress transcription. *Nature Genetics* **19**, 187-191, doi:10.1038/561 (1998).

13 Struhl, K. Histone acetylation and transcriptional regulatory mechanisms. *Genes & Development* **12**, 599-606, doi:10.1101/gad.12.5.599 (1998).

14 Jaenisch, R. & Jahner, D. METHYLATION, EXPRESSION AND CHROMOSOMAL POSITION OF GENES IN MAMMALS. *Biochimica Et Biophysica Acta* **782**, 1-9, doi:10.1016/0167-4781(84)90099-x (1984).

15 Bestor, T. H. CLONING OF A MAMMALIAN DNA METHYLTRANSFERASE. *Gene* **74**, 9-12, doi:10.1016/0378-1119(88)90238-7 (1988).

16 Leonhardt, H., Page, A. W., Weier, H. U. & Bestor, T. H. A TARGETING SEQUENCE DIRECTS DNA METHYLTRANSFERASE TO SITES OF DNA-REPLICATION IN MAMMALIAN NUCLEI. *Cell* **71**, 865-873, doi:10.1016/0092-8674(92)90561-p (1992).

17 Finch, J. T. *et al.* STRUCTURE OF NUCLEOSOME CORE PARTICLES OF CHROMATIN. *Nature* **269**, 29-36, doi:10.1038/269029a0 (1977).

18 Kornberg, R. D. & Thomas, J. O. CHROMATIN STRUCTURE - OLIGOMERS OF HISTONES. *Science* **184**, 865-868, doi:10.1126/science.184.4139.865 (1974).

19 Kornberg, R. D. CHROMATIN STRUCTURE - REPEATING UNIT OF HISTONES AND DNA. *Science* **184**, 868-871, doi:10.1126/science.184.4139.868 (1974).

20 Noll, M. SUBUNIT STRUCTURE OF CHROMATIN. *Nature* **251**, 249-251, doi:10.1038/251249a0 (1974).

21 Pardon, J. F. & Wilkins, M. H. F. SUPER-COIL MODEL FOR NUCLEOHISTONE. *Journal of Molecular Biology* **68**, 115-& (1972).

22 Thomas, J. O. & Kornberg, R. D. OCTAMER OF HISTONES IN CHROMATIN AND FREE IN SOLUTION. *Proceedings of the National Academy of Sciences of the United States of America* **72**, 2626-2630, doi:10.1073/pnas.72.7.2626 (1975).

23 Thomas, J. O. & Kornberg, R. D. CLEAVABLE CROSS-LINKS IN ANALYSIS OF HISTONE-HISTONE ASSOCIATIONS. *Febs Letters* **58**, 353-358, doi:10.1016/0014-5793(75)80296-1 (1975).

24 Woodcock, C. L. F. ULTRASTRUCTURE OF INACTIVE CHROMATIN. *Journal of Cell Biology* **59**, 368 (1973).

25 Olins, A. L. & Olins, D. E. SPHEROID CHROMATIN UNITS (RU BODIES). *Science* **183**, 330-332, doi:10.1126/science.183.4122.330 (1974).

26 Noll, M. INTERNAL STRUCTURE OF CHROMATIN SUBUNIT. *Nucleic Acids Research* **1**, 1573-&, doi:10.1093/nar/1.11.1573 (1974).

27 Finch, J. T., Noll, M. & Kornberg, R. D. ELECTRON-MICROSCOPY OF DEFINED LENGTHS OF CHROMATIN. *Proceedings of the National Academy of Sciences of the United States of America* **72**, 3320-3322, doi:10.1073/pnas.72.9.3320 (1975).

28 Binastein, M. & Simpson, R. T. SPECIFIC FOLDING AND CONTRACTION OF DNA BY HISTONES H-3 AND H-4. *Cell* **11**, 609-618, doi:10.1016/0092-8674(77)90078-2 (1977).

29 Roth, S. Y. & Allis, C. D. Histone acetylation and chromatin assembly: A single escort, multiple dances? *Cell* **87**, 5-8, doi:10.1016/s0092-8674(00)81316-1 (1996).

30 Ling, X. F., Harkness, T. A. A., Schultz, M. C., FisherAdams, G. & Grunstein, M. Yeast histone H3 and H4 amino termini are important for nucleosome assembly in vivo and in vitro: Redundant and position-independent functions in assembly but not in gene regulation. *Genes & Development* **10**, 686-699, doi:10.1101/gad.10.6.686 (1996).

31 Lorch, Y., Lapointe, J. W. & Kornberg, R. D. NUCLEOSOMES INHIBIT THE INITIATION OF TRANSCRIPTION BUT ALLOW CHAIN ELONGATION WITH THE DISPLACEMENT OF HISTONES. *Cell* **49**, 203-210, doi:10.1016/0092-8674(87)90561-7 (1987).

32 Chicoine, L. G., Richman, R., Cook, R. G., Gorovsky, M. A. & Allis, C. D. A SINGLE HISTONE ACETYLTRANSFERASE FROM TETRAHYMENA MACRONUCLEI CATALYZES DEPOSITION-RELATED ACETYLATION OF FREE HISTONES AND TRANSCRIPTION-RELATED ACETYLATION OF NUCLEOSOMAL HISTONES. *Journal of Cell Biology* **105**, 127-135, doi:10.1083/jcb.105.1.127 (1987).

33 Allis, C. D., Chicoine, L. G., Richman, R. & Schulman, I. G. DEPOSITION-RELATED HISTONE ACETYLATION IN MICRONUCLEI OF CONJUGATING TETRAHYMENA. *Proceedings of the National Academy of Sciences of the United States of America* **82**, 8048-8052, doi:10.1073/pnas.82.23.8048 (1985).

34 Allis, C. D., Bowen, J. K., Abraham, G. N., Glover, C. V. C. & Gorovsky, M. A. PROTEOLYTIC PROCESSING OF HISTONE-H3 IN CHROMATIN - A PHYSIOLOGICALLY REGULATED EVENT IN TETRAHYMENA MICRONUCLEI. *Cell* **20**, 55-64 (1980).

35 Vavra, K. J., Allis, C. D. & Gorovsky, M. A. REGULATION OF HISTONE ACETYLATION IN TETRAHYMENA MACRONUCLEI AND MICRONUCLEI. *Journal of Biological Chemistry* **257**, 2591-2598 (1982).

36 Allis, C. D., Ziegler, Y. S., Gorovsky, M. A. & Olmsted, J. B. A CONSERVED HISTONE VARIANT ENRICHED IN NUCLEOLI OF MAMMALIAN-CELLS. *Cell* **31**, 131-136, doi:10.1016/0092-8674(82)90412-3 (1982).

37 Allis, C. D., Glover, C. V. C., Bowen, J. K. & Gorovsky, M. A. HISTONE VARIANTS SPECIFIC TO THE TRANSCRIPTIONALLY ACTIVE, AMITOTICALLY DIVIDING MACRONUCLEUS OF THE UNICELLULAR EUCARYOTE, TETRAHYMENA-THERMOPHILA. *Cell* **20**, 609-617, doi:10.1016/0092-8674(80)90307-4 (1980).

38 White, E. M., Shapiro, D. L., Allis, C. D. & Gorovsky, M. A. SEQUENCE AND PROPERTIES OF THE MESSAGE ENCODING TETRAHYMENA HV1, A HIGHLY EVOLUTIONARILY CONSERVED HISTONE H2A VARIANT THAT IS ASSOCIATED WITH ACTIVE GENES. *Nucleic Acids Research* **16**, 179-198, doi:10.1093/nar/16.1.179 (1988).

39 Chicoine, L. G., Schulman, I. G., Richman, R., Cook, R. G. & Allis, C. D. NONRANDOM UTILIZATION OF ACETYLATION SITES IN HISTONES ISOLATED FROM TETRAHYMENA - EVIDENCE FOR FUNCTIONALLY DISTINCT H-4 ACETYLATION SITES. *Journal of Biological Chemistry* **261**, 1071-1076 (1986).

40 Rea, S. *et al.* Regulation of chromatin structure by site-specific histone H3 methyltransferases. *Nature* **406**, 593-599 (2000).

41 VetteseDadey, M. *et al.* Acetylation of histone H4 plays a primary role in enhancing transcription factor binding to nucleosomal DNA in vitro. *Embo Journal* **15**, 2508-2518 (1996).

42 Jenuwein, T. & Allis, C. D. Translating the histone code. *Science* **293**, 1074-1080, doi:10.1126/science.1063127 (2001).

43 Goto, Y. & Kimura, H. Inactive X chromosome-specific histone H3 modifications and CpG hypomethylation flank a chromatin boundary between an X-inactivated and an escape gene. *Nucleic Acids Research* **37**, 7416-7428, doi:10.1093/nar/gkp860 (2009).

44 Sun, H., Zhou, X., Chen, H. B., Li, Q. & Costa, M. Modulation of histone methylation and MLH1 gene silencing by hexavalent chromium. *Toxicology and Applied Pharmacology* **237**, 258-266, doi:10.1016/j.taap.2009.04.008 (2009).

45 Zhou, X., Li, Q., Arita, A., Sun, H. & Costa, M. Effects of nickel, chromate, and arsenite on histone 3 lysine methylation. *Toxicology and Applied Pharmacology* **236**, 78-84, doi:10.1016/j.taap.2009.01.009 (2009).

46 Berger, S. L. An embarrassment of niches: the many covalent modifications of histones in transcriptional regulation. *Oncogene* **20**, 3007-3013, doi:10.1038/sj.onc.1204324 (2001).

47 Taplick, J., Kurtev, V., Lagger, G. & Seiser, C. Histone H4 acetylation during interleukin-2 stimulation of mouse T cells. *Febs Letters* **436**, 349-352, doi:10.1016/s0014-5793(98)01164-8 (1998).

48 Grant, P. A. & Berger, S. L. Histone acetyltransferase complexes. *Seminars in Cell & Developmental Biology* **10**, 169-177, doi:10.1006/scdb.1999.0298 (1999).

49 Chahal, S. S., Matthews, H. R. & Bradbury, E. M. ACETYLATION OF HISTONE H-4 AND ITS ROLE IN CHROMATIN STRUCTURE AND FUNCTION. *Nature* **287**, 76-79, doi:10.1038/287076a0 (1980).

50 Richards, B. M. & Pardon, J. F. MOLECULAR STRUCTURE OF NUCLEOHISTONE (DNH). *Experimental Cell Research* **62**, 184-&, doi:10.1016/0014-4827(79)90519-6 (1970).

51 Noll, M. & Kornberg, R. D. ACTION OF MICROCOCCAL NUCLEASE ON CHROMATIN AND LOCATION OF HISTONE H-1. *Journal of Molecular Biology* **109**, 393-404, doi:10.1016/s0022-2836(77)80019-3 (1977).

52 Littau, V. C., Burdick, C. J., Allfrey, V. G. & Mirsky, A. E. ROLE OF HISTONES IN MAINTENANCE OF CHROMATIN STRUCTURE. *Proceedings of the National Academy of Sciences of the United States of America* **54**, 1204-&, doi:10.1073/pnas.54.4.1204 (1965).

53 Bradbury, E. M., Inglis, R. J. & Matthews, H. R. CONTROL OF CELL-DIVISION BY VERY LYSINE RICH HISTONE (F1) PHOSPHORYLATION. *Nature* **247**, 257-261, doi:10.1038/247257a0 (1974).

54 Prunell, A. & Kornberg, R. D. VARIABLE CENTER TO CENTER DISTANCE OF NUCLEOSOMES IN CHROMATIN. *Journal of Molecular Biology* **154**, 515-523, doi:10.1016/s0022-2836(82)80010-7 (1982).

55 Vaissiere, T., Sawan, C. & Herceg, Z. Epigenetic interplay between histone modifications and DNA methylation in gene silencing. *Mutation Research-Reviews in Mutation Research* **659**, 40-48, doi:10.1016/j.mrrev.2008.02.004 (2008).

56 Ryu, J. K. *et al.* SK-7041, a new histone deacetylase inhibitor, induces G2-M cell cycle arrest and apoptosis in pancreatic cancer cell lines. *Cancer Letters* **237**, 143-154, doi:10.1016/j.canlet.2005.05.040 (2006).

57 Kang, J. H., Lin, C. J., Chen, J. & Liu, Q. Copper induces histone hypoacetylation through directly inhibiting histone acetyltransferase activity. *Chemico-Biological Interactions* **148**, 115-123, doi:10.1016/j.cbi.2004.05.003 (2004).

58 Winston, F. & Allis, C. D. The bromodomain: a chromatin-targeting module? *Nature Structural Biology* **6**, 601-604, doi:10.1038/10640 (1999).

59 Giri, C. P., West, M. H. P. & Smulson, M. NUCLEAR PROTEIN MODIFICATION AND CHROMATIN SUBSTRUCTURE .1. DIFFERENTIAL POLY(ADENOSINE DIPHOSPHATE) RIBOSYLATION OF CHROMOSOMAL-PROTEINS IN NUCLEI VERSUS ISOLATED NUCLEOSOMES. *Biochemistry* **17**, 3495-3500, doi:10.1021/bi00610a011 (1978).

60 Giri, C. P., West, M. H. P., Ramirez, M. L. & Smulson, M. NUCLEAR PROTEIN MODIFICATION AND CHROMATIN SUBSTRUCTURE .2. INTERNUCLEOSOMAL LOCALIZATION OF POLY(ADENOSINE DIPHOSPHATE-RIBOSE) POLYMERASE. *Biochemistry* **17**, 3501-3504, doi:10.1021/bi00610a012 (1978).

61 Phillips, D. M. PRESENCE OF ACETYL GROUPS IN HISTONES. *Biochemical Journal* **87**, 258-& (1963).

62 Gershey, E. L., Vidali, G. & Allfrey, V. G. CHEMICAL STUDIES OF HISTONE ACETYLATION - OCCURRENCE OF EPSILON-N-ACETYLLYSINE IN F2A1 HISTONE. *Journal of Biological Chemistry* **243**, 5018-& (1968).

63 Grant, P. A. *et al.* A subset of TAF(II)s are integral components of the SAGA complex required for nucleosome acetylation and transcriptional stimulation. *Cell* **94**, 45-53, doi:10.1016/s0092-8674(00)81220-9 (1998).

64 Grant, P. A., Sterner, D. E., Duggan, L. J., Workman, J. L. & Berger, S. L. The SAGA unfolds: convergence of transcription regulators in chromatin-modifying complexes. *Trends in Cell Biology* **8**, 193-197, doi:10.1016/s0962-8924(98)01263-x (1998).

65 Mizzen, C. A. *et al.* The TAF(II)250 subunit of TFIID has histone acetyltransferase activity. *Cell* **87**, 1261-1270, doi:10.1016/s0092-8674(00)81821-8 (1996).

66 Berger, S. L. Gene activation by histone and factor acetyltransferases. *Current Opinion in Cell Biology* **11**, 336-341, doi:10.1016/s0955-0674(99)80046-5 (1999).

67 Fenn, J. B. Electrospray wings for molecular elephants (Nobel lecture). *Angewandte Chemie-International Edition* **42**, 3871-3894, doi:10.1002/anie.200300605 (2003).

68 Tanaka, K. The origin of macromolecule ionization by laser irradiation (Nobel lecture). *Angewandte Chemie-International Edition* **42**, 3860-3870, doi:10.1002/anie.200300585 (2003).

69 O'Farrell, P., H. High resolution two dimensional electrophoresis of proteins. *Journal of Biological Chemistry* **250**, 4007-4021 (1975).

70 Siuti, N. & Kelleher, N. L. Decoding protein modifications using top-down mass spectrometry. *Nature Methods* **4**, 817-821, doi:10.1038/nmeth1097 (2007).

71 Macht, M. Mass spectrometric top-down analysis of proteins. *Bioanalysis* **1**, 1131-1148, doi:10.4155/bio.09.93 (2009).

72 Reid, G. E. & McLuckey, S. A. 'Top down' protein characterization via tandem mass spectrometry. *Journal of Mass Spectrometry* **37**, 663-675, doi:10.1002/jms.346 (2002).

73 Han, X. M., Jin, M., Breuker, K. & McLafferty, F. W. Extending top-down mass spectrometry to proteins with masses greater than 200 kilodaltons. *Science* **314**, 109-112, doi:10.1126/science.1128868 (2006).

74 Boyne, M. T. *et al.* Tandem Mass Spectrometry with Ultrahigh Mass Accuracy Clarifies Peptide Identification by Database Retrieval. *Journal of Proteome Research* **8**, 374-379, doi:10.1021/pr800635m (2009).

75 Vestling, M. M., Kelly, M. A. & Fenselau, C. OPTIMIZATION BY MASS-SPECTROMETRY OF A TRYPTOPHAN-SPECIFIC PROTEIN CLEAVAGE REACTION. *Rapid Communications in Mass Spectrometry* **8**, 786-790, doi:10.1002/rcm.1290080925 (1994).

76 Bogdanov, B. & Smith, R. D. Proteomics by FTICR mass spectrometry: Top down and bottom up. *Mass Spectrometry Reviews* **24**, 168-200, doi:10.1002/mas.20015 (2005).

77 Domon, B. & Aebersold, R. Review - Mass spectrometry and protein analysis. *Science* **312**, 212-217, doi:10.1126/science.1124619 (2006).

78 Khalsa-Moyers, G. & McDonald, W. H. Developments in mass spectrometry for the analysis of complex protein mixtures. *Briefings in Functional Genomics & Proteomics* **5**, 98-111, doi:10.1093/bfgp/ell023 (2006).

79 Karas, M., Bachmann, D. & Hillenkamp, F. INFLUENCE OF THE WAVELENGTH IN HIGH-IRRADIANCE ULTRAVIOLET-LASER DESORPTION MASS-SPECTROMETRY OF ORGANIC-MOLECULES. *Analytical Chemistry* **57**, 2935-2939, doi:10.1021/ac00291a042 (1985).

80 Dole, M., Mack, L. L. & Hines, R. L. MOLECULAR BEAMS OF MACROIONS. *Journal of Chemical Physics* **49**, 2240-&, doi:10.1063/1.1670391 (1968).

81 Hillenkamp, F., Karas, M. & Rosmarinowsky, J. PROCESSES OF LASER-INDUCED ION FORMATION IN MASS-SPECTROMETRY. *Acs Symposium Series* **291**, 69-82 (1985).

82 Hillenkamp, F., Bahr, U., Karas, M. & Spengler, B. MECHANISMS OF LASER ION FORMATION FOR MASS-SPECTROMETRIC ANALYSIS. *Scanning Microscopy*, 33-39 (1987).

83 Karas, M., Bachmann, D., Bahr, U. & Hillenkamp, F. MATRIX-ASSISTED ULTRAVIOLET-LASER DESORPTION OF NONVOLATILE COMPOUNDS. *International Journal of Mass Spectrometry and Ion Processes* **78**, 53-68, doi:10.1016/0168-1176(87)87041-6 (1987).

84 G, T. Disintegration of Water Droplets in an Electric Field. *Proc. Roy. Soc. London. Ser. A* **280**, 383 (1964).

85 Gaskell, S. Electrospray: Principles and practice (vol 32, pg 677, 1997). *Journal of Mass Spectrometry* **32**, 1378-1378, doi:10.1002/(sici)1096-9888(199712)32:12<1378::aid-jms1600>3.3.co;2-g (1997).

86 Hendrickson, C. L. & Emmett, M. R. Electrospray ionization Fourier transform ion cyclotron resonance mass spectrometry. *Annual Review of Physical Chemistry* **50**, 517-536, doi:10.1146/annurev.physchem.50.1.517 (1999).

87 Kebarle, P. A brief overview of the present status of the mechanisms involved in electrospray mass spectrometry. *Journal of Mass Spectrometry* **35**, 804-817, doi:10.1002/1096-9888(200007)35:7<804::aid-jms22>3.3.co;2-h (2000).

88 Nguyen, S. & Fenn, J. B. Gas-phase ions of solute species from charged droplets of solutions. *Proceedings of the National Academy of Sciences of the United States of America* **104**, 1111-1117, doi:10.1073/pnas.0609969104 (2007).

89 Iribarne, J. V. & Thomson, B. A. EVAPORATION OF SMALL IONS FROM CHARGED DROPLETS. *Journal of Chemical Physics* **64**, 2287-2294, doi:10.1063/1.432536 (1976).

90 Thomson, B. A. & Iribarne, J. V. FIELD-INDUCED ION EVAPORATION FROM LIQUID SURFACES AT ATMOSPHERIC-PRESSURE. *Journal of Chemical Physics* **71**, 4451-4463, doi:10.1063/1.438198 (1979).

91 Comisaro.Mb & Marshall, A. G. FOURIER-TRANSFORM ION-CYCLOTRON RESONANCE SPECTROSCOPY. *Chemical Physics Letters* **25**, 282-283, doi:10.1016/0009-2614(74)89137-2 (1974).

92 Comisaro.Mb & Marshall, A. G. FREQUENCY-SWEEP FOURIER-TRANSFORM ION-CYCLOTRON RESONANCE SPECTROSCOPY. *Chemical Physics Letters* **26**, 489-490, doi:10.1016/0009-2614(74)80397-0 (1974).

93 Comisarow, M. B. & Marshall, A. G. THEORY OF FOURIER-TRANSFORM ION-CYCLOTRON RESONANCE MASS-SPECTROSCOPY .1. FUNDAMENTAL EQUATIONS AND LOW-PRESSURE LINE-SHAPE. *Journal of Chemical Physics* **64**, 110-119, doi:10.1063/1.431959 (1976).

94 Marshall, A. G., Hendrickson, C. L. & Jackson, G. S. Fourier transform ion cyclotron resonance mass spectrometry: A primer. *Mass Spectrometry Reviews* **17**, 1-35, doi:10.1002/(sici)1098-2787(1998)17:1<1::aid-mas1>3.0.co;2-k (1998).

95 Amster, I. J. Fourier transform mass spectrometry. *Journal of Mass Spectrometry* **31**, 1325-1337 (1996).

96 Marshall, A. G. & Hendrickson, C. L. Fourier transform ion cyclotron resonance detection: principles and experimental configurations. *International Journal of Mass Spectrometry* **215**, 59-75, doi:10.1016/s1387-3806(01)00588-7 (2002).

97 Opsal, R. B., Owens, K. G. & Reilly, J. P. RESOLUTION IN THE LINEAR TIME-OF-FLIGHT MASS-SPECTROMETER. *Analytical Chemistry* **57**, 1884-1889, doi:10.1021/ac00286a020 (1985).

98 Clauser, K. R., Baker, P. & Burlingame, A. L. Role of accurate mass measurement (+/- 10 ppm) in protein identification strategies employing MS or MS MS and database searching. *Analytical Chemistry* **71**, 2871-2882, doi:10.1021/ac9810516 (1999).

99 Guan, S. H. & Marshall, A. G. ION TRAPS FOR FOURIER-TRANSFORM ION-CYCLOTRON RESONANCE MASS-SPECTROMETRY - PRINCIPLES AND DESIGN OF GEOMETRIC AND ELECTRIC CONFIGURATIONS. *International Journal of Mass Spectrometry* **146**, 261-296, doi:10.1016/0168-1176(95)04190-v (1995).

100 Biemann, K. NOMENCLATURE FOR PEPTIDE FRAGMENT IONS (POSITIVE-IONS). *Methods in Enzymology* **193**, 886-887, doi:10.1016/0076-6879(90)93460-3 (1990).

101 Hayes, R. N. & Gross, M. L. COLLISION-INDUCED DISSOCIATION. *Methods in Enzymology* **193**, 237-263, doi:10.1016/0076-6879(90)93418-k (1990).

102 Shukla, A. K. & Futrell, J. H. Tandem mass spectrometry: dissociation of ions by collisional activation. *Journal of Mass Spectrometry* **35**, 1069-1090, doi:10.1002/1096-9888(200009)35:9<1069::aid-jms54>3.0.co;2-c (2000).

103 Sleno, L. & Volmer, D. A. Ion activation methods for tandem mass spectrometry. *Journal of Mass Spectrometry* **39**, 1091-1112, doi:10.1002/jms.703 (2004).

104 Wells, J. M. & McLuckey, S. A. in *Biological Mass Spectrometry* Vol. 402 *Methods in Enzymology* (ed A. L. Burlingame) 148-185 (Elsevier Academic Press Inc, 2005).

105 Biemann, K. SEQUENCING OF PEPTIDES BY TANDEM MASS-SPECTROMETRY AND HIGH-ENERGY COLLISION-INDUCED DISSOCIATION. *Methods in Enzymology* **193**, 455-479, doi:10.1016/0076-6879(90)93433-l (1990).

106 Little, D. P., Speir, J. P., Senko, M. W., Oconnor, P. B. & McLafferty, F. W. INFRARED MULTIPHOTON DISSOCIATION OF LARGE MULTIPLY-CHARGED IONS FOR BIOMOLECULE SEQUENCING. *Analytical Chemistry* **66**, 2809-2815, doi:10.1021/ac00090a004 (1994).

107 McLuckey, S. A. & Goeringer, D. E. Slow heating methods in tandem mass spectrometry. *Journal of Mass Spectrometry* **32**, 461-474, doi:10.1002/(sici)1096-9888(199705)32:5<461::aid-jms515>3.3.co;2-8 (1997).

108 Silivra, O. A., Kjeldsen, F., Ivonin, I. A. & Zubarev, R. A. Electron capture dissociation of polypeptides in a three-dimensional quadrupole ion trap: Implementation and first results. *Journal of the American Society for Mass Spectrometry* **16**, 22-27, doi:10.1016/j.jasms.2004.09..015 (2005).

109 Satake, H., Hasegawa, H., Hirabayashi, A., Hashimoto, Y. & Baba, T. Fast multiple electron capture dissociation in a linear radio frequency quadrupole ion trap. *Analytical Chemistry* **79**, 8755-8761, doi:10.1021/ac071462z (2007).

110 Zubarev, R. A., Kelleher, N. L. & McLafferty, F. W. Electron capture dissociation of multiply charged protein cations. A nonergodic process. *Journal of the American Chemical Society* **120**, 3265-3266, doi:10.1021/ja973478k (1998).

111 McLafferty, F. W. *et al.* Electron capture dissociation of gaseous multiply charged ions by Fourier-transform ion cyclotron resonance. *Journal of the American Society for Mass Spectrometry* **12**, 245-249, doi:10.1016/s1044-0305(00)00223-3 (2001).

112 Sweet, S. M. M. & Cooper, H. J. Electron capture dissociation in the analysis of protein phosphorylation. *Expert Review of Proteomics* **4**, 149-159, doi:10.1586/147894503.4.2.149 (2007).

113 Kelleher, N. L. *et al.* Localization of labile posttranslational modifications by electron capture dissociation: the case of gamma-carboxyglutamic acid. *Analytical chemistry* **71**, 4250-4253, doi:10.1021/ac990684x (1999).

114 Horn, D. M., Ge, Y. & McLafferty, F. W. Activated ion electron capture dissociation for mass spectral sequencing of larger (42 kDa) proteins. *Analytical Chemistry* **72**, 4778-4784, doi:10.1021/ac000494i (2000).

115 Cooper, H. J., Hakansson, K. & Marshall, A. G. The role of electron capture dissociation in biomolecular analysis. *Mass Spectrometry Reviews* **24**, 201-222, doi:10.1002/mas.20014 (2005).

116 Zubarev, R. A. Electron-capture dissociation tandem mass spectrometry. *Current Opinion in Biotechnology* **15**, 12-16, doi:10.1016/j.copbio.2003.12.002 (2004).

117 Syka, J. E. P., Coon, J. J., Schroeder, M. J., Shabanowitz, J. & Hunt, D. F. Peptide and protein sequence analysis by electron transfer dissociation mass spectrometry. *Proceedings of the National Academy of Sciences of the United States of America* **101**, 9528-9533, doi:10.1073/pnas.0402700101 (2004).

118 Zubarev, R. A., Haselmann, K. F., Budnik, B., Kjeldsen, F. & Jensen, F. Towards an understanding of the mechanism of electron-capture dissociation: a historical

perspective and modern ideas. *European Journal of Mass Spectrometry* **8**, 337-349, doi:10.1255/ejms.517 (2002).

119 Syrstad, E. A. & Turecek, F. Toward a general mechanism of electron capture dissociation. *Journal of the American Society for Mass Spectrometry* **16**, 208-224, doi:10.1016/j.jasms.2004.11.001 (2005).

120 Breuker, K., Oh, H. B., Lin, C., Carpenter, B. K. & McLafferty, F. W. Nonergodic and conformational control of the electron capture dissociation of protein cations. *Proceedings of the National Academy of Sciences of the United States of America* **101**, 14011-14016, doi:10.1073/pnas.0406095101 (2004).

121 Sohn, C. H. *et al.* Probing the Mechanism of Electron Capture and Electron Transfer Dissociation Using Tags with Variable Electron Affinity. *Journal of the American Chemical Society* **131**, 5444-5459, doi:10.1021/ja806534r (2009).

122 Jones, A. W. & Cooper, H. J. Probing the mechanisms of electron capture dissociation mass spectrometry with nitrated peptides. *Physical Chemistry Chemical Physics* **12**, 13394-13399, doi:10.1039/c0cp00623h (2010).

123 Simons, J. Mechanisms for S-S and N-C-alpha bond cleavage in peptide ECD and ETD mass spectrometry. *Chemical Physics Letters* **484**, 81-95, doi:10.1016/j.cplett.2009.10.062 (2010).

124 Lozzio, C. B. & Lozzio, B. B. HUMAN CHRONIC MYELOGENOUS LEUKEMIA CELL LINE WITH POSITIVE PHILADELPHIA CHROMOSOME. *Blood* **45**, 321-334 (1975).

125 Tsuchiya, S. *et al.* ESTABLISHMENT AND CHARACTERIZATION OF A HUMAN ACUTE MONOCYTIC LEUKEMIA-CELL LINE (THP-1). *International Journal of Cancer* **26**, 171-176, doi:10.1002/ijc.2910260208 (1980).

126 Brattain, M. G. *et al.* ENHANCEMENT OF GROWTH OF HUMAN-COLON TUMOR-CELL LINES BY FEEDER LAYERS OF MURINE FIBROBLASTS. *Journal of the National Cancer Institute* **69**, 767-771 (1982).

127 Quentmeier, H. *et al.* Cell line OCI/AML3 bears exon-12 NPM gene mutation-A and cytoplasmic expression of nucleophosmin. *Leukemia* **19**, 1760-1767, doi:10.1038/sj.leu.2403899 (2005).

128 Lange, B. *et al.* GROWTH-FACTOR REQUIREMENTS OF CHILDHOOD ACUTE-LEUKEMIA - ESTABLISHMENT OF GM-CSF DEPENDENT CELL-LINES. *Blood* **70**, 192-199 (1987).

129 Seon, B. K., Negoro, S. & Barcos, M. P. MONOCLONAL-ANTIBODY THAT DEFINES A UNIQUE HUMAN T-CELL LEUKEMIA ANTIGEN. *Proceedings of the National Academy of Sciences of the United States of America-Biological Sciences* **80**, 845-849, doi:10.1073/pnas.80.3.845 (1983).

130 Pulvertaft, R. J. V. CYTOLOGY OF BURKITTS TUMOUR (AFRICAN LYMPHOMA). *Lancet* **1**, 238-& (1964).

131 Caravatti, P. & Allemann, M. THE INFINITY CELL - A NEW TRAPPED-ION CELL WITH RADIOFREQUENCY COVERED TRAPPING ELECTRODES FOR FOURIER-TRANSFORM ION-CYCLOTRON RESONANCE MASS-SPECTROMETRY. *Organic Mass Spectrometry* **26**, 514-518, doi:10.1002/oms.1210260527 (1991).

132 Brenton, A. G. & Godfrey, A. R. Accurate Mass Measurement: Terminology and Treatment of Data. *Journal of the American Society for Mass Spectrometry* **21**, 1821-1835, doi:10.1016/j.jasms.2010.06.006 (2010).

133 LeDuc, R. D. *et al.* ProSight PTM: an integrated environment for protein identification and characterization by top-down mass spectrometry. *Nucleic Acids Research* **32**, W340-W345, doi:10.1093/nar/gkh447 (2004).

134 Larkin, M. A. *et al.* Clustal W and clustal X version 2.0. *Bioinformatics* **23**, 2947-2948, doi:10.1093/bioinformatics/btm404 (2007).

135 Lindsey, G. G., Thompson, P., Purves, L. R. & Vonholt, C. THE RECONSTITUTION OF HISTONE H3-H4 TETRAMER FROM ACID EXTRACTED HISTONES IN THE ABSENCE OF UREA. *Febs Letters* **145**, 131-136, doi:10.1016/0014-5793(82)81221-0 (1982).

136 Kouzarides, T. Chromatin modifications and their function. *Cell* **128**, 693-705, doi:10.1016/j.cell.2007.02.005 (2007).

137 Xu, W. S., Parmigiani, R. B. & Marks, P. A. Histone deacetylase inhibitors: molecular mechanisms of action. *Oncogene* **26**, 5541-5552, doi:10.1038/sj.onc.1210620 (2007).

138 Leggatt, G. R. & Gabrielli, B. Histone deacetylase inhibitors in the generation of the anti-tumour immune response. *Immunology and Cell Biology* **90**, 33-38, doi:10.1038/icb.2011.94 (2012).

139 Wu, Y. & Guo, S. W. Histone deacetylase inhibitors trichostatin A and valproic acid induce cell cycle arrest and p21 expression in immortalized human endometrial stromal cells. *European Journal of Obstetrics Gynecology and Reproductive Biology* **137**, 198-203, doi:10.1016/j.ejogrb.2007.02.014 (2008).

140 Sutherland, J. E., Peng, W., Zhang, Q. W. & Costa, M. The histone deacetylase inhibitor trichostatin A reduces nickel-induced gene silencing in yeast and mammalian cells. *Mutation Research-Fundamental and Molecular Mechanisms of Mutagenesis* **479**, 225-233, doi:10.1016/s0027-5107(01)00163-4 (2001).

141 Cortez, C. C. & Jones, P. A. Chromatin, cancer and drug therapies. *Mutation Research-Fundamental and Molecular Mechanisms of Mutagenesis* **647**, 44-51, doi:10.1016/j.mrfmmm.2008.07.006 (2008).

142 Hasan, A., Mitchell, A., Schneider, A., Halene, T. & Akbarian, S. Epigenetic dysregulation in schizophrenia: molecular and clinical aspects of histone deacetylase inhibitors. *European archives of psychiatry and clinical neuroscience* **263**, 273-284, doi:10.1007/s00406-013-0395-2 (2013).

143 Li, J. Y., Li, G. Q. & Xu, W. Q. Histone Deacetylase Inhibitors: An Attractive Strategy for Cancer Therapy. *Current Medicinal Chemistry* **20**, 1858-1886 (2013).

144 Yoshida, M., Horinouchi, S. & Beppu, T. TRICHOSTATIN-A AND TRAPOXIN - NOVEL CHEMICAL PROBES FOR THE ROLE OF HISTONE ACETYLATION IN CHROMATIN STRUCTURE AND FUNCTION. *Bioessays* **17**, 423-430, doi:10.1002/bies.950170510 (1995).

145 Vigushin, D. M. *et al.* Trichostatin A is a histone deacetylase inhibitor with potent antitumor activity against breast cancer in vivo. *Clinical Cancer Research* **7**, 971-976 (2001).

146 Yoshida, M. Potent and specific inhibition of mammalian histone deacetylase both in vivo and in vitro by trichostatin A. *Tanpakushitsu kakusan koso. Protein, nucleic acid, enzyme* **52**, 1788-1789 (2007).

147 Lachner, M. & Jenuwein, T. The many faces of histone lysine methylation. *Current Opinion in Cell Biology* **14**, 286-298, doi:10.1016/s0955-0674(02)00335-6 (2002).

148 Zee, B. M., Levin, R. S., DiMaggio, P. A. & Garcia, B. A. Global turnover of histone post-translational modifications and variants in human cells. *Epigenetics & Chromatin* **3**, 11, doi:10.1186/1756-8935-3-22 (2010).

149 Evertts, A. G. *et al.* Quantitative Dynamics of the Link between Cellular Metabolism and Histone Acetylation. *Journal of Biological Chemistry* **288**, 12142-12151, doi:10.1074/jbc.M112.428318 (2013).

150 Pesavento, J. J., Yang, H., Kelleher, N. L. & Mizzen, C. A. Certain and progressive methylation of histone H4 at lysine 20 during the cell cycle. *Molecular and Cellular Biology* **28**, 468-486, doi:10.1128/mcb.01517-07 (2008).

151 Lee, M. G. *et al.* Functional interplay between histone demethylase and deacetylase enzymes. *Molecular and Cellular Biology* **26**, 6395-6402, doi:10.1128/mcb.00723-06 (2006).

152 Prasad, K. N. & Sinha, P. K. EFFECT OF SODIUM BUTYRATE ON MAMMALIAN CELLS IN CULTURE A REVIEW. *In Vitro (Rockville)* **12**, 125-132, doi:10.1007/bf02796360 (1976).

153 Riggs, M. G., Whittaker, R. G., Neumann, J. R. & Ingram, V. M. NORMAL-BUTYRATE CAUSES HISTONE MODIFICATION IN HELA AND FRIEND ERYTHROLEUKEMIA CELLS. *Nature* **268**, 462-464, doi:10.1038/268462a0 (1977).

154 Davie, J. R. Inhibition of histone deacetylase activity by butyrate. *Journal of Nutrition* **133**, 2485S-2493S (2003).

155 Olmo, S. *et al.* Analysis of human histone H4 by capillary electrophoresis in a pullulan-coated capillary, LC-ESI-MS and MALDI-TOF-MS. *Analytical and Bioanalytical Chemistry* **390**, 1881-1888, doi:10.1007/s00216-008-1903-5 (2008).

156 Tsuji, N., Kobayashi, M., Nagashima, K., Wakisaka, Y. & Koizumi, K. NEW ANTIFUNGAL ANTIBIOTIC, TRICHOSTATIN. *Journal of Antibiotics* **29**, 1-6 (1976).

157 Bonenfant, D. *et al.* Analysis of dynamic changes in post-translational modifications of human histones during cell cycle by mass spectrometry. *Molecular & Cellular Proteomics* **6**, 1917-1932, doi:10.1074/mcp.M700070-MCP200 (2007).

158 Vanhaecke, T., Papeleu, P., Elaut, G. & Rogiers, V. Trichostatin A - like hydroxamate histone deacetylase inhibitors as therapeutic agents: Toxicological point of view. *Current Medicinal Chemistry* **11**, 1629-1643 (2004).

159 Smith, C. M. *et al.* Mass spectrometric quantification of acetylation at specific lysines within the amino-terminal tail of histone H4. *Analytical Biochemistry* **316**, 23-33, doi:10.1016/s0003-2697(03)00032-0 (2003).

160 Smith, C. M. Quantification of acetylation at proximal lysine residues using isotopic labeling and tandem mass spectrometry. *Methods* **36**, 395-403, doi:10.1016/j.ymeth.2005.03.007 (2005).

161 Su, X. D. *et al.* Histone H4 acetylation dynamics determined by stable isotope labeling with amino acids in cell culture and mass spectrometry. *Analytical Biochemistry* **363**, 22-34, doi:10.1016/j.ab.2006.12.031 (2007).

162 Ren, C. *et al.* Peptide mass mapping of acetylated isoforms of histone H4 from mouse lymphosarcoma cells treated with histone deacetylase (HDACs) inhibitors. *Journal of the American Society for Mass Spectrometry* **16**, 1641-1653, doi:10.1016/j.jasms.2005.06.001 (2005).

163 Zhang, K. L. & Tang, H. Analysis of core histones by liquid chromatography-mass spectrometry and peptide mapping. *Journal of Chromatography B-Analytical Technologies in the Biomedical and Life Sciences* **783**, 173-179, doi:10.1016/s1570-0232(02)00631-1 (2003).

164 Gatenby, R. A. & Gillies, R. J. Why do cancers have high aerobic glycolysis? *Nature Reviews Cancer* **4**, 891-899, doi:10.1038/nrc1478 (2004).

165 Icard, P. & Lincet, H. A global view of the biochemical pathways involved in the regulation of the metabolism of cancer cells. *Biochimica Et Biophysica Acta-Reviews on Cancer* **1826**, 423-433, doi:10.1016/j.bbcan.2012.07.001 (2012).

166 Lodish, H. *et al. Molecular Cell Biology*. (W. H. Freeman and Company, 2008).

167 Zwerschke, W. *et al.* Metabolic analysis of senescent human fibroblasts reveals a role for AMP in cellular senescence. *Biochemical Journal* **376**, 403-411, doi:10.1042/bj20030816 (2003).

168 Stryer, L. *Biochemistry*. 4th edn, 497 (W.H. Freeman & Company, 1997).

169 Putman, C. T. *et al.* SKELETAL-MUSCLE PYRUVATE-DEHYDROGENASE ACTIVITY DURING MAXIMAL EXERCISE IN HUMANS. *American Journal of Physiology-Endocrinology and Metabolism* **269**, E458-E468 (1995).

170 Prasad, K. N. & Sinha, P. K. EFFECT OF SODIUM BUTYRATE ON MAMMALIAN-CELLS IN CULTURE - REVIEW. *In Vitro-Journal of the Tissue Culture Association* **12**, 125-132 (1976).

171 Stern, R., Shuster, S., Neudecker, B. A. & Fromby, B. Lactate stimulates fibroblast expression of hyaluronan and CD44: The Warburg effect revisited. *Experimental Cell Research* **276**, 24-31, doi:10.1006/excr.2002.5508 (2002).

172 Warburg, O. ORIGIN OF CANCER CELLS. *Science* **123**, 309-314, doi:10.1126/science.123.3191.309 (1956).

173 Warburg, O., Wind, F. & Negelein, E. Metabolism of tumors in the body. *Klin Wochenschr* **5**, 829-832, doi:10.1007/bf01726240 (1926).

174 Zu, X. L. & Guppy, M. Cancer metabolism: facts, fantasy, and fiction. *Biochemical and Biophysical Research Communications* **313**, 459-465, doi:10.1016/j.bbrc.2003.11.136 (2004).

175 Walenta, S. *et al.* High lactate levels predict likelihood of metastases, tumor recurrence, and restricted patient survival in human cervical cancers. *Cancer Research* **60**, 916-921 (2000).

176 Altenberg, B. & Greulich, K. O. Genes of glycolysis are ubiquitously overexpressed in 24 cancer classes. *Genomics* **84**, 1014-1020, doi:10.1016/j.ygeno.2004.08.010 (2004).

177 Semenza, G. L. *et al.* Hypoxia response elements in the aldolase A, enolase 1, and lactate dehydrogenase A gene promoters contain essential binding sites for hypoxia-inducible factor 1. *Journal of Biological Chemistry* **271**, 32529-32537 (1996).

178 Shim, H. *et al.* c-Myc transactivation of LDH-A: Implications for tumor metabolism and growth. *Proceedings of the National Academy of Sciences of the United States of America* **94**, 6658-6663, doi:10.1073/pnas.94.13.6658 (1997).

179 Antone, P. D. Energy metabolism in cancer cells: How to explain the Warburg and Crabtree effects? *Medical Hypotheses* **79**, 388-392, doi:10.1016/j.mehy.2012.06.002 (2012).

180 Schultz, B. E. *et al.* Kinetics and comparative reactivity of human class I and class IIb histone deacetylases. *Biochemistry* **43**, 11083-11091, doi:10.1021/bi0494471 (2004).

181 Hagberg, B. RETTS SYNDROME - PREVALENCE AND IMPACT ON PROGRESSIVE SEVERE MENTAL-RETARDATION IN GIRLS. *Acta Paediatrica Scandinavica* **74**, 405-408, doi:10.1111/j.1651-2227.1985.tb10993.x (1985).

182 Quaderi, N. A. *et al.* GENETIC AND PHYSICAL MAPPING OF A GENE ENCODING A METHYL CPG BINDING-PROTEIN, MECP2 TO THE MOUSE X-CHROMOSOME. *Genomics* **22**, 648-651, doi:10.1006/geno.1994.1442 (1994).

183 Guy, J., Cheval, H., Selfridge, J. & Bird, A. in *Annual Review of Cell and Developmental Biology, Vol 27* Vol. 27 *Annual Review of Cell and Developmental Biology* (eds R. Schekman, L. Goldstein, & R. Lehmann) 631-652 (Annual Reviews, 2011).

184 Amir, R. E. *et al.* Rett syndrome is caused by mutations in X-linked MECP2, encoding methyl-CpG-binding protein 2. *Nature Genetics* **23**, 185-188 (1999).

185 Roux, J. C. & Villard, L. Biogenic Amines in Rett Syndrome: The Usual Suspects. *Behavior Genetics* **40**, 59-75, doi:10.1007/s10519-009-9303-y (2010).

186 Rett, A. On a unusual brain atrophy syndrome in hyperammonemia in childhood. *Wiener medizinische Wochenschrift (1946)* **116**, 723-726 (1966).

187 Chahrour, M. & Zoghbi, H. Y. The story of Rett syndrome: From clinic to neurobiology. *Neuron* **56**, 422-437, doi:10.1016/j.neuron.2007.10.001 (2007).

188 Nikitina, T. *et al.* MeCP2-chromatin interactions include the formation of chromatosome-like structures and are altered in mutations causing Rett syndrome.

Journal of Biological Chemistry **282**, 28237-28245, doi:10.1074/jbc.M704304200 (2007).

189 Skene, P. J. *et al.* Neuronal MeCP2 Is Expressed at Near Histone-Octamer Levels and Globally Alters the Chromatin State. *Molecular Cell* **37**, 457-468, doi:10.1016/j.molcel.2010.01.030 (2010).

190 De Filippis, B., Ricceri, L. & Laviola, G. in *Transgenic and Mutant Tools to Model Brain Disorders* Vol. 44 *Neuromethods* (eds A. V. Kalueff & C. L. Bergner) 151-178 (Humana Press Inc, 2010).

191 Nan, X. S., Tate, P., Li, E. & Bird, A. DNA methylation specifies chromosomal localization of MeCP2. *Molecular and Cellular Biology* **16**, 414-421 (1996).

192 Hendrich, B. & Bird, A. Identification and characterization of a family of mammalian methyl-CpG binding proteins. *Molecular and Cellular Biology* **18**, 6538-6547 (1998).

193 Shahbazian, M. D. & Zoghbi, H. Y. Rett syndrome and MeCP2: Linking epigenetics and neuronal function. *American Journal of Human Genetics* **71**, 1259-1272, doi:10.1086/345360 (2002).

194 Nan, X. S., Campoy, F. J. & Bird, A. MeCP2 is a transcriptional repressor with abundant binding sites in genomic chromatin. *Cell* **88**, 471-481, doi:10.1016/s0092-8674(00)81887-5 (1997).

195 Nan, X. S. *et al.* Transcriptional repression by the methyl-CpG-binding protein MeCP2 involves a histone deacetylase complex. *Nature* **393**, 386-389 (1998).

196 Giacometti, E., Luikenhuis, S., Beard, C. & Jaenisch, R. Partial rescue of MeCP2 deficiency by postnatal activation of MeCP2. *Proceedings of the National Academy of Sciences of the United States of America* **104**, 1931-1936, doi:10.1073/pnas.0610593104 (2007).

197 Guy, J., Gan, J., Selfridge, J., Cobb, S. & Bird, A. Reversal of neurological defects in a mouse model of Rett syndrome. *Science* **315**, 1143-1147, doi:10.1126/science.1138389 (2007).

198 Fichou, Y. *et al.* The first missense mutation causing Rett syndrome specifically affecting the MeCP2_e1 isoform. *Neurogenetics* **10**, 127-133, doi:10.1007/s10048-008-0161-1 (2009).

199 Hendrich, B., Guy, J., Ramsahoye, B., Wilson, V. A. & Bird, A. Closely related proteins MBD2 and MBD3 play distinctive but interacting roles in mouse development. *Genes & Development* **15**, 710-723, doi:10.1101/gad.194101 (2001).

200 Ghosh, R. P., Horowitz-Scherer, R. A., Nikitina, T., Shlyakhtenko, L. S. & Woodcock, C. L. MeCP2 Binds Cooperatively to Its Substrate and Competes with Histone H1 for Chromatin Binding Sites. *Molecular and Cellular Biology* **30**, 4656-4670, doi:10.1128/mcb.00379-10 (2010).

201 Fuks, F. *et al.* The Methyl-CpG-binding protein MeCP2 links DNA methylation to histone methylation. *Journal of Biological Chemistry* **278**, 4035-4040, doi:10.1074/jbc.M210256200 (2003).

202 Williamson, S. L. & Christodoulou, J. Rett syndrome: new clinical and molecular insights. *European Journal of Human Genetics* **14**, 896-903, doi:10.1038/sj.ejhg.5201580 (2006).

203 Shahbazian, M. D. *et al.* Mice with truncated MeCP2 recapitulate many Rett syndrome features and display hyperacetylation of histone H3. *Neuron* **35**, 243-254, doi:10.1016/s0896-6273(02)00768-7 (2002).

204 Nguyen, C. T., Gonzales, F. A. & Jones, P. A. Altered chromatin structure associated with methylation-induced gene silencing in cancer cells: correlation of accessibility, methylation, MeCP2 binding and acetylation. *Nucleic Acids Research* **29**, 4598-4606, doi:10.1093/nar/29.22.4598 (2001).

205 Wan, M. M., Zhao, K. J., Lee, S. S. J. & Francke, U. MECP2 truncating mutations cause histone H4 hyperacetylation in Rett syndrome. *Human Molecular Genetics* **10**, 1085-1092, doi:10.1093/hmg/10.10.1085 (2001).

206 Lorincz, M. C., Schubeler, D. & Groudine, M. Methylation-mediated proviral silencing is associated with MeCP2 recruitment and localized histone H3 deacetylation. *Molecular and Cellular Biology* **21**, 7913-7922, doi:10.1128/mcb.21.23.7913-7922.2001 (2001).

207 Trelle, M. B., Salcedo-Amaya, A. M., Cohen, A. M., Stunnenberg, H. G. & Jensen, O. N. Global Histone Analysis by Mass Spectrometry Reveals a High Content of Acetylated Lysine Residues in the Malaria Parasite Plasmodium

falciparum. *Journal of Proteome Research* **8**, 3439-3450, doi:10.1021/pr9000898 (2009).

208 Zhang, K. L. *et al.* Differentiation between peptides containing acetylated or tri-methylated lysines by mass spectrometry: An application for determining lysine 9 acetylation and methylation of histone H3. *Proteomics* **4**, 1-10, doi:10.1002/pmic.200300503 (2004).

209 Snijders, A. P. L., Hung, M. L., Wilson, S. A. & Dickman, M. J. Analysis of Arginine and Lysine Methylation Utilizing Peptide Separations at Neutral pH and Electron Transfer Dissociation Mass Spectrometry. *Journal of the American Society for Mass Spectrometry* **21**, 88-96, doi:10.1016/j.jasms.2009.09.010 (2010).

210 Pesavento, J. J., Mizzen, C. A. & Kelleher, N. L. Quantitative analysis of modified proteins and their positional isomers by tandem mass spectrometry: Human histone H4. *Analytical Chemistry* **78**, 4271-4280, doi:10.1021/ac0600050 (2006).

211 Schotta, G. *et al.* A silencing pathway to induce H3-K9 and H4-K20 trimethylation at constitutive heterochromatin. *Genes & Development* **18**, 1251-1262, doi:10.1101/gad.300704 (2004).

212 Sarg, B., Koutzamani, E., Helliger, W., Rundquist, I. & Lindner, H. H. Postsynthetic trimethylation of histone H4 at lysine 20 in mammalian tissues is associated with aging. *Journal of Biological Chemistry* **277**, 39195-39201, doi:10.1074/jbc.M205166200 (2002).

213 Thambirajah, A. A. *et al.* MeCP2 binds to nucleosome free (linker DNA) regions and to H3K9/H3K27 methylated nucleosomes in the brain. *Nucleic Acids Research* **40**, 2884-2897, doi:10.1093/nar/gkr1066 (2012).

Appendices

Appendix A.1

Assigned fragment ions from CID of HCT-116 cells after treatment with 50 nM TSA (precursor ion at 883.6 *m/z*).

Ion	Observed Mass (Da)	Theoretical Mass (Da)	Mass Error (Da)	Mass Error (PPM)
y_{94}	10613.9	10613.99	-0.0865	-8.15
y_{63}	7084.84	7084.868	-0.0283	-4
	7084.84	7084.868	-0.0283	-4
y_{49}	5526.98	5527.006	-0.0257	-4.64
	5526.98	5527.006	-0.0257	-4.64
y_{42}	4773.51	4773.52	-0.0096	-2
y_{41}	4626.45	4626.451	-0.0012	-0.25
y_{40}	4513.36	4513.367	-0.0071	-1.57
y_{39}	4384.31	4384.325	-0.0145	-3.31
	4384.31	4384.325	-0.0145	-3.31
y_{32}	3616.89	3616.896	-0.0055	-1.53
y_{30}	3352.78	3352.785	-0.0045	-1.35
y_{29}	3251.73	3251.737	-0.0069	-2.11
y_{28}	3122.68	3122.694	-0.0143	-4.57
	3122.68	3122.694	-0.0143	-4.57
y_{27}	2985.62	2985.635	-0.0154	-5.14
y_{26}	2914.59	2914.598	-0.0082	-2.83
y_{23}	2502.31	2502.307	0.0028	1.11
y_{22}	2401.25	2401.26	-0.0095	-3.97
y_{21}	2302.19	2302.191	-0.0011	-0.49
y_{20}	2201.14	2201.143	-0.0034	-1.56
y_{19}	2130.1	2130.106	-0.0063	-2.97
y_{18}	1999.06	1999.066	-0.0058	-2.92
y_{17}	1884.03	1884.039	-0.0089	-4.72
y_{16}	1784.96	1784.971	-0.0105	-5.88
	1784.96	1784.971	-0.0105	-5.88
y_{15}	1685.89	1685.902	-0.0121	-7.17
	1685.89	1685.902	-0.0121	-7.17
y_{14}	1522.83	1522.839	-0.0087	-5.75
y_{13}	1451.79	1451.802	-0.0116	-8.02
y_{12}	1338.71	1338.718	-0.0076	-5.66
y_{11}	1210.62	1210.623	-0.0026	-2.16
y_{10}	1054.52	1054.522	-0.0015	-1.43

Ion	Observed Mass (Da)	Theoretical Mass (Da)	Mass Error (Da)	Mass Error (PPM)
b_{100}	11335.3	11335.37	-0.0716	-6.32
b_{98}	11131.2	11131.28	-0.0817	-7.34
b_{88}	9944.55	9944.588	-0.0383	-3.85
b_{87}	9781.48	9781.525	-0.0449	-4.59
	9781.48	9781.525	-0.0449	-4.59
b_{86}	9682.41	9682.457	-0.0465	-4.81
	9682.41	9682.457	-0.0465	-4.81
b_{85}	9583.35	9583.388	-0.0381	-3.98
	9583.35	9583.388	-0.0381	-3.98
b_{84}	9468.32	9468.361	-0.0412	-4.35
	9468.32	9468.361	-0.0412	-4.35
b_{83}	9337.28	9337.321	-0.0407	-4.36
b_{81}	9165.2	9165.236	-0.0359	-3.92
b_{74}	8344.71	8344.733	-0.0228	-2.73
b_{71}	7951.56	7951.579	-0.0192	-2.41
b_{70}	7850.5	7850.532	-0.0315	-4.01
b_{63}	7083.07	7083.103	-0.0325	-4.59
	7083.07	7083.103	-0.0325	-4.59
b_{55}	6197.54	6197.57	-0.0301	-4.86
b_{53}	5940.4	5940.421	-0.0214	-3.6
	5940.4	5940.421	-0.0214	-3.6
b_{52}	5811.35	5811.379	-0.0288	-4.95
	5811.35	5811.379	-0.0288	-4.95
b_{51}	5682.3	5682.336	-0.0362	-6.37
b_{45}	5035.95	5035.967	-0.0172	-3.41
b_{40}	4538.64	4538.66	-0.0198	-4.36
b_{39}	4382.54	4382.559	-0.0187	-4.26
b_{35}	3886.22	3886.235	-0.0153	-3.93
	3886.22	3886.235	-0.0153	-3.93
b_{25}	2808.56	2808.569	-0.0094	-3.36
b_{24}	2694.52	2694.527	-0.0065	-2.42
b_{19}	2055.11	2055.12	-0.0097	-4.72
b_{10}	1023.54	1023.546	-0.0061	-5.93
b_{9}	910.46	910.462	-0.002	-2.21
	910.46	910.462	-0.002	-2.21
b_{7}	683.333	683.3351	-0.0021	-3
b_{5}	569.292	569.2921	-0.0001	-0.23

Appendix A.2

Assigned fragment ions from ECD of HCT-116 cells after treatment with 50 nM TSA (precursor ion at 883.6 *m/z*).

Ion	Observed Mass (Da)	Theoretical Mass (Da)	Mass Error (Da)	Mass Error (PPM)
z_{101}	11322.4	11322.36	0.0362	3.2
z_{97}	10882.2	10882.11	0.0858	7.88
z_{96}	10825.2	10825.09	0.1072	9.91
z_{80}	9028.07	9028.008	0.0621	6.88
z_{79}	8871.95	8871.907	0.0432	4.87
z_{76}	8529.81	8529.753	0.0571	6.7
	8529.81	8529.753	0.0571	6.7
z_{68}	7721.32	7721.272	0.0478	6.19
	7721.32	7721.272	0.0478	6.19
z_{67}	7565.21	7565.171	0.0389	5.14
z_{64}	7225	7224.949	0.0512	7.09
z_{63}	7068.86	7068.848	0.0123	1.74
z_{62}	6912.77	6912.747	0.0234	3.39
z_{59}	6699.67	6699.635	0.0347	5.19
z_{58}	6571.5	6571.54	-0.0403	-6.13
z_{57}	6415.42	6415.439	-0.0192	-2.99
z_{56}	6302.33	6302.355	-0.0251	-3.99
z_{55}	6215.32	6215.323	-0.0031	-0.5
z_{54}	6158.3	6158.302	-0.0016	-0.26
z_{51}	5769.05	5769.07	-0.0202	-3.5
	5769.05	5769.07	-0.0202	-3.5
z_{50}	5640.05	5640.028	0.0224	3.97
z_{49}	5511.02	5510.985	0.035	6.35
z_{48}	5409.97	5409.937	0.0327	6.04
z_{47}	5253.83	5253.836	-0.0062	-1.18
	5253.83	5253.836	-0.0062	-1.18
z_{43}	4856.57	4856.567	0.0027	0.55
z_{42}	4757.51	4757.499	0.0111	2.33
z_{39}	4368.33	4368.304	0.0261	5.99
z_{32}	3600.9	3600.875	0.0251	6.98
z_{31}	3499.84	3499.827	0.0128	3.66
z_{15}	1669.88	1669.881	-0.0014	-0.85
z_{14}	1506.81	1506.818	-0.0081	-5.37

Ion	Observed Mass (Da)	Theoretical Mass (Da)	Mass Error (Da)	Mass Error (PPM)
z_{11}	1194.6	1194.602	-0.002	-1.64
z_{10}	1038.51	1038.501	0.0091	8.81
z_{9}	910.45	910.4423	0.0077	8.49
c_{100}	11352.3	11352.4	-0.0979	-8.63
c_{63}	7100.18	7100.129	0.0511	7.2
c_{60}	6710.98	6710.934	0.0462	6.88
c_{59}	6611.87	6611.865	0.0046	0.7
c_{55}	6214.63	6214.597	0.0335	5.39
c_{52}	5828.42	5828.405	0.0149	2.55
c_{48}	5310.16	5310.131	0.0289	5.45
c_{44}	4896.9	4896.892	0.0076	1.55
c_{41}	4612.69	4612.708	-0.0176	-3.81
c_{40}	4555.67	4555.686	-0.0161	-3.54
c_{38}	4243.5	4243.484	0.0161	3.79
c_{37}	4172.46	4172.447	0.0132	3.16
c_{36}	4059.37	4059.363	0.0073	1.79
c_{34}	3747.19	3747.161	0.0295	7.87
c_{24}	2711.57	2711.553	0.0171	6.32
c_{22}	2440.43	2440.425	0.0052	2.13
c_{21}	2327.33	2327.341	-0.0107	-4.62
c_{18}	1916.06	1916.045	0.0151	7.87
c_{17}	1779	1778.986	0.014	7.86
c_{14}	1381.73	1381.742	-0.0123	-8.9
c_{13}	1324.71	1324.721	-0.0108	-8.18
c_{8}	870.472	870.4669	0.0051	5.86

Appendix A.3

Assigned fragment ions from CID of HCT-116 cells after treatment with 100 nM TSA (precursor ion at 870.6 *m/z*).

Ion	Observed Mass (Da)	Theoretical Mass (Da)	Mass Error (Da)	Mass Error (PPM)
y_{63}	7084.8	7084.868	-0.0683	-9.65
y_{15}	1685.89	1685.902	-0.0121	-7.17
	1685.89	1685.902	-0.0121	-7.17
y_{14}	1522.83	1522.839	-0.0087	-5.75
y_{13}	1451.8	1451.802	-0.0016	-1.13
y_{12}	1338.71	1338.718	-0.0076	-5.66
y_{11}	1210.62	1210.623	-0.0026	-2.16
b_{99}	11020.2	11020.26	-0.061	-5.54
b_{88}	9776.47	9776.546	-0.0761	-7.79
b_{87}	9613.41	9613.483	-0.0728	-7.57
b_{86}	9514.33	9514.414	-0.0844	-8.87
	9514.33	9514.414	-0.0844	-8.87
b_{85}	9415.28	9415.346	-0.066	-7.01
b_{84}	9300.25	9300.319	-0.069	-7.42
	9300.25	9300.319	-0.069	-7.42
b_{83}	9169.19	9169.279	-0.0885	-9.66
b_{81}	8997.11	8997.194	-0.0837	-9.31
b_{71}	7783.46	7783.537	-0.077	-9.89
b_{63}	6915.01	6915.06	-0.0504	-7.28
b_{55}	6029.5	6029.528	-0.028	-4.64
b_{53}	5772.34	5772.379	-0.0392	-6.79
	5772.34	5772.379	-0.0392	-6.79
b_{52}	5643.3	5643.337	-0.0366	-6.49
	5643.3	5643.337	-0.0366	-6.49
b_{51}	5514.27	5514.294	-0.024	-4.36
b_{40}	4370.61	4370.618	-0.0076	-1.74
b_{39}	4214.49	4214.517	-0.0265	-6.29
b_{35}	3718.18	3718.193	-0.0131	-3.53
b_{19}	1887.08	1887.078	0.0025	1.31
b_{17}	1593.91	1593.918	-0.0075	-4.71
b_{12}	1124.64	1124.641	-0.0014	-1.25
b_{11}	996.55	996.5465	0.0035	3.56
b_{10}	939.529	939.525	0.004	4.27

Ion	Observed Mass (Da)	Theoretical Mass (Da)	Mass Error (Da)	Mass Error (PPM)
b_8	769.42	769.4195	0.0005	0.69
	769.42	769.4195	0.0005	0.69
b_7	641.324	641.3245	-0.0005	-0.8

Appendix A.4

Assigned fragment ions from CID of HCT-116 cells after treatment with 500 nM TSA (precursor ion at 883.6 *m/z*).

Ion	Observed Mass (Da)	Theoretical Mass (Da)	Mass Error (Da)	Mass Error (PPM)
y_{94}	10614	10613.99	0.0135	1.27
y_{63}	7084.86	7084.868	-0.0084	-1.18
y_{49}	5527	5527.006	-0.0057	-1.02
	5527	5527.006	-0.0057	-1.02
y_{42}	4773.52	4773.52	0.0004	0.09
y_{39}	4384.31	4384.325	-0.0145	-3.31
y_{30}	3352.78	3352.785	-0.0045	-1.35
y_{29}	3251.74	3251.737	0.0031	0.97
y_{28}	3122.69	3122.694	-0.0043	-1.36
	3122.69	3122.694	-0.0043	-1.36
y_{27}	2985.63	2985.635	-0.0053	-1.79
y_{26}	2914.59	2914.598	-0.0082	-2.83
y_{21}	2302.19	2302.191	-0.0011	-0.49
y_{20}	2201.14	2201.143	-0.0034	-1.56
y_{19}	2130.1	2130.106	-0.0063	-2.97
y_{18}	1999.06	1999.066	-0.0058	-2.92
y_{17}	1884.04	1884.039	0.0011	0.58
y_{16}	1784.97	1784.971	-0.0005	-0.27
y_{15}	1685.9	1685.902	-0.0021	-1.23
	1685.9	1685.902	-0.0021	-1.23
y_{14}	1522.84	1522.839	0.0013	0.82
y_{13}	1451.8	1451.802	-0.0016	-1.13
y_{12}	1338.71	1338.718	-0.0076	-5.66
y_{11}	1210.62	1210.623	-0.0026	-2.16
y_{10}	1054.52	1054.522	-0.0015	-1.43
b_{100}	11335.4	11335.37	0.0284	2.51
b_{99}	11188.3	11188.3	-0.0032	-0.29
b_{94}	10598	10597.99	0.0145	1.36
b_{88}	9944.58	9944.588	-0.0083	-0.83
b_{87}	9781.52	9781.525	-0.0049	-0.51
	9781.52	9781.525	-0.0049	-0.51
b_{86}	9682.45	9682.457	-0.0065	-0.67
	9682.45	9682.457	-0.0065	-0.67

Ion	Observed Mass (Da)	Theoretical Mass (Da)	Mass Error (Da)	Mass Error (PPM)
b_{85}	9583.38	9583.388	-0.0081	-0.85
	9583.38	9583.388	-0.0081	-0.85
b_{84}	9468.35	9468.361	-0.0112	-1.18
	9468.35	9468.361	-0.0112	-1.18
b_{83}	9337.31	9337.321	-0.0107	-1.14
b_{82}	9266.29	9266.284	0.0064	0.69
b_{81}	9165.23	9165.236	-0.0059	-0.64
b_{71}	7951.59	7951.579	0.0108	1.36
b_{70}	7850.52	7850.532	-0.0115	-1.46
b_{63}	7083.09	7083.103	-0.0125	-1.77
	7083.09	7083.103	-0.0125	-1.77
b_{55}	6197.56	6197.57	-0.0101	-1.64
b_{53}	5940.42	5940.421	-0.0014	-0.23
	5940.42	5940.421	-0.0014	-0.23
b_{52}	5811.37	5811.379	-0.0088	-1.51
	5811.37	5811.379	-0.0088	-1.51
b_{51}	5682.33	5682.336	-0.0062	-1.09
b_{45}	5035.96	5035.967	-0.0072	-1.43
b_{40}	4538.65	4538.66	-0.0098	-2.15
b_{39}	4382.56	4382.559	0.0013	0.3
b_{35}	3886.23	3886.235	-0.0053	-1.36
b_{25}	2808.56	2808.569	-0.0094	-3.36
b_{24}	2694.52	2694.527	-0.0065	-2.42
b_{19}	2055.12	2055.12	0.0003	0.15
b_{9}	910.461	910.462	-0.001	-1.11
	910.461	910.462	-0.001	-1.11
b_{5}	569.291	569.2921	-0.0011	-1.98

Appendix A.5

Assigned fragment ions from CID of OCI-AML cells after treatment with 50 nM TSA (precursor ion at 870.6 *m/z*).

Ion	Observed Mass (Da)	Theoretical Mass (Da)	Mass Error (Da)	Mass Error (PPM)
y_{37}	4171.19	4171.213	-0.0232	-5.55
y_{29}	3251.71	3251.737	-0.0269	-8.26
y_{26}	2914.57	2914.598	-0.0282	-9.69
y_{19}	2130.09	2130.106	-0.0163	-7.67
y_{18}	1999.05	1999.066	-0.0158	-7.92
y_{16}	1784.96	1784.971	-0.0105	-5.88
y_{15}	1685.89	1685.902	-0.0121	-7.17
	1685.89	1685.902	-0.0121	-7.17
y_{14}	1522.83	1522.839	-0.0087	-5.75
y_{13}	1451.79	1451.802	-0.0116	-8.02
y_{12}	1338.71	1338.718	-0.0076	-5.66
y_{11}	1210.62	1210.623	-0.0026	-2.16
y_{9}	926.454	926.4629	-0.0089	-9.64
y_{8}	869.435	869.4415	-0.0065	-7.44
y_{5}	499.206	499.2086	-0.0026	-5.25
b_{87}	9613.42	9613.483	-0.0628	-6.53
b_{86}	9514.36	9514.414	-0.0544	-5.71
b_{85}	9415.27	9415.346	-0.076	-8.07
b_{84}	9300.29	9300.319	-0.029	-3.12
b_{69}	7583.37	7583.421	-0.0509	-6.71
b_{68}	7512.31	7512.384	-0.0738	-9.82
b_{63}	6915.01	6915.06	-0.0504	-7.28
b_{59}	6426.75	6426.797	-0.0469	-7.29
b_{58}	6298.65	6298.702	-0.0519	-8.24
b_{53}	5772.35	5772.379	-0.0292	-5.06
b_{52}	5643.3	5643.337	-0.0366	-6.49
	5643.3	5643.337	-0.0366	-6.49
b_{35}	3718.17	3718.193	-0.0231	-6.22
b_{31}	3280.9	3280.918	-0.0181	-5.51
b_{25}	2640.52	2640.527	-0.0073	-2.76
b_{24}	2526.47	2526.484	-0.0144	-5.68
b_{23}	2411.45	2411.457	-0.0074	-3.07
	2411.45	2411.457	-0.0074	-3.07

Ion	Observed Mass (Da)	Theoretical Mass (Da)	Mass Error (Da)	Mass Error (PPM)
b_{19}	1887.07	1887.078	-0.0075	-3.99
b_{17}	1593.91	1593.918	-0.0075	-4.71
b_{16}	1437.81	1437.816	-0.0064	-4.45
b_{15}	1309.72	1309.721	-0.0014	-1.1
b_{12}	1124.64	1124.641	-0.0014	-1.25
b_{11}	996.541	996.5465	-0.0055	-5.47
	996.541	996.5465	-0.0055	-5.47
b_{10}	939.521	939.525	-0.004	-4.25
	939.521	939.525	-0.004	-4.25
b_9	826.438	826.4409	-0.0029	-3.55
b_8	769.416	769.4195	-0.0035	-4.51
	769.416	769.4195	-0.0035	-4.51
b_7	641.323	641.3245	-0.0015	-2.35
b_5	527.28	527.2816	-0.0016	-3.02
b_3	342.164	342.1652	-0.0012	-3.42

Appendix A.6

Assigned fragment ions from ECD of OCI-AML cells after treatment with 50 nM TSA (precursor ion at 870.6 *m/z*).

Ion	Observed Mass (Da)	Theoretical Mass (Da)	Mass Error (Da)	Mass Error (PPM)
z_{100}	11097.2	11097.3	-0.1001	-9.02
	11097.2	11097.3	-0.1001	-9.02
z_{99}	10941.1	10941.2	-0.099	-9.05
z_{98}	10884.1	10884.18	-0.0776	-7.13
	10884.1	10884.18	-0.0776	-7.13
z_{96}	10699	10699.06	-0.0612	-5.72
z_{95}	10642	10642.04	-0.0397	-3.73
z_{93}	10456.9	10456.92	-0.0233	-2.23
	10456.9	10456.92	-0.0233	-2.23
	10456.9	10456.92	-0.0233	-2.23
z_{92}	10343.8	10343.84	-0.0392	-3.79
z_{90}	10158.7	10158.72	-0.0228	-2.24
z_{88}	10044.6	10044.68	-0.0799	-7.95
	10044.6	10044.68	-0.0799	-7.95
z_{87}	9973.58	9973.643	-0.0628	-6.29
	9973.58	9973.643	-0.0628	-6.29
z_{86}	9845.49	9845.548	-0.0578	-5.87
z_{85}	9689.38	9689.447	-0.0667	-6.88
z_{84}	9552.34	9552.388	-0.0478	-5
z_{80}	9027.95	9028.008	-0.0579	-6.41
z_{79}	8871.87	8871.907	-0.0368	-4.15
z_{78}	8756.82	8756.88	-0.0599	-6.83
z_{76}	8529.7	8529.753	-0.0529	-6.2
z_{73}	8231.57	8231.589	-0.0188	-2.28
z_{72}	8130.52	8130.541	-0.0211	-2.59
z_{70}	7905.45	7905.393	0.0566	7.16
z_{68}	7721.27	7721.272	-0.0022	-0.28
	7721.27	7721.272	-0.0022	-0.28
z_{67}	7565.23	7565.171	0.0589	7.79
	7565.23	7565.171	0.0589	7.79
	7565.23	7565.171	0.0589	7.79
z_{66}	7409.08	7409.07	0.01	1.35
z_{65}	7295.99	7295.986	0.0041	0.56

Ion	Observed Mass (Da)	Theoretical Mass (Da)	Mass Error (Da)	Mass Error (PPM)
z_{64}	7224.97	7224.949	0.0212	2.93
	7224.97	7224.949	0.0212	2.93
	7224.97	7224.949	0.0212	2.93
z_{63}	7068.83	7068.848	-0.0177	-2.5
z_{62}	6912.77	6912.747	0.0234	3.39
	6912.77	6912.747	0.0234	3.39
z_{59}	6699.67	6699.635	0.0347	5.19
	6699.67	6699.635	0.0347	5.19
z_{58}	6571.59	6571.54	0.0497	7.56
z_{57}	6415.46	6415.439	0.0208	3.25
z_{56}	6302.38	6302.355	0.0249	3.95
z_{55}	6215.33	6215.323	0.0069	1.11
z_{54}	6158.31	6158.302	0.0084	1.36
z_{52}	5932.12	5932.134	-0.0135	-2.28
z_{51}	5769.1	5769.07	0.0298	5.17
	5769.1	5769.07	0.0298	5.17
z_{50}	5640	5640.028	-0.0276	-4.89
z_{49}	5510.95	5510.985	-0.035	-6.35
z_{48}	5409.91	5409.937	-0.0273	-5.05
z_{47}	5253.85	5253.836	0.0138	2.62
	5253.85	5253.836	0.0138	2.62
z_{43}	4856.57	4856.567	0.0027	0.55
z_{42}	4757.49	4757.499	-0.0089	-1.87
z_{39}	4368.28	4368.304	-0.0239	-5.46
z_{35}	3886	3886.007	-0.0073	-1.89
	3886	3886.007	-0.0073	-1.89
z_{34}	3770.99	3770.98	0.0096	2.55
z_{32}	3600.86	3600.875	-0.0149	-4.13
z_{31}	3499.82	3499.827	-0.0072	-2.06
	3499.82	3499.827	-0.0072	-2.06
z_{28}	3106.66	3106.674	-0.0136	-4.38
z_{21}	2286.16	2286.171	-0.0105	-4.58
z_{18}	1983.03	1983.045	-0.0152	-7.66
z_{15}	1669.88	1669.881	-0.0014	-0.85
z_{14}	1506.83	1506.818	0.0119	7.9
z_{11}	1194.6	1194.602	-0.002	-1.64
z_{10}	1038.5	1038.501	-0.0009	-0.82
z_{9}	910.439	910.4423	-0.0033	-3.59
z_{8}	853.419	853.4208	-0.0018	-2.12

Ion	Observed Mass (Da)	Theoretical Mass (Da)	Mass Error (Da)	Mass Error (PPM)
c_{101}	11241.3	11241.38	-0.0772	-6.87
	11241.3	11241.38	-0.0772	-6.87
	11241.3	11241.38	-0.0772	-6.87
	11241.3	11241.38	-0.0772	-6.87
	11241.3	11241.38	-0.0772	-6.87
c_{93}	10389.9	10389.95	-0.0483	-4.65
c_{91}	10105.7	10105.79	-0.0886	-8.77
	10105.7	10105.79	-0.0886	-8.77
c_{81}	9014.15	9014.22	-0.0701	-7.78
c_{71}	7800.5	7800.563	-0.0633	-8.12
c_{70}	7699.46	7699.516	-0.0557	-7.23
c_{63}	6932.05	6932.087	-0.0367	-5.29
	6932.05	6932.087	-0.0367	-5.29
	6932.05	6932.087	-0.0367	-5.29
c_{60}	6542.86	6542.892	-0.0316	-4.84
	6542.86	6542.892	-0.0316	-4.84
c_{54}	5890.44	5890.453	-0.0132	-2.25
c_{53}	5789.36	5789.406	-0.0455	-7.87
c_{52}	5660.35	5660.363	-0.013	-2.29
	5660.35	5660.363	-0.013	-2.29
c_{51}	5531.31	5531.32	-0.0104	-1.87
	5531.31	5531.32	-0.0104	-1.87
c_{49}	5255.2	5255.173	0.027	5.14
c_{48}	5142.1	5142.089	0.0111	2.15
	5142.1	5142.089	0.0111	2.15
	5142.1	5142.089	0.0111	2.15
c_{47}	5085.11	5085.068	0.0425	8.37
c_{44}	4728.88	4728.85	0.0297	6.29
	4728.88	4728.85	0.0297	6.29
	4728.88	4728.85	0.0297	6.29
c_{43}	4600.79	4600.755	0.0347	7.54
	4600.79	4600.755	0.0347	7.54
c_{42}	4501.71	4501.687	0.0231	5.13
c_{41}	4444.67	4444.665	0.0046	1.03
	4444.67	4444.665	0.0046	1.03
c_{40}	4387.68	4387.644	0.036	8.21
c_{39}	4231.57	4231.543	0.0271	6.41
	4231.57	4231.543	0.0271	6.41
c_{38}	4075.48	4075.442	0.0383	9.39

Ion	Observed Mass (Da)	Theoretical Mass (Da)	Mass Error (Da)	Mass Error (PPM)
	4075.48	4075.442	0.0383	9.39
c_{37}	4004.44	4004.405	0.0354	8.83
	4004.44	4004.405	0.0354	8.83
c_{35}	3735.25	3735.22	0.0305	8.17
	3735.25	3735.22	0.0305	8.17
	3735.25	3735.22	0.0305	8.17
c_{34}	3579.13	3579.118	0.0116	3.25
	3579.13	3579.118	0.0116	3.25
c_{27}	2898.72	2898.696	0.0237	8.19
c_{26}	2770.66	2770.638	0.0223	8.05
	2770.66	2770.638	0.0223	8.05
c_{21}	2159.32	2159.299	0.0214	9.92
c_{19}	1904.12	1904.104	0.0161	8.47
	1904.12	1904.104	0.0161	8.47
c_{8}	786.447	786.4458	0.0012	1.5

Appendix A.7

Assigned fragment ions from CID of OCI-AML cells after treatment with 50 nM TSA (precursor ion at 873.8 *m/z*).

Ion	Observed Mass (Da)	Theoretical Mass (Da)	Mass Error (Da)	Mass Error (PPM)
y_{49}	5527	5527.006	-0.0057	-1.02
y_{43}	4872.59	4872.588	0.002	0.41
y_{42}	4773.51	4773.52	-0.0096	-2
y_{39}	4384.32	4384.325	-0.0045	-1.03
y_{31}	3515.84	3515.848	-0.0079	-2.24
y_{30}	3352.79	3352.785	0.0055	1.63
y_{29}	3251.73	3251.737	-0.0069	-2.11
y_{28}	3122.69	3122.694	-0.0043	-1.36
	3122.69	3122.694	-0.0043	-1.36
y_{27}	2985.63	2985.635	-0.0053	-1.79
y_{26}	2914.59	2914.598	-0.0082	-2.83
y_{24}	2630.4	2630.402	-0.0022	-0.82
y_{23}	2502.31	2502.307	0.0028	1.11
y_{22}	2401.26	2401.26	0.0005	0.2
y_{21}	2302.19	2302.191	-0.0011	-0.49
y_{20}	2201.14	2201.143	-0.0034	-1.56
y_{19}	2130.1	2130.106	-0.0063	-2.97
y_{18}	1999.06	1999.066	-0.0058	-2.92
y_{17}	1884.03	1884.039	-0.0089	-4.72
y_{16}	1784.96	1784.971	-0.0105	-5.88
y_{15}	1685.89	1685.902	-0.0121	-7.17
y_{14}	1522.83	1522.839	-0.0087	-5.75
y_{13}	1451.8	1451.802	-0.0016	-1.13
y_{12}	1338.71	1338.718	-0.0076	-5.66
y_{11}	1210.62	1210.623	-0.0026	-2.16
y_{10}	1054.52	1054.522	-0.0015	-1.43
y_{9}	926.459	926.4629	-0.0039	-4.24
y_{8}	869.438	869.4415	-0.0035	-3.99
y_{5}	499.207	499.2086	-0.0016	-3.25
b_{70}	7724.47	7724.5	-0.0299	-3.87
b_{69}	7625.43	7625.431	-0.0014	-0.19
	7625.43	7625.431	-0.0014	-0.19
b_{63}	6957.05	6957.071	-0.0209	-3

Ion	Observed Mass (Da)	Theoretical Mass (Da)	Mass Error (Da)	Mass Error (PPM)
b_{53}	5814.37	5814.39	-0.0197	-3.4
b_{52}	5685.33	5685.347	-0.0172	-3.02
	5685.33	5685.347	-0.0172	-3.02
b_{51}	5556.29	5556.305	-0.0146	-2.62
b_{40}	4412.61	4412.628	-0.0182	-4.12
b_{39}	4256.52	4256.527	-0.0071	-1.66
b_{35}	3760.19	3760.204	-0.0137	-3.63
b_{34}	3604.09	3604.103	-0.0126	-3.48
b_{31}	3322.92	3322.929	-0.0086	-2.59
b_{25}	2682.53	2682.538	-0.0078	-2.92
b_{24}	2568.49	2568.495	-0.0049	-1.9
	2568.49	2568.495	-0.0049	-1.9
b_{23}	2453.46	2453.468	-0.008	-3.24
	2453.46	2453.468	-0.008	-3.24
b_{19}	1929.08	1929.088	-0.0081	-4.18
b_{18}	1772.98	1772.987	-0.007	-3.93
b_{17}	1635.92	1635.928	-0.008	-4.92
b_{16}	1479.82	1479.827	-0.0069	-4.69
b_{12}	1166.65	1166.652	-0.002	-1.67
b_{11}	996.546	996.5465	-0.0005	-0.45
	996.546	996.5465	-0.0005	-0.45
b_{10}	939.526	939.525	0.001	1.08
	939.526	939.525	0.001	1.08
b_{9}	826.446	826.4409	0.0051	6.13
b_{8}	769.421	769.4195	0.0015	1.99
	769.421	769.4195	0.0015	1.99
b_{7}	641.323	641.3245	-0.0015	-2.35
b_{5}	527.282	527.2816	0.0004	0.78
b_{4}	399.189	399.1866	0.0024	5.94

Appendix A.8

Assigned fragment ions from ECD of OCI-AML cells after treatment with 50 nM TSA (precursor ion at 873.8 *m/z*).

Ion	Observed Mass (Da)	Theoretical Mass (Da)	Mass Error (Da)	Mass Error (PPM)
z_{95}	10684	10684.05	-0.0502	-4.7
z_{94}	10555.9	10555.96	-0.0553	-5.24
z_{90}	10200.7	10200.73	-0.0333	-3.27
z_{87}	10015.6	10015.65	-0.0533	-5.32
z_{85}	9689.42	9689.447	-0.0267	-2.75
z_{80}	9027.99	9028.008	-0.0179	-1.98
z_{79}	8871.88	8871.907	-0.0268	-3.02
z_{78}	8756.85	8756.88	-0.0299	-3.41
z_{76}	8529.74	8529.753	-0.0129	-1.51
z_{67}	7565.12	7565.171	-0.0511	-6.75
z_{66}	7409.03	7409.07	-0.04	-5.39
z_{64}	7224.91	7224.949	-0.0388	-5.37
z_{63}	7068.82	7068.848	-0.0277	-3.92
z_{62}	6912.72	6912.747	-0.0266	-3.85
z_{61}	6855.69	6855.725	-0.0351	-5.12
z_{59}	6699.58	6699.635	-0.0553	-8.25
z_{58}	6571.49	6571.54	-0.0503	-7.65
z_{57}	6415.4	6415.439	-0.0392	-6.11
z_{56}	6302.32	6302.355	-0.0351	-5.57
z_{55}	6215.29	6215.323	-0.0331	-5.32
z_{54}	6158.27	6158.302	-0.0316	-5.14
z_{52}	5932.11	5932.134	-0.0235	-3.96
z_{51}	5769.05	5769.07	-0.0202	-3.5
z_{49}	5510.97	5510.985	-0.015	-2.72
z_{48}	5409.93	5409.937	-0.0073	-1.35
z_{47}	5253.8	5253.836	-0.0362	-6.89
z_{43}	4856.54	4856.567	-0.0273	-5.63
z_{42}	4757.48	4757.499	-0.0189	-3.97
z_{39}	4368.3	4368.304	-0.0039	-0.88
z_{32}	3600.87	3600.875	-0.0049	-1.36
	3600.87	3600.875	-0.0049	-1.36
z_{31}	3499.82	3499.827	-0.0072	-2.06
z_{14}	1506.81	1506.818	-0.0081	-5.37

Ion	Observed Mass (Da)	Theoretical Mass (Da)	Mass Error (Da)	Mass Error (PPM)
z_{11}	1194.6	1194.602	-0.002	-1.64
z_{10}	1038.5	1038.501	-0.0009	-0.82
c_{101}	11283.3	11283.39	-0.0878	-7.78
	11283.3	11283.39	-0.0878	-7.78
	11283.3	11283.39	-0.0878	-7.78
c_{92}	10303.9	10303.9	-0.0002	-0.02
c_{81}	9056.21	9056.231	-0.0206	-2.28
c_{71}	7842.56	7842.574	-0.0139	-1.77
c_{70}	7741.51	7741.526	-0.0162	-2.09
c_{63}	6974.09	6974.097	-0.0072	-1.04
c_{59}	6485.82	6485.834	-0.0138	-2.12
c_{55}	6088.55	6088.565	-0.0149	-2.44
c_{54}	5932.11	5932.07	0.0396	6.68
c_{52}	5702.36	5702.374	-0.0135	-2.37
c_{51}	5573.32	5573.331	-0.0109	-1.96
c_{48}	5184.08	5184.1	-0.0195	-3.75
	5184.08	5184.1	-0.0195	-3.75
c_{44}	4770.84	4770.861	-0.0208	-4.36
	4770.84	4770.861	-0.0208	-4.36
c_{43}	4642.76	4642.766	-0.0058	-1.26
c_{41}	4486.66	4486.676	-0.016	-3.56
c_{40}	4429.64	4429.655	-0.0145	-3.28
c_{39}	4273.55	4273.553	-0.0034	-0.8
c_{37}	4046.41	4046.415	-0.0052	-1.28
c_{36}	3933.31	3933.331	-0.0211	-5.37
	3933.31	3933.331	-0.0211	-5.37
c_{35}	3777.22	3777.23	-0.01	-2.65
c_{34}	3621.12	3621.129	-0.0089	-2.46
	3621.12	3621.129	-0.0089	-2.46
c_{26}	2812.64	2812.648	-0.0082	-2.93
	2812.64	2812.648	-0.0082	-2.93
c_{24}	2585.5	2585.521	-0.0212	-8.21
c_{23}	2470.47	2470.494	-0.0243	-9.84
c_{22}	2314.39	2314.393	-0.0032	-1.38
c_{21}	2201.3	2201.309	-0.0091	-4.15
c_{16}	1496.85	1496.853	-0.0033	-2.2
c_{15}	1326.74	1326.748	-0.0078	-5.87
c_{13}	1198.68	1198.689	-0.0092	-7.69
c_{7}	658.346	658.3509	-0.0049	-7.38

Appendix A.9

Assigned fragment ions from CID of OCI-AML cells after treatment with 50 nM TSA (precursor ion at 950.1 *m/z*).

Ion	Observed Mass (Da)	Theoretical Mass (Da)	Mass Error (Da)	Mass Error (PPM)
y_{26}	2914.57	2914.598	-0.0282	-9.69
y_{16}	1784.96	1784.971	-0.0105	-5.88
y_{15}	1685.89	1685.902	-0.0121	-7.17
y_{14}	1522.83	1522.839	-0.0087	-5.75
y_{13}	1451.79	1451.802	-0.0116	-8.02
y_{12}	1338.71	1338.718	-0.0076	-5.66
y_{11}	1210.62	1210.623	-0.0026	-2.16
y_{8}	869.434	869.4415	-0.0075	-8.59
y_{5}	499.206	499.2086	-0.0026	-5.25
b_{63}	6999.02	6999.081	-0.0614	-8.78
	6999.02	6999.081	-0.0614	-8.78
b_{53}	5856.36	5856.4	-0.0403	-6.88
	5856.36	5856.4	-0.0403	-6.88
b_{52}	5727.32	5727.358	-0.0377	-6.58
	5727.32	5727.358	-0.0377	-6.58
b_{51}	5598.29	5598.315	-0.0251	-4.48
b_{40}	4454.62	4454.639	-0.0187	-4.2
b_{39}	4298.51	4298.538	-0.0276	-6.42
b_{35}	3802.2	3802.214	-0.0142	-3.73
b_{25}	2724.54	2724.548	-0.0084	-3.07
b_{24}	2610.5	2610.505	-0.0054	-2.08
b_{23}	2495.47	2495.479	-0.0085	-3.4
	2495.47	2495.479	-0.0085	-3.4
b_{17}	1677.93	1677.939	-0.0086	-5.12
b_{12}	1166.65	1166.652	-0.002	-1.67
b_{11}	996.544	996.5465	-0.0025	-2.46
b_{10}	939.523	939.525	-0.002	-2.12
b_{8}	769.416	769.4195	-0.0035	-4.51
	769.416	769.4195	-0.0035	-4.51
b_{7}	641.323	641.3245	-0.0015	-2.35
b_{5}	527.281	527.2816	-0.0006	-1.12

Appendix A.10

Assigned fragment ions from CID of OCI-AML cells after treatment with 100 nM TSA (precursor ion at 873.9 *m/z*).

Ion	Observed Mass (Da)	Theoretical Mass (Da)	Mass Error (Da)	Mass Error (PPM)
y_{49}	5527	5527.006	-0.0057	-1.02
y_{43}	4872.59	4872.588	0.002	0.41
y_{42}	4773.53	4773.52	0.0104	2.18
y_{39}	4384.32	4384.325	-0.0045	-1.03
y_{32}	3616.9	3616.896	0.0045	1.23
y_{30}	3352.78	3352.785	-0.0045	-1.35
y_{29}	3251.73	3251.737	-0.0069	-2.11
y_{28}	3122.69	3122.694	-0.0043	-1.36
	3122.69	3122.694	-0.0043	-1.36
y_{27}	2985.63	2985.635	-0.0053	-1.79
y_{26}	2914.59	2914.598	-0.0082	-2.83
y_{24}	2630.41	2630.402	0.0078	2.98
y_{23}	2502.31	2502.307	0.0028	1.11
y_{22}	2401.26	2401.26	0.0005	0.2
y_{21}	2302.19	2302.191	-0.0011	-0.49
y_{20}	2201.14	2201.143	-0.0034	-1.56
y_{19}	2130.1	2130.106	-0.0063	-2.97
y_{18}	1999.06	1999.066	-0.0058	-2.92
y_{17}	1884.03	1884.039	-0.0089	-4.72
y_{16}	1784.96	1784.971	-0.0105	-5.88
y_{15}	1685.89	1685.902	-0.0121	-7.17
y_{14}	1522.83	1522.839	-0.0087	-5.75
y_{13}	1451.79	1451.802	-0.0116	-8.02
y_{12}	1338.71	1338.718	-0.0076	-5.66
y_{11}	1210.62	1210.623	-0.0026	-2.16
y_{10}	1054.52	1054.522	-0.0015	-1.43
y_{9}	926.458	926.4629	-0.0049	-5.32
y_{8}	869.437	869.4415	-0.0045	-5.14
y_{5}	499.206	499.2086	-0.0026	-5.25
b_{70}	7724.47	7724.5	-0.0299	-3.87
b_{69}	7625.42	7625.431	-0.0114	-1.5
	7625.42	7625.431	-0.0114	-1.5
b_{63}	6957.05	6957.071	-0.0209	-3

Ion	Observed Mass (Da)	Theoretical Mass (Da)	Mass Error (Da)	Mass Error (PPM)
b_{53}	5814.36	5814.39	-0.0297	-5.11
b_{52}	5685.32	5685.347	-0.0272	-4.78
b_{39}	4256.51	4256.527	-0.0171	-4.01
b_{35}	3760.19	3760.204	-0.0137	-3.63
b_{31}	3322.92	3322.929	-0.0086	-2.59
b_{25}	2682.53	2682.538	-0.0078	-2.92
b_{24}	2568.48	2568.495	-0.0149	-5.8
	2568.48	2568.495	-0.0149	-5.8
b_{23}	2453.46	2453.468	-0.008	-3.24
b_{19}	1929.08	1929.088	-0.0081	-4.18
b_{17}	1635.92	1635.928	-0.008	-4.92
b_{16}	1479.82	1479.827	-0.0069	-4.69
b_{12}	1124.64	1124.641	-0.0014	-1.25
b_{11}	996.545	996.5465	-0.0015	-1.46
	996.545	996.5465	-0.0015	-1.46
b_{10}	939.524	939.525	-0.001	-1.05
	939.524	939.525	-0.001	-1.05
b_{9}	826.44	826.4409	-0.0009	-1.13
	826.44	826.4409	-0.0009	-1.13
b_{8}	769.419	769.4195	-0.0005	-0.61
	769.419	769.4195	-0.0005	-0.61
b_{7}	641.322	641.3245	-0.0025	-3.91
b_{5}	527.281	527.2816	-0.0006	-1.12
b_{3}	342.168	342.1652	0.0028	8.27

Appendix A.11

Assigned fragment ions from ECD of OCI-AML cells after treatment with 100 nM TSA (precursor ion at 873.9 *m/z*).

Ion	Observed Mass (Da)	Theoretical Mass (Da)	Mass Error (Da)	Mass Error (PPM)
z_{99}	10983.3	10983.21	0.0904	8.23
z_{98}	10926.2	10926.19	0.0119	1.09
z_{95}	10684.1	10684.05	0.0498	4.66
z_{94}	10556	10555.96	0.0447	4.24
z_{89}	10143.8	10143.71	0.0881	8.69
z_{87}	10015.7	10015.65	0.0467	4.66
z_{85}	9689.49	9689.447	0.0433	4.47
z_{80}	9028.04	9028.008	0.0321	3.56
z_{79}	8871.95	8871.907	0.0432	4.87
z_{78}	8756.93	8756.88	0.0501	5.73
z_{76}	8529.8	8529.753	0.0471	5.53
z_{68}	7721.32	7721.272	0.0478	6.19
z_{66}	7409.14	7409.07	0.07	9.45
z_{64}	7225.01	7224.949	0.0612	8.47
	7225.01	7224.949	0.0612	8.47
z_{62}	6912.79	6912.747	0.0434	6.28
z_{54}	6158.36	6158.302	0.0584	9.48
z_{51}	5769.11	5769.07	0.0398	6.9
z_{49}	5511.03	5510.985	0.045	8.17
z_{43}	4856.61	4856.567	0.0427	8.79
z_{42}	4757.54	4757.499	0.0411	8.64
z_{39}	4368.33	4368.304	0.0261	5.99
z_{32}	3600.9	3600.875	0.0251	6.98
	3600.9	3600.875	0.0251	6.98
z_{31}	3499.85	3499.827	0.0228	6.51
z_{11}	1194.61	1194.602	0.008	6.73
z_{10}	1038.51	1038.501	0.0091	8.81
c_{101}	11283.4	11283.39	0.0122	1.08
	11283.4	11283.39	0.0122	1.08
	11283.4	11283.39	0.0122	1.08
	11283.4	11283.39	0.0122	1.08
c_{81}	9056.28	9056.231	0.0494	5.45
c_{71}	7842.61	7842.574	0.0361	4.6

Ion	Observed Mass (Da)	Theoretical Mass (Da)	Mass Error (Da)	Mass Error (PPM)
c_{70}	7741.56	7741.526	0.0338	4.36
c_{63}	6974.14	6974.097	0.0428	6.13
c_{52}	5702.42	5702.374	0.0465	8.15
c_{38}	4117.49	4117.452	0.0377	9.16
c_{34}	3621.15	3621.129	0.0211	5.83
c_{11}	1013.58	1013.573	0.0072	7.1

Appendix A.12

Assigned fragment ions from CID of OCI-AML cells after treatment with 100 nM TSA (precursor ion at 880.4 *m/z*).

Ion	Observed Mass (Da)	Theoretical Mass (Da)	Mass Error (Da)	Mass Error (PPM)
y_{49}	5527.02	5527.006	0.0143	2.59
y_{42}	4773.55	4773.52	0.0304	6.37
y_{39}	4384.34	4384.325	0.0155	3.53
y_{32}	3616.92	3616.896	0.0245	6.76
y_{30}	3352.8	3352.785	0.0155	4.61
y_{29}	3251.75	3251.737	0.0131	4.04
y_{28}	3122.7	3122.694	0.0057	1.84
	3122.7	3122.694	0.0057	1.84
y_{27}	2985.64	2985.635	0.0046	1.56
y_{26}	2914.6	2914.598	0.0018	0.6
y_{23}	2502.32	2502.307	0.0128	5.11
y_{22}	2401.28	2401.26	0.0205	8.52
y_{21}	2302.2	2302.191	0.0089	3.86
y_{20}	2201.15	2201.143	0.0066	2.98
y_{19}	2130.11	2130.106	0.0037	1.72
y_{18}	1999.07	1999.066	0.0042	2.08
y_{17}	1884.04	1884.039	0.0011	0.58
y_{16}	1784.97	1784.971	-0.0005	-0.27
y_{15}	1685.9	1685.902	-0.0021	-1.23
y_{14}	1522.83	1522.839	-0.0087	-5.75
y_{13}	1451.79	1451.802	-0.0116	-8.02
y_{12}	1338.71	1338.718	-0.0076	-5.66
y_{11}	1210.62	1210.623	-0.0026	-2.16
y_{10}	1054.52	1054.522	-0.0015	-1.43
y_{9}	926.46	926.4629	-0.0029	-3.16
b_{53}	5898.39	5898.411	-0.0208	-3.53
b_{52}	5769.35	5769.368	-0.0182	-3.16
b_{39}	4340.54	4340.548	-0.0081	-1.87
b_{35}	3844.21	3844.225	-0.0147	-3.83
b_{29}	3177.78	3177.807	-0.0271	-8.52
b_{24}	2652.5	2652.516	-0.016	-6.02
b_{23}	2537.48	2537.489	-0.009	-3.56
b_{17}	1719.95	1719.949	0.0009	0.51

Ion	Observed Mass (Da)	Theoretical Mass (Da)	Mass Error (Da)	Mass Error (PPM)
b_{12}	1208.66	1208.663	-0.0025	-2.06
b_9	910.462	910.462	0	-0.01
b_8	853.439	853.4406	-0.0016	-1.82
b_5	569.29	569.2921	-0.0021	-3.74
b_3	342.167	342.1652	0.0018	5.35

Appendix A.13

Assigned fragment ions from ECD of OCI-AML cells after treatment with 100 nM TSA (precursor ion at 880.4 *m/z*).

Ion	Observed Mass (Da)	Theoretical Mass (Da)	Mass Error (Da)	Mass Error (PPM)
z_{78}	8756.82	8756.88	-0.0599	-6.83
z_{76}	8529.74	8529.753	-0.0129	-1.51
z_{39}	4368.28	4368.304	-0.0239	-5.46
c_{101}	11367.3	11367.41	-0.1089	-9.58
	11367.3	11367.41	-0.1089	-9.58
	11367.3	11367.41	-0.1089	-9.58
c_{63}	7058.11	7058.118	-0.0083	-1.18

Appendix A.14

Assigned fragment ions from CID of OCI-AML cells after treatment with 250 nM TSA (precursor ion at 873.1 *m/z*).

Ion	Observed Mass (Da)	Theoretical Mass (Da)	Mass Error (Da)	Mass Error (PPM)
y_{49}	5526.98	5527.006	-0.0257	-4.64
y_{39}	4384.3	4384.325	-0.0245	-5.59
y_{32}	3616.88	3616.896	-0.0155	-4.3
y_{30}	3352.77	3352.785	-0.0145	-4.33
y_{28}	3122.68	3122.694	-0.0143	-4.57
	3122.68	3122.694	-0.0143	-4.57
y_{27}	2985.62	2985.635	-0.0154	-5.14
y_{26}	2914.58	2914.598	-0.0182	-6.26
y_{24}	2630.39	2630.402	-0.0122	-4.63
y_{22}	2401.25	2401.26	-0.0095	-3.97
y_{21}	2302.18	2302.191	-0.0111	-4.83
y_{20}	2201.13	2201.143	-0.0134	-6.11
y_{19}	2130.1	2130.106	-0.0063	-2.97
y_{18}	1999.05	1999.066	-0.0158	-7.92
y_{17}	1884.03	1884.039	-0.0089	-4.72
y_{16}	1784.96	1784.971	-0.0105	-5.88
y_{15}	1685.89	1685.902	-0.0121	-7.17
y_{14}	1522.83	1522.839	-0.0087	-5.75
y_{13}	1451.79	1451.802	-0.0116	-8.02
y_{12}	1338.71	1338.718	-0.0076	-5.66
y_{11}	1210.63	1210.623	0.0074	6.1
y_{9}	926.457	926.4629	-0.0059	-6.4
y_{8}	869.436	869.4415	-0.0055	-6.29
y_{5}	499.207	499.2086	-0.0016	-3.25
b_{63}	6957.04	6957.071	-0.0309	-4.44
	6957.04	6957.071	-0.0309	-4.44
b_{53}	5814.36	5814.39	-0.0297	-5.11
	5814.36	5814.39	-0.0297	-5.11
b_{52}	5685.32	5685.347	-0.0272	-4.78
b_{39}	4256.51	4256.527	-0.0171	-4.01
b_{35}	3760.19	3760.204	-0.0137	-3.63
b_{25}	2682.53	2682.538	-0.0078	-2.92

b_{24}	2568.49	2568.495	-0.0049	-1.9

Ion	Observed Mass (Da)	Theoretical Mass (Da)	Mass Error (Da)	Mass Error (PPM)
b_{23}	2453.46	2453.468	-0.008	-3.24
b_{19}	1929.08	1929.088	-0.0081	-4.18
b_{17}	1635.92	1635.928	-0.008	-4.92
b_{16}	1479.82	1479.827	-0.0069	-4.69
b_{12}	1124.64	1124.641	-0.0014	-1.25
b_{11}	996.545	996.5465	-0.0015	-1.46
	996.545	996.5465	-0.0015	-1.46
b_{10}	939.527	939.525	0.002	2.14
b_9	826.439	826.4409	-0.0019	-2.34
	826.439	826.4409	-0.0019	-2.34
b_8	769.42	769.4195	0.0005	0.69
	769.42	769.4195	0.0005	0.69
b_7	641.323	641.3245	-0.0015	-2.35
b_5	527.281	527.2816	-0.0006	-1.12

Appendix A.15

Assigned fragment ions from CID of OCI-AML cells after treatment with 500 nM TSA (precursor ion at 873.9 *m/z*).

Ion	Observed Mass (Da)	Theoretical Mass (Da)	Mass Error (Da)	Mass Error (PPM)
y_{49}	5526.99	5527.006	-0.0157	-2.83
y_{43}	4872.58	4872.588	-0.008	-1.64
y_{41}	4626.46	4626.451	0.0088	1.91
y_{39}	4384.31	4384.325	-0.0145	-3.31
y_{34}	3786.99	3787.001	-0.0111	-2.92
y_{32}	3616.89	3616.896	-0.0055	-1.53
y_{31}	3515.83	3515.848	-0.0179	-5.08
y_{30}	3352.78	3352.785	-0.0045	-1.35
y_{29}	3251.73	3251.737	-0.0069	-2.11
y_{28}	3122.68	3122.694	-0.0143	-4.57
	3122.68	3122.694	-0.0143	-4.57
y_{26}	2914.58	2914.598	-0.0182	-6.26
y_{24}	2630.4	2630.402	-0.0022	-0.82
y_{23}	2502.3	2502.307	-0.0072	-2.88
y_{22}	2401.25	2401.26	-0.0095	-3.97
y_{21}	2302.18	2302.191	-0.0111	-4.83
y_{20}	2201.14	2201.143	-0.0034	-1.56
y_{19}	2130.1	2130.106	-0.0063	-2.97
y_{18}	1999.06	1999.066	-0.0058	-2.92
y_{17}	1884.03	1884.039	-0.0089	-4.72
y_{16}	1784.96	1784.971	-0.0105	-5.88
y_{15}	1685.89	1685.902	-0.0121	-7.17
y_{14}	1522.83	1522.839	-0.0087	-5.75
y_{13}	1451.79	1451.802	-0.0116	-8.02
y_{12}	1338.71	1338.718	-0.0076	-5.66
	1338.71	1338.718	-0.0076	-5.66
y_{11}	1210.62	1210.623	-0.0026	-2.16
y_{9}	926.458	926.4629	-0.0049	-5.32
y_{8}	869.437	869.4415	-0.0045	-5.14
y_{5}	499.205	499.2086	-0.0036	-7.25
b_{70}	7724.46	7724.5	-0.0399	-5.16
b_{53}	5814.36	5814.39	-0.0297	-5.11
b_{35}	3760.19	3760.204	-0.0137	-3.63

Ion	Observed Mass (Da)	Theoretical Mass (Da)	Mass Error (Da)	Mass Error (PPM)
b_{25}	2682.53	2682.538	-0.0078	-2.92
b_{24}	2568.49	2568.495	-0.0049	-1.9
	2568.49	2568.495	-0.0049	-1.9
b_{23}	2453.46	2453.468	-0.008	-3.24
b_{19}	1929.08	1929.088	-0.0081	-4.18
b_{17}	1635.92	1635.928	-0.008	-4.92
	1635.92	1635.928	-0.008	-4.92
b_{16}	1479.82	1479.827	-0.0069	-4.69
	1479.82	1479.827	-0.0069	-4.69
b_{12}	1124.64	1124.641	-0.0014	-1.25
b_{11}	996.543	996.5465	-0.0035	-3.46
	996.543	996.5465	-0.0035	-3.46
b_{10}	939.521	939.525	-0.004	-4.25
	939.521	939.525	-0.004	-4.25
b_9	826.439	826.4409	-0.0019	-2.34
	826.439	826.4409	-0.0019	-2.34
b_8	769.417	769.4195	-0.0025	-3.21
	769.417	769.4195	-0.0025	-3.21
b_7	641.322	641.3245	-0.0025	-3.91
b_5	527.28	527.2816	-0.0016	-3.02
b_3	342.164	342.1652	-0.0012	-3.42

Appendix A.16

Assigned fragment ions from ECD of OCI-AML cells after treatment with 500 nM TSA (precursor ion at 873.9 *m/z*).

Ion	Observed Mass (Da)	Theoretical Mass (Da)	Mass Error (Da)	Mass Error (PPM)
z_{101}	11196.4	11196.33	0.0679	6.06
z_{95}	10684.1	10684.05	0.0498	4.66
z_{84}	9552.41	9552.388	0.0222	2.33
z_{73}	8231.56	8231.589	-0.0288	-3.49
z_{72}	8130.47	8130.541	-0.0711	-8.74
z_{64}	7224.91	7224.949	-0.0388	-5.37
	7224.91	7224.949	-0.0388	-5.37
z_{63}	7068.83	7068.848	-0.0177	-2.5
	7068.83	7068.848	-0.0177	-2.5
	7068.83	7068.848	-0.0177	-2.5
z_{42}	4757.51	4757.499	0.0111	2.33
	4757.51	4757.499	0.0111	2.33
z_{11}	1194.61	1194.602	0.008	6.73
c_{92}	10303.9	10303.9	-0.0002	-0.02
c_{91}	10147.7	10147.8	-0.0991	-9.77
	10147.7	10147.8	-0.0991	-9.77
c_{67}	7456.44	7456.394	0.0463	6.2
c_{60}	6584.86	6584.902	-0.0422	-6.41
	6584.86	6584.902	-0.0422	-6.41
c_{59}	6485.89	6485.834	0.0562	8.67
c_{52}	5702.36	5702.374	-0.0135	-2.37
c_{51}	5573.38	5573.331	0.0491	8.81
c_{44}	4770.84	4770.861	-0.0208	-4.36
c_{26}	2812.66	2812.648	0.0118	4.18
c_{13}	1198.7	1198.689	0.0108	8.99
c_{10}	956.547	956.5513	-0.0043	-4.54

Appendix A.17

Assigned fragment ions from CID of OCI-AML cells after treatment with 500 nM TSA (precursor ion at 877.1 *m/z*).

Ion	Observed Mass (Da)	Theoretical Mass (Da)	Mass Error (Da)	Mass Error (PPM)
y_{41}	4626.41	4626.451	-0.0412	-8.9
y_{30}	3352.77	3352.785	-0.0145	-4.33
	3352.77	3352.785	-0.0145	-4.33
y_{26}	2914.57	2914.598	-0.0282	-9.69
y_{19}	2130.09	2130.106	-0.0163	-7.67
y_{18}	1999.05	1999.066	-0.0158	-7.92
y_{16}	1784.96	1784.971	-0.0105	-5.88
y_{15}	1685.89	1685.902	-0.0121	-7.17
y_{14}	1522.83	1522.839	-0.0087	-5.75
y_{13}	1451.79	1451.802	-0.0116	-8.02
y_{12}	1338.71	1338.718	-0.0076	-5.66
	1338.71	1338.718	-0.0076	-5.66
y_{11}	1210.62	1210.623	-0.0026	-2.16
y_{9}	926.454	926.4629	-0.0089	-9.64
y_{8}	869.434	869.4415	-0.0075	-8.59
y_{5}	499.206	499.2086	-0.0026	-5.25
b_{53}	5856.35	5856.4	-0.0503	-8.59
b_{52}	5727.32	5727.358	-0.0377	-6.58
b_{51}	5598.27	5598.315	-0.0451	-8.06
b_{35}	3802.18	3802.214	-0.0342	-8.99
b_{31}	3364.93	3364.939	-0.0092	-2.72
b_{27}	2965.68	2965.691	-0.011	-3.71
b_{25}	2724.55	2724.548	0.0016	0.6
b_{24}	2610.49	2610.505	-0.0154	-5.91
b_{23}	2495.47	2495.479	-0.0085	-3.4
	2495.47	2495.479	-0.0085	-3.4
b_{19}	1971.09	1971.099	-0.0086	-4.37
b_{17}	1677.93	1677.939	-0.0086	-5.12
b_{12}	1166.65	1166.652	-0.002	-1.67
	1166.65	1166.652	-0.002	-1.67
b_{11}	996.539	996.5465	-0.0075	-7.48
	996.539	996.5465	-0.0075	-7.48
b_{10}	939.523	939.525	-0.002	-2.12

Ion	Observed Mass (Da)	Theoretical Mass (Da)	Mass Error (Da)	Mass Error (PPM)
b_9	826.439	826.4409	-0.0019	-2.34
b_8	769.416	769.4195	-0.0035	-4.51
	769.416	769.4195	-0.0035	-4.51
b_7	641.323	641.3245	-0.0015	-2.35
b_5	527.28	527.2816	-0.0016	-3.02
b_3	342.165	342.1652	-0.0002	-0.5

Appendix A.18

Assigned fragment ions from ECD of OCI-AML cells after treatment with 500 nM TSA (precursor ion at 877.1 *m/z*).

Ion	Observed Mass (Da)	Theoretical Mass (Da)	Mass Error (Da)	Mass Error (PPM)
z_{101}	11238.3	11238.343	-0.0427	-3.8
	11238.3	11238.343	-0.0427	-3.8
	11238.3	11238.343	-0.0427	-3.8
	11238.3	11238.343	-0.0427	-3.8
z_{100}	11181.3	11181.321	-0.0212	-1.9
z_{98}	10968.2	10968.199	0.0013	0.12
z_{95}	10726	10726.061	-0.0608	-5.67
z_{90}	10200.7	10200.733	-0.0333	-3.27
z_{89}	10143.7	10143.712	-0.0119	-1.17
	10143.7	10143.712	-0.0119	-1.17
z_{88}	10086.7	10086.69	0.0096	0.95
	10086.7	10086.69	0.0096	0.95
z_{87}	10015.6	10015.653	-0.0533	-5.32
z_{85}	9689.41	9689.4467	-0.0367	-3.79
z_{83}	9396.24	9396.2867	-0.0467	-4.97
	9396.24	9396.2867	-0.0467	-4.97
z_{80}	9027.99	9028.0079	-0.0179	-1.98
z_{79}	8871.86	8871.9068	-0.0468	-5.27
z_{78}	8756.84	8756.8799	-0.0399	-4.55
z_{76}	8529.73	8529.7529	-0.0229	-2.68
z_{75}	8401.67	8401.6943	-0.0243	-2.89
z_{72}	8130.49	8130.5411	-0.0511	-6.28
z_{68}	7721.24	7721.2722	-0.0322	-4.17
	7721.24	7721.2722	-0.0322	-4.17
	7721.24	7721.2722	-0.0322	-4.17
z_{66}	7409	7409.07	-0.07	-9.44
z_{65}	7295.92	7295.9859	-0.0659	-9.03
z_{64}	7224.89	7224.9488	-0.0588	-8.14
z_{63}	7068.8	7068.8477	-0.0477	-6.75
z_{62}	6912.68	6912.7466	-0.0666	-9.63
	6912.68	6912.7466	-0.0666	-9.63
z_{55}	6215.27	6215.3231	-0.0531	-8.54
z_{52}	5932.09	5932.1335	-0.0435	-7.33
z_{50}	5639.99	5640.0276	-0.0376	-6.67

Ion	Observed Mass (Da)	Theoretical Mass (Da)	Mass Error (Da)	Mass Error (PPM)
z_{49}	5510.96	5510.985	-0.025	-4.54
z_{48}	5409.9	5409.9373	-0.0373	-6.9
	5409.9	5409.9373	-0.0373	-6.9
z_{47}	5253.79	5253.8362	-0.0462	-8.8
	5253.79	5253.8362	-0.0462	-8.8
z_{43}	4856.53	4856.5673	-0.0373	-7.68
z_{42}	4757.47	4757.4989	-0.0289	-6.08
z_{39}	4368.29	4368.3039	-0.0139	-3.17
z_{35}	3886.01	3886.0073	0.0027	0.68
z_{34}	3770.97	3770.9804	-0.0104	-2.76
	3770.97	3770.9804	-0.0104	-2.76
z_{32}	3600.86	3600.8749	-0.0149	-4.13
	3600.86	3600.8749	-0.0149	-4.13
z_{29}	3235.71	3235.7162	-0.0062	-1.91
	3235.71	3235.7162	-0.0062	-1.91
z_{21}	2286.16	2286.1705	-0.0105	-4.58
z_{20}	2185.11	2185.1228	-0.0128	-5.85
z_{15}	1669.88	1669.8814	-0.0014	-0.85
z_{14}	1506.82	1506.8181	0.0019	1.27
z_{10}	1038.5	1038.5009	-0.0009	-0.82
z_{9}	910.443	910.4423	0.0007	0.8
z_{8}	853.421	853.4208	0.0002	0.22
c_{101}	11325.3	11325.398	-0.0983	-8.68
	11325.3	11325.398	-0.0983	-8.68
	11325.3	11325.398	-0.0983	-8.68
	11325.3	11325.398	-0.0983	-8.68
c_{100}	11268.3	11268.377	-0.0769	-6.82
c_{99}	11121.2	11121.309	-0.1085	-9.75
c_{91}	10189.8	10189.81	-0.0097	-0.95
	10189.8	10189.81	-0.0097	-0.95
c_{71}	7884.58	7884.5844	-0.0044	-0.56
c_{70}	7783.54	7783.5367	0.0033	0.42
c_{67}	7498.41	7498.4043	0.0057	0.76
c_{63}	7016.1	7016.1078	-0.0078	-1.11
	7016.1	7016.1078	-0.0078	-1.11
	7016.1	7016.1078	-0.0078	-1.11
c_{60}	6626.91	6626.9127	-0.0027	-0.41
	6626.91	6626.9127	-0.0027	-0.41
c_{59}	6527.84	6527.8443	-0.0043	-0.66

Ion	Observed Mass (Da)	Theoretical Mass (Da)	Mass Error (Da)	Mass Error (PPM)
c_{55}	6130.57	6130.5754	-0.0054	-0.88
c_{54}	5974.48	5974.4743	0.0057	0.95
	5974.48	5974.4743	0.0057	0.95
c_{53}	5873.42	5873.4266	-0.0066	-1.13
	5873.42	5873.4266	-0.0066	-1.13
c_{52}	5744.38	5744.384	-0.004	-0.7
	5744.38	5744.384	-0.004	-0.7
c_{51}	5615.34	5615.3414	-0.0014	-0.26
	5615.34	5615.3414	-0.0014	-0.26
c_{50}	5452.28	5452.2781	0.0019	0.34
	5452.28	5452.2781	0.0019	0.34
c_{48}	5226.11	5226.11	0	0
	5226.11	5226.11	0	0
c_{47}	5169.08	5169.0885	-0.0085	-1.65
	5169.08	5169.0885	-0.0085	-1.65
c_{46}	5082.05	5082.0565	-0.0065	-1.28
	5082.05	5082.0565	-0.0065	-1.28
c_{45}	4968.95	4968.9724	-0.0224	-4.52
c_{44}	4812.86	4812.8713	-0.0113	-2.36
	4812.86	4812.8713	-0.0113	-2.36
	4812.86	4812.8713	-0.0113	-2.36
c_{43}	4684.77	4684.7764	-0.0064	-1.36
c_{41}	4528.68	4528.6865	-0.0065	-1.44
c_{40}	4471.66	4471.665	-0.005	-1.13
c_{39}	4315.56	4315.5639	-0.0039	-0.91
	4315.56	4315.5639	-0.0039	-0.91
c_{38}	4159.46	4159.4628	-0.0028	-0.68
	4159.46	4159.4628	-0.0028	-0.68
c_{37}	4088.42	4088.4257	-0.0057	-1.4
c_{36}	3975.33	3975.3417	-0.0117	-2.93
	3975.33	3975.3417	-0.0117	-2.93
c_{35}	3819.23	3819.2405	-0.0105	-2.76
	3819.23	3819.2405	-0.0105	-2.76
	3819.23	3819.2405	-0.0105	-2.76
c_{34}	3663.14	3663.1394	0.0006	0.15
	3663.14	3663.1394	0.0006	0.15
c_{32}	3479.02	3479.0183	0.0017	0.5
c_{30}	3253.86	3253.8705	-0.0105	-3.24
	3253.86	3253.8705	-0.0105	-3.24

Ion	Observed Mass (Da)	Theoretical Mass (Da)	Mass Error (Da)	Mass Error (PPM)
	3253.86	3253.8705	-0.0105	-3.24
c_{29}	3152.8	3152.8229	-0.0229	-7.25
	3152.8	3152.8229	-0.0229	-7.25
c_{27}	2982.72	2982.7173	0.0027	0.89
c_{26}	2854.65	2854.6588	-0.0088	-3.07
	2854.65	2854.6588	-0.0088	-3.07
c_{24}	2627.51	2627.5318	-0.0218	-8.29
c_{23}	2512.49	2512.5048	-0.0148	-5.91
	2512.49	2512.5048	-0.0148	-5.91
c_{22}	2356.4	2356.4037	-0.0037	-1.58
c_{21}	2243.32	2243.3197	0.0003	0.15
c_{19}	1988.12	1988.125	-0.005	-2.49
	1988.12	1988.125	-0.005	-2.49
c_{18}	1832.02	1832.0238	-0.0038	-2.1
c_{17}	1694.95	1694.9649	-0.0149	-8.81
	1694.95	1694.9649	-0.0149	-8.81
c_{16}	1538.85	1538.8638	-0.0138	-8.99
	1538.85	1538.8638	-0.0138	-8.99
c_{15}	1368.75	1368.7583	-0.0083	-6.09
	1368.75	1368.7583	-0.0083	-6.09
c_{14}	1297.71	1297.7212	-0.0112	-8.65
	1297.71	1297.7212	-0.0112	-8.65
c_{13}	1240.69	1240.6998	-0.0098	-7.87
	1240.69	1240.6998	-0.0098	-7.87
c_{12}	1183.67	1183.6783	-0.0083	-7.01
	1183.67	1183.6783	-0.0083	-7.01
c_{8}	828.457	828.4564	0.0006	0.77
c_{7}	658.347	658.3509	-0.0039	-5.86

Appendix A.19

Assigned fragment ions from ECD of OCI-AML cells after treatment with 500 nM TSA (precursor ion at 880.4 *m/z*).

Ion	Observed Mass (Da)	Theoretical Mass (Da)	Mass Error (Da)	Mass Error (PPM)
z_{101}	11280.4	11280.35	0.0468	4.15
	11280.4	11280.35	0.0468	4.15
	11280.4	11280.35	0.0468	4.15
z_{99}	11067.3	11067.23	0.0693	6.27
z_{98}	11010.2	11010.21	-0.0092	-0.83
z_{94}	10598	10597.97	0.0342	3.23
	10598	10597.97	0.0342	3.23
z_{93}	10541	10540.94	0.0556	5.28
z_{92}	10427.9	10427.86	0.0397	3.81
z_{90}	10200.7	10200.73	-0.0333	-3.27
z_{89}	10143.8	10143.71	0.0881	8.69
z_{88}	10086.7	10086.69	0.0096	0.95
z_{87}	10015.7	10015.65	0.0467	4.66
z_{85}	9689.45	9689.447	0.0033	0.34
	9689.45	9689.447	0.0033	0.34
z_{83}	9396.3	9396.287	0.0133	1.42
	9396.3	9396.287	0.0133	1.42
z_{80}	9028.06	9028.008	0.0521	5.77
z_{79}	8871.89	8871.907	-0.0168	-1.89
	8871.89	8871.907	-0.0168	-1.89
z_{78}	8756.9	8756.88	0.0201	2.3
z_{76}	8529.77	8529.753	0.0171	2.01
	8529.77	8529.753	0.0171	2.01
	8529.77	8529.753	0.0171	2.01
z_{68}	7721.29	7721.272	0.0178	2.31
z_{67}	7565.15	7565.171	-0.0211	-2.79
	7565.15	7565.171	-0.0211	-2.79
z_{66}	7409	7409.07	-0.07	-9.44
	7409	7409.07	-0.07	-9.44
	7409	7409.07	-0.07	-9.44
z_{65}	7295.99	7295.986	0.0041	0.56
	7295.99	7295.986	0.0041	0.56
z_{64}	7224.92	7224.949	-0.0288	-3.99

Ion	Observed Mass (Da)	Theoretical Mass (Da)	Mass Error (Da)	Mass Error (PPM)
	7224.92	7224.949	-0.0288	-3.99
	7224.92	7224.949	-0.0288	-3.99
z_{63}	7068.82	7068.848	-0.0277	-3.92
	7068.82	7068.848	-0.0277	-3.92
	7068.82	7068.848	-0.0277	-3.92
z_{62}	6912.74	6912.747	-0.0066	-0.95
z_{61}	6855.67	6855.725	-0.0551	-8.04
	6855.67	6855.725	-0.0551	-8.04
z_{59}	6699.59	6699.635	-0.0453	-6.75
	6699.59	6699.635	-0.0453	-6.75
z_{58}	6571.48	6571.54	-0.0603	-9.17
	6571.48	6571.54	-0.0603	-9.17
z_{57}	6415.38	6415.439	-0.0592	-9.22
z_{56}	6302.3	6302.355	-0.0551	-8.75
z_{55}	6215.29	6215.323	-0.0331	-5.32
z_{54}	6158.27	6158.302	-0.0316	-5.14
z_{53}	6045.19	6045.218	-0.0276	-4.56
z_{52}	5932.12	5932.134	-0.0135	-2.28
z_{50}	5640.03	5640.028	0.0024	0.43
z_{49}	5511	5510.985	0.015	2.72
z_{48}	5409.96	5409.937	0.0227	4.19
z_{47}	5253.81	5253.836	-0.0262	-4.99
	5253.81	5253.836	-0.0262	-4.99
z_{45}	5097.71	5097.746	-0.0363	-7.13
z_{43}	4856.55	4856.567	-0.0173	-3.57
z_{42}	4757.49	4757.499	-0.0089	-1.87
z_{39}	4368.32	4368.304	0.0161	3.7
z_{35}	3886.03	3886.007	0.0227	5.83
z_{34}	3771	3770.98	0.0196	5.2
z_{32}	3600.88	3600.875	0.0051	1.42
	3600.88	3600.875	0.0051	1.42
z_{31}	3499.84	3499.827	0.0128	3.66
	3499.84	3499.827	0.0128	3.66
z_{28}	3106.69	3106.674	0.0164	5.28
z_{21}	2286.17	2286.171	-0.0005	-0.2
	2286.17	2286.171	-0.0005	-0.2
z_{15}	1669.89	1669.881	0.0086	5.14
z_{11}	1194.6	1194.602	-0.002	-1.64
z_{10}	1038.51	1038.501	0.0091	8.81

Ion	Observed Mass (Da)	Theoretical Mass (Da)	Mass Error (Da)	Mass Error (PPM)
z_9	910.448	910.4423	0.0057	6.29
z_8	853.425	853.4208	0.0042	4.91
c_{101}	11367.4	11367.41	-0.0089	-0.78
	11367.4	11367.41	-0.0089	-0.78
	11367.4	11367.41	-0.0089	-0.78
	11367.4	11367.41	-0.0089	-0.78
c_{93}	10516	10515.98	0.0201	1.91
c_{81}	9140.3	9140.252	0.0483	5.28
c_{71}	7926.64	7926.595	0.045	5.68
c_{70}	7825.59	7825.547	0.0427	5.46
c_{63}	7058.16	7058.118	0.0417	5.91
c_{60}	6668.94	6668.923	0.0167	2.51
c_{59}	6569.88	6569.855	0.0252	3.83
	6569.88	6569.855	0.0252	3.83
c_{54}	6016.51	6016.485	0.0252	4.18
c_{52}	5786.42	5786.395	0.0254	4.39
	5786.42	5786.395	0.0254	4.39
c_{51}	5657.36	5657.352	0.008	1.42
	5657.36	5657.352	0.008	1.42
c_{50}	5494.28	5494.289	-0.0087	-1.58
c_{48}	5268.12	5268.121	-0.0005	-0.1
	5268.12	5268.121	-0.0005	-0.1
c_{47}	5211.07	5211.099	-0.0291	-5.58
c_{45}	5010.94	5010.983	-0.043	-8.58
c_{44}	4854.88	4854.882	-0.0019	-0.39
	4854.88	4854.882	-0.0019	-0.39
	4854.88	4854.882	-0.0019	-0.39
c_{43}	4726.78	4726.787	-0.0069	-1.46
c_{40}	4513.66	4513.676	-0.0156	-3.45
c_{39}	4357.57	4357.575	-0.0045	-1.03
	4357.57	4357.575	-0.0045	-1.03
c_{38}	4201.47	4201.473	-0.0034	-0.8
	4201.47	4201.473	-0.0034	-0.8
c_{37}	4130.45	4130.436	0.0137	3.33
c_{36}	4017.35	4017.352	-0.0022	-0.55
c_{35}	3861.24	3861.251	-0.0111	-2.87
	3861.24	3861.251	-0.0111	-2.87
	3861.24	3861.251	-0.0111	-2.87
c_{34}	3705.16	3705.15	0.01	2.7

Ion	Observed Mass (Da)	Theoretical Mass (Da)	Mass Error (Da)	Mass Error (PPM)
	3705.16	3705.15	0.01	2.7
c_{30}	3295.89	3295.881	0.0089	2.7
c_{29}	3194.84	3194.833	0.0066	2.06
c_{27}	3024.74	3024.728	0.0121	4
c_{26}	2896.67	2896.669	0.0007	0.24
	2896.67	2896.669	0.0007	0.24
c_{23}	2554.49	2554.515	-0.0254	-9.94
	2554.49	2554.515	-0.0254	-9.94
c_{22}	2398.42	2398.414	0.0057	2.39
c_{18}	1874.05	1874.034	0.0156	8.33
c_{16}	1580.87	1580.874	-0.0044	-2.76
c_{9}	885.483	885.4778	0.0052	5.85
c_{8}	828.459	828.4564	0.0026	3.19

Appendix A.20

Assigned fragment ions from CID of OCI-AML cells after treatment with 500 nM TSA (precursor ion at 883.6 *m/z*).

Ion	Observed Mass (Da)	Theoretical Mass (Da)	Mass Error (Da)	Mass Error (PPM)
y_{43}	4872.54	4872.588	-0.048	-9.85
y_{41}	4626.41	4626.451	-0.0412	-8.9
y_{30}	3352.76	3352.785	-0.0245	-7.32
y_{29}	3251.71	3251.737	-0.0269	-8.26
y_{28}	3122.67	3122.694	-0.0243	-7.77
	3122.67	3122.694	-0.0243	-7.77
y_{27}	2985.61	2985.635	-0.0253	-8.49
y_{26}	2914.57	2914.598	-0.0282	-9.69
y_{19}	2130.09	2130.106	-0.0163	-7.67
y_{18}	1999.05	1999.066	-0.0158	-7.92
y_{17}	1884.03	1884.039	-0.0089	-4.72
y_{16}	1784.96	1784.971	-0.0105	-5.88
	1784.96	1784.971	-0.0105	-5.88
y_{15}	1685.89	1685.902	-0.0121	-7.17
	1685.89	1685.902	-0.0121	-7.17
y_{14}	1522.83	1522.839	-0.0087	-5.75
y_{13}	1451.8	1451.802	-0.0016	-1.13
y_{12}	1338.71	1338.718	-0.0076	-5.66
y_{11}	1210.62	1210.623	-0.0026	-2.16
	1210.62	1210.623	-0.0026	-2.16
y_{9}	926.456	926.4629	-0.0069	-7.48
y_{8}	869.436	869.4415	-0.0055	-6.29
y_{5}	499.205	499.2086	-0.0036	-7.25
b_{87}	9781.48	9781.525	-0.0449	-4.59
b_{86}	9682.41	9682.457	-0.0465	-4.81
b_{85}	9583.33	9583.388	-0.0581	-6.06
b_{70}	7850.47	7850.532	-0.0615	-7.83
	7850.47	7850.532	-0.0615	-7.83
b_{69}	7751.42	7751.463	-0.0431	-5.56
	7751.42	7751.463	-0.0431	-5.56
b_{68}	7680.39	7680.426	-0.036	-4.68
b_{63}	7083.06	7083.103	-0.0425	-6
	7083.06	7083.103	-0.0425	-6

Ion	Observed Mass (Da)	Theoretical Mass (Da)	Mass Error (Da)	Mass Error (PPM)
b_{53}	5940.39	5940.421	-0.0314	-5.28
	5940.39	5940.421	-0.0314	-5.28
b_{52}	5811.35	5811.379	-0.0288	-4.95
	5811.35	5811.379	-0.0288	-4.95
b_{51}	5682.32	5682.336	-0.0162	-2.85
b_{39}	4382.54	4382.559	-0.0187	-4.26
b_{35}	3886.22	3886.235	-0.0153	-3.93
	3886.22	3886.235	-0.0153	-3.93
b_{25}	2808.56	2808.569	-0.0094	-3.36
b_{24}	2694.52	2694.527	-0.0065	-2.42
b_{23}	2579.49	2579.5	-0.0096	-3.71
	2579.49	2579.5	-0.0096	-3.71
b_{22}	2423.39	2423.399	-0.0085	-3.49
b_{17}	1761.95	1761.96	-0.0097	-5.49
b_{11}	1080.56	1080.568	-0.0075	-6.97
b_{10}	1023.54	1023.546	-0.0061	-5.93
b_{9}	910.458	910.462	-0.004	-4.4
	910.458	910.462	-0.004	-4.4
b_{8}	853.437	853.4406	-0.0036	-4.16
	853.437	853.4406	-0.0036	-4.16
b_{7}	683.333	683.3351	-0.0021	-3
b_{6}	626.312	626.3136	-0.0016	-2.54
b_{5}	569.291	569.2921	-0.0011	-1.98
b_{4}	399.185	399.1866	-0.0016	-4.08
b_{3}	342.163	342.1652	-0.0022	-6.34

Appendix A.21

Assigned fragment ions from ECD of OCI-AML cells after treatment with 500 nM TSA (precursor ion at 883.6 *m/z*).

Ion	Observed Mass (Da)	Theoretical Mass (Da)	Mass Error (Da)	Mass Error (PPM)
z_{101}	11322.3	11322.36	-0.0638	-5.63
	11322.3	11322.36	-0.0638	-5.63
	11322.3	11322.36	-0.0638	-5.63
z_{99}	11109.2	11109.24	-0.0412	-3.71
z_{97}	10882.1	10882.11	-0.0142	-1.31
	10882.1	10882.11	-0.0142	-1.31
z_{96}	10825	10825.09	-0.0928	-8.57
	10825	10825.09	-0.0928	-8.57
	10825	10825.09	-0.0928	-8.57
z_{94}	10597.9	10597.97	-0.0658	-6.21
z_{93}	10540.9	10540.94	-0.0444	-4.21
	10540.9	10540.94	-0.0444	-4.21
	10540.9	10540.94	-0.0444	-4.21
z_{88}	10086.6	10086.69	-0.0904	-8.96
z_{87}	10015.6	10015.65	-0.0533	-5.32
z_{85}	9689.38	9689.447	-0.0667	-6.88
z_{84}	9552.32	9552.388	-0.0678	-7.1
	9552.32	9552.388	-0.0678	-7.1
z_{83}	9396.22	9396.287	-0.0667	-7.1
	9396.22	9396.287	-0.0667	-7.1
z_{81}	9141.05	9141.092	-0.042	-4.59
z_{80}	9027.96	9028.008	-0.0479	-5.31
z_{79}	8871.85	8871.907	-0.0568	-6.4
z_{78}	8756.82	8756.88	-0.0599	-6.83
z_{76}	8529.7	8529.753	-0.0529	-6.2
	8529.7	8529.753	-0.0529	-6.2
	8529.7	8529.753	-0.0529	-6.2
z_{75}	8401.65	8401.694	-0.0443	-5.27
z_{72}	8130.49	8130.541	-0.0511	-6.28
	8130.49	8130.541	-0.0511	-6.28
z_{68}	7721.23	7721.272	-0.0422	-5.46
	7721.23	7721.272	-0.0422	-5.46
z_{67}	7565.13	7565.171	-0.0411	-5.43

Ion	Observed Mass (Da)	Theoretical Mass (Da)	Mass Error (Da)	Mass Error (PPM)
z_{66}	7409.02	7409.07	-0.05	-6.74
	7409.02	7409.07	-0.05	-6.74
z_{65}	7295.94	7295.986	-0.0459	-6.29
z_{64}	7224.9	7224.949	-0.0488	-6.75
	7224.9	7224.949	-0.0488	-6.75
z_{63}	7068.8	7068.848	-0.0477	-6.75
	7068.8	7068.848	-0.0477	-6.75
	7068.8	7068.848	-0.0477	-6.75
z_{62}	6912.69	6912.747	-0.0566	-8.19
	6912.69	6912.747	-0.0566	-8.19
z_{61}	6855.67	6855.725	-0.0551	-8.04
	6855.67	6855.725	-0.0551	-8.04
z_{59}	6699.59	6699.635	-0.0453	-6.75
	6699.59	6699.635	-0.0453	-6.75
z_{58}	6571.49	6571.54	-0.0503	-7.65
z_{57}	6415.38	6415.439	-0.0592	-9.22
z_{55}	6215.28	6215.323	-0.0431	-6.93
z_{54}	6158.25	6158.302	-0.0516	-8.38
z_{52}	5932.09	5932.134	-0.0435	-7.33
z_{51}	5769.03	5769.07	-0.0402	-6.96
z_{50}	5639.99	5640.028	-0.0376	-6.67
z_{49}	5510.95	5510.985	-0.035	-6.35
z_{48}	5409.9	5409.937	-0.0373	-6.9
z_{47}	5253.8	5253.836	-0.0362	-6.89
	5253.8	5253.836	-0.0362	-6.89
z_{45}	5097.7	5097.746	-0.0463	-9.09
z_{43}	4856.53	4856.567	-0.0373	-7.68
z_{42}	4757.47	4757.499	-0.0289	-6.08
z_{39}	4368.28	4368.304	-0.0239	-5.46
z_{35}	3885.99	3886.007	-0.0173	-4.46
z_{34}	3770.97	3770.98	-0.0104	-2.76
z_{32}	3600.86	3600.875	-0.0149	-4.13
	3600.86	3600.875	-0.0149	-4.13
z_{31}	3499.82	3499.827	-0.0072	-2.06
z_{29}	3235.71	3235.716	-0.0062	-1.91
	3235.71	3235.716	-0.0062	-1.91
z_{21}	2286.16	2286.171	-0.0105	-4.58
	2286.16	2286.171	-0.0105	-4.58
z_{18}	1983.04	1983.045	-0.0052	-2.61

Ion	Observed Mass (Da)	Theoretical Mass (Da)	Mass Error (Da)	Mass Error (PPM)
z_{15}	1669.88	1669.881	-0.0014	-0.85
z_{14}	1506.82	1506.818	0.0019	1.27
z_{10}	1038.5	1038.501	-0.0009	-0.82
z_{9}	910.439	910.4423	-0.0033	-3.59
z_{8}	853.42	853.4208	-0.0008	-0.95
c_{93}	10557.9	10557.99	-0.0904	-8.57
c_{91}	10273.8	10273.83	-0.0307	-2.99
c_{81}	9182.21	9182.262	-0.0522	-5.69
c_{71}	7968.57	7968.606	-0.0355	-4.46
c_{70}	7867.5	7867.558	-0.0578	-7.35
c_{63}	7100.1	7100.129	-0.0289	-4.06
	7100.1	7100.129	-0.0289	-4.06
	7100.1	7100.129	-0.0289	-4.06
c_{60}	6710.91	6710.934	-0.0238	-3.55
	6710.91	6710.934	-0.0238	-3.55
c_{59}	6611.85	6611.865	-0.0154	-2.33
	6611.85	6611.865	-0.0154	-2.33
c_{57}	6370.68	6370.686	-0.0064	-1
c_{55}	6214.59	6214.597	-0.0065	-1.05
	6214.59	6214.597	-0.0065	-1.05
c_{53}	5957.43	5957.448	-0.0177	-2.97
	5957.43	5957.448	-0.0177	-2.97
c_{52}	5828.39	5828.405	-0.0151	-2.59
	5828.39	5828.405	-0.0151	-2.59
c_{51}	5699.34	5699.363	-0.0225	-3.95
c_{48}	5310.12	5310.131	-0.0111	-2.09
	5310.12	5310.131	-0.0111	-2.09
c_{47}	5253.11	5253.11	0.0004	0.07
	5253.11	5253.11	0.0004	0.07
c_{46}	5166.08	5166.078	0.0024	0.47
	5166.08	5166.078	0.0024	0.47
c_{45}	5053	5052.994	0.0065	1.28
c_{44}	4896.89	4896.892	-0.0024	-0.49
c_{43}	4768.8	4768.798	0.0025	0.53
c_{41}	4612.71	4612.708	0.0024	0.52
c_{40}	4555.69	4555.686	0.0039	0.85
	4555.69	4555.686	0.0039	0.85
c_{39}	4399.58	4399.585	-0.005	-1.14
	4399.58	4399.585	-0.005	-1.14

Ion	Observed Mass (Da)	Theoretical Mass (Da)	Mass Error (Da)	Mass Error (PPM)
c_{38}	4243.48	4243.484	-0.0039	-0.92
c_{37}	4172.44	4172.447	-0.0068	-1.63
c_{36}	4059.36	4059.363	-0.0027	-0.67
c_{35}	3903.26	3903.262	-0.0016	-0.42
	3903.26	3903.262	-0.0016	-0.42
c_{34}	3747.15	3747.161	-0.0105	-2.81
c_{32}	3563.03	3563.039	-0.0093	-2.62
c_{30}	3337.89	3337.892	-0.0016	-0.49
c_{29}	3236.84	3236.844	-0.0039	-1.22
c_{27}	3066.72	3066.738	-0.0184	-6.01
c_{26}	2938.67	2938.68	-0.0098	-3.35
	2938.67	2938.68	-0.0098	-3.35
c_{25}	2825.6	2825.596	0.0042	1.49
c_{24}	2711.55	2711.553	-0.0029	-1.05
c_{23}	2596.53	2596.526	0.0041	1.57
	2596.53	2596.526	0.0041	1.57
c_{22}	2440.42	2440.425	-0.0048	-1.97
c_{21}	2327.34	2327.341	-0.0007	-0.32
c_{19}	2072.15	2072.146	0.004	1.91
c_{18}	1916.04	1916.045	-0.0049	-2.57
c_{17}	1778.98	1778.986	-0.006	-3.38
c_{16}	1622.87	1622.885	-0.0149	-9.19
c_{15}	1452.77	1452.779	-0.0094	-6.48
c_{14}	1381.73	1381.742	-0.0123	-8.9
c_{13}	1324.71	1324.721	-0.0108	-8.18
c_{8}	870.466	870.4669	-0.0009	-1.03
c_{7}	700.363	700.3614	0.0016	2.29
c_{6}	643.343	643.3399	0.0031	4.76
c_{5}	586.323	586.3185	0.0045	7.71

Appendix A.22

Assigned fragment ions from CID of wild type pooled mouse brain sample (precursor ion at 754 *m/z*).

Ion	Observed Mass (Da)	Theoretical Mass (Da)	Mass Error (Da)	Mass Error (PPM)
y_{63}	7084.85	7084.868	-0.0183	-2.59
y_{50}	5656.03	5656.048	-0.0183	-3.23
y_{49}	5526.99	5527.006	-0.0157	-2.83
	5526.99	5527.006	-0.0157	-2.83
y_{42}	4773.5	4773.52	-0.0196	-4.1
y_{41}	4626.43	4626.451	-0.0212	-4.57
y_{40}	4513.35	4513.367	-0.0171	-3.79
y_{39}	4384.31	4384.325	-0.0145	-3.31
y_{32}	3616.88	3616.896	-0.0155	-4.3
	3616.88	3616.896	-0.0155	-4.3
y_{31}	3515.83	3515.848	-0.0179	-5.08
y_{30}	3352.77	3352.785	-0.0145	-4.33
y_{28}	3122.68	3122.694	-0.0143	-4.57
	3122.68	3122.694	-0.0143	-4.57
	3122.68	3122.694	-0.0143	-4.57
y_{27}	2985.62	2985.635	-0.0154	-5.14
y_{26}	2914.58	2914.598	-0.0182	-6.26
y_{23}	2502.3	2502.307	-0.0072	-2.88
y_{22}	2401.24	2401.26	-0.0195	-8.13
y_{21}	2302.18	2302.191	-0.0111	-4.83
y_{20}	2201.13	2201.143	-0.0134	-6.11
y_{19}	2130.09	2130.106	-0.0163	-7.67
y_{18}	1999.06	1999.066	-0.0058	-2.92
y_{17}	1884.03	1884.039	-0.0089	-4.72
	1884.03	1884.039	-0.0089	-4.72
y_{16}	1784.96	1784.971	-0.0105	-5.88
	1784.96	1784.971	-0.0105	-5.88
y_{15}	1685.9	1685.902	-0.0021	-1.23
	1685.9	1685.902	-0.0021	-1.23
y_{14}	1522.83	1522.839	-0.0087	-5.75
y_{13}	1451.8	1451.802	-0.0016	-1.13
y_{12}	1338.71	1338.718	-0.0076	-5.66
y_{11}	1210.62	1210.623	-0.0026	-2.16
b_{101}	11224.3	11224.35	-0.0509	-4.53
b_{99}	11020.2	11020.26	-0.061	-5.54

Ion	Observed Mass (Da)	Theoretical Mass (Da)	Mass Error (Da)	Mass Error (PPM)
	11020.2	11020.26	-0.061	-5.54
b_{90}	9960.62	9960.667	-0.0473	-4.75
b_{88}	9776.51	9776.546	-0.0361	-3.69
b_{87}	9613.45	9613.483	-0.0328	-3.41
	9613.45	9613.483	-0.0328	-3.41
b_{86}	9514.38	9514.414	-0.0344	-3.61
	9514.38	9514.414	-0.0344	-3.61
	9514.38	9514.414	-0.0344	-3.61
b_{85}	9415.32	9415.346	-0.026	-2.76
	9415.32	9415.346	-0.026	-2.76
	9415.32	9415.346	-0.026	-2.76
b_{84}	9300.29	9300.319	-0.029	-3.12
	9300.29	9300.319	-0.029	-3.12
	9300.29	9300.319	-0.029	-3.12
b_{82}	9098.22	9098.241	-0.0214	-2.35
b_{81}	8997.16	8997.194	-0.0337	-3.75
b_{71}	7783.52	7783.537	-0.017	-2.18
b_{70}	7682.47	7682.489	-0.0193	-2.51
	7682.47	7682.489	-0.0193	-2.51
b_{69}	7583.41	7583.421	-0.0109	-1.44
	7583.41	7583.421	-0.0109	-1.44
b_{63}	6915.04	6915.06	-0.0204	-2.94
b_{60}	6525.84	6525.865	-0.0253	-3.88
	6525.84	6525.865	-0.0253	-3.88
	6525.84	6525.865	-0.0253	-3.88
b_{59}	6426.78	6426.797	-0.0169	-2.63
	6426.78	6426.797	-0.0169	-2.63
	6426.78	6426.797	-0.0169	-2.63
b_{58}	6298.69	6298.702	-0.0119	-1.89
b_{57}	6185.59	6185.618	-0.0279	-4.5
b_{55}	6029.51	6029.528	-0.018	-2.98
b_{53}	5772.36	5772.379	-0.0192	-3.33
	5772.36	5772.379	-0.0192	-3.33
	5772.36	5772.379	-0.0192	-3.33
b_{52}	5643.32	5643.337	-0.0166	-2.94
	5643.32	5643.337	-0.0166	-2.94

b_{51}	5514.28	5514.294	-0.014	-2.54
	5514.28	5514.294	-0.014	-2.54
b_{50}	5351.22	5351.231	-0.0107	-2
	5351.22	5351.231	-0.0107	-2
b_{40}	4370.6	4370.618	-0.0176	-4.03
b_{39}	4214.5	4214.517	-0.0165	-3.92
	4214.5	4214.517	-0.0165	-3.92
b_{35}	3718.18	3718.193	-0.0131	-3.53
b_{24}	2526.48	2526.484	-0.0044	-1.72
	2526.48	2526.484	-0.0044	-1.72
b_{19}	1887.07	1887.078	-0.0075	-3.99
	1887.07	1887.078	-0.0075	-3.99
b_{12}	1124.64	1124.641	-0.0014	-1.25
b_{11}	996.543	996.5465	-0.0035	-3.46
b_{10}	939.522	939.525	-0.003	-3.18
b_{8}	769.417	769.4195	-0.0025	-3.21
b_{5}	527.28	527.2816	-0.0016	-3.02

Appendix A.23

Assigned fragment ions from ECD of wild type pooled mouse brain sample (precursor ion at 754 *m/z*).

Ion	Observed Mass (Da)	Theoretical Mass (Da)	Mass Error (Da)	Mass Error (PPM)
z_{101}	11154.3	11154.32	-0.0216	-1.94
z_{95}	10642	10642.04	-0.0397	-3.73
z_{94}	10513.9	10513.94	-0.0447	-4.25
z_{93}	10456.9	10456.92	-0.0233	-2.23
	10456.9	10456.92	-0.0233	-2.23
z_{90}	10158.7	10158.72	-0.0228	-2.24
z_{89}	10101.7	10101.7	-0.0013	-0.13
	10101.7	10101.7	-0.0013	-0.13
z_{86}	9845.54	9845.548	-0.0078	-0.79
z_{85}	9689.43	9689.447	-0.0167	-1.72
	9689.43	9689.447	-0.0167	-1.72
z_{80}	9027.98	9028.008	-0.0279	-3.09
z_{79}	8871.9	8871.907	-0.0068	-0.77
z_{78}	8756.87	8756.88	-0.0099	-1.12
	8756.87	8756.88	-0.0099	-1.12
	8756.87	8756.88	-0.0099	-1.12
z_{76}	8529.74	8529.753	-0.0129	-1.51
	8529.74	8529.753	-0.0129	-1.51
	8529.74	8529.753	-0.0129	-1.51
z_{68}	7721.27	7721.272	-0.0022	-0.28
	7721.27	7721.272	-0.0022	-0.28
	7721.27	7721.272	-0.0022	-0.28
z_{67}	7565.16	7565.171	-0.0111	-1.46
	7565.16	7565.171	-0.0111	-1.46
z_{66}	7409.07	7409.07	0	0
	7409.07	7409.07	0	0
z_{65}	7295.98	7295.986	-0.0059	-0.81
	7295.98	7295.986	-0.0059	-0.81
z_{64}	7224.94	7224.949	-0.0088	-1.22
	7224.94	7224.949	-0.0088	-1.22
	7224.94	7224.949	-0.0088	-1.22
z_{63}	7068.84	7068.848	-0.0077	-1.09
	7068.84	7068.848	-0.0077	-1.09
	7068.84	7068.848	-0.0077	-1.09

Ion	Observed Mass (Da)	Theoretical Mass (Da)	Mass Error (Da)	Mass Error (PPM)
z_{62}	6912.74	6912.747	-0.0066	-0.95
	6912.74	6912.747	-0.0066	-0.95
z_{61}	6855.72	6855.725	-0.0051	-0.75
	6855.72	6855.725	-0.0051	-0.75
	6855.72	6855.725	-0.0051	-0.75
z_{59}	6699.63	6699.635	-0.0053	-0.78
z_{58}	6571.54	6571.54	-0.0003	-0.04
z_{57}	6415.44	6415.439	0.0008	0.13
	6415.44	6415.439	0.0008	0.13
z_{56}	6302.36	6302.355	0.0049	0.77
	6302.36	6302.355	0.0049	0.77
z_{55}	6215.33	6215.323	0.0069	1.11
z_{54}	6158.3	6158.302	-0.0016	-0.26
z_{52}	5932.13	5932.134	-0.0035	-0.59
z_{51}	5769.07	5769.07	-0.0002	-0.03
	5769.07	5769.07	-0.0002	-0.03
	5769.07	5769.07	-0.0002	-0.03
z_{50}	5640.03	5640.028	0.0024	0.43
	5640.03	5640.028	0.0024	0.43
	5640.03	5640.028	0.0024	0.43
z_{49}	5510.98	5510.985	-0.005	-0.91
	5510.98	5510.985	-0.005	-0.91
z_{48}	5409.94	5409.937	0.0027	0.5
	5409.94	5409.937	0.0027	0.5
	5409.94	5409.937	0.0027	0.5
z_{47}	5253.83	5253.836	-0.0062	-1.18
z_{45}	5097.75	5097.746	0.0037	0.72
z_{43}	4856.56	4856.567	-0.0073	-1.51
	4856.56	4856.567	-0.0073	-1.51
	4856.56	4856.567	-0.0073	-1.51
	4856.56	4856.567	-0.0073	-1.51
z_{42}	4757.5	4757.499	0.0011	0.23
	4757.5	4757.499	0.0011	0.23
	4757.5	4757.499	0.0011	0.23
z_{39}	4368.3	4368.304	-0.0039	-0.88
	4368.3	4368.304	-0.0039	-0.88
z_{38}	4254.26	4254.261	-0.0009	-0.22
z_{35}	3886	3886.007	-0.0073	-1.89
z_{34}	3770.97	3770.98	-0.0104	-2.76
z_{32}	3600.87	3600.875	-0.0049	-1.36

Ion	Observed Mass (Da)	Theoretical Mass (Da)	Mass Error (Da)	Mass Error (PPM)
	3600.87	3600.875	-0.0049	-1.36
z_{31}	3499.82	3499.827	-0.0072	-2.06
z_{29}	3235.71	3235.716	-0.0062	-1.91
z_{27}	2969.61	2969.615	-0.0047	-1.58
z_{24}	2614.38	2614.382	-0.0015	-0.58
z_{23}	2486.28	2486.287	-0.0066	-2.63
z_{21}	2286.17	2286.171	-0.0005	-0.2
	2286.17	2286.171	-0.0005	-0.2
z_{20}	2185.12	2185.123	-0.0028	-1.27
	2185.12	2185.123	-0.0028	-1.27
z_{19}	2114.08	2114.086	-0.0057	-2.68
z_{18}	1983.04	1983.045	-0.0052	-2.61
z_{15}	1669.88	1669.881	-0.0014	-0.85
z_{13}	1435.78	1435.781	-0.001	-0.68
z_{12}	1322.7	1322.697	0.0031	2.33
z_{11}	1194.6	1194.602	-0.002	-1.64
	1194.6	1194.602	-0.002	-1.64
	1194.6	1194.602	-0.002	-1.64
z_{10}	1038.5	1038.501	-0.0009	-0.82
	1038.5	1038.501	-0.0009	-0.82
z_{9}	910.442	910.4423	-0.0003	-0.3
z_{8}	853.422	853.4208	0.0012	1.39
c_{101}	11241.3	11241.38	-0.0772	-6.87
	11241.3	11241.38	-0.0772	-6.87
	11241.3	11241.38	-0.0772	-6.87
	11241.3	11241.38	-0.0772	-6.87
	11241.3	11241.38	-0.0772	-6.87
c_{92}	10261.9	10261.89	0.0103	1
c_{91}	10105.8	10105.79	0.0114	1.13
c_{88}	9793.57	9793.573	-0.0025	-0.25
c_{81}	9014.21	9014.22	-0.0101	-1.12
c_{76}	8401.8	8401.813	-0.013	-1.54
c_{74}	8193.73	8193.717	0.0131	1.59
c_{71}	7800.55	7800.563	-0.0133	-1.71
c_{63}	6932.08	6932.087	-0.0067	-0.97
c_{60}	6542.89	6542.892	-0.0016	-0.25
	6542.89	6542.892	-0.0016	-0.25
c_{59}	6443.82	6443.823	-0.0032	-0.5
c_{55}	6046.55	6046.554	-0.0043	-0.72
	6046.55	6046.554	-0.0043	-0.72

Ion	Observed Mass (Da)	Theoretical Mass (Da)	Mass Error (Da)	Mass Error (PPM)
c_{54}	5890.45	5890.453	-0.0032	-0.55
c_{53}	5789.4	5789.406	-0.0055	-0.96
c_{52}	5660.36	5660.363	-0.003	-0.52
	5660.36	5660.363	-0.003	-0.52
	5660.36	5660.363	-0.003	-0.52
c_{51}	5531.32	5531.32	-0.0004	-0.07
	5531.32	5531.32	-0.0004	-0.07
	5531.32	5531.32	-0.0004	-0.07
c_{50}	5368.25	5368.257	-0.007	-1.31
c_{49}	5254.84	5254.79	0.0498	9.48
c_{48}	5142.09	5142.089	0.0011	0.21
c_{47}	5085.07	5085.068	0.0025	0.5
c_{46}	4998.03	4998.035	-0.0054	-1.09
c_{45}	4884.95	4884.951	-0.0014	-0.28
c_{44}	4728.85	4728.85	-0.0003	-0.05
	4728.85	4728.85	-0.0003	-0.05
	4728.85	4728.85	-0.0003	-0.05
c_{43}	4600.75	4600.755	-0.0053	-1.15
c_{41}	4444.66	4444.665	-0.0054	-1.22
	4444.66	4444.665	-0.0054	-1.22
c_{40}	4387.64	4387.644	-0.004	-0.9
	4387.64	4387.644	-0.004	-0.9
c_{39}	4231.54	4231.543	-0.0029	-0.68
	4231.54	4231.543	-0.0029	-0.68
c_{38}	4075.44	4075.442	-0.0017	-0.43
	4075.44	4075.442	-0.0017	-0.43
	4075.44	4075.442	-0.0017	-0.43
c_{37}	4004.4	4004.405	-0.0046	-1.16
c_{36}	3891.32	3891.321	-0.0006	-0.15
	3891.32	3891.321	-0.0006	-0.15
c_{35}	3735.22	3735.22	0.0005	0.14
	3735.22	3735.22	0.0005	0.14
c_{34}	3579.12	3579.118	0.0016	0.46
	3579.12	3579.118	0.0016	0.46
	3579.12	3579.118	0.0016	0.46
	3579.12	3579.118	0.0016	0.46
c_{32}	3394.99	3394.997	-0.0072	-2.12
c_{29}	3068.8	3068.802	-0.0018	-0.58
c_{27}	2898.7	2898.696	0.0037	1.29
c_{26}	2770.61	2770.638	-0.0277	-9.99

Ion	Observed Mass (Da)	Theoretical Mass (Da)	Mass Error (Da)	Mass Error (PPM)
	2770.61	2770.638	-0.0277	-9.99
	2770.61	2770.638	-0.0277	-9.99
	2770.61	2770.638	-0.0277	-9.99
c_{25}	2657.55	2657.554	-0.0036	-1.37
c_{24}	2543.51	2543.511	-0.0007	-0.27
	2543.51	2543.511	-0.0007	-0.27
	2543.51	2543.511	-0.0007	-0.27
c_{23}	2428.49	2428.484	0.0062	2.57
	2428.49	2428.484	0.0062	2.57
	2428.49	2428.484	0.0062	2.57
	2428.49	2428.484	0.0062	2.57
c_{22}	2272.38	2272.383	-0.0026	-1.17
	2272.38	2272.383	-0.0026	-1.17
c_{21}	2159.3	2159.299	0.0014	0.65
	2159.3	2159.299	0.0014	0.65
c_{20}	2060.23	2060.23	-0.0002	-0.09
c_{19}	1904.11	1904.104	0.0061	3.21
	1904.11	1904.104	0.0061	3.21
	1904.11	1904.104	0.0061	3.21
c_{18}	1748	1748.003	-0.0028	-1.58
	1748	1748.003	-0.0028	-1.58
	1748	1748.003	-0.0028	-1.58
c_{17}	1610.95	1610.944	0.0061	3.81
c_{16}	1454.84	1454.843	-0.0027	-1.89
	1454.84	1454.843	-0.0027	-1.89
c_{15}	1326.75	1326.748	0.0022	1.67
	1326.75	1326.748	0.0022	1.67
	1326.75	1326.748	0.0022	1.67
c_{14}	1255.71	1255.711	-0.0007	-0.54
	1255.71	1255.711	-0.0007	-0.54
	1255.71	1255.711	-0.0007	-0.54
c_{13}	1198.69	1198.689	0.0008	0.65
	1198.69	1198.689	0.0008	0.65
	1198.69	1198.689	0.0008	0.65
c_{12}	1141.67	1141.668	0.0022	1.96
	1141.67	1141.668	0.0022	1.96
c_{11}	1013.57	1013.573	-0.0028	-2.76
	1013.57	1013.573	-0.0028	-2.76
c_{9}	843.469	843.4673	0.0017	2.04
	843.469	843.4673	0.0017	2.04

Ion	Observed Mass (Da)	Theoretical Mass (Da)	Mass Error (Da)	Mass Error (PPM)
c_8	786.448	786.4458	0.0022	2.77
	786.448	786.4458	0.0022	2.77
c_7	658.351	658.3509	0.0001	0.21
c_6	601.33	601.3294	0.0006	1
c_5	544.309	544.3079	0.0011	1.95
c_4	416.215	416.213	0.002	4.86

Appendix A.24

Assigned fragment ions from CID of wild type pooled mouse brain sample (precursor ion at 756 *m/z*).

Ion	Observed Mass (Da)	Theoretical Mass (Da)	Mass Error (Da)	Mass Error (PPM)
y_{68}	7737.31	7737.293	0.0167	2.15
y_{39}	4384.362	4384.325	0.0373	8.5
	4384.362	4384.325	0.0373	8.5
y_{14}	1522.832	1522.839	-0.0071	-4.68
	1522.832	1522.839	-0.0071	-4.68
y_{13}	1451.799	1451.802	-0.0028	-1.9
y_{12}	1338.717	1338.718	-0.0005	-0.37
y_{11}	1210.624	1210.623	0.0017	1.44
y_{5}	499.2051	499.2086	-0.0035	-6.97
b_{101}	11238.27	11238.37	-0.0978	-8.71
	11238.27	11238.37	-0.0978	-8.71
b_{86}	9528.36	9528.43	-0.07	-7.35
	9528.36	9528.43	-0.07	-7.35
	9528.36	9528.43	-0.07	-7.35
b_{85}	9429.283	9429.362	-0.0785	-8.32
b_{83}	9183.228	9183.294	-0.0659	-7.18
	9183.228	9183.294	-0.0659	-7.18
b_{60}	6539.876	6539.881	-0.0051	-0.78
b_{59}	6440.785	6440.813	-0.0275	-4.27
	6440.785	6440.813	-0.0275	-4.27
b_{58}	6312.717	6312.718	-0.0002	-0.04
b_{55}	6043.551	6043.544	0.0077	1.28
b_{53}	5786.374	5786.395	-0.0213	-3.67
	5786.374	5786.395	-0.0213	-3.67
	5786.374	5786.395	-0.0213	-3.67
b_{52}	5657.346	5657.352	-0.0062	-1.09
	5657.346	5657.352	-0.0062	-1.09
	5657.346	5657.352	-0.0062	-1.09
b_{51}	5528.314	5528.31	0.0045	0.81
b_{50}	5365.231	5365.246	-0.015	-2.79
	5365.231	5365.246	-0.015	-2.79
b_{39}	4228.532	4228.532	-0.0002	-0.04
	4228.532	4228.532	-0.0002	-0.04
b_{25}	2654.544	2654.543	0.001	0.37

Ion	Observed Mass (Da)	Theoretical Mass (Da)	Mass Error (Da)	Mass Error (PPM)
b_{24}	2540.496	2540.5	-0.0039	-1.55
b_{19}	1887.078	1887.078	0.0001	0.07
	1887.078	1887.078	0.0001	0.07
b_{17}	1593.917	1593.918	-0.0002	-0.14
b_{12}	1124.645	1124.641	0.0035	3.09
b_{11}	996.5444	996.5465	-0.0021	-2.11
b_{10}	939.5188	939.525	-0.0062	-6.59
b_{7}	641.3262	641.3245	0.0017	2.65
b_{5}	527.282	527.2816	0.0004	0.8

Appendix A.25

Assigned fragment ions from ECD of wild type pooled mouse brain sample (precursor ion at 756 *m/z*).

Ion	Observed Mass (Da)	Theoretical Mass (Da)	Mass Error (Da)	Mass Error (PPM)
z_{95}	10656.06	10656.06	0.0082	0.77
z_{91}	10300.8	10300.83	-0.0321	-3.12
z_{76}	8529.78	8529.753	0.0271	3.17
z_{68}	7721.272	7721.272	-0.0003	-0.04
	7721.272	7721.272	-0.0003	-0.04
z_{65}	7295.984	7295.986	-0.0024	-0.33
z_{64}	7224.94	7224.949	-0.0091	-1.26
z_{63}	7068.846	7068.848	-0.002	-0.28
z_{61}	6855.721	6855.725	-0.0044	-0.64
z_{57}	6415.436	6415.439	-0.0027	-0.43
z_{54}	6158.299	6158.302	-0.0024	-0.4
z_{51}	5769.068	5769.07	-0.0021	-0.37
z_{50}	5640.027	5640.028	-0.0003	-0.06
z_{49}	5510.982	5510.985	-0.003	-0.54
z_{48}	5409.932	5409.937	-0.0057	-1.06
z_{47}	5253.835	5253.836	-0.0017	-0.32
	5253.835	5253.836	-0.0017	-0.32
z_{42}	4757.496	4757.499	-0.003	-0.63
	4757.496	4757.499	-0.003	-0.63
z_{39}	4368.303	4368.304	-0.0008	-0.19
z_{34}	3770.974	3770.98	-0.0064	-1.7
	3770.974	3770.98	-0.0064	-1.7
z_{32}	3600.869	3600.875	-0.0058	-1.61
z_{31}	3499.823	3499.827	-0.0041	-1.17
z_{28}	3106.673	3106.674	-0.0008	-0.25
z_{20}	2185.118	2185.123	-0.0048	-2.21
	2185.118	2185.123	-0.0048	-2.21
z_{18}	1983.043	1983.045	-0.0021	-1.03
z_{15}	1669.881	1669.881	-0.0003	-0.19
z_{14}	1506.822	1506.818	0.0041	2.73
z_{12}	1322.698	1322.697	0.0008	0.6
z_{11}	1194.599	1194.602	-0.0029	-2.4
	1194.599	1194.602	-0.0029	-2.4

z_{10}	1038.501	1038.501	0.0001	0.09

Ion	Observed Mass (Da)	Theoretical Mass (Da)	Mass Error (Da)	Mass Error (PPM)
z_9	910.443	910.4423	0.0007	0.78
c_{101}	11255.32	11255.39	-0.0726	-6.45
	11255.32	11255.39	-0.0726	-6.45
	11255.32	11255.39	-0.0726	-6.45
	11255.32	11255.39	-0.0726	-6.45
c_{100}	11198.33	11198.37	-0.0412	-3.68
	11198.33	11198.37	-0.0412	-3.68
c_{93}	10403.94	10403.96	-0.0192	-1.85
c_{91}	10119.8	10119.8	-0.0078	-0.77
c_{81}	9028.228	9028.236	-0.0082	-0.91
c_{71}	7814.575	7814.579	-0.0043	-0.55
c_{67}	7428.395	7428.399	-0.0035	-0.47
c_{63}	6946.105	6946.102	0.0022	0.32
c_{60}	6556.903	6556.907	-0.0045	-0.69
c_{59}	6457.84	6457.839	0.0006	0.09
	6457.84	6457.839	0.0006	0.09
c_{55}	6060.574	6060.57	0.0036	0.6
c_{52}	5674.382	5674.379	0.0035	0.61
	5674.382	5674.379	0.0035	0.61
c_{51}	5545.343	5545.336	0.0068	1.23
c_{40}	4401.667	4401.66	0.0069	1.56
c_{39}	4245.554	4245.559	-0.005	-1.17
	4245.554	4245.559	-0.005	-1.17
c_{38}	4089.46	4089.457	0.003	0.72
	4089.46	4089.457	0.003	0.72
c_{37}	4018.423	4018.42	0.0022	0.56
c_{36}	3905.344	3905.336	0.0077	1.96
c_{34}	3593.138	3593.134	0.0037	1.02
	3593.138	3593.134	0.0037	1.02
c_{26}	2784.656	2784.653	0.0028	1
	2784.656	2784.653	0.0028	1
c_{24}	2557.529	2557.526	0.0026	1.01
c_{23}	2442.508	2442.499	0.0085	3.47
	2442.508	2442.499	0.0085	3.47
c_{21}	2173.318	2173.314	0.0041	1.91
	2173.318	2173.314	0.0041	1.91
c_{19}	1904.108	1904.104	0.0044	2.32
	1904.108	1904.104	0.0044	2.32

	1904.108	1904.104	0.0044	2.32

Ion	Observed Mass (Da)	Theoretical Mass (Da)	Mass Error (Da)	Mass Error (PPM)
c_{18}	1748.006	1748.003	0.0033	1.87
	1748.006	1748.003	0.0033	1.87
	1748.006	1748.003	0.0033	1.87
c_{17}	1610.95	1610.944	0.0064	3.95
c_{16}	1454.846	1454.843	0.0028	1.95
	1454.846	1454.843	0.0028	1.95
c_{15}	1326.751	1326.748	0.003	2.24
	1326.751	1326.748	0.003	2.24
	1326.751	1326.748	0.003	2.24
c_{14}	1255.714	1255.711	0.0037	2.95
	1255.714	1255.711	0.0037	2.95
	1255.714	1255.711	0.0037	2.95
c_{13}	1198.693	1198.689	0.0035	2.89
	1198.693	1198.689	0.0035	2.89
	1198.693	1198.689	0.0035	2.89
c_{12}	1141.67	1141.668	0.0022	1.88
	1141.67	1141.668	0.0022	1.88
c_{11}	1013.575	1013.573	0.0022	2.15
	1013.575	1013.573	0.0022	2.15
c_{10}	956.5557	956.5514	0.0044	4.55
	956.5557	956.5514	0.0044	4.55
c_9	843.4705	843.4673	0.0032	3.76
	843.4705	843.4673	0.0032	3.76
c_8	786.4505	786.4458	0.0046	5.89
	786.4505	786.4458	0.0046	5.89
c_7	658.3517	658.3509	0.0008	1.28
c_6	601.3309	601.3294	0.0015	2.5
c_5	544.3102	544.308	0.0022	4.01
c_4	416.2171	416.213	0.0041	9.88

Appendix A.26

Assigned fragment ions from CID of MeCP2 Knockout pooled mouse brain sample (precursor ion at 754 *m/z*).

Ion	Observed Mass (Da)	Theoretical Mass (Da)	Mass Error (Da)	Mass Error (PPM)
y_{14}	1522.83	1522.839	-0.0087	-5.75
y_{13}	1451.8	1451.802	-0.0016	-1.13
y_{12}	1338.72	1338.718	0.0024	1.81
y_{11}	1210.62	1210.623	-0.0026	-2.16
b_{101}	11224.3	11224.35	-0.0509	-4.53
b_{87}	9613.39	9613.483	-0.0928	-9.65
	9613.39	9613.483	-0.0928	-9.65
b_{86}	9514.33	9514.414	-0.0844	-8.87
	9514.33	9514.414	-0.0844	-8.87
	9514.33	9514.414	-0.0844	-8.87
b_{85}	9415.27	9415.346	-0.076	-8.07
	9415.27	9415.346	-0.076	-8.07
	9415.27	9415.346	-0.076	-8.07
b_{84}	9300.27	9300.319	-0.049	-5.27
	9300.27	9300.319	-0.049	-5.27
	9300.27	9300.319	-0.049	-5.27
b_{82}	9098.19	9098.241	-0.0514	-5.65
b_{59}	6426.8	6426.797	0.0031	0.49
b_{55}	6029.54	6029.528	0.012	1.99
b_{53}	5772.35	5772.379	-0.0292	-5.06
	5772.35	5772.379	-0.0292	-5.06
b_{52}	5643.31	5643.337	-0.0266	-4.72
	5643.31	5643.337	-0.0266	-4.72
b_{51}	5514.26	5514.294	-0.034	-6.17
b_{50}	5351.22	5351.231	-0.0107	-2
	5351.22	5351.231	-0.0107	-2
b_{45}	4867.93	4867.925	0.005	1.02
b_{40}	4370.63	4370.618	0.0124	2.83
b_{39}	4214.52	4214.517	0.0035	0.83
	4214.52	4214.517	0.0035	0.83
b_{35}	3718.2	3718.193	0.0069	1.85

b_{19}	1887.06	1887.078	-0.0175	-9.29

Appendix A.27

Assigned fragment ions from ECD of MeCP2 Knockout pooled mouse brain sample (precursor ion at 754 *m/z*).

Ion	Observed Mass (Da)	Theoretical Mass (Da)	Mass Error (Da)	Mass Error (PPM)
z_{47}	5253.88	5253.836	0.0438	8.33
c_{34}	3579.09	3579.118	-0.0284	-7.92
c_{26}	2770.61	2770.638	-0.0277	-9.99
c_{24}	2543.49	2543.511	-0.0207	-8.14
c_{23}	2428.46	2428.484	-0.0238	-9.78
c_{17}	1610.93	1610.944	-0.0139	-8.6
c_{15}	1326.74	1326.748	-0.0078	-5.87
c_{13}	1198.68	1198.689	-0.0092	-7.69
c_{12}	1141.66	1141.668	-0.0078	-6.8

Appendix A.28

Assigned fragment ions from CID of MeCP2 Knockout pooled mouse brain sample (precursor ion at 756 *m/z*).

Ion	Observed Mass (Da)	Theoretical Mass (Da)	Mass Error (Da)	Mass Error (PPM)
y_{49}	5527.004	5527.006	-0.0018	-0.33
y_{47}	5269.952	5269.857	0.0948	18
y_{19}	2130.103	2130.106	-0.0038	-1.79
y_{18}	1999.077	1999.066	0.0114	5.71
	1999.077	1999.066	0.0114	5.71
y_{17}	1884.037	1884.039	-0.0016	-0.86
	1884.037	1884.039	-0.0016	-0.86
y_{16}	1784.969	1784.971	-0.0013	-0.71
	1784.969	1784.971	-0.0013	-0.71
y_{15}	1685.91	1685.902	0.0081	4.82
	1685.91	1685.902	0.0081	4.82
y_{14}	1522.839	1522.839	0.0003	0.16
y_{13}	1451.803	1451.802	0.0011	0.77
y_{12}	1338.716	1338.718	-0.0019	-1.45
y_{11}	1210.621	1210.623	-0.0021	-1.74
b_{99}	11020.25	11020.26	-0.0061	-0.55
b_{70}	7682.507	7682.489	0.0176	2.29
b_{69}	7583.423	7583.421	0.0016	0.21
b_{59}	6426.797	6426.797	-0.0003	-0.05
b_{58}	6298.707	6298.702	0.0055	0.88
b_{53}	5772.38	5772.379	0.0011	0.19
	5772.38	5772.379	0.0011	0.19
b_{52}	5643.339	5643.337	0.0019	0.34
	5643.339	5643.337	0.0019	0.34
b_{50}	5351.236	5351.231	0.0055	1.03
b_{40}	4370.615	4370.618	-0.0026	-0.59
b_{39}	4214.518	4214.517	0.0011	0.26
	4214.518	4214.517	0.0011	0.26
b_{24}	2526.483	2526.484	-0.0013	-0.52
b_{19}	1887.078	1887.078	0.0005	0.24
b_{12}	1124.642	1124.641	0.0007	0.61
b_{10}	939.5247	939.525	-0.0003	-0.31
b_{8}	769.4187	769.4195	-0.0008	-0.99

Appendix A.29

Assigned fragment ions from ECD of MeCP2 Knockout pooled mouse brain sample (precursor ion at 756 *m/z*).

Ion	Observed Mass (Da)	Theoretical Mass (Da)	Mass Error (Da)	Mass Error (PPM)
z_{18}	1983.043	1983.045	-0.0021	-1.03
z_{15}	1669.881	1669.881	0	-0.01
z_{12}	1322.697	1322.697	-0.0001	-0.08
z_{11}	1194.602	1194.602	-0.0004	-0.29
z_{10}	1038.502	1038.501	0.0007	0.63
c_{38}	4089.457	4089.457	-0.0005	-0.12
c_{24}	2557.524	2557.526	-0.0023	-0.9
c_{23}	2442.501	2442.499	0.0012	0.48
c_{18}	1748.002	1748.003	-0.0007	-0.39
	1748.002	1748.003	-0.0007	-0.39
c_{16}	1454.842	1454.843	-0.0007	-0.51
c_{15}	1326.748	1326.748	-0.0001	-0.08
c_{14}	1255.711	1255.711	-0.0001	-0.06
c_{13}	1198.69	1198.689	0.0005	0.42
c_{12}	1141.669	1141.668	0.0012	1.05
c_{10}	956.5524	956.5514	0.001	1.06
c_{9}	843.4686	843.4673	0.0013	1.51
c_{7}	658.3513	658.3509	0.0004	0.58

Appendix A.30

Assigned fragment ions from CID of Wild T*y*pe single mouse brain sample (precursor ion at 870.6 *m/z*).

Ion	Observed Mass (Da)	Theoretical Mass (Da)	Mass Error (Da)	Mass Error (PPM)
y_{51}	5785.05	5785.091	-0.0408	-7.06
y_{50}	5656.05	5656.048	0.0018	0.31
y_{49}	5527.01	5527.006	0.0043	0.79
y_{47}	5269.85	5269.857	-0.0069	-1.3
y_{43}	4872.59	4872.588	0.002	0.41
y_{42}	4773.51	4773.52	-0.0096	-2
y_{41}	4626.45	4626.451	-0.0012	-0.25
y_{39}	4384.32	4384.325	-0.0045	-1.03
y_{35}	3902.01	3902.028	-0.018	-4.61
y_{34}	3786.99	3787.001	-0.0111	-2.92
y_{32}	3616.9	3616.896	0.0045	1.23
y_{31}	3515.84	3515.848	-0.0079	-2.24
y_{30}	3352.77	3352.785	-0.0145	-4.33
y_{29}	3251.73	3251.737	-0.0069	-2.11
y_{28}	3122.69	3122.694	-0.0043	-1.36
	3122.69	3122.694	-0.0043	-1.36
y_{27}	2985.63	2985.635	-0.0053	-1.79
y_{26}	2914.59	2914.598	-0.0082	-2.83
y_{25}	2786.5	2786.503	-0.0033	-1.18
y_{24}	2630.39	2630.402	-0.0122	-4.63
y_{23}	2502.31	2502.307	0.0028	1.11
y_{22}	2401.26	2401.26	0.0005	0.2
y_{21}	2302.19	2302.191	-0.0011	-0.49
y_{20}	2201.14	2201.143	-0.0034	-1.56
y_{19}	2130.1	2130.106	-0.0063	-2.97
y_{18}	1999.06	1999.066	-0.0058	-2.92
y_{17}	1884.03	1884.039	-0.0089	-4.72
y_{16}	1784.97	1784.971	-0.0005	-0.27
	1784.97	1784.971	-0.0005	-0.27
y_{15}	1685.9	1685.902	-0.0021	-1.23
	1685.9	1685.902	-0.0021	-1.23
	1685.9	1685.902	-0.0021	-1.23
y_{14}	1522.84	1522.839	0.0013	0.82

Ion	Observed Mass (Da)	Theoretical Mass (Da)	Mass Error (Da)	Mass Error (PPM)
	1522.84	1522.839	0.0013	0.82
y_{13}	1451.8	1451.802	-0.0016	-1.13
y_{12}	1338.72	1338.718	0.0024	1.81
y_{11}	1210.63	1210.623	0.0074	6.1
	1210.63	1210.623	0.0074	6.1
	1210.63	1210.623	0.0074	6.1
y_{10}	1054.52	1054.522	-0.0015	-1.43
y_{9}	926.46	926.4629	-0.0029	-3.16
y_{8}	869.439	869.4415	-0.0025	-2.84
y_{5}	499.207	499.2086	-0.0016	-3.25
b_{69}	7583.42	7583.421	-0.0009	-0.12
	7583.42	7583.421	-0.0009	-0.12
b_{68}	7512.38	7512.384	-0.0038	-0.51
	7512.38	7512.384	-0.0038	-0.51
b_{63}	6915.04	6915.06	-0.0204	-2.94
b_{59}	6426.79	6426.797	-0.0069	-1.07
b_{58}	6298.7	6298.702	-0.0019	-0.3
	6298.7	6298.702	-0.0019	-0.3
b_{53}	5772.37	5772.379	-0.0092	-1.59
	5772.37	5772.379	-0.0092	-1.59
b_{52}	5643.33	5643.337	-0.0066	-1.17
b_{35}	3718.19	3718.193	-0.0031	-0.84
	3718.19	3718.193	-0.0031	-0.84
b_{31}	3280.92	3280.918	0.0019	0.59
b_{25}	2640.53	2640.527	0.0027	1.03
b_{23}	2411.46	2411.457	0.0026	1.07
	2411.46	2411.457	0.0026	1.07
b_{19}	1887.08	1887.078	0.0025	1.31
b_{17}	1593.92	1593.918	0.0025	1.56
	1593.92	1593.918	0.0025	1.56
b_{16}	1437.81	1437.816	-0.0064	-4.45
	1437.81	1437.816	-0.0064	-4.45
b_{13}	1181.66	1181.663	-0.0029	-2.43
b_{12}	1124.64	1124.641	-0.0014	-1.25
	1124.64	1124.641	-0.0014	-1.25
b_{11}	996.546	996.5465	-0.0005	-0.45
	996.546	996.5465	-0.0005	-0.45
b_{10}	939.524	939.525	-0.001	-1.05
	939.524	939.525	-0.001	-1.05

Ion	Observed Mass (Da)	Theoretical Mass (Da)	Mass Error (Da)	Mass Error (PPM)
b_9	826.441	826.4409	0.0001	0.08
	826.441	826.4409	0.0001	0.08
b_8	769.42	769.4195	0.0005	0.69
	769.42	769.4195	0.0005	0.69
b_7	641.325	641.3245	0.0005	0.76
b_5	527.282	527.2816	0.0004	0.78
b_4	399.187	399.1866	0.0004	0.93
b_3	342.166	342.1652	0.0008	2.43

Appendix A.31

Assigned fragment ions from ECD of wild type single mouse brain sample (precursor ion at 870.6 *m/z*).

Ion	Observed Mass (Da)	Theoretical Mass (Da)	Mass Error (Da)	Mass Error (PPM)
z_{101}	11154.3	11154.32	-0.0216	-1.94
	11154.3	11154.32	-0.0216	-1.94
	11154.3	11154.32	-0.0216	-1.94
z_{100}	11097.3	11097.3	-0.0001	-0.01
	11097.3	11097.3	-0.0001	-0.01
z_{95}	10642	10642.04	-0.0397	-3.73
	10642	10642.04	-0.0397	-3.73
z_{94}	10513.9	10513.94	-0.0447	-4.25
	10513.9	10513.94	-0.0447	-4.25
z_{93}	10456.9	10456.92	-0.0233	-2.23
z_{92}	10343.8	10343.84	-0.0392	-3.79
z_{90}	10158.7	10158.72	-0.0228	-2.24
z_{89}	10101.7	10101.7	-0.0013	-0.13
	10101.7	10101.7	-0.0013	-0.13
	10101.7	10101.7	-0.0013	-0.13
z_{88}	10044.7	10044.68	0.0201	2
	10044.7	10044.68	0.0201	2
	10044.7	10044.68	0.0201	2
z_{87}	9973.64	9973.643	-0.0028	-0.28
	9973.64	9973.643	-0.0028	-0.28
z_{85}	9689.44	9689.447	-0.0067	-0.69
	9689.44	9689.447	-0.0067	-0.69
z_{83}	9396.29	9396.287	0.0033	0.35
z_{80}	9028	9028.008	-0.0079	-0.88
	9028	9028.008	-0.0079	-0.88
z_{79}	8871.91	8871.907	0.0032	0.36
	8871.91	8871.907	0.0032	0.36
	8871.91	8871.907	0.0032	0.36
z_{78}	8756.88	8756.88	0.0001	0.02
z_{76}	8529.76	8529.753	0.0071	0.84
	8529.76	8529.753	0.0071	0.84
	8529.76	8529.753	0.0071	0.84
z_{75}	8401.69	8401.694	-0.0043	-0.51

Ion	Observed Mass (Da)	Theoretical Mass (Da)	Mass Error (Da)	Mass Error (PPM)
z_{73}	8231.59	8231.589	0.0012	0.15
	8231.59	8231.589	0.0012	0.15
z_{72}	8130.54	8130.541	-0.0011	-0.13
z_{70}	7905.39	7905.393	-0.0034	-0.43
	7905.39	7905.393	-0.0034	-0.43
z_{68}	7721.27	7721.272	-0.0022	-0.28
	7721.27	7721.272	-0.0022	-0.28
z_{67}	7565.17	7565.171	-0.0011	-0.14
	7565.17	7565.171	-0.0011	-0.14
	7565.17	7565.171	-0.0011	-0.14
z_{66}	7409.07	7409.07	0	0
	7409.07	7409.07	0	0
z_{65}	7295.98	7295.986	-0.0059	-0.81
z_{64}	7224.95	7224.949	0.0012	0.17
z_{63}	7068.85	7068.848	0.0023	0.33
	7068.85	7068.848	0.0023	0.33
z_{62}	6912.76	6912.747	0.0134	1.94
z_{61}	6855.73	6855.725	0.0049	0.71
	6855.73	6855.725	0.0049	0.71
z_{59}	6699.64	6699.635	0.0047	0.71
	6699.64	6699.635	0.0047	0.71
	6699.64	6699.635	0.0047	0.71
z_{58}	6571.54	6571.54	-0.0003	-0.04
z_{57}	6415.44	6415.439	0.0008	0.13
z_{56}	6302.35	6302.355	-0.0051	-0.81
z_{55}	6215.32	6215.323	-0.0031	-0.5
z_{54}	6158.3	6158.302	-0.0016	-0.26
z_{52}	5932.14	5932.134	0.0065	1.09
z_{51}	5769.06	5769.07	-0.0102	-1.76
	5769.06	5769.07	-0.0102	-1.76
z_{50}	5640.03	5640.028	0.0024	0.43
	5640.03	5640.028	0.0024	0.43
z_{49}	5510.99	5510.985	0.005	0.91
	5510.99	5510.985	0.005	0.91
z_{48}	5409.94	5409.937	0.0027	0.5
	5409.94	5409.937	0.0027	0.5
z_{47}	5253.83	5253.836	-0.0062	-1.18
	5253.83	5253.836	-0.0062	-1.18

z_{43}	4856.57	4856.567	0.0027	0.55

Ion	Observed Mass (Da)	Theoretical Mass (Da)	Mass Error (Da)	Mass Error (PPM)
z_{42}	4757.5	4757.499	0.0011	0.23
	4757.5	4757.499	0.0011	0.23
	4757.5	4757.499	0.0011	0.23
z_{39}	4368.31	4368.304	0.0061	1.41
z_{35}	3886.01	3886.007	0.0027	0.68
	3886.01	3886.007	0.0027	0.68
z_{34}	3770.98	3770.98	-0.0004	-0.11
	3770.98	3770.98	-0.0004	-0.11
z_{32}	3600.87	3600.875	-0.0049	-1.36
	3600.87	3600.875	-0.0049	-1.36
z_{31}	3499.83	3499.827	0.0028	0.8
	3499.83	3499.827	0.0028	0.8
	3499.83	3499.827	0.0028	0.8
z_{29}	3235.72	3235.716	0.0038	1.18
	3235.72	3235.716	0.0038	1.18
z_{28}	3106.68	3106.674	0.0064	2.06
z_{24}	2614.38	2614.382	-0.0015	-0.58
	2614.38	2614.382	-0.0015	-0.58
z_{21}	2286.17	2286.171	-0.0005	-0.2
	2286.17	2286.171	-0.0005	-0.2
z_{20}	2185.13	2185.123	0.0072	3.3
z_{18}	1983.04	1983.045	-0.0052	-2.61
z_{15}	1669.88	1669.881	-0.0014	-0.85
z_{14}	1506.82	1506.818	0.0019	1.27
z_{11}	1194.6	1194.602	-0.002	-1.64
z_{10}	1038.5	1038.501	-0.0009	-0.82
z_{9}	910.443	910.4423	0.0007	0.8
z_{8}	853.421	853.4208	0.0002	0.22
c_{101}	11241.3	11241.38	-0.0772	-6.87
	11241.3	11241.38	-0.0772	-6.87
	11241.3	11241.38	-0.0772	-6.87
	11241.3	11241.38	-0.0772	-6.87
c_{94}	10447	10446.97	0.0303	2.9
c_{93}	10389.9	10389.95	-0.0483	-4.65
c_{91}	10105.8	10105.79	0.0114	1.13
	10105.8	10105.79	0.0114	1.13
c_{88}	9793.59	9793.573	0.0175	1.79
c_{82}	9115.27	9115.268	0.0022	0.24

Ion	Observed Mass (Da)	Theoretical Mass (Da)	Mass Error (Da)	Mass Error (PPM)
c_{81}	9014.22	9014.22	-0.0001	-0.01
c_{77}	8529.76	8529.908	-0.1479	-17.34
	8529.76	8529.908	-0.1479	-17.34
	8529.76	8529.908	-0.1479	-17.34
c_{76}	8401.69	8401.813	-0.123	-14.64
c_{71}	7800.56	7800.563	-0.0033	-0.43
c_{70}	7699.52	7699.516	0.0043	0.56
c_{67}	7414.38	7414.383	-0.0032	-0.43
c_{63}	6932.09	6932.087	0.0033	0.48
	6932.09	6932.087	0.0033	0.48
	6932.09	6932.087	0.0033	0.48
c_{60}	6542.89	6542.892	-0.0016	-0.25
	6542.89	6542.892	-0.0016	-0.25
	6542.89	6542.892	-0.0016	-0.25
c_{59}	6443.83	6443.823	0.0068	1.05
c_{58}	6315.73	6315.728	0.0017	0.27
	6315.73	6315.728	0.0017	0.27
c_{57}	6202.65	6202.644	0.0058	0.93
c_{55}	6046.47	6046.554	-0.0843	-13.95
	6046.47	6046.554	-0.0843	-13.95
c_{54}	5890.45	5890.453	-0.0032	-0.55
	5890.45	5890.453	-0.0032	-0.55
c_{53}	5789.4	5789.406	-0.0055	-0.96
	5789.4	5789.406	-0.0055	-0.96
c_{52}	5660.37	5660.363	0.007	1.24
	5660.37	5660.363	0.007	1.24
c_{51}	5531.32	5531.32	-0.0004	-0.07
	5531.32	5531.32	-0.0004	-0.07
c_{48}	5142.09	5142.089	0.0011	0.21
	5142.09	5142.089	0.0011	0.21
	5142.09	5142.089	0.0011	0.21
c_{46}	4998.03	4998.035	-0.0054	-1.09
	4998.03	4998.035	-0.0054	-1.09
c_{45}	4884.95	4884.951	-0.0014	-0.28
c_{44}	4728.85	4728.85	-0.0003	-0.05
	4728.85	4728.85	-0.0003	-0.05
	4728.85	4728.85	-0.0003	-0.05
c_{43}	4600.75	4600.755	-0.0053	-1.15
	4600.75	4600.755	-0.0053	-1.15

	4600.75	4600.755	-0.0053	-1.15
Ion	**Observed Mass (Da)**	**Theoretical Mass (Da)**	**Mass Error (Da)**	**Mass Error (PPM)**
c_{42}	4501.69	4501.687	0.0031	0.69
c_{41}	4444.66	4444.665	-0.0054	-1.22
	4444.66	4444.665	-0.0054	-1.22
c_{40}	4387.64	4387.644	-0.004	-0.9
	4387.64	4387.644	-0.004	-0.9
c_{39}	4231.54	4231.543	-0.0029	-0.68
	4231.54	4231.543	-0.0029	-0.68
	4231.54	4231.543	-0.0029	-0.68
c_{38}	4075.44	4075.442	-0.0017	-0.43
	4075.44	4075.442	-0.0017	-0.43
	4075.44	4075.442	-0.0017	-0.43
c_{37}	4004.4	4004.405	-0.0046	-1.16
	4004.4	4004.405	-0.0046	-1.16
c_{36}	3891.32	3891.321	-0.0006	-0.15
	3891.32	3891.321	-0.0006	-0.15
c_{35}	3735.22	3735.22	0.0005	0.14
	3735.22	3735.22	0.0005	0.14
	3735.22	3735.22	0.0005	0.14
c_{34}	3579.12	3579.118	0.0016	0.46
	3579.12	3579.118	0.0016	0.46
c_{32}	3395	3394.997	0.0028	0.83
	3395	3394.997	0.0028	0.83
c_{30}	3169.85	3169.85	0.0005	0.17
	3169.85	3169.85	0.0005	0.17
c_{29}	3068.8	3068.802	-0.0018	-0.58
c_{27}	2898.7	2898.696	0.0037	1.29
	2898.7	2898.696	0.0037	1.29
c_{26}	2770.63	2770.638	-0.0077	-2.78
	2770.63	2770.638	-0.0077	-2.78
	2770.63	2770.638	-0.0077	-2.78
c_{25}	2657.55	2657.554	-0.0036	-1.37
c_{24}	2543.51	2543.511	-0.0007	-0.27
	2543.51	2543.511	-0.0007	-0.27
c_{23}	2428.48	2428.484	-0.0038	-1.55
	2428.48	2428.484	-0.0038	-1.55
	2428.48	2428.484	-0.0038	-1.55
c_{22}	2272.38	2272.383	-0.0026	-1.17
	2272.38	2272.383	-0.0026	-1.17

	2272.38	2272.383	-0.0026	-1.17

Ion	Observed Mass (Da)	Theoretical Mass (Da)	Mass Error (Da)	Mass Error (PPM)
c_{21}	2159.3	2159.299	0.0014	0.65
c_{19}	1904.1	1904.104	-0.0039	-2.04
	1904.1	1904.104	-0.0039	-2.04
c_{18}	1748	1748.003	-0.0028	-1.58
	1748	1748.003	-0.0028	-1.58
c_{17}	1610.95	1610.944	0.0061	3.81
	1610.95	1610.944	0.0061	3.81
c_{16}	1454.84	1454.843	-0.0027	-1.89
	1454.84	1454.843	-0.0027	-1.89
c_{15}	1326.75	1326.748	0.0022	1.67
	1326.75	1326.748	0.0022	1.67
c_{14}	1255.71	1255.711	-0.0007	-0.54
	1255.71	1255.711	-0.0007	-0.54
c_{13}	1198.69	1198.689	0.0008	0.65
	1198.69	1198.689	0.0008	0.65
c_{12}	1141.67	1141.668	0.0022	1.96
	1141.67	1141.668	0.0022	1.96
c_{11}	1013.57	1013.573	-0.0028	-2.76
	1013.57	1013.573	-0.0028	-2.76
c_{10}	956.552	956.5513	0.0007	0.69
	956.552	956.5513	0.0007	0.69
c_9	843.468	843.4673	0.0007	0.85
	843.468	843.4673	0.0007	0.85
c_8	786.446	786.4458	0.0002	0.23
c_7	658.351	658.3509	0.0001	0.21
c_6	601.33	601.3294	0.0006	1
c_5	544.309	544.3079	0.0011	1.95
c_4	416.214	416.213	0.001	2.45
c_3	359.193	359.1915	0.0015	4.12

Appendix A.32

Assigned fragment ions from CID of wild type single mouse brain sample (precursor ion at 871.8 *m/z*).

Ion	Observed Mass (Da)	Theoretical Mass (Da)	Mass Error (Da)	Mass Error (PPM)
y_{49}	5527.01	5527.006	0.0043	0.79
	5527.01	5527.006	0.0043	0.79
y_{42}	4773.52	4773.52	0.0004	0.09
y_{40}	4513.37	4513.367	0.0029	0.64
y_{39}	4384.32	4384.325	-0.0045	-1.03
y_{30}	3352.78	3352.785	-0.0045	-1.35
y_{29}	3251.73	3251.737	-0.0069	-2.11
y_{28}	3122.69	3122.694	-0.0043	-1.36
	3122.69	3122.694	-0.0043	-1.36
y_{27}	2985.63	2985.635	-0.0053	-1.79
y_{26}	2914.59	2914.598	-0.0082	-2.83
y_{24}	2630.41	2630.402	0.0078	2.98
y_{23}	2502.31	2502.307	0.0028	1.11
y_{22}	2401.26	2401.26	0.0005	0.2
y_{21}	2302.19	2302.191	-0.0011	-0.49
y_{20}	2201.14	2201.143	-0.0034	-1.56
y_{19}	2130.1	2130.106	-0.0063	-2.97
y_{18}	1999.06	1999.066	-0.0058	-2.92
y_{17}	1884.04	1884.039	0.0011	0.58
y_{16}	1784.97	1784.971	-0.0005	-0.27
	1784.97	1784.971	-0.0005	-0.27
y_{15}	1685.91	1685.902	0.0079	4.7
	1685.91	1685.902	0.0079	4.7
y_{14}	1522.84	1522.839	0.0013	0.82
y_{13}	1451.8	1451.802	-0.0016	-1.13
y_{12}	1338.72	1338.718	0.0024	1.81
y_{11}	1210.62	1210.623	-0.0026	-2.16
y_{10}	1054.52	1054.522	-0.0015	-1.43
y_{9}	926.461	926.4629	-0.0019	-2.08
y_{5}	499.207	499.2086	-0.0016	-3.25
b_{86}	9528.43	9528.394	0.0364	3.82
b_{85}	9429.38	9429.325	0.0548	5.82
b_{84}	9314.36	9314.298	0.0618	6.63

Ion	Observed Mass (Da)	Theoretical Mass (Da)	Mass Error (Da)	Mass Error (PPM)
b_{69}	7597.44	7597.4	0.0399	5.25
b_{68}	7526.4	7526.363	0.037	4.92
b_{53}	5786.4	5786.358	0.0416	7.19
b_{52}	5657.35	5657.316	0.0342	6.04
	5657.35	5657.316	0.0342	6.04
b_{39}	4228.53	4228.496	0.0343	8.11
b_{12}	1124.64	1124.641	-0.0014	-1.25
b_{11}	996.546	996.5465	-0.0005	-0.45
b_{10}	939.525	939.525	0	0.01
b_{9}	826.441	826.4409	0.0001	0.08
b_{8}	769.42	769.4195	0.0005	0.69
	769.42	769.4195	0.0005	0.69
b_{7}	641.324	641.3245	-0.0005	-0.8
b_{5}	527.282	527.2816	0.0004	0.78
b_{4}	399.187	399.1866	0.0004	0.93
b_{3}	342.166	342.1652	0.0008	2.43

Appendix A.33

Assigned fragment ions from ECD of wild type single mouse brain sample (precursor ion at 871.8 *m/z*).

Ion	Observed Mass (Da)	Theoretical Mass (Da)	Mass Error (Da)	Mass Error (PPM)
z_{101}	11168.33	11168.34	-0.0106	-0.95
	11168.33	11168.34	-0.0106	-0.95
	11168.33	11168.34	-0.0106	-0.95
z_{99}	10955.2	10955.21	-0.0181	-1.65
z_{98}	10898.18	10898.19	-0.0166	-1.53
z_{95}	10656.04	10656.06	-0.0162	-1.52
z_{92}	10357.85	10357.85	-0.0096	-0.92
z_{91}	10300.82	10300.83	-0.015	-1.45
z_{90}	10172.73	10172.74	-0.0112	-1.1
z_{88}	10058.69	10058.7	-0.0011	-0.11
	10058.69	10058.7	-0.0011	-0.11
z_{87}	9987.645	9987.658	-0.0138	-1.38
z_{86}	9859.551	9859.564	-0.0126	-1.28
z_{85}	9703.452	9703.462	-0.0101	-1.04
z_{84}	9566.396	9566.403	-0.0078	-0.82
	9566.396	9566.403	-0.0078	-0.82
	9566.396	9566.403	-0.0078	-0.82
z_{83}	9410.294	9410.302	-0.0083	-0.88
	9410.294	9410.302	-0.0083	-0.88
z_{79}	8871.895	8871.907	-0.0117	-1.32
z_{78}	8756.869	8756.88	-0.0112	-1.28
z_{77}	8642.829	8642.837	-0.0085	-0.98
z_{76}	8529.744	8529.753	-0.0089	-1.05
z_{75}	8401.683	8401.694	-0.0118	-1.4
z_{72}	8130.523	8130.541	-0.0178	-2.19
z_{68}	7721.26	7721.272	-0.012	-1.55
	7721.26	7721.272	-0.012	-1.55
z_{67}	7565.157	7565.171	-0.0144	-1.91
	7565.157	7565.171	-0.0144	-1.91
z_{66}	7409.058	7409.07	-0.0116	-1.56
z_{65}	7295.978	7295.986	-0.0075	-1.03
z_{64}	7224.937	7224.949	-0.0119	-1.64
z_{63}	7068.839	7068.848	-0.0091	-1.29

Ion	Observed Mass (Da)	Theoretical Mass (Da)	Mass Error (Da)	Mass Error (PPM)
z_{62}	6912.741	6912.747	-0.006	-0.87
z_{61}	6855.704	6855.725	-0.0208	-3.03
z_{59}	6699.619	6699.635	-0.0166	-2.48
z_{58}	6571.529	6571.54	-0.011	-1.68
z_{57}	6415.427	6415.439	-0.0119	-1.86
z_{54}	6158.294	6158.302	-0.0076	-1.23
z_{53}	6045.207	6045.218	-0.0109	-1.81
z_{52}	5932.126	5932.134	-0.0074	-1.25
z_{51}	5769.064	5769.07	-0.006	-1.04
z_{50}	5640.016	5640.028	-0.0119	-2.11
z_{49}	5510.984	5510.985	-0.001	-0.18
z_{48}	5409.937	5409.937	-0.0003	-0.06
z_{47}	5253.829	5253.836	-0.0073	-1.38
	5253.829	5253.836	-0.0073	-1.38
z_{43}	4856.561	4856.567	-0.0063	-1.31
z_{42}	4757.492	4757.499	-0.0065	-1.37
z_{39}	4368.302	4368.304	-0.0022	-0.5
z_{35}	3886.002	3886.007	-0.005	-1.28
	3886.002	3886.007	-0.005	-1.28
z_{32}	3600.872	3600.875	-0.0033	-0.93
	3600.872	3600.875	-0.0033	-0.93
z_{31}	3499.825	3499.827	-0.0027	-0.76
	3499.825	3499.827	-0.0027	-0.76
z_{18}	1983.044	1983.045	-0.001	-0.5
z_{15}	1669.881	1669.881	-0.0009	-0.52
z_{14}	1506.818	1506.818	-0.0006	-0.38
	1506.818	1506.818	-0.0006	-0.38
z_{11}	1194.602	1194.602	-0.0003	-0.23
z_{9}	910.4432	910.4423	0.0009	1.02
z_{8}	853.4201	853.4208	-0.0007	-0.83
c_{100}	11198.32	11198.37	-0.051	-4.55
	11198.32	11198.37	-0.051	-4.55
	11198.32	11198.37	-0.051	-4.55
c_{92}	10275.89	10275.91	-0.0124	-1.21
c_{71}	7814.573	7814.579	-0.0066	-0.84
c_{70}	7713.525	7713.531	-0.0065	-0.84
c_{67}	7428.394	7428.399	-0.0045	-0.6
c_{63}	6946.094	6946.102	-0.008	-1.15
	6946.094	6946.102	-0.008	-1.15

Ion	Observed Mass (Da)	Theoretical Mass (Da)	Mass Error (Da)	Mass Error (PPM)
c_{60}	6556.903	6556.907	-0.0049	-0.74
	6556.903	6556.907	-0.0049	-0.74
c_{59}	6457.833	6457.839	-0.0064	-1
	6457.833	6457.839	-0.0064	-1
c_{55}	6060.564	6060.57	-0.0064	-1.06
	6060.564	6060.57	-0.0064	-1.06
c_{54}	5904.465	5904.469	-0.0043	-0.73
c_{52}	5674.373	5674.379	-0.0053	-0.93
c_{51}	5545.332	5545.336	-0.0041	-0.73
	5545.332	5545.336	-0.0041	-0.73
c_{50}	5382.266	5382.273	-0.0065	-1.2
c_{48}	5156.099	5156.105	-0.0059	-1.14
	5156.099	5156.105	-0.0059	-1.14
c_{47}	5099.073	5099.083	-0.0098	-1.93
c_{46}	5012.044	5012.051	-0.0073	-1.46
c_{45}	4898.956	4898.967	-0.0107	-2.19
c_{44}	4742.859	4742.866	-0.0067	-1.42
	4742.859	4742.866	-0.0067	-1.42
	4742.859	4742.866	-0.0067	-1.42
c_{43}	4614.763	4614.771	-0.008	-1.73
	4614.763	4614.771	-0.008	-1.73
	4614.763	4614.771	-0.008	-1.73
c_{41}	4458.674	4458.681	-0.0071	-1.6
c_{40}	4401.655	4401.66	-0.0049	-1.11
c_{39}	4245.552	4245.559	-0.0065	-1.53
	4245.552	4245.559	-0.0065	-1.53
c_{38}	4089.449	4089.457	-0.0088	-2.15
	4089.449	4089.457	-0.0088	-2.15
c_{37}	4018.416	4018.42	-0.0046	-1.16
	4018.416	4018.42	-0.0046	-1.16
c_{36}	3905.328	3905.336	-0.0079	-2.02
	3905.328	3905.336	-0.0079	-2.02
c_{35}	3749.229	3749.235	-0.0058	-1.54
	3749.229	3749.235	-0.0058	-1.54
	3749.229	3749.235	-0.0058	-1.54
c_{34}	3593.129	3593.134	-0.0047	-1.31
	3593.129	3593.134	-0.0047	-1.31
c_{32}	3409.005	3409.013	-0.0079	-2.33
c_{30}	3183.862	3183.865	-0.0032	-1.01

Ion	Observed Mass (Da)	Theoretical Mass (Da)	Mass Error (Da)	Mass Error (PPM)
c_{29}	3082.811	3082.818	-0.0062	-2.02
	3082.811	3082.818	-0.0062	-2.02
c_{27}	2912.709	2912.712	-0.0027	-0.92
c_{26}	2784.649	2784.653	-0.0042	-1.49
	2784.649	2784.653	-0.0042	-1.49
c_{25}	2671.564	2671.569	-0.0049	-1.82
c_{24}	2557.522	2557.526	-0.0044	-1.71
	2557.522	2557.526	-0.0044	-1.71
c_{23}	2442.494	2442.499	-0.0054	-2.22
	2442.494	2442.499	-0.0054	-2.22
c_{21}	2173.309	2173.314	-0.0057	-2.61
	2173.309	2173.314	-0.0057	-2.61
c_{20}	2074.24	2074.246	-0.006	-2.88
	2074.24	2074.246	-0.006	-2.88
c_{19}	1904.102	1904.104	-0.0015	-0.77
	1904.102	1904.104	-0.0015	-0.77
c_{18}	1748.001	1748.003	-0.0016	-0.94
	1748.001	1748.003	-0.0016	-0.94
c_{17}	1610.942	1610.944	-0.0021	-1.3
	1610.942	1610.944	-0.0021	-1.3
c_{16}	1454.844	1454.843	0.0011	0.74
c_{15}	1326.746	1326.748	-0.0022	-1.64
	1326.746	1326.748	-0.0022	-1.64
c_{14}	1255.708	1255.711	-0.003	-2.43
c_{13}	1198.687	1198.689	-0.0027	-2.29
	1198.687	1198.689	-0.0027	-2.29
c_{12}	1141.664	1141.668	-0.0041	-3.63
c_{10}	956.5487	956.5514	-0.0026	-2.75
	956.5487	956.5514	-0.0026	-2.75
c_{9}	843.467	843.4673	-0.0003	-0.41
c_{8}	786.4452	786.4458	-0.0006	-0.77
c_{7}	658.3497	658.3509	-0.0012	-1.78
c_{6}	601.3278	601.3294	-0.0016	-2.64
c_{5}	544.3058	544.308	-0.0021	-3.95
c_{4}	416.2095	416.213	-0.0035	-8.5

Appendix A.34

Assigned fragment ions from CID of wild type single mouse brain sample (precursor ion at 873.8 *m/z*).

Ion	Observed Mass (Da)	Theoretical Mass (Da)	Mass Error (Da)	Mass Error (PPM)
y_{63}	7084.85	7084.868	-0.0183	-2.59
y_{49}	5527	5527.006	-0.0057	-1.02
y_{47}	5269.85	5269.857	-0.0069	-1.3
y_{43}	4872.59	4872.588	0.002	0.41
y_{42}	4773.51	4773.52	-0.0096	-2
y_{41}	4626.45	4626.451	-0.0012	-0.25
y_{40}	4513.35	4513.367	-0.0171	-3.79
y_{39}	4384.32	4384.325	-0.0045	-1.03
y_{35}	3902.02	3902.028	-0.008	-2.05
y_{34}	3787	3787.001	-0.0011	-0.28
y_{32}	3616.9	3616.896	0.0045	1.23
y_{31}	3515.84	3515.848	-0.0079	-2.24
y_{30}	3352.78	3352.785	-0.0045	-1.35
y_{28}	3122.69	3122.694	-0.0043	-1.36
	3122.69	3122.694	-0.0043	-1.36
y_{27}	2985.63	2985.635	-0.0053	-1.79
y_{26}	2914.59	2914.598	-0.0082	-2.83
y_{24}	2630.4	2630.402	-0.0022	-0.82
y_{23}	2502.31	2502.307	0.0028	1.11
y_{22}	2401.26	2401.26	0.0005	0.2
y_{21}	2302.19	2302.191	-0.0011	-0.49
y_{20}	2201.14	2201.143	-0.0034	-1.56
y_{19}	2130.1	2130.106	-0.0063	-2.97
y_{18}	1999.06	1999.066	-0.0058	-2.92
y_{17}	1884.03	1884.039	-0.0089	-4.72
y_{16}	1784.97	1784.971	-0.0005	-0.27
	1784.97	1784.971	-0.0005	-0.27
y_{15}	1685.91	1685.902	0.0079	4.7
	1685.91	1685.902	0.0079	4.7
y_{14}	1522.84	1522.839	0.0013	0.82
y_{13}	1451.8	1451.802	-0.0016	-1.13
y_{12}	1338.72	1338.718	0.0024	1.81
y_{11}	1210.62	1210.623	-0.0026	-2.16

Ion	Observed Mass (Da)	Theoretical Mass (Da)	Mass Error (Da)	Mass Error (PPM)
	1210.62	1210.623	-0.0026	-2.16
y_{10}	1054.52	1054.522	-0.0015	-1.43
y_9	926.463	926.4629	0.0001	0.08
	926.463	926.4629	0.0001	0.08
y_8	869.44	869.4415	-0.0015	-1.69
y_5	499.207	499.2086	-0.0016	-3.25
b_{68}	7554.39	7554.394	-0.0043	-0.57
	7554.39	7554.394	-0.0043	-0.57
b_{63}	6957.07	6957.071	-0.0009	-0.13
b_{59}	6468.83	6468.807	0.0226	3.49
b_{53}	5814.39	5814.39	0.0003	0.04
b_{52}	5685.35	5685.347	0.0028	0.5
	5685.35	5685.347	0.0028	0.5
	5685.35	5685.347	0.0028	0.5
b_{51}	5556.32	5556.305	0.0154	2.78
b_{35}	3760.21	3760.204	0.0063	1.69
b_{27}	2923.68	2923.681	-0.0005	-0.16
b_{25}	2682.54	2682.538	0.0022	0.81
b_{24}	2568.49	2568.495	-0.0049	-1.9
	2568.49	2568.495	-0.0049	-1.9
b_{23}	2453.47	2453.468	0.002	0.84
	2453.47	2453.468	0.002	0.84
b_{19}	1929.09	1929.088	0.0019	1
b_{17}	1635.93	1635.928	0.002	1.19
	1635.93	1635.928	0.002	1.19
	1635.93	1635.928	0.002	1.19
b_{13}	1181.66	1181.663	-0.0029	-2.43
b_{12}	1124.64	1124.641	-0.0014	-1.25
b_{11}	996.546	996.5465	-0.0005	-0.45
	996.546	996.5465	-0.0005	-0.45
b_{10}	939.525	939.525	0	0.01
b_9	826.441	826.4409	0.0001	0.08
b_8	769.42	769.4195	0.0005	0.69
	769.42	769.4195	0.0005	0.69
b_7	641.325	641.3245	0.0005	0.76
b_6	584.303	584.303	0	-0.09
b_5	527.282	527.2816	0.0004	0.78
b_4	399.187	399.1866	0.0004	0.93
b_3	342.165	342.1652	-0.0002	-0.5

Appendix A.35

Assigned fragment ions from ECD of wild type single mouse brain sample (precursor ion at 873.8 *m/z*).

Ion	Observed Mass (Da)	Theoretical Mass (Da)	Mass Error (Da)	Mass Error (PPM)
z_{101}	11196.3	11196.33	-0.0321	-2.87
	11196.3	11196.33	-0.0321	-2.87
	11196.3	11196.33	-0.0321	-2.87
z_{100}	11139.3	11139.31	-0.0107	-0.96
z_{99}	10983.2	10983.21	-0.0096	-0.87
z_{98}	10926.2	10926.19	0.0119	1.09
z_{96}	10741.1	10741.07	0.0283	2.64
z_{95}	10684.1	10684.05	0.0498	4.66
z_{94}	10555.9	10555.96	-0.0553	-5.24
	10555.9	10555.96	-0.0553	-5.24
z_{90}	10200.7	10200.73	-0.0333	-3.27
z_{88}	10086.7	10086.69	0.0096	0.95
z_{87}	10015.6	10015.65	-0.0533	-5.32
z_{85}	9689.44	9689.447	-0.0067	-0.69
	9689.44	9689.447	-0.0067	-0.69
z_{83}	9396.28	9396.287	-0.0067	-0.71
	9396.28	9396.287	-0.0067	-0.71
z_{79}	8871.9	8871.907	-0.0068	-0.77
	8871.9	8871.907	-0.0068	-0.77
z_{78}	8756.87	8756.88	-0.0099	-1.12
	8756.87	8756.88	-0.0099	-1.12
z_{73}	8231.59	8231.589	0.0012	0.15
z_{68}	7721.27	7721.272	-0.0022	-0.28
	7721.27	7721.272	-0.0022	-0.28
	7721.27	7721.272	-0.0022	-0.28
z_{67}	7565.17	7565.171	-0.0011	-0.14
z_{66}	7409.06	7409.07	-0.01	-1.35
	7409.06	7409.07	-0.01	-1.35
z_{64}	7224.94	7224.949	-0.0088	-1.22
	7224.94	7224.949	-0.0088	-1.22
z_{63}	7068.84	7068.848	-0.0077	-1.09
z_{62}	6912.74	6912.747	-0.0066	-0.95
	6912.74	6912.747	-0.0066	-0.95

Ion	**Observed Mass (Da)**	**Theoretical Mass (Da)**	**Mass Error (Da)**	**Mass Error (PPM)**
z_{61}	6855.71	6855.725	-0.0151	-2.21
	6855.71	6855.725	-0.0151	-2.21
z_{59}	6699.63	6699.635	-0.0053	-0.78
	6699.63	6699.635	-0.0053	-0.78
z_{58}	6571.53	6571.54	-0.0103	-1.57
z_{57}	6415.43	6415.439	-0.0092	-1.43
z_{56}	6302.36	6302.355	0.0049	0.77
z_{55}	6215.32	6215.323	-0.0031	-0.5
z_{54}	6158.29	6158.302	-0.0116	-1.89
	6158.29	6158.302	-0.0116	-1.89
z_{53}	6045.19	6045.218	-0.0276	-4.56
z_{51}	5769.06	5769.07	-0.0102	-1.76
	5769.06	5769.07	-0.0102	-1.76
z_{50}	5640.01	5640.028	-0.0176	-3.12
	5640.01	5640.028	-0.0176	-3.12
z_{49}	5510.97	5510.985	-0.015	-2.72
z_{48}	5409.93	5409.937	-0.0073	-1.35
z_{47}	5253.83	5253.836	-0.0062	-1.18
	5253.83	5253.836	-0.0062	-1.18
z_{43}	4856.56	4856.567	-0.0073	-1.51
z_{42}	4757.49	4757.499	-0.0089	-1.87
	4757.49	4757.499	-0.0089	-1.87
z_{39}	4368.3	4368.304	-0.0039	-0.88
z_{35}	3886	3886.007	-0.0073	-1.89
	3886	3886.007	-0.0073	-1.89
z_{32}	3600.87	3600.875	-0.0049	-1.36
	3600.87	3600.875	-0.0049	-1.36
z_{31}	3499.82	3499.827	-0.0072	-2.06
	3499.82	3499.827	-0.0072	-2.06
z_{29}	3235.71	3235.716	-0.0062	-1.91
	3235.71	3235.716	-0.0062	-1.91
z_{28}	3106.68	3106.674	0.0064	2.06
z_{21}	2286.17	2286.171	-0.0005	-0.2
z_{15}	1669.88	1669.881	-0.0014	-0.85
z_{14}	1506.82	1506.818	0.0019	1.27
z_{11}	1194.6	1194.602	-0.002	-1.64
z_{10}	1038.5	1038.501	-0.0009	-0.82
z_{9}	910.443	910.4423	0.0007	0.8

Ion	Observed Mass (Da)	Theoretical Mass (Da)	Mass Error (Da)	Mass Error (PPM)
z_8	853.42	853.4208	-0.0008	-0.95
c_{67}	7456.39	7456.394	-0.0037	-0.5
c_{63}	6974.09	6974.097	-0.0072	-1.04
c_{60}	6584.89	6584.902	-0.0122	-1.85
	6584.89	6584.902	-0.0122	-1.85
c_{59}	6485.83	6485.834	-0.0038	-0.58
c_{53}	5831.41	5831.416	-0.0061	-1.04
c_{52}	5702.37	5702.374	-0.0035	-0.61
	5702.37	5702.374	-0.0035	-0.61
c_{51}	5573.33	5573.331	-0.0009	-0.16
	5573.33	5573.331	-0.0009	-0.16
c_{48}	5184.09	5184.1	-0.0095	-1.82
	5184.09	5184.1	-0.0095	-1.82
c_{46}	5040.04	5040.046	-0.006	-1.18
c_{44}	4770.85	4770.861	-0.0108	-2.26
	4770.85	4770.861	-0.0108	-2.26
	4770.85	4770.861	-0.0108	-2.26
c_{43}	4642.77	4642.766	0.0042	0.9
	4642.77	4642.766	0.0042	0.9
c_{41}	4486.67	4486.676	-0.006	-1.33
c_{39}	4273.55	4273.553	-0.0034	-0.8
	4273.55	4273.553	-0.0034	-0.8
c_{37}	4046.41	4046.415	-0.0052	-1.28
c_{36}	3933.33	3933.331	-0.0011	-0.28
	3933.33	3933.331	-0.0011	-0.28
c_{35}	3777.22	3777.23	-0.01	-2.65
	3777.22	3777.23	-0.01	-2.65
c_{34}	3621.13	3621.129	0.0011	0.3
	3621.13	3621.129	0.0011	0.3
c_{32}	3437	3437.008	-0.0077	-2.25
c_{30}	3211.85	3211.86	-0.01	-3.12
c_{29}	3110.81	3110.812	-0.0023	-0.75
	3110.81	3110.812	-0.0023	-0.75
c_{26}	2812.64	2812.648	-0.0082	-2.93
	2812.64	2812.648	-0.0082	-2.93
c_{24}	2585.52	2585.521	-0.0012	-0.48
	2585.52	2585.521	-0.0012	-0.48
c_{23}	2470.49	2470.494	-0.0043	-1.74

Ion	Observed Mass (Da)	Theoretical Mass (Da)	Mass Error (Da)	Mass Error (PPM)
c_{22}	2314.39	2314.393	-0.0032	-1.38
	2314.39	2314.393	-0.0032	-1.38
c_{21}	2201.31	2201.309	0.0009	0.4
c_{19}	1946.11	1946.114	-0.0044	-2.27
	1946.11	1946.114	-0.0044	-2.27
c_{18}	1790.01	1790.013	-0.0033	-1.85
c_{17}	1652.95	1652.954	-0.0044	-2.66
	1652.95	1652.954	-0.0044	-2.66
c_{16}	1496.85	1496.853	-0.0033	-2.2
c_{15}	1326.75	1326.748	0.0022	1.67
c_{14}	1255.71	1255.711	-0.0007	-0.54
	1255.71	1255.711	-0.0007	-0.54
c_{13}	1198.69	1198.689	0.0008	0.65
	1198.69	1198.689	0.0008	0.65
c_{12}	1141.67	1141.668	0.0022	1.96
	1141.67	1141.668	0.0022	1.96
c_{10}	956.549	956.5513	-0.0023	-2.45
	956.549	956.5513	-0.0023	-2.45
c_{9}	843.467	843.4673	-0.0003	-0.33
c_{8}	786.445	786.4458	-0.0008	-1.04
c_{7}	658.35	658.3509	-0.0009	-1.3
c_{6}	601.328	601.3294	-0.0014	-2.33
c_{5}	544.306	544.3079	-0.0019	-3.56
c_{4}	416.21	416.213	-0.003	-7.16

Appendix A.36

Assigned fragment ions from CID of wild type single mouse brain sample (precursor ion at 875.0 *m/z*).

Ion	Observed Mass (Da)	Theoretical Mass (Da)	Mass Error (Da)	Mass Error (PPM)
y_{49}	5527.003	5527.006	-0.0026	-0.47
y_{42}	4773.533	4773.52	0.0132	2.76
y_{39}	4384.328	4384.325	0.0036	0.82
y_{29}	3251.732	3251.737	-0.0045	-1.37
y_{28}	3122.692	3122.694	-0.0025	-0.81
	3122.692	3122.694	-0.0025	-0.81
y_{27}	2985.631	2985.635	-0.0039	-1.32
y_{26}	2914.595	2914.598	-0.0028	-0.96
y_{22}	2401.261	2401.26	0.0018	0.76
y_{21}	2302.189	2302.191	-0.002	-0.86
y_{20}	2201.143	2201.143	-0.0008	-0.37
y_{19}	2130.105	2130.106	-0.0018	-0.85
y_{18}	1999.064	1999.066	-0.0023	-1.18
y_{17}	1884.037	1884.039	-0.0018	-0.96
y_{16}	1784.973	1784.971	0.0029	1.6
	1784.973	1784.971	0.0029	1.6
y_{15}	1685.901	1685.902	-0.001	-0.62
y_{14}	1522.839	1522.839	-0.0002	-0.15
y_{13}	1451.8	1451.802	-0.0012	-0.85
y_{12}	1338.715	1338.718	-0.003	-2.27
y_{11}	1210.621	1210.623	-0.0022	-1.78
y_{10}	1054.52	1054.522	-0.0019	-1.77
y_{9}	926.461	926.4629	-0.0019	-2.08
y_{5}	499.2067	499.2086	-0.0019	-3.85
b_{68}	7568.43	7568.41	0.0196	2.59
b_{53}	5828.407	5828.406	0.0017	0.28
b_{52}	5699.365	5699.363	0.0018	0.32
b_{39}	4270.536	4270.543	-0.0069	-1.61
b_{35}	3774.221	3774.219	0.0014	0.38
b_{24}	2582.511	2582.511	0.0001	0.03
b_{23}	2467.478	2467.484	-0.0057	-2.32
b_{17}	1635.929	1635.928	0.0008	0.51

Ion	Observed Mass (Da)	Theoretical Mass (Da)	Mass Error (Da)	Mass Error (PPM)
b_{12}	1124.641	1124.641	-0.0006	-0.51
b_{11}	996.5463	996.5465	-0.0002	-0.15
b_{10}	939.5248	939.525	-0.0003	-0.27
b_9	826.4412	826.441	0.0002	0.25
b_8	769.42	769.4195	0.0005	0.69
	769.42	769.4195	0.0005	0.69
b_7	641.3245	641.3245	-0.0001	-0.09
b_6	584.3028	584.3031	-0.0003	-0.51
b_5	527.2815	527.2816	-0.0001	-0.25
b_4	399.1869	399.1867	0.0002	0.5
b_3	342.1657	342.1652	0.0005	1.52

Appendix A.37

Assigned fragment ions from ECD of wild type single mouse brain sample (precursor ion at 875.0 *m/z*).

Ion	Observed Mass (Da)	Theoretical Mass (Da)	Mass Error (Da)	Mass Error (PPM)
z_{101}	11210.34	11210.35	-0.0031	-0.28
	11210.34	11210.35	-0.0031	-0.28
z_{100}	11153.33	11153.33	-0.0013	-0.12
z_{99}	10997.22	10997.23	-0.0041	-0.37
z_{85}	9703.462	9703.462	-0.0005	-0.05
z_{84}	9566.401	9566.403	-0.0022	-0.23
z_{79}	8871.903	8871.907	-0.0039	-0.44
z_{78}	8756.872	8756.88	-0.0074	-0.85
z_{76}	8529.749	8529.753	-0.0036	-0.42
z_{75}	8401.697	8401.694	0.0027	0.32
z_{68}	7721.274	7721.272	0.0021	0.27
z_{67}	7565.161	7565.171	-0.0098	-1.29
z_{66}	7409.057	7409.07	-0.0132	-1.78
z_{64}	7224.943	7224.949	-0.0063	-0.88
z_{63}	7068.837	7068.848	-0.0107	-1.51
z_{62}	6912.743	6912.747	-0.0041	-0.59
z_{61}	6855.723	6855.725	-0.0026	-0.38
z_{59}	6699.626	6699.635	-0.0095	-1.42
	6699.626	6699.635	-0.0095	-1.42
z_{58}	6571.525	6571.54	-0.0157	-2.39
z_{57}	6415.428	6415.439	-0.0117	-1.82
z_{54}	6158.29	6158.302	-0.0119	-1.92
	6158.29	6158.302	-0.0119	-1.92
z_{51}	5769.064	5769.07	-0.0067	-1.15
	5769.064	5769.07	-0.0067	-1.15
z_{47}	5253.829	5253.836	-0.0069	-1.31
	5253.829	5253.836	-0.0069	-1.31
z_{43}	4856.564	4856.567	-0.0035	-0.71
z_{42}	4757.493	4757.499	-0.0063	-1.33
z_{39}	4368.304	4368.304	0.0002	0.06
z_{32}	3600.873	3600.875	-0.0022	-0.61
	3600.873	3600.875	-0.0022	-0.61
z_{31}	3499.827	3499.827	-0.0001	-0.04

Ion	Observed Mass (Da)	Theoretical Mass (Da)	Mass Error (Da)	Mass Error (PPM)
z_{14}	1506.818	1506.818	-0.0001	-0.09
z_{11}	1194.602	1194.602	-0.0002	-0.2
z_{10}	1038.501	1038.501	0.0006	0.56
z_{9}	910.442	910.4423	-0.0003	-0.32
c_{101}	11297.37	11297.4	-0.0376	-3.33
	11297.37	11297.4	-0.0376	-3.33
	11297.37	11297.4	-0.0376	-3.33
	11297.37	11297.4	-0.0376	-3.33
c_{71}	7856.583	7856.59	-0.0071	-0.91
c_{70}	7755.545	7755.542	0.0026	0.33
c_{67}	7470.404	7470.41	-0.0057	-0.76
c_{63}	6988.109	6988.113	-0.0042	-0.6
c_{60}	6598.909	6598.918	-0.0086	-1.31
c_{59}	6499.846	6499.85	-0.004	-0.62
c_{55}	6102.58	6102.581	-0.0007	-0.12
	6102.58	6102.581	-0.0007	-0.12
c_{52}	5716.388	5716.389	-0.0011	-0.19
c_{51}	5587.344	5587.347	-0.0031	-0.55
c_{50}	5424.281	5424.283	-0.0024	-0.45
c_{45}	4940.976	4940.978	-0.002	-0.41
c_{44}	4784.874	4784.877	-0.0026	-0.55
	4784.874	4784.877	-0.0026	-0.55
c_{43}	4656.778	4656.782	-0.0039	-0.83
	4656.778	4656.782	-0.0039	-0.83
c_{41}	4500.693	4500.692	0.0012	0.27
c_{40}	4443.666	4443.67	-0.0039	-0.89
c_{39}	4287.568	4287.569	-0.0014	-0.32
	4287.568	4287.569	-0.0014	-0.32
c_{38}	4131.468	4131.468	-0.0003	-0.08
c_{36}	3947.342	3947.347	-0.0047	-1.19
c_{35}	3791.244	3791.246	-0.002	-0.52
c_{34}	3635.144	3635.145	-0.0012	-0.33
	3635.144	3635.145	-0.0012	-0.33
c_{26}	2826.661	2826.664	-0.0026	-0.91
c_{24}	2599.533	2599.537	-0.0037	-1.43
	2599.533	2599.537	-0.0037	-1.43
c_{23}	2484.507	2484.51	-0.0033	-1.34
	2484.507	2484.51	-0.0033	-1.34
c_{22}	2328.41	2328.409	0.0006	0.28

Ion	Observed Mass (Da)	Theoretical Mass (Da)	Mass Error (Da)	Mass Error (PPM)
c_{21}	2215.325	2215.325	0	0
c_{19}	1946.115	1946.115	0.0002	0.08
c_{18}	1790.014	1790.013	0.0004	0.24
c_{17}	1652.955	1652.955	0	0
c_{16}	1496.853	1496.853	-0.0002	-0.16
c_{15}	1326.747	1326.748	-0.0013	-1.01
c_{13}	1198.687	1198.689	-0.0019	-1.56

Appendix A.38

Assigned fragment ions from CID of MeCP2 Knockout single mouse brain sample (precursor ion at 870.6 *m/z*).

Ion	Observed Mass (Da)	Theoretical Mass (Da)	Mass Error (Da)	Mass Error (PPM)
y_{49}	5527	5527.006	-0.0057	-1.02
	5527	5527.006	-0.0057	-1.02
y_{47}	5269.85	5269.857	-0.0069	-1.3
y_{43}	4872.59	4872.588	0.002	0.41
y_{42}	4773.51	4773.52	-0.0096	-2
y_{41}	4626.45	4626.451	-0.0012	-0.25
y_{40}	4513.36	4513.367	-0.0071	-1.57
y_{39}	4384.32	4384.325	-0.0045	-1.03
	4384.32	4384.325	-0.0045	-1.03
y_{37}	4171.22	4171.213	0.0068	1.64
y_{34}	3786.99	3787.001	-0.0111	-2.92
y_{32}	3616.89	3616.896	-0.0055	-1.53
y_{31}	3515.84	3515.848	-0.0079	-2.24
y_{30}	3352.78	3352.785	-0.0045	-1.35
y_{29}	3251.73	3251.737	-0.0069	-2.11
y_{28}	3122.69	3122.694	-0.0043	-1.36
	3122.69	3122.694	-0.0043	-1.36
y_{27}	2985.63	2985.635	-0.0053	-1.79
y_{26}	2914.59	2914.598	-0.0082	-2.83
y_{24}	2630.39	2630.402	-0.0122	-4.63
y_{23}	2502.31	2502.307	0.0028	1.11
y_{22}	2401.26	2401.26	0.0005	0.2
y_{21}	2302.19	2302.191	-0.0011	-0.49
y_{20}	2201.14	2201.143	-0.0034	-1.56
y_{19}	2130.1	2130.106	-0.0063	-2.97
y_{18}	1999.06	1999.066	-0.0058	-2.92
y_{17}	1884.03	1884.039	-0.0089	-4.72
y_{16}	1784.97	1784.971	-0.0005	-0.27
	1784.97	1784.971	-0.0005	-0.27
y_{15}	1685.9	1685.902	-0.0021	-1.23
y_{14}	1522.84	1522.839	0.0013	0.82
y_{13}	1451.8	1451.802	-0.0016	-1.13
y_{12}	1338.72	1338.718	0.0024	1.81

Ion	Observed Mass (Da)	Theoretical Mass (Da)	Mass Error (Da)	Mass Error (PPM)
y_{11}	1210.62	1210.623	-0.0026	-2.16
	1210.62	1210.623	-0.0026	-2.16
y_{10}	1054.52	1054.522	-0.0015	-1.43
y_{9}	926.46	926.4629	-0.0029	-3.16
y_{8}	869.439	869.4415	-0.0025	-2.84
y_{7}	713.339	713.3404	-0.0014	-1.91
y_{5}	499.207	499.2086	-0.0016	-3.25
b_{87}	9613.48	9613.483	-0.0028	-0.29
b_{86}	9514.4	9514.414	-0.0144	-1.51
b_{85}	9415.34	9415.346	-0.006	-0.63
b_{83}	9169.32	9169.279	0.0415	4.52
b_{71}	7783.54	7783.537	0.003	0.39
b_{69}	7583.41	7583.421	-0.0109	-1.44
b_{68}	7512.38	7512.384	-0.0038	-0.51
	7512.38	7512.384	-0.0038	-0.51
	7512.38	7512.384	-0.0038	-0.51
b_{63}	6915.06	6915.06	-0.0004	-0.05
	6915.06	6915.06	-0.0004	-0.05
b_{62}	6786.03	6786.018	0.0122	1.8
b_{53}	5772.37	5772.379	-0.0092	-1.59
	5772.37	5772.379	-0.0092	-1.59
b_{52}	5643.33	5643.337	-0.0066	-1.17
	5643.33	5643.337	-0.0066	-1.17
b_{51}	5514.29	5514.294	-0.004	-0.73
b_{40}	4370.62	4370.618	0.0024	0.54
b_{39}	4214.52	4214.517	0.0035	0.83
b_{35}	3718.19	3718.193	-0.0031	-0.84
b_{31}	3280.92	3280.918	0.0019	0.59
b_{25}	2640.53	2640.527	0.0027	1.03
b_{23}	2411.46	2411.457	0.0026	1.07
	2411.46	2411.457	0.0026	1.07
b_{19}	1887.08	1887.078	0.0025	1.31
b_{17}	1593.92	1593.918	0.0025	1.56
b_{15}	1309.73	1309.721	0.0086	6.54
b_{13}	1181.66	1181.663	-0.0029	-2.43
b_{12}	1124.64	1124.641	-0.0014	-1.25

Ion	Observed Mass (Da)	Theoretical Mass (Da)	Mass Error (Da)	Mass Error (PPM)
b_{11}	996.547	996.5465	0.0005	0.55
b_{10}	939.524	939.525	-0.001	-1.05
b_9	826.441	826.4409	0.0001	0.08
b_8	769.42	769.4195	0.0005	0.69
	769.42	769.4195	0.0005	0.69
b_7	641.325	641.3245	0.0005	0.76
b_6	584.303	584.303	0	-0.09
b_5	527.282	527.2816	0.0004	0.78
b_4	399.187	399.1866	0.0004	0.93
b_3	342.165	342.1652	-0.0002	-0.5

Appendix A.39

Assigned fragment ions from ECD of MeCP2 Knockout single mouse brain sample (precursor ion at 870.6 *m/z*).

Ion	Observed Mass (Da)	Theoretical Mass (Da)	Mass Error (Da)	Mass Error (PPM)
z_{101}	11154.3	11154.32	-0.0216	-1.94
	11154.3	11154.32	-0.0216	-1.94
	11154.3	11154.32	-0.0216	-1.94
z_{98}	10884.2	10884.18	0.0224	2.06
	10884.2	10884.18	0.0224	2.06
z_{95}	10642	10642.04	-0.0397	-3.73
	10642	10642.04	-0.0397	-3.73
z_{94}	10513.9	10513.94	-0.0447	-4.25
z_{93}	10456.9	10456.92	-0.0233	-2.23
	10456.9	10456.92	-0.0233	-2.23
z_{92}	10343.8	10343.84	-0.0392	-3.79
z_{90}	10158.7	10158.72	-0.0228	-2.24
z_{89}	10101.7	10101.7	-0.0013	-0.13
z_{88}	10044.7	10044.68	0.0201	2
z_{87}	9973.63	9973.643	-0.0128	-1.28
z_{85}	9689.44	9689.447	-0.0067	-0.69
z_{79}	8871.9	8871.907	-0.0068	-0.77
	8871.9	8871.907	-0.0068	-0.77
z_{78}	8756.87	8756.88	-0.0099	-1.12
	8756.87	8756.88	-0.0099	-1.12
z_{76}	8529.75	8529.753	-0.0029	-0.34
z_{73}	8231.58	8231.589	-0.0088	-1.06
z_{70}	7905.39	7905.393	-0.0034	-0.43
z_{68}	7721.27	7721.272	-0.0022	-0.28
z_{67}	7565.16	7565.171	-0.0111	-1.46
z_{66}	7409.06	7409.07	-0.01	-1.35
z_{64}	7224.94	7224.949	-0.0088	-1.22
z_{63}	7068.84	7068.848	-0.0077	-1.09
z_{62}	6912.74	6912.747	-0.0066	-0.95
z_{61}	6855.71	6855.725	-0.0151	-2.21
z_{60}	6798.69	6798.704	-0.0137	-2.01
z_{59}	6699.62	6699.635	-0.0153	-2.28
	6699.62	6699.635	-0.0153	-2.28

Ion	Observed Mass (Da)	Theoretical Mass (Da)	Mass Error (Da)	Mass Error (PPM)
z_{58}	6571.52	6571.54	-0.0203	-3.09
	6571.52	6571.54	-0.0203	-3.09
z_{57}	6415.43	6415.439	-0.0092	-1.43
z_{54}	6158.29	6158.302	-0.0116	-1.89
	6158.29	6158.302	-0.0116	-1.89
z_{52}	5932.13	5932.134	-0.0035	-0.59
z_{51}	5769.06	5769.07	-0.0102	-1.76
	5769.06	5769.07	-0.0102	-1.76
z_{50}	5640.02	5640.028	-0.0076	-1.35
z_{49}	5510.98	5510.985	-0.005	-0.91
z_{48}	5409.93	5409.937	-0.0073	-1.35
z_{43}	4856.56	4856.567	-0.0073	-1.51
z_{42}	4757.5	4757.499	0.0011	0.23
z_{39}	4368.3	4368.304	-0.0039	-0.88
z_{35}	3886	3886.007	-0.0073	-1.89
	3886	3886.007	-0.0073	-1.89
z_{34}	3770.98	3770.98	-0.0004	-0.11
	3770.98	3770.98	-0.0004	-0.11
z_{32}	3600.87	3600.875	-0.0049	-1.36
	3600.87	3600.875	-0.0049	-1.36
z_{31}	3499.83	3499.827	0.0028	0.8
	3499.83	3499.827	0.0028	0.8
z_{29}	3235.71	3235.716	-0.0062	-1.91
z_{28}	3106.68	3106.674	0.0064	2.06
z_{21}	2286.17	2286.171	-0.0005	-0.2
z_{15}	1669.88	1669.881	-0.0014	-0.85
z_{14}	1506.82	1506.818	0.0019	1.27
	1506.82	1506.818	0.0019	1.27
z_{11}	1194.6	1194.602	-0.002	-1.64
z_{10}	1038.5	1038.501	-0.0009	-0.82
z_{9}	910.443	910.4423	0.0007	0.8
z_{8}	853.42	853.4208	-0.0008	-0.95
c_{101}	11241.3	11241.38	-0.0772	-6.87
	11241.3	11241.38	-0.0772	-6.87
	11241.3	11241.38	-0.0772	-6.87
	11241.3	11241.38	-0.0772	-6.87
c_{81}	9014.21	9014.22	-0.0101	-1.12
c_{71}	7800.56	7800.563	-0.0033	-0.43
c_{70}	7699.51	7699.516	-0.0057	-0.74

Ion	Observed Mass (Da)	Theoretical Mass (Da)	Mass Error (Da)	Mass Error (PPM)
c_{63}	6932.08	6932.087	-0.0067	-0.97
	6932.08	6932.087	-0.0067	-0.97
	6932.08	6932.087	-0.0067	-0.97
c_{60}	6542.89	6542.892	-0.0016	-0.25
c_{59}	6443.82	6443.823	-0.0032	-0.5
	6443.82	6443.823	-0.0032	-0.5
c_{55}	6046.54	6046.554	-0.0143	-2.37
c_{54}	5890.45	5890.453	-0.0032	-0.55
	5890.45	5890.453	-0.0032	-0.55
c_{53}	5789.4	5789.406	-0.0055	-0.96
c_{52}	5660.36	5660.363	-0.003	-0.52
	5660.36	5660.363	-0.003	-0.52
c_{51}	5531.32	5531.32	-0.0004	-0.07
	5531.32	5531.32	-0.0004	-0.07
c_{50}	5368.25	5368.257	-0.007	-1.31
c_{48}	5142.08	5142.089	-0.0089	-1.73
	5142.08	5142.089	-0.0089	-1.73
c_{47}	5085.06	5085.068	-0.0075	-1.47
c_{45}	4884.94	4884.951	-0.0114	-2.33
c_{44}	4728.84	4728.85	-0.0103	-2.17
	4728.84	4728.85	-0.0103	-2.17
	4728.84	4728.85	-0.0103	-2.17
c_{41}	4444.66	4444.665	-0.0054	-1.22
	4444.66	4444.665	-0.0054	-1.22
c_{40}	4387.63	4387.644	-0.014	-3.18
c_{39}	4231.54	4231.543	-0.0029	-0.68
	4231.54	4231.543	-0.0029	-0.68
c_{38}	4075.43	4075.442	-0.0117	-2.88
c_{37}	4004.4	4004.405	-0.0046	-1.16
	4004.4	4004.405	-0.0046	-1.16
c_{36}	3891.31	3891.321	-0.0106	-2.72
	3891.31	3891.321	-0.0106	-2.72
c_{35}	3735.21	3735.22	-0.0095	-2.54
	3735.21	3735.22	-0.0095	-2.54
	3735.21	3735.22	-0.0095	-2.54
c_{34}	3579.11	3579.118	-0.0084	-2.34
	3579.11	3579.118	-0.0084	-2.34
c_{30}	3169.84	3169.85	-0.0095	-2.99
c_{29}	3068.79	3068.802	-0.0118	-3.84

Ion	Observed Mass (Da)	Theoretical Mass (Da)	Mass Error (Da)	Mass Error (PPM)
c_{27}	2898.69	2898.696	-0.0063	-2.16
c_{26}	2770.63	2770.638	-0.0077	-2.78
	2770.63	2770.638	-0.0077	-2.78
c_{24}	2543.51	2543.511	-0.0007	-0.27
	2543.51	2543.511	-0.0007	-0.27
c_{23}	2428.48	2428.484	-0.0038	-1.55
	2428.48	2428.484	-0.0038	-1.55
c_{22}	2272.38	2272.383	-0.0026	-1.17
	2272.38	2272.383	-0.0026	-1.17
c_{21}	2159.3	2159.299	0.0014	0.65
c_{19}	1904.1	1904.104	-0.0039	-2.04
c_{18}	1748	1748.003	-0.0028	-1.58
c_{17}	1610.94	1610.944	-0.0039	-2.4
	1610.94	1610.944	-0.0039	-2.4
c_{16}	1454.84	1454.843	-0.0027	-1.89
c_{15}	1326.75	1326.748	0.0022	1.67
c_{14}	1255.71	1255.711	-0.0007	-0.54
c_{13}	1198.69	1198.689	0.0008	0.65
	1198.69	1198.689	0.0008	0.65
c_{12}	1141.66	1141.668	-0.0078	-6.8
c_{10}	956.548	956.5513	-0.0033	-3.49
	956.548	956.5513	-0.0033	-3.49
c_{9}	843.467	843.4673	-0.0003	-0.33
c_{8}	786.445	786.4458	-0.0008	-1.04
c_{7}	658.35	658.3509	-0.0009	-1.3
c_{6}	601.328	601.3294	-0.0014	-2.33
c_{5}	544.306	544.3079	-0.0019	-3.56
c_{4}	416.209	416.213	-0.004	-9.56

Appendix A.40

Assigned fragment ions from CID of MeCP2 Knockout single mouse brain sample (precursor ion at 871.8 *m/z*).

Ion	Observed Mass (Da)	Theoretical Mass (Da)	Mass Error (Da)	Mass Error (PPM)
y_{49}	5527.01	5527.006	0.0043	0.79
	5527.01	5527.006	0.0043	0.79
y_{43}	4872.59	4872.588	0.002	0.41
y_{42}	4773.52	4773.52	0.0004	0.09
y_{40}	4513.36	4513.367	-0.0071	-1.57
y_{39}	4384.33	4384.325	0.0055	1.25
y_{34}	3787.01	3787.001	0.0089	2.36
y_{32}	3616.9	3616.896	0.0045	1.23
y_{31}	3515.85	3515.848	0.0021	0.61
y_{30}	3352.78	3352.785	-0.0045	-1.35
y_{29}	3251.73	3251.737	-0.0069	-2.11
y_{28}	3122.69	3122.694	-0.0043	-1.36
	3122.69	3122.694	-0.0043	-1.36
y_{27}	2985.63	2985.635	-0.0053	-1.79
y_{26}	2914.6	2914.598	0.0018	0.6
y_{24}	2630.4	2630.402	-0.0022	-0.82
y_{23}	2502.3	2502.307	-0.0072	-2.88
y_{22}	2401.27	2401.26	0.0105	4.36
y_{21}	2302.19	2302.191	-0.0011	-0.49
y_{20}	2201.14	2201.143	-0.0034	-1.56
y_{19}	2130.1	2130.106	-0.0063	-2.97
y_{18}	1999.06	1999.066	-0.0058	-2.92
y_{17}	1884.04	1884.039	0.0011	0.58
y_{16}	1784.97	1784.971	-0.0005	-0.27
	1784.97	1784.971	-0.0005	-0.27
y_{15}	1685.9	1685.902	-0.0021	-1.23
	1685.9	1685.902	-0.0021	-1.23
y_{14}	1522.84	1522.839	0.0013	0.82
y_{13}	1451.8	1451.802	-0.0016	-1.13
y_{12}	1338.72	1338.718	0.0024	1.81
y_{11}	1210.62	1210.623	-0.0026	-2.16
y_{10}	1054.52	1054.522	-0.0015	-1.43
y_{9}	926.461	926.4629	-0.0019	-2.08

Ion	Observed Mass (Da)	Theoretical Mass (Da)	Mass Error (Da)	Mass Error (PPM)
y_5	499.207	499.2086	-0.0016	-3.25
b_{86}	9528.44	9528.394	0.0464	4.87
b_{84}	9314.35	9314.298	0.0518	5.56
b_{70}	7696.51	7696.469	0.0415	5.39
	7696.51	7696.469	0.0415	5.39
b_{69}	7597.43	7597.4	0.0299	3.93
b_{68}	7526.4	7526.363	0.037	4.92
b_{53}	5786.4	5786.358	0.0416	7.19
	5786.4	5786.358	0.0416	7.19
b_{52}	5657.36	5657.316	0.0442	7.81
	5657.36	5657.316	0.0442	7.81
b_{39}	4228.53	4228.496	0.0343	8.11
b_{12}	1124.64	1124.641	-0.0014	-1.25
b_{11}	996.546	996.5465	-0.0005	-0.45
	996.546	996.5465	-0.0005	-0.45
b_{10}	939.525	939.525	0	0.01
b_9	826.441	826.4409	0.0001	0.08
b_8	769.42	769.4195	0.0005	0.69
	769.42	769.4195	0.0005	0.69
b_7	641.325	641.3245	0.0005	0.76
b_6	584.303	584.303	0	-0.09
b_5	527.282	527.2816	0.0004	0.78
b_4	399.187	399.1866	0.0004	0.93
b_3	342.166	342.1652	0.0008	2.43

Appendix A.41

Assigned fragment ions from ECD of MeCP2 Knockout single mouse brain sample (precursor ion at 871.8 *m/z*).

Ion	Observed Mass (Da)	Theoretical Mass (Da)	Mass Error (Da)	Mass Error (PPM)
z_{101}	11168.3	11168.3	-0.0008	-0.07
z_{99}	10955.2	10955.18	0.0218	1.99
z_{98}	10898.2	10898.16	0.0432	3.97
z_{92}	10357.8	10357.82	-0.0184	-1.78
z_{89}	10115.7	10115.68	0.0195	1.92
z_{87}	9987.63	9987.622	0.008	0.8
	9987.63	9987.622	0.008	0.8
z_{81}	9141.08	9141.092	-0.012	-1.31
z_{79}	8871.89	8871.907	-0.0168	-1.89
z_{78}	8756.86	8756.88	-0.0199	-2.27
z_{76}	8529.74	8529.753	-0.0129	-1.51
z_{68}	7721.26	7721.272	-0.0122	-1.58
z_{67}	7565.17	7565.171	-0.0011	-0.14
z_{66}	7409.06	7409.07	-0.01	-1.35
z_{63}	7068.84	7068.848	-0.0077	-1.09
z_{59}	6699.64	6699.635	0.0047	0.71
z_{58}	6571.54	6571.54	-0.0003	-0.04
z_{54}	6158.3	6158.302	-0.0016	-0.26
z_{51}	5769.07	5769.07	-0.0002	-0.03
z_{47}	5253.84	5253.836	0.0038	0.72
z_{43}	4856.56	4856.567	-0.0073	-1.51
z_{42}	4757.49	4757.499	-0.0089	-1.87
z_{39}	4368.3	4368.304	-0.0039	-0.88
z_{32}	3600.87	3600.875	-0.0049	-1.36
z_{31}	3499.82	3499.827	-0.0072	-2.06
	3499.82	3499.827	-0.0072	-2.06
z_{11}	1194.6	1194.602	-0.002	-1.64
z_{10}	1038.5	1038.501	-0.0009	-0.82
c_{71}	7814.56	7814.543	0.0175	2.23
c_{70}	7713.51	7713.495	0.0151	1.96
c_{63}	6946.09	6946.066	0.0241	3.47
	6946.09	6946.066	0.0241	3.47
c_{59}	6457.82	6457.802	0.0176	2.72

Ion	Observed Mass (Da)	Theoretical Mass (Da)	Mass Error (Da)	Mass Error (PPM)
c_{55}	6060.56	6060.534	0.0265	4.37
c_{51}	5545.32	5545.3	0.0204	3.68
c_{48}	5156.09	5156.068	0.0219	4.24
	5156.09	5156.068	0.0219	4.24
c_{44}	4742.85	4742.83	0.0205	4.33
	4742.85	4742.83	0.0205	4.33
c_{39}	4245.54	4245.522	0.0179	4.23
c_{36}	3905.32	3905.3	0.0202	5.18
c_{35}	3749.22	3749.199	0.0213	5.69
c_{34}	3593.12	3593.098	0.0224	6.25
c_{26}	2784.64	2784.617	0.0231	8.3
c_{15}	1326.74	1326.748	-0.0078	-5.87
c_{13}	1198.69	1198.689	0.0008	0.65
c_{12}	1141.66	1141.668	-0.0078	-6.8

Appendix A.42

Assigned fragment ions from CID of MeCP2 Knockout single mouse brain sample (precursor ion at 873.8 *m/z*).

Ion	Observed Mass (Da)	Theoretical Mass (Da)	Mass Error (Da)	Mass Error (PPM)
y_{63}	7084.86	7084.868	-0.0084	-1.18
y_{62}	6928.79	6928.767	0.0228	3.28
y_{50}	5656.05	5656.048	0.0018	0.31
y_{49}	5527	5527.006	-0.0057	-1.02
	5527	5527.006	-0.0057	-1.02
y_{43}	4872.59	4872.588	0.002	0.41
y_{42}	4773.51	4773.52	-0.0096	-2
y_{40}	4513.36	4513.367	-0.0071	-1.57
y_{39}	4384.32	4384.325	-0.0045	-1.03
y_{35}	3902.03	3902.028	0.002	0.51
y_{34}	3787	3787.001	-0.0011	-0.28
y_{32}	3616.89	3616.896	-0.0055	-1.53
y_{31}	3515.84	3515.848	-0.0079	-2.24
y_{30}	3352.78	3352.785	-0.0045	-1.35
y_{29}	3251.73	3251.737	-0.0069	-2.11
y_{28}	3122.69	3122.694	-0.0043	-1.36
	3122.69	3122.694	-0.0043	-1.36
y_{27}	2985.63	2985.635	-0.0053	-1.79
y_{26}	2914.59	2914.598	-0.0082	-2.83
y_{24}	2630.4	2630.402	-0.0022	-0.82
y_{23}	2502.31	2502.307	0.0028	1.11
y_{22}	2401.26	2401.26	0.0005	0.2
y_{21}	2302.19	2302.191	-0.0011	-0.49
y_{20}	2201.14	2201.143	-0.0034	-1.56
y_{19}	2130.1	2130.106	-0.0063	-2.97
y_{18}	1999.06	1999.066	-0.0058	-2.92
y_{17}	1884.04	1884.039	0.0011	0.58
y_{16}	1784.97	1784.971	-0.0005	-0.27
	1784.97	1784.971	-0.0005	-0.27
y_{15}	1685.9	1685.902	-0.0021	-1.23
y_{14}	1522.84	1522.839	0.0013	0.82
y_{13}	1451.8	1451.802	-0.0016	-1.13
y_{12}	1338.72	1338.718	0.0024	1.81

Ion	Observed Mass (Da)	Theoretical Mass (Da)	Mass Error (Da)	Mass Error (PPM)
y_{11}	1210.62	1210.623	-0.0026	-2.16
	1210.62	1210.623	-0.0026	-2.16
y_{10}	1054.52	1054.522	-0.0015	-1.43
y_{9}	926.46	926.4629	-0.0029	-3.16
y_{5}	499.207	499.2086	-0.0016	-3.25
b_{100}	11209.3	11209.34	-0.04	-3.57
b_{99}	11062.3	11062.27	0.0284	2.57
b_{85}	9457.37	9457.357	0.0135	1.43
b_{74}	8218.7	8218.701	-0.0011	-0.14
b_{70}	7724.49	7724.5	-0.0099	-1.28
b_{68}	7554.38	7554.394	-0.0143	-1.9
b_{63}	6957.08	6957.071	0.0091	1.31
b_{62}	6828.03	6828.028	0.0017	0.25
b_{53}	5814.39	5814.39	0.0003	0.04
	5814.39	5814.39	0.0003	0.04
b_{52}	5685.35	5685.347	0.0028	0.5
	5685.35	5685.347	0.0028	0.5
b_{51}	5556.31	5556.305	0.0054	0.98
b_{40}	4412.63	4412.628	0.0018	0.42
b_{39}	4256.53	4256.527	0.0029	0.69
	4256.53	4256.527	0.0029	0.69
b_{35}	3760.2	3760.204	-0.0037	-0.97
b_{31}	3322.93	3322.929	0.0014	0.42
b_{25}	2682.54	2682.538	0.0022	0.81
b_{24}	2568.49	2568.495	-0.0049	-1.9
	2568.49	2568.495	-0.0049	-1.9
b_{23}	2453.47	2453.468	0.002	0.84
	2453.47	2453.468	0.002	0.84
b_{19}	1929.09	1929.088	0.0019	1
b_{17}	1635.93	1635.928	0.002	1.19
	1635.93	1635.928	0.002	1.19
b_{15}	1309.73	1309.721	0.0086	6.54
b_{12}	1124.64	1124.641	-0.0014	-1.25
b_{11}	996.546	996.5465	-0.0005	-0.45
b_{10}	939.524	939.525	-0.001	-1.05
	939.524	939.525	-0.001	-1.05
b_{9}	826.441	826.4409	0.0001	0.08
b_{8}	769.42	769.4195	0.0005	0.69
	769.42	769.4195	0.0005	0.69

Ion	Observed Mass (Da)	Theoretical Mass (Da)	Mass Error (Da)	Mass Error (PPM)
b_7	641.325	641.3245	0.0005	0.76
b_6	584.303	584.303	0	-0.09
b_5	527.282	527.2816	0.0004	0.78
b_4	399.187	399.1866	0.0004	0.93
b_3	342.165	342.1652	-0.0002	-0.5

Appendix A.43

Assigned fragment ions from ECD of MeCP2 Knockout single mouse brain sample (precursor ion at 873.8 *m/z*).

Ion	Observed Mass (Da)	Theoretical Mass (Da)	Mass Error (Da)	Mass Error (PPM)
z_{101}	11196.3	11196.33	-0.0321	-2.87
z_{100}	11139.3	11139.31	-0.0107	-0.96
z_{99}	10983.2	10983.21	-0.0096	-0.87
	10983.2	10983.21	-0.0096	-0.87
z_{95}	10684	10684.05	-0.0502	-4.7
z_{89}	10143.7	10143.71	-0.0119	-1.17
	10143.7	10143.71	-0.0119	-1.17
z_{87}	10015.6	10015.65	-0.0533	-5.32
z_{85}	9689.43	9689.447	-0.0167	-1.72
z_{80}	9028	9028.008	-0.0079	-0.88
z_{79}	8871.9	8871.907	-0.0068	-0.77
	8871.9	8871.907	-0.0068	-0.77
z_{78}	8756.88	8756.88	0.0001	0.02
	8756.88	8756.88	0.0001	0.02
z_{76}	8529.75	8529.753	-0.0029	-0.34
	8529.75	8529.753	-0.0029	-0.34
	8529.75	8529.753	-0.0029	-0.34
z_{67}	7565.14	7565.171	-0.0311	-4.11
z_{66}	7409.06	7409.07	-0.01	-1.35
z_{65}	7295.97	7295.986	-0.0159	-2.18
z_{64}	7224.94	7224.949	-0.0088	-1.22
	7224.94	7224.949	-0.0088	-1.22
z_{63}	7068.84	7068.848	-0.0077	-1.09
	7068.84	7068.848	-0.0077	-1.09
z_{61}	6855.71	6855.725	-0.0151	-2.21
z_{59}	6699.63	6699.635	-0.0053	-0.78
	6699.63	6699.635	-0.0053	-0.78
z_{58}	6571.53	6571.54	-0.0103	-1.57
	6571.53	6571.54	-0.0103	-1.57
z_{54}	6158.29	6158.302	-0.0116	-1.89
z_{51}	5769.06	5769.07	-0.0102	-1.76
	5769.06	5769.07	-0.0102	-1.76
z_{50}	5640.01	5640.028	-0.0176	-3.12

Ion	Observed Mass (Da)	Theoretical Mass (Da)	Mass Error (Da)	Mass Error (PPM)
z_{49}	5510.98	5510.985	-0.005	-0.91
z_{47}	5253.83	5253.836	-0.0062	-1.18
	5253.83	5253.836	-0.0062	-1.18
z_{43}	4856.56	4856.567	-0.0073	-1.51
z_{42}	4757.49	4757.499	-0.0089	-1.87
z_{39}	4368.3	4368.304	-0.0039	-0.88
	4368.3	4368.304	-0.0039	-0.88
z_{32}	3600.87	3600.875	-0.0049	-1.36
z_{31}	3499.82	3499.827	-0.0072	-2.06
	3499.82	3499.827	-0.0072	-2.06
z_{29}	3235.72	3235.716	0.0038	1.18
z_{15}	1669.88	1669.881	-0.0014	-0.85
z_{14}	1506.82	1506.818	0.0019	1.27
z_{11}	1194.6	1194.602	-0.002	-1.64
z_{10}	1038.5	1038.501	-0.0009	-0.82
c_{91}	10147.8	10147.8	0.0009	0.09
c_{73}	8106.67	8106.685	-0.0149	-1.84
c_{55}	6088.56	6088.565	-0.0049	-0.8
c_{52}	5702.37	5702.374	-0.0035	-0.61
c_{47}	5127.08	5127.078	0.002	0.39
c_{44}	4770.86	4770.861	-0.0008	-0.17
c_{43}	4642.76	4642.766	-0.0058	-1.26
c_{41}	4486.67	4486.676	-0.006	-1.33
c_{40}	4429.65	4429.655	-0.0045	-1.02
c_{39}	4273.55	4273.553	-0.0034	-0.8
c_{37}	4046.41	4046.415	-0.0052	-1.28
c_{35}	3777.23	3777.23	0	0
c_{34}	3621.13	3621.129	0.0011	0.3
c_{26}	2812.65	2812.648	0.0018	0.63
	2812.65	2812.648	0.0018	0.63
c_{24}	2585.52	2585.521	-0.0012	-0.48
	2585.52	2585.521	-0.0012	-0.48
c_{23}	2470.49	2470.494	-0.0043	-1.74
c_{22}	2314.39	2314.393	-0.0032	-1.38
c_{21}	2201.31	2201.309	0.0009	0.4
c_{18}	1790.01	1790.013	-0.0033	-1.85
c_{17}	1652.95	1652.954	-0.0044	-2.66
	1652.95	1652.954	-0.0044	-2.66
c_{16}	1496.85	1496.853	-0.0033	-2.2

Ion	Observed Mass (Da)	Theoretical Mass (Da)	Mass Error (Da)	Mass Error (PPM)
c_{15}	1326.75	1326.748	0.0022	1.67
c_{14}	1255.71	1255.711	-0.0007	-0.54
	1255.71	1255.711	-0.0007	-0.54
c_{13}	1198.69	1198.689	0.0008	0.65
	1198.69	1198.689	0.0008	0.65
c_{12}	1141.67	1141.668	0.0022	1.96
c_{10}	956.549	956.5513	-0.0023	-2.45
c_{9}	843.467	843.4673	-0.0003	-0.33
c_{8}	786.446	786.4458	0.0002	0.23
c_{7}	658.35	658.3509	-0.0009	-1.3
c_{6}	601.329	601.3294	-0.0004	-0.66

Appendix A.44

Assigned fragment ions from CID of MeCP2 Knockout single mouse brain sample (precursor ion at 875.0 *m/z*).

Ion	Observed Mass (Da)	Theoretical Mass (Da)	Mass Error (Da)	Mass Error (PPM)
y_{49}	5527	5527.006	-0.0057	-1.02
	5527	5527.006	-0.0057	-1.02
y_{43}	4872.59	4872.588	0.002	0.41
y_{42}	4773.51	4773.52	-0.0096	-2
y_{40}	4513.36	4513.367	-0.0071	-1.57
y_{32}	3616.89	3616.896	-0.0055	-1.53
y_{30}	3352.78	3352.785	-0.0045	-1.35
y_{29}	3251.73	3251.737	-0.0069	-2.11
y_{28}	3122.69	3122.694	-0.0043	-1.36
	3122.69	3122.694	-0.0043	-1.36
y_{27}	2985.63	2985.635	-0.0053	-1.79
y_{26}	2914.59	2914.598	-0.0082	-2.83
y_{24}	2630.4	2630.402	-0.0022	-0.82
y_{23}	2502.31	2502.307	0.0028	1.11
y_{22}	2401.26	2401.26	0.0005	0.2
y_{21}	2302.19	2302.191	-0.0011	-0.49
y_{20}	2201.14	2201.143	-0.0034	-1.56
y_{19}	2130.1	2130.106	-0.0063	-2.97
y_{18}	1999.06	1999.066	-0.0058	-2.92
y_{17}	1884.04	1884.039	0.0011	0.58
y_{16}	1784.97	1784.971	-0.0005	-0.27
	1784.97	1784.971	-0.0005	-0.27
y_{15}	1685.9	1685.902	-0.0021	-1.23
y_{14}	1522.84	1522.839	0.0013	0.82
y_{13}	1451.8	1451.802	-0.0016	-1.13
y_{12}	1338.72	1338.718	0.0024	1.81
y_{11}	1210.62	1210.623	-0.0026	-2.16
y_{10}	1054.52	1054.522	-0.0015	-1.43
y_{9}	926.461	926.4629	-0.0019	-2.08
y_{8}	869.44	869.4415	-0.0015	-1.69
y_{5}	499.207	499.2086	-0.0016	-3.25
b_{85}	9471.38	9471.336	0.0443	4.68
b_{70}	7738.51	7738.479	0.0309	4

Ion	Observed Mass (Da)	Theoretical Mass (Da)	Mass Error (Da)	Mass Error (PPM)
b_{69}	7639.45	7639.411	0.0394	5.15
b_{53}	5828.41	5828.369	0.0411	7.04
	5828.41	5828.369	0.0411	7.04
b_{52}	5699.36	5699.326	0.0336	5.9
	5699.36	5699.326	0.0336	5.9
b_{35}	3774.22	3774.183	0.0371	9.84
b_{11}	996.546	996.5465	-0.0005	-0.45
b_{10}	939.525	939.525	0	0.01
b_{9}	826.441	826.4409	0.0001	0.08
b_{8}	769.42	769.4195	0.0005	0.69
	769.42	769.4195	0.0005	0.69
b_{7}	641.325	641.3245	0.0005	0.76
b_{5}	527.282	527.2816	0.0004	0.78
b_{3}	342.166	342.1652	0.0008	2.43

Appendix A.45

Assigned fragment ions from ECD of MeCP2 Knockout single mouse brain sample (precursor ion at 875.0 *m/z*).

Ion	Observed Mass (Da)	Theoretical Mass (Da)	Mass Error (Da)	Mass Error (PPM)
z_{101}	11210.33	11210.35	-0.0178	-1.59
z_{85}	9703.46	9703.462	-0.002	-0.2
	9703.46	9703.462	-0.002	-0.2
z_{84}	9566.397	9566.403	-0.0062	-0.65
	9566.397	9566.403	-0.0062	-0.65
z_{79}	8871.898	8871.907	-0.0093	-1.05
z_{78}	8756.877	8756.88	-0.0033	-0.38
z_{76}	8529.745	8529.753	-0.0081	-0.95
z_{68}	7721.268	7721.272	-0.0039	-0.5
z_{66}	7409.07	7409.07	-0.0003	-0.04
z_{64}	7224.953	7224.949	0.0045	0.62
z_{63}	7068.859	7068.848	0.0112	1.58
z_{59}	6699.649	6699.635	0.0138	2.06
z_{54}	6158.3	6158.302	-0.0019	-0.3
z_{51}	5769.071	5769.07	0.0008	0.14
z_{43}	4856.566	4856.567	-0.001	-0.2
z_{42}	4757.505	4757.499	0.0061	1.28
z_{39}	4368.305	4368.304	0.0013	0.31
z_{32}	3600.871	3600.875	-0.0037	-1.03
z_{31}	3499.819	3499.827	-0.0079	-2.24
z_{14}	1506.817	1506.818	-0.0013	-0.84
z_{11}	1194.603	1194.602	0.0014	1.16
z_{10}	1038.501	1038.501	0	0.02
c_{101}	11297.37	11297.4	-0.0359	-3.18
	11297.37	11297.4	-0.0359	-3.18
	11297.37	11297.4	-0.0359	-3.18
	11297.37	11297.4	-0.0359	-3.18
c_{100}	11240.35	11240.38	-0.0362	-3.22
c_{63}	6988.107	6988.113	-0.0065	-0.93
c_{60}	6598.904	6598.918	-0.0138	-2.09
c_{52}	5716.381	5716.389	-0.0081	-1.41
c_{51}	5587.336	5587.347	-0.011	-1.97
c_{26}	2826.657	2826.664	-0.0068	-2.42

Ion	Observed Mass (Da)	Theoretical Mass (Da)	Mass Error (Da)	Mass Error (PPM)
c_{24}	2599.529	2599.537	-0.0079	-3.03
c_{23}	2484.503	2484.51	-0.0068	-2.75
c_{18}	1790.011	1790.013	-0.002	-1.09
c_{17}	1652.952	1652.955	-0.0021	-1.27
c_{16}	1496.85	1496.853	-0.0032	-2.14
c_{15}	1326.744	1326.748	-0.0038	-2.89

Appendix A.46

Assigned fragment ions from CID of wild type single mouse brain sample digested with endo-proteinase Asp-N (precursor ion at 408 *m/z*). The list shows ions corresponding to a tri-methylated precursor.

Ion	Observed Mass (Da)	Theoretical Mass (Da)	Mass Error (Da)	Mass Error (PPM)
y_{22}	2314.435	2314.443	-0.0085	-3.66
	2314.435	2314.443	-0.0085	-3.66
y_{18}	1916.197	1916.204	-0.007	-3.65
	1916.197	1916.204	-0.007	-3.65
	1916.197	1916.204	-0.007	-3.65
y_{17}	1859.177	1859.183	-0.0056	-3
y_{15}	1674.062	1674.066	-0.0039	-2.34
	1674.062	1674.066	-0.0039	-2.34
y_{14}	1617.042	1617.045	-0.0029	-1.82
y_{13}	1503.956	1503.961	-0.005	-3.32
	1503.956	1503.961	-0.005	-3.32
	1503.956	1503.961	-0.005	-3.32
y_{12}	1446.935	1446.939	-0.0041	-2.83
y_{11}	1318.837	1318.844	-0.0068	-5.18
	1318.837	1318.844	-0.0068	-5.18
	1318.837	1318.844	-0.0068	-5.18
y_{10}	1261.816	1261.823	-0.0072	-5.75
y_{6}	849.5627	849.5681	-0.0053	-6.27
y_{5}	712.5024	712.5092	-0.0067	-9.42
y_{4}	556.4058	556.408	-0.0022	-3.99
y_{3}	386.2623	386.2661	-0.0038	-9.86
b_{12}	1124.638	1124.641	-0.0031	-2.75
	1124.638	1124.641	-0.0031	-2.75
b_{11}	996.5446	996.5465	-0.0019	-1.93
b_{10}	939.5226	939.525	-0.0024	-2.52
b_{9}	826.4417	826.441	0.0008	0.92
b_{8}	769.4174	769.4195	-0.0021	-2.68
	769.4174	769.4195	-0.0021	-2.68
b_{7}	641.3248	641.3245	0.0003	0.41
b_{5}	527.2812	527.2816	-0.0005	-0.85
b_{3}	342.1627	342.1652	-0.0025	-7.22

Assigned fragment ions from CID of wild type single mouse brain sample digested with endo-proteinase Asp-N (precursor ion at 408 *m/z*). The list shows ions corresponding to a di-methylated precursor.

Ion	Observed Mass (Da)	Theoretical Mass (Da)	Mass Error (Da)	Mass Error (PPM)
y_{18}	1902.182	1902.188	-0.0063	-3.29
y_{15}	1660.047	1660.05	-0.003	-1.84
y_{14}	1603.026	1603.029	-0.0029	-1.83
y_{13}	1489.94	1489.945	-0.0045	-3.02
y_{12}	1432.919	1432.923	-0.0045	-3.12
y_{11}	1304.823	1304.829	-0.0056	-4.28
	1304.823	1304.829	-0.0056	-4.28
y_{6}	835.5473	835.5524	-0.005	-6.03
y_{4}	542.3899	542.3923	-0.0024	-4.42
y_{3}	386.2623	386.2661	-0.0038	-9.86
b_{22}	2255.36	2255.356	0.0032	1.44
b_{12}	1124.638	1124.641	-0.0031	-2.75
	1124.638	1124.641	-0.0031	-2.75
b_{11}	996.5446	996.5465	-0.0019	-1.93
b_{10}	939.5226	939.525	-0.0024	-2.52
b_{9}	826.4417	826.441	0.0008	0.92
b_{8}	769.4174	769.4195	-0.0021	-2.68
	769.4174	769.4195	-0.0021	-2.68
b_{7}	641.3248	641.3245	0.0003	0.41
b_{5}	527.2812	527.2816	-0.0005	-0.85
b_{3}	342.1627	342.1652	-0.0025	-7.22

Appendix A.47

Assigned fragment ions from ECD of wild type single mouse brain sample digested with endo-proteinase Asp-N (precursor ion at 408 *m/z*). The list shows ions corresponding to a tri-methylated precursor.

Ion	Observed Mass (Da)	Theoretical Mass (Da)	Mass Error (Da)	Mass Error (PPM)
z_{22}	2298.396	2298.422	-0.0268	-11.64
	2298.396	2298.422	-0.0268	-11.64
z_{21}	2241.376	2241.401	-0.0252	-11.23
z_{20}	2085.276	2085.3	-0.0234	-11.23
z_{19}	2028.256	2028.278	-0.0224	-11.04
z_{16}	1786.12	1786.14	-0.0207	-11.6
z_{15}	1658.026	1658.045	-0.019	-11.47
z_{14}	1601.007	1601.024	-0.0171	-10.7
z_{12}	1430.903	1430.919	-0.0154	-10.79
z_{10}	1245.788	1245.802	-0.0139	-11.17
z_{9}	1188.768	1188.781	-0.0128	-10.78
z_{8}	1117.731	1117.744	-0.0123	-11.02
z_{7}	989.6377	989.6485	-0.0109	-10.97
z_{6}	833.5375	833.5474	-0.0099	-11.91
z_{5}	696.4789	696.4885	-0.0096	-13.81
c_{22}	2286.373	2286.398	-0.0258	-11.28
c_{21}	2173.29	2173.314	-0.0239	-11
c_{20}	2074.223	2074.246	-0.0232	-11.2
c_{19}	1904.083	1904.104	-0.0214	-11.24
	1904.083	1904.104	-0.0214	-11.24
c_{18}	1747.983	1748.003	-0.0196	-11.21
c_{17}	1610.927	1610.944	-0.0174	-10.78
c_{16}	1454.827	1454.843	-0.0154	-10.61
c_{15}	1326.733	1326.748	-0.015	-11.28
c_{14}	1255.696	1255.711	-0.0149	-11.88
c_{11}	1013.562	1013.573	-0.011	-10.86
c_{8}	786.4361	786.4458	-0.0097	-12.35

Assigned fragment ions from ECD of wild type single mouse brain sample digested with endo-proteinase Asp-N (precursor ion at 408 *m/z*). The list shows ions corresponding to a di-methylated precursor.

Ion	Observed Mass (Da)	Theoretical Mass (Da)	Mass Error (Da)	Mass Error (PPM)
z_{15}	1644.011	1644.03	-0.0183	-11.16
c_{19}	1904.083	1904.104	-0.0214	-11.24
	1904.083	1904.104	-0.0214	-11.24
c_{18}	1747.983	1748.003	-0.0196	-11.21
c_{17}	1610.927	1610.944	-0.0174	-10.78
c_{16}	1454.827	1454.843	-0.0154	-10.61
c_{15}	1326.733	1326.748	-0.015	-11.28
c_{14}	1255.696	1255.711	-0.0149	-11.88
c_{11}	1013.562	1013.573	-0.011	-10.86
c_{8}	786.4361	786.4458	-0.0097	-12.35

Appendix A.48

Assigned fragment ions from CID of wild type single mouse brain sample digested with endo-proteinase Asp-N (precursor ion at 490 *m/z*). The list shows ions corresponding to a tri-methylated precursor.

Ion	Observed Mass (Da)	Theoretical Mass (Da)	Mass Error (Da)	Mass Error (PPM)
y_{22}	2314.441	2314.443	-0.0019	-0.81
	2314.441	2314.443	-0.0019	-0.81
y_{20}	2101.318	2101.32	-0.0024	-1.14
y_{18}	1916.204	1916.204	0.0002	0.08
	1916.204	1916.204	0.0002	0.08
y_{17}	1859.171	1859.183	-0.0116	-6.23
	1859.171	1859.183	-0.0116	-6.23
	1859.171	1859.183	-0.0116	-6.23
y_{16}	1802.159	1802.161	-0.0026	-1.44
	1802.159	1802.161	-0.0026	-1.44
y_{15}	1674.064	1674.066	-0.002	-1.2
	1674.064	1674.066	-0.002	-1.2
	1674.064	1674.066	-0.002	-1.2
y_{14}	1617.035	1617.045	-0.0097	-6
	1617.035	1617.045	-0.0097	-6
	1617.035	1617.045	-0.0097	-6
y_{13}	1503.957	1503.961	-0.0033	-2.22
	1503.957	1503.961	-0.0033	-2.22
	1503.957	1503.961	-0.0033	-2.22
y_{11}	1318.842	1318.844	-0.0021	-1.63
	1318.842	1318.844	-0.0021	-1.63
y_{10}	1261.819	1261.823	-0.0036	-2.88
y_{6}	849.5659	849.5681	-0.0022	-2.57
	849.5659	849.5681	-0.0022	-2.57
y_{5}	712.5065	712.5092	-0.0026	-3.69
b_{22}	2269.372	2269.372	0.0001	0.07
b_{19}	1887.075	1887.078	-0.003	-1.6
b_{17}	1593.917	1593.918	-0.0008	-0.48
b_{12}	1124.641	1124.641	-0.0005	-0.42
	1124.641	1124.641	-0.0005	-0.42
b_{11}	996.546	996.5465	-0.0005	-0.51
	996.546	996.5465	-0.0005	-0.51
b_{10}	939.5246	939.525	-0.0004	-0.47

Ion	Observed Mass (Da)	Theoretical Mass (Da)	Mass Error (Da)	Mass Error (PPM)
	939.5246	939.525	-0.0004	-0.47
b_9	826.4405	826.441	-0.0004	-0.51
b_8	769.4191	769.4195	-0.0004	-0.53
	769.4191	769.4195	-0.0004	-0.53
b_7	641.3246	641.3245	0.0001	0.16
b_6	584.303	584.3031	-0.0001	-0.22
b_5	527.2816	527.2816	0	0.04
b_4	399.1866	399.1867	-0.0001	-0.25
b_3	342.165	342.1652	-0.0002	-0.47

Assigned fragment ions from CID of wild type single mouse brain sample digested with endo-proteinase Asp-N (precursor ion at 490 *m/z*). The list shows ions corresponding to a di-methylated precursor.

Ion	Observed Mass (Da)	Theoretical Mass (Da)	Mass Error (Da)	Mass Error (PPM)
y_{18}	1902.186	1902.188	-0.0021	-1.08
	1902.186	1902.188	-0.0021	-1.08
y_{15}	1660.048	1660.05	-0.0022	-1.34
	1660.048	1660.05	-0.0022	-1.34
y_{14}	1603.027	1603.029	-0.0016	-0.99
y_{13}	1489.938	1489.945	-0.0065	-4.35
	1489.938	1489.945	-0.0065	-4.35
	1489.938	1489.945	-0.0065	-4.35
y_{11}	1304.828	1304.829	-0.0009	-0.67
	1304.828	1304.829	-0.0009	-0.67
y_6	835.5501	835.5524	-0.0023	-2.75
y_4	542.3904	542.3923	-0.0019	-3.54
b_{19}	1887.075	1887.078	-0.003	-1.6
b_{17}	1593.917	1593.918	-0.0008	-0.48
b_{12}	1124.641	1124.641	-0.0005	-0.42
	1124.641	1124.641	-0.0005	-0.42
b_{11}	996.546	996.5465	-0.0005	-0.51
	996.546	996.5465	-0.0005	-0.51
b_{10}	939.5246	939.525	-0.0004	-0.47
	939.5246	939.525	-0.0004	-0.47

Ion	Observed Mass (Da)	Theoretical Mass (Da)	Mass Error (Da)	Mass Error (PPM)
b_9	826.4405	826.441	-0.0004	-0.51
b_8	769.4191	769.4195	-0.0004	-0.53
	769.4191	769.4195	-0.0004	-0.53
b_7	641.3246	641.3245	0.0001	0.16
b_6	584.303	584.3031	-0.0001	-0.22
b_5	527.2816	527.2816	0	0.04
b_4	399.1866	399.1867	-0.0001	-0.25
b_3	342.165	342.1652	-0.0002	-0.47

Appendix A.49

Assigned fragment ions from ECD of wild type single mouse brain sample digested with endo-proteinase Asp-N (precursor ion at 490 *m/z*). The list shows ions corresponding to a tri-methylated precursor.

Ion	Observed Mass (Da)	Theoretical Mass (Da)	Mass Error (Da)	Mass Error (PPM)
y_{22}	2314.441	2314.443	-0.0019	-0.81
	2314.441	2314.443	-0.0019	-0.81
y_{20}	2101.318	2101.32	-0.0024	-1.14
y_{18}	1916.204	1916.204	0.0002	0.08
	1916.204	1916.204	0.0002	0.08
y_{17}	1859.171	1859.183	-0.0116	-6.23
	1859.171	1859.183	-0.0116	-6.23
	1859.171	1859.183	-0.0116	-6.23
y_{16}	1802.159	1802.161	-0.0026	-1.44
	1802.159	1802.161	-0.0026	-1.44
y_{15}	1674.064	1674.066	-0.002	-1.2
	1674.064	1674.066	-0.002	-1.2
	1674.064	1674.066	-0.002	-1.2
y_{14}	1617.035	1617.045	-0.0097	-6
	1617.035	1617.045	-0.0097	-6
	1617.035	1617.045	-0.0097	-6
y_{13}	1503.957	1503.961	-0.0033	-2.22
	1503.957	1503.961	-0.0033	-2.22
	1503.957	1503.961	-0.0033	-2.22
y_{11}	1318.842	1318.844	-0.0021	-1.63
	1318.842	1318.844	-0.0021	-1.63
y_{10}	1261.819	1261.823	-0.0036	-2.88
y_{6}	849.5659	849.5681	-0.0022	-2.57
	849.5659	849.5681	-0.0022	-2.57
y_{5}	712.5065	712.5092	-0.0026	-3.69
b_{22}	2269.372	2269.372	0.0001	0.07
b_{19}	1887.075	1887.078	-0.003	-1.6
b_{17}	1593.917	1593.918	-0.0008	-0.48
b_{12}	1124.641	1124.641	-0.0005	-0.42
	1124.641	1124.641	-0.0005	-0.42
b_{11}	996.546	996.5465	-0.0005	-0.51
	996.546	996.5465	-0.0005	-0.51

b_{10}	939.5246	939.525	-0.0004	-0.47

Ion	Observed Mass (Da)	Theoretical Mass (Da)	Mass Error (Da)	Mass Error (PPM)
	939.5246	939.525	-0.0004	-0.47
b_9	826.4405	826.441	-0.0004	-0.51
b_8	769.4191	769.4195	-0.0004	-0.53
	769.4191	769.4195	-0.0004	-0.53
b_7	641.3246	641.3245	0.0001	0.16
b_6	584.303	584.3031	-0.0001	-0.22
b_5	527.2816	527.2816	0	0.04
b_4	399.1866	399.1867	-0.0001	-0.25
b_3	342.165	342.1652	-0.0002	-0.47

Assigned fragment ions from ECD of wild type single mouse brain sample digested with endo-proteinase Asp-N (precursor ion at 490 *m/z*). The list shows ions corresponding to a di-methylated precursor.

Ion	Observed Mass (Da)	Theoretical Mass (Da)	Mass Error (Da)	Mass Error (PPM)
y_{18}	1902.186	1902.188	-0.0021	-1.08
	1902.186	1902.188	-0.0021	-1.08
y_{15}	1660.048	1660.05	-0.0022	-1.34
	1660.048	1660.05	-0.0022	-1.34
y_{14}	1603.027	1603.029	-0.0016	-0.99
y_{13}	1489.938	1489.945	-0.0065	-4.35
	1489.938	1489.945	-0.0065	-4.35
	1489.938	1489.945	-0.0065	-4.35
y_{11}	1304.828	1304.829	-0.0009	-0.67
	1304.828	1304.829	-0.0009	-0.67
y_6	835.5501	835.5524	-0.0023	-2.75
y_4	542.3904	542.3923	-0.0019	-3.54
b_{19}	1887.075	1887.078	-0.003	-1.6
b_{17}	1593.917	1593.918	-0.0008	-0.48
b_{12}	1124.641	1124.641	-0.0005	-0.42
	1124.641	1124.641	-0.0005	-0.42
b_{11}	996.546	996.5465	-0.0005	-0.51
	996.546	996.5465	-0.0005	-0.51
b_{10}	939.5246	939.525	-0.0004	-0.47
	939.5246	939.525	-0.0004	-0.47

Ion	Observed Mass (Da)	Theoretical Mass (Da)	Mass Error (Da)	Mass Error (PPM)
b_9	826.4405	826.441	-0.0004	-0.51
b_8	769.4191	769.4195	-0.0004	-0.53
	769.4191	769.4195	-0.0004	-0.53
b_7	641.3246	641.3245	0.0001	0.16
b_6	584.303	584.3031	-0.0001	-0.22
b_5	527.2816	527.2816	0	0.04
b_4	399.1866	399.1867	-0.0001	-0.25
b_3	342.165	342.1652	-0.0002	-0.47

Appendix B

Conference Attendance and Presentations

3rd Annual RASOR Conference (November 2008). *Drymen, UK.*

Poster: Tracking Histone modifications with FT-ICR MS.

6th EMSG Symposium (September 2009). *Ardgour, UK.*

Oral Presentation: Development of a novel ESI source for protein structural studies.

4th Annual RASOR Conference (December 2009). *Stirling, UK.*

Poster: Lactate is an Inhibitor of Histone De-Acetylation.

Summer School in Mass Spectrometry for Biotechnology and Medicine (July 2010). *Dubrovnik, Croatia.*

Poster and Oral Presentation: Characterising Histone Modifications during senescence by FT-ICR MS.

Edinburgh Physical Chemistry PhD Meeting (August 2010). *Firbush, UK.*

Poster: Lactate is an inhibitor of Histone Deacetylation.

7th EMSG Symposium (September 2010). *Ardgour, UK.*

Oral Presentation: Characterising Histone Modifications in senescent cells by FT-ICR MS

Mass Spectrometry for the Medical and Life Sciences: The Role of High Field FT-ICR Mass Spectrometry (September 2010). *Edinburgh, UK.*

Delegate.

59th ASMS Conference on Mass Spectrometry and Allied Topics (May 2011). *Denver, Colorado, USA.*

Poster: Analysis of histone post-translational modifications specific to Rett syndrome by FT-ICR mass spectrometry.

Poster: Top-Down Precursor Acquisition Independent From Ion Count.

Edinburgh Physical Chemistry PhD Meeting (August 2011). *Firbush, UK*.

Oral Presentation: Fourier Transform Ion Cyclotron Resonance Mass Spectrometry of Histone Proteins. **Winner, Best Talk!**

8th EMSG Symposium (September 2011). *Ardgour, UK*.

Oral Presentation: Fourier Transform Ion Cyclotron Resonance Mass Spectrometry of Histone Proteins.

Publication Reprints